

THE UNIVERSITY *of* EDINBURGH

This thesis has been submitted in fulfilment of the requirements for a postgraduate degree (e. g. PhD, MPhil, DClinPsychol) at the University of Edinburgh. Please note the following terms and conditions of use:

- This work is protected by copyright and other intellectual property rights, which are retained by the thesis author, unless otherwise stated.
- A copy can be downloaded for personal non-commercial research or study, without prior permission or charge.
- This thesis cannot be reproduced or quoted extensively from without first obtaining permission in writing from the author.
- The content must not be changed in any way or sold commercially in any format or medium without the formal permission of the author.
- When referring to this work, full bibliographic details including the author, title, awarding institution and date of the thesis must be given.



THE UNIVERSITY of EDINBURGH

Developing active biomaterials for implantable devices

Platforms to investigate capacitive charge based control of biofouling

Paul Sullivan BVMS MRCVS

A thesis presented for the degree of

Doctor of Philosophy

School of Engineering

University of Edinburgh

2022

I declare that this thesis has been composed solely by myself and that it has not been submitted, in whole or in part, in any previous application for a degree. Except where stated otherwise by reference or acknowledgment, the work presented is entirely my own.

Paul Sullivan

24/01/2023

Abstract

Implantable devices, in particular biosensors, have clear utility within medicine, but face a hurdle to long-term function due to adsorption of biomolecules (biofouling) and subsequent immune response to implants, the foreign body response (FBR). Strategies to control this immune reaction have included material selection, drug release and, more recently, engineered surface properties. The increasing use of embedded electronics within many classes of implanted devices presents an opportunity to exploit electromagnetic phenomena at the device surface to mitigate biofouling and FBR. Such active biomaterials would allow dynamic modification of the apparent material properties of an implanted device.

A hypothesis was developed that biological interaction with a biomaterial surface can be altered by capacitive charging. A platform was constructed to test this and related hypotheses around cell and protein surface interactions *in vitro* and adapted into a second platform for initial characterisation work on an early *in vivo* model using chick eggs. These platforms were designed to be easy to fabricate and to provide multiple electrical connections into a substrate in contact with biological solutions or tissue.

Electrodes were fabricated from fluoropolymer coated tantalum pentoxide, a high-κ dielectric, and compared against adjacent, identically coated, silicon dioxide regions. Cells from the MDA-MB-231 cancer cell line were cultured on these regions under electrical stimulation. A voltage dependent reduction of cell attachment and spreading was detected on capacitively charged surfaces compared to uncharged controls. The tentative results, suggest capacitively charged surfaces hold promise as active biomaterials. A second cell type MCF-7 did not reproduce the effect, implying a more coherent understanding is required of the mechanisms behind cell surface interactions on these surfaces.

Multiple independent bioelectrochemical cell-surface interactions were observed using the platform and several quantification techniques were successfully employed. It is therefore argued that the platform may have wide applicability as a future research tool.

Lay Summary

Implantable sensors have the potential to greatly impact the management, detection and monitoring of disease. However, significant obstacles to the development of sensors for chronic implantation are the interdependent effects of biofouling and tissue foreign body response(FBR). Biofouling is the 'sticking' of proteins to the surface of an implant, which can effect sensor function, but can also cause the immune system to react, further impeding the function of the sensor. These effects often result in premature sensor failure, contributing a significant source of noise and inaccuracy in measurements. Strategies such as developing new biomaterials or releasing drugs from within implanted devices have been attempted. Electric stimulation of the body forms the basis of one of these strategies. This is attractive as many sensors now contain embedded electronics, meaning implementing a electrical solution would be possible almost universally. However, causing electrical currents to flow between tissues and implants creates by-products that can be toxic to cells and may exacerbate reaction. A hypothesis was explored, that biological interaction with an implant surface could be controlled electrically and without significant current by creating implant surfaces that behave like capacitors. In a capacitor, charge can be built up on one side of the device by applying a voltage and an insulation layer prevents current from continuously flowing.

This idea was explored by creating experimental platforms to allow capacitive charge to be tested with cultured cancer cells. A voltage dependent effect was found where cell attachment to the simulated implant surface was reduced compared to control surfaces lacking additional charge. This was observation is consistent with known cell behaviour on conventional electrodes and with current biophysical understanding.

The platform was adapted for application to an animal model using chicken eggs. The viability of this approach was investigated. It was concluded that this model may be useful for early stage research into biological interaction with electrical phenomena.

Acknowledgements

I am grateful to the EPSRC and CDT-ISM for accepting me as a student, funding my PhD research and providing a solid foundation in the science of sensing and measurement.

I would like to thank all those at the SMC for contributing to a such friendly environment in which to work. The great conversations in the break room were equal parts intellectually stimulating and hilarious. All the friends I have made, with whom I shared the highs and lows of research and life.

In particular, Cami and Andreas for their help with tools and processing. Also Stewart Ramsay, Ewan Macdonald and Richard Blair for keeping the tools running, particularly after I had been near them! Anthony Walton and Yifan Li for the many useful discussions over the years.

At the IGMM: Carol Ward, Mark Gray, James Meehan and Maria Bonello for showing me the ropes of mammalian cell culture and helping with protocols. At the Roslin Institute: Lynn McTeir and Tatiany Silveira for their help with the egg work, Rhona Muirhead for all things lab related, Scott Maxwell for sharing his knowledge of histopathology processing and Graeme Robertson for his help with microscopy.

I am grateful Alan Murray for sharing his wisdom and for providing a unique opportunity to participate in, and contribute to, the IMPACT project.

To my supervisor, Jon, for his input, the professional excellence of his supervision and patient advice throughout my PhD I extend many thanks and respect.

My parents for their help and support, particularly my father for his sage advice and proofreading.

I am indebted to my partner Jaynie, whose constant support, cups of tea, encouragement and understanding of the trials of PhD life went far and beyond any reasonable expectation, and without whom this thesis would not exist. Lastly, our daughter Poppy for the inspiration she provides every day.

Contents

Abstract i

Lay summary ii

Acknowledgements iii

Figures x

1 Introduction 1

1.1 Historical perspective 4

1.2 The case for active biomaterials 4

1.3 Hypothesis 5

1.4 Aims & objectives 6

1.5 Key outcomes 6

1.6 Overview of the thesis 7

2 Background 9

2.1 Immune response 9

2.1.1 Innate vs acquired immunity 10

2.1.2 Injury 11

2.1.3 Blood coagulation 11

2.1.4 Provisional matrix formation 12

2.1.5 Acute inflammation 13

2.1.6 Chronic inflammation 13

2.1.7 Granulation tissue 14

2.1.8 Foreign body response 14

2.1.9 Quiescence & reactivation . . . 15
2.1.10 Effects of disease . . . 15
2.2 Biofouling . . . 15
2.2.1 Adsorption phenomena . . . 16
2.2.2 Vroman effect . . . 18
2.2.3 Adsorption examples . . . 20
2.2.4 Measurements . . . 23
2.2.5 Biophysical basis . . . 23
Thermodynamic . . . 24
Intermolecular forces . . . 26
2.3 Consequences for implants . . . 28
2.4 Electrically active biomaterials . . . 29
2.4.1 Irreversible . . . 31
2.4.2 Reversible . . . 34
2.4.3 Capacitive . . . 36
Active . . . 37
Passive . . . 39
2.4.4 Literature analysis . . . 42
2.5 Platforms for electrical stimulation . . . 46
2.6 Conclusion . . . 51

3 *in vitro* device platform **52**

3.1 Platform design . . . 53
3.2 Device design . . . 55
3.3 Mask design . . . 55
3.4 Silicon wafers . . . 57
3.5 Thermal oxidation . . . 59
3.6 Photolithography . . . 59
3.7 Electrode Deposition . . . 59
3.8 Contact deposition . . . 60
3.9 Anodisation . . . 60
3.9.1 Anodisation setup . . . 61

3.10 Anodisation test structure . . . 63
3.11 Fluoropolymer Layer . . . 71
3.11.1 Deposition . . . 71
3.11.2 Contact angle measurements . . . 71
3.12 Atomic force microscopy . . . 72
3.13 Dicing & storage . . . 74
3.14 Ancillary platform components . . . 74
3.14.1 PCB . . . 74
3.14.2 PCB design . . . 75
3.14.3 Well assembly and holder . . . 76
3.14.4 Power supply and connection setup . . . 78
3.15 Discussion . . . 79
3.15.1 Fluoropolymers . . . 82
3.16 Conclusion . . . 86

4 *in vitro* experiments **87**

4.1 Cell culture . . . 88
4.1.1 Subculturing . . . 89
4.2 Preparing a cell stimulation experiment . . . 90
4.3 Microscopy . . . 92
4.4 Quantification algorithms . . . 93
4.4.1 Cellularity measure . . . 94
4.4.2 Labelling . . . 94
4.4.3 Interpretation of Edge density . . . 95
4.4.4 Springback . . . 96
4.4.5 Aluminium electrode cell distribution . . . 96
Calculation . . . 96
Process . . . 98
4.4.6 Luminance . . . 99
4.4.7 pH tracking . . . 100
4.5 Statistical analysis . . . 100
4.6 Staining and fluorescence imaging . . . 101

4.6.1 Fluorescence protocol . . . 101
4.7 Gasket and leachate test . . . 103
4.8 Cell survival on Cytop® . . . 104
4.9 Electrical stimulation . . . 104
4.10 Springback effect . . . 104
4.11 Capacitive charging . . . 110
4.12 Cell distribution near an aluminium electrode . . . 113
4.13 Discussion . . . 116
4.13.1 Measurement and quantification . . . 118
4.13.2 Protein adsorption . . . 122
4.13.3 Protocol . . . 123
4.13.4 Cell lines . . . 124
4.13.5 Springback . . . 125
4.13.6 Aluminium electrodes . . . 126
4.13.7 Cell properties . . . 128
4.13.8 Material properties . . . 132
4.13.9 Electrical . . . 133
4.14 Conclusion . . . 134

5 *in vivo* device platform **136**

5.1 Parametric design . . . 137
5.2 Processes . . . 141
5.3 Maskless photolithography . . . 143
5.4 Metals deposition . . . 143
5.5 PECVD silicon nitride . . . 144
5.6 Reactive Ion Etching (RIE) window . . . 144
5.7 Anodisation . . . 144
5.8 Deep reactive ion etching . . . 144
5.9 Fluoropolymer . . . 146
5.10 Dicing . . . 146
5.11 Needle test structures . . . 146
5.12 Ancillary platform components . . . 147

5.13 Bilayer resist processed using maskless lithography . . . 150
5.13.1 Bilayer test structures . . . 153
5.14 Discussion . . . 160
5.15 Conclusion . . . 163

6 *in vivo* model 164

6.1 Egg collection . . . 165
6.2 Culturing . . . 166
6.3 Device sterilisation . . . 166
6.4 Batches . . . 166
6.5 Experimental procedure . . . 168
6.5.1 Opening procedure . . . 168
6.5.2 Implantation procedure . . . 169
6.5.3 Monitoring . . . 169
6.6 Live imaging . . . 172
6.7 Collection and histology . . . 172
6.8 Microscopy . . . 173
6.9 Measurement of responses . . . 174
6.10 Candling . . . 174
6.11 Candling accuracy . . . 175
6.12 Egg mortality . . . 175
6.13 Embryo survival . . . 176
6.13.1 Storage . . . 177
6.13.2 Batch comparison . . . 178
6.13.3 Effects of implantation and opening . . . 178
6.13.4 Membrane disruption . . . 180
6.13.5 Needle parameters . . . 181
6.14 Pathologies . . . 181
6.15 Histopathology . . . 183
6.15.1 Z-stack imaging . . . 185
6.16 Discussion . . . 191
CAM as a model . . . 191

Egg survival and optimisations 194
Quantification and histology 199
Needle insertion and optimisation 201
CAM sensors 202
6.16.1 Recommendations 204
6.17 Conclusion 205

7 Conclusions **208**
7.1 Summary 208
7.2 Conclusions 209
7.3 Future work 210

Glossary **211**

References **217**

List of Figures

1.1 Overview of the issues in implanted sensor design. 2

1.2 Analogy of maritime biofouling with implanted biomaterials. 3

2.1 Phases of the immune response 11

2.2 Protein adsorption phenomena 17

2.3 Simplified representation of cell adhesion mechanisms. 22

2.4 List of measurement techniques used to quantify biofouling 23

2.5 Protein energy landscape 25

2.6 The elbow effect. Electric double layer (EDL) 26

2.7 Platform literature examples: images. 47

2.8 Platform literature example: multi-well stimulation device 48

2.9 Platform literature examples: schematics. 49

2.10 Platform literature examples: schematics - continued. 50

3.1 *in vitro* platform setup overview. 53

3.2 *in vitro* platform culture chamber. 54

3.3 *in vitro* platform layer stack. 55

3.4 Microfabrication steps to produce the *in vitro* platform. 56

3.5 *in vitro* platform variants. 57

3.6 Key features of the fabricated components of the *in vitro* platform. 58

3.7 *in vitro* platform mask pseudocontact. 58

3.8 Anodisation setup. 61

3.9 Closeup view of anodisation setup. 62

3.10 Tantalum pentoxide film colours. 63

3.11 Ta_2O_5 anodisation curves: test structures 66

3.12 Ta_2O_5 anodisation curves: initial current 67
3.13 Ta_2O_5 anodisation curves: cumulative charge 67
3.14 Capacitance test structure profilometry. 68
3.15 Capacitance test structure heat map. 69
3.16 Capacitance test structure examples. 70
3.17 Capacitance test structure anodisation window. 70
3.18 Droplet morphologies on varying substrates. 73
3.19 Atomic force microscopy of spin coated fluoropolymers. 74
3.20 Surface roughness, atomic force microscopy. 75
3.21 Printed circuit board. 76
3.23 *in vitro* platform comparison. 77
3.24 Equivalent circuit of device stackup. 81

4.1 MDA-MB-231 and MCF-7 cell lines. 90
4.2 Assembled *in vitro* device with culture media. 91
4.3 Image processing crop mask. 93
4.4 Example microscopy field showing device electrodes. 94
4.5 Example microscopy image processing. 95
4.6 Interpretation of edge density. 95
4.7 Example edge-electrode distance calculation. 97
4.8 Edge-electrode distance geometry. 98
4.9 Aluminium electric fence image processing. 99
4.10 Fluorescent microscopy image. 103
4.11 Springback MDA-MB-231 Permanox®. 106
4.12 Springback MDA-MB-231 5V. 107
4.13 Springback MDA-MB-231 17V. 107
4.14 Springback MCF-7 15V. 108
4.15 Springback gradients. 108
4.16 Mean image hue after removing from incubator. 109
4.17 Edge density distributions on electrode and control regions. 112
4.18 Aluminium electrode: cell redistribution example. 113
4.19 Aluminium electrode: edges and pixels 114

4.20 Aluminium electrode: edge density . . . 115
4.21 MDA-MB-231 5v 24hr uniformity . . . 115

5.1 Schematic setup of CAM *in vivo* electrical stimulation. . . . 137
5.2 Schematic *in vivo* needle device with parameters and fabricated device. . . . 140
5.3 Microfabrication steps to produce the *in vivo* platform. . . . 141
5.4 Microfabrication steps to produce the *in vivo* platform - continued. . . . 142
5.5 Scanning electron microscopy (SEM) image of a needle device . . . 145
5.6 Needle test structure wafer map . . . 148
5.7 Needle test structures diced. . . . 148
5.8 3D printed holder for *in vivo* devices. . . . 149
5.9 3D printed holder for *in vivo* devices - assembled. . . . 149
5.10 Comparison of photoresist approaches. . . . 150
5.11 Lift-off failure of patterned aluminium film. . . . 150
5.12 Example of maskless processing of a bilayer resist. . . . 151
5.13 Bilayer linewidth test structure. . . . 155
5.14 Bilayer test structure feature formation. . . . 156
5.15 Bilayer test structure QR code processing. . . . 156
5.16 Bilayer test structure kernel. . . . 157
5.17 Bilayer test structure analysis. . . . 157
5.18 Bilayer test structure features classified. . . . 158
5.19 Bilayer test structure results. . . . 158
5.20 Bilayer photoresist, patterned with platinum electrode. . . . 159

6.1 Major anatomical features of the CAM. . . . 165
6.2 Sterilised *in vivo* device and needle test structures ready for implantation. . . . 167
6.3 Timeline for batches A and B. . . . 167
6.4 Egg candling showing airspace. . . . 168
6.5 Open egg showing the the edge of removed shell membrane. . . . 169
6.6 An opened egg with the shell membrane removed. . . . 170
6.7 Setup for egg opening and implantation. . . . 171
6.8 Live image implant site. . . . 171

6.9 Live image of the surface of the CAM showing the micro-vasculature. 172
6.10 Excised egg CAM tissue showing implants. 173
6.11 Candling classification and egg state on opening. 176
6.12 Egg viability on opening. 177
6.13 Kaplan-Meier curve showing embryo survival. 180
6.14 Egg pathology examples 184
6.15 CAM vascular structures - histopathology 185
6.16 Cross-section of normal CAM - H&E. 186
6.17 Exised CAM tissue and implant site at three magnifications. 187
6.18 Example whole-slide image of CAM, H&E. 188
6.19 3D reconstruction of z-stack whole-slide scan. 188
6.20 Live image of implanted test structure. 189
6.21 Test structure (central design) *in-situ* examined during experiment. 189
6.22 Identified implant site on whole-slide scan. 190

List of Tables

2.1 Physical characteristics and order of Vroman proteins (human). 19

2.2 Comparison of electrically active biomaterials literature. 44

2.3 Comparison of electrically active biomaterials literature – continued. 45

3.1 Specifications of the *in vitro* platform. 54

3.2 Tantalum capacitance test structures. 66

3.3 Water contact angles of substrate materials. 72

4.1 Key properties of the two cell lines used in the *in vitro* work. 90

4.2 Cellularity edge densities 111

4.3 Cellularity paired statistical analysis. 111

4.4 Electrolytes composition of Dulbecco's Modified Eagle Medium(DMEM) . . . 130

5.1 *In vivo* device and test structure parameters. 139

6.1 Batch survival statistics 179

6.2 Egg survival statistics. 180

6.3 Egg survival statistics - shell membrane removal. 181

6.4 Egg survival statistics - structure parameters. 182

Chapter 1

Introduction

"Biocompatibility is the single most complex issue facing any *in vivo* sensor developer."

Marc Madou, *Fundamentals of microfabrication*, CRC Press[1].

Implanted devices, and in particular sensors, have great potential utility within medicine. Their increased adoption could lead to improvements in the accuracy of diagnosis, prognosis and monitoring of disease. This is through promised availability of hitherto inaccessible measurements, both in terms of precision, and spatial & temporal resolution. This is a consequence of the intimate association of such devices with biological tissues, which can remain in contact continuously.

In recent years, some devices (most notably glucose sensors), have successfully reached a sufficient level of technological maturity to allow commercialisation. This has in part resulted in a worldwide health sensors market that is projected to reach $83.2 billion by 2025[2].

However, several challenges have been perpetually present since the earliest achievements in this area, resulting in the failure of many promising systems to advance past proof of concept and bench phases of development. In particular, two interdependent mechanisms: the immune response to implanted materials, sometimes termed the foreign body response (FBR) and the accumulation of biological material on a biological surface (biofouling).

These effects often result in premature failure of the sensor, through passivation of

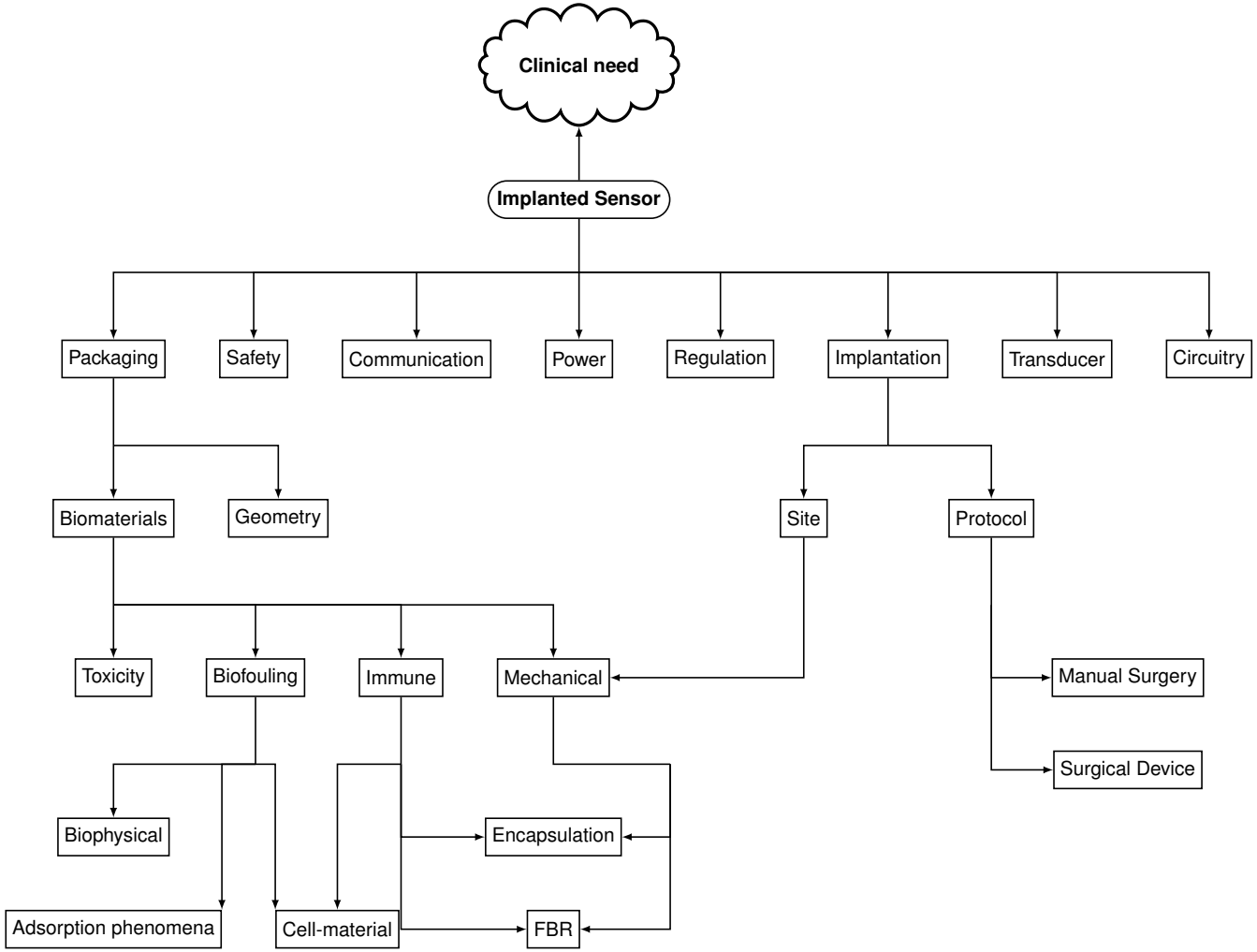


Figure 1.1: Overview of the issues in implanted sensor design.

electrodes, degradation of packaging and finally isolation from the analyte or measurand of interest. Despite many proposed strategies, a reliable solution to chronic implantation has remained illusory. An overview of the issues involved in developing implanted sensors, expanded in the areas that this thesis focuses on can be seen in Fig 1.1. Strangely, the two most prominent subjects of biofouling research simultaneously appear on the surface to have little in common: biomaterials and maritime applications. In the latter, accumulation of flora and fauna on ships hulls is responsible for significant increases in fuel consumption to shipping[3]. This results in requirement for lengthy and frequent dry docking of ships for cleaning and has stimulated intense research into coatings and other strategies to prevent and reduce the issue[4]. In the case of biomaterials, it is ultimately a combination of intermolecular and surface forces between biological molecules and foreign material that results in interference with transducers and exacerbates the immune response. Parallels can be drawn between these seemingly disparate areas by considering that both involve setting artificial objects loose into a salty solution which is teeming with life, hostile to its presence and willing to take any opportunity to cause its destruction, Fig 1.2.



Source: Glenn Batuyong , licensed under CC BY 2.0.

(a) A worker cleans biofouled material from the hull of a ship.



Source: 1887, wood engraving by Edgar Etherington, 'The Kraken, as seen by the eye of the imagination.', Public domain.

(b) Fortunately, events analogous to immune response are rare at sea.

Figure 1.2: Analogy of maritime biofouling with implanted biomaterials.

1.1 Historical perspective

Implanted electronic devices have a long history of application within medicine, beginning with the early success of the first cardiac pacemakers[5] in the 1950's, closely followed by cochlear implants[6]. These ultimately built upon electrophysiological insights tracing back to Volta and Galvani. The vision of autonomous devices that could monitor health and track the progression of disease, even intervene where appropriate emerged soon after the invention of the transistor. The replacement of vacuum tubes made fully implantable electronic devices, including transducers, possessing integrated power and communication systems, a realisable goal[7]. As a result, the evolution of implanted medical devices along with much of modern medicine has in many ways been inextricably linked with progress in electronics and in particular miniaturisation, along with the reduced power consumption that this entails.

Concurrently, development of new classes of materials, and in particular polymers started a tradition of testing any new material for biological response to implantation. Such empirical investigation of the 'biocompatibility' of a material is routinely carried out on any newly developed material, for the purposes of safety but also in the hopes of identifying materials with combinations of properties that would be desirable in a biologically contacting material. This approach has its roots with the famous example of the discovery of the low tissue reactivity of Poly(methyl-methacrylate) PMMA[8]. Harold Ridely discovered an apparent lack of reaction to intraocular foreign bodies composed of the material in contrast to similarly positioned glass particles in Royal Air Force pilots during the second World War.

More recently, numerous continuous glucose monitors, for control of diabetes have been marketed and neuroprosthetics is recognised as an emerging technology[9] with many concurrent efforts to commercialise devices to restore function in cases of stroke, paralysis, epilepsy and neurodegenerative disorders[10].

1.2 The case for active biomaterials

Much work has been done in characterising and explaining the deleterious effects of the FBR, partially in terms of biofouling. Biofouling is in turn dependent upon forces, inter-

molecular and thermodynamic in origin, that can be related to material properties. Investigation of the role of material interactions with immune cells and proteins has proven fruitful in producing heuristics that can aid the rational design of biomaterials. A consistent goal has been to prevent biofouling by creating anti-fouling surfaces. The biological response to materials is, however, a dynamic process and prevention of protein adsorption is not always well aligned with desired outcomes in terms of biocompatibility. As a result, material selection alone, despite ever increasing sophistication has proven insufficient in producing acceptable outcomes.

A potential solution is to design biomaterials with a dynamic component, that can evolve and respond along with the tissue into which it is implanted. Several examples of such 'active biomaterials' have been proposed, however two factors influenced the decision to focus on electrical phenomena. Firstly, many functions of cells, tissues and proteins, as well their interactions with foreign materials can be explained and, in some cases, manipulated using electric phenomena. Secondly, the routine embedding of electronics within implantable biosensor designs provides an opportunity to use and modify pre-existing techniques and processes with very little increase in manufacturing, or design, complexity.

Electrical stimulation of tissue has a long history, but a desire to avoid the adverse effects of electrochemical interactions that normally accompany use of bioelectrodes led to consideration of purely capacitive means of altering surface properties.

1.3 Hypothesis

This thesis examines the hypothesis that constructing an electrified biointerface, including an interposed dielectric layer between the electrode and the solution and tuned surface chemistry, allows manipulation of the biological response to a surface while avoiding the deleterious consequences of charge transfer seen with bioelectrodes. If biological interaction with a surface could be directed capacitively then another question followed. By enforcing capacitive charge only, using device construction rather than through electronic control are physical states dynamically accessible, that would otherwise not be possible, without damaging side effects?

1.4 Aims & objectives

This thesis aimed to develop strategies for integrating sensors into tissue using active biomaterials. Specifically by evaluating the use of capacitive charging on biological interactions with surfaces.

To achieve this, a reliable means of performing experiments had to be established through the development of experimental platforms.

Biofouling and immune response of the body will be reviewed. To relate material properties, surface charge and interfacial phenomena to cell material interactions and the outcome of the immune response. Through this process a basis for rational design of this class of biomaterials may be established. Following this *in vitro* and *in vivo* testing of the hypothesis was pursued.

Ultimately the thesis aims to provide further insight on the question of whether the effects of electrical modulation, and capacitive charging in particular, of healing and dynamic manipulation of surface properties has a place in the growing toolbox of biointegration strategies for implanted devices. It will do so by meeting several key objectives:

- Construct and validate a platform to enable *in vitro* investigation of microfabricated structures, in particular for cell and protein interactions with surfaces that are electrically charged.
- Construct a platform for use with a developed *in vivo* model to study the same phenomena.
- Develop mechanisms to quantify the responses provoked within each platform.
- Perform, analyse and interpret tests of the platforms with *in vitro* and *in vivo* models.

1.5 Key outcomes

- Capacitively charged surfaces can dynamically influence the biology of the interface.
- Biologically impactful capacitive charge can be achieved using physical construction of a surface, rather than circuit based control.

- The developed *in vitro* platform can be used to investigate biointerfacial phenomena.
- An model based on chick embryos can be used with a parameterised needle electrode platform to observe an immune response *in vivo* .

1.6 Overview of the thesis

Chapter 2 contains background on the the twin issues of FBR and biofouling along with a review of the literature on electrical approaches to the creation of active biomaterials that are relevant to the thesis. Also included is a survey of platforms that have been described for performing these investigations.

Chapter 3 describes the development of a platform for *in vitro* investigation of capacitively charged surfaces. Aspects of design, processes, fabrication and characterisation are discussed.

Chapter 4 details *in vitro* experiments carried out using the platform which was developed in Chapter 3 and demonstrates the utility of the platform. These investigations sought to answer the research question on capacitive charging biomaterial surfaces and centred on the characterising the ability of two immortalised cancer cell lines to attach and spread on the device surface in the presence and absence of applied charge. Voltage dependent effects on cell-surface interactions are demonstrated along with influence on cell detachment rates.

Chapter 5 describes the development of a second platform, this time aimed at *in vivo* investigation. This platform shares many features of the *in vivo* platform and take the form of needle electrodes designed to be implanted into chick embryos. Novel software was created to aid the development of this platform involved parameterisation of designs and process development, which also benefitted from novel automation of process development, particularly in the use of maskless lithography.

Chapter 6 details the development of an *in vivo* model based on the chorio-allantoic membrane, which is found within developing chick eggs. This model was compatible with the *in vivo* platform developed in Chapter 5. Here the details of working with chick eggs including factors influencing survival of the embryos. Implantation of fabricated needles is described and visualisation of an immune response at the implant site is demonstrating the capacity

of the model to allow investigation of the immune response to electrified interfaces. Performance of the model to implantation is discussed with reference to recent literature and recommendations for optimisations are made.

Chapter 7 summarises the thesis, draws together the conclusions and suggests the direction of future work.

Chapter 2

Background

Biomaterials encompass a wide field, crossing several disciplines, from immunology, material science, chemistry and biochemistry with, more recent, contributions from microfabrication and electronics. These are materials that are selected for their ability to interact favourably when placed in contact with biology. A related term, biocompatibility, refers to a material or device that is able to achieve the function for which it was engineered after implantation or other association with the body.

When investigating active electrically modifiable surfaces multiple issues must be considered. There is a wide-based literature covering many aspects, mechanisms and principles of control of the foreign body response and biofouling. This chapter provides a concise background in Sections 2.1 - 2.2, while including details pertinent to an understanding of the rationale behind electrically active biomaterials and the remainder of the thesis. This is followed by a more detailed review of electrically active biomaterials, Section 2.4, and the platforms, Section 2.5 used to investigate them.

2.1 Immune response

Implantation of any material will bring it into contact with the biological milieu. Especially where an injury has been created at the implantation site, a swift immune response follows involving components of the innate immune system. Failure to restore normal tissue architecture leads to a chronic manifestation of the immune response – termed the foreign body response (FBR). The immune response to implants represents an interconnected

sequence of events and behaviours orchestrated by multiple types of immune cell. Some of these occur in parallel and others overlap in time, see Fig 2.1. For the purposes of understanding this complex system, it has been separated into a generally accepted sequence of reactions, an overview of which is provided below, based on excellent, detailed reviews[11,12,13,14]:

1. Injury
2. Blood coagulation
3. Provisional matrix formation
4. Acute inflammation
5. Chronic inflammation
6. Granulation tissue
7. Foreign body reaction
8. Fibrous encapsulation
9. Quiescence
10. Reactivation

Steps 1-6 are common to most injuries such as the healing of a wound. Failure of the normal homeostatic mechanisms meant to restore the tissue architecture is caused by continued presence of foreign material that cannot be degraded or absorbed. Ultimately, this results in a frustrated process, that leads to a variety of deleterious outcomes, particularly if the material forms part of a sensor. The timings of these stages depend on a number of variables, however approximate intervals are given for context.

The response in the brain differs in several ways from this general picture with different specialised cells fulfilling the roles that are described for other immune cells here. Comparative responses in the brain are the subject of some excellent reviews[15,16].

2.1.1 Innate vs acquired immunity

The immune system of mammals, including humans, is composed of two components: innate and acquired. Each component contains a number of subsystems that contribute to its function. The development of acquired immunity is often associated with response to an infectious disease through the production of antibodies. In sterilised implants using inert inorganic materials that aspect of the acquired part of the immune system is rarely considered important, all responses are assumed to originate in the innate system. However, some parts of the acquired system, specifically helper T cells, play a regulatory role

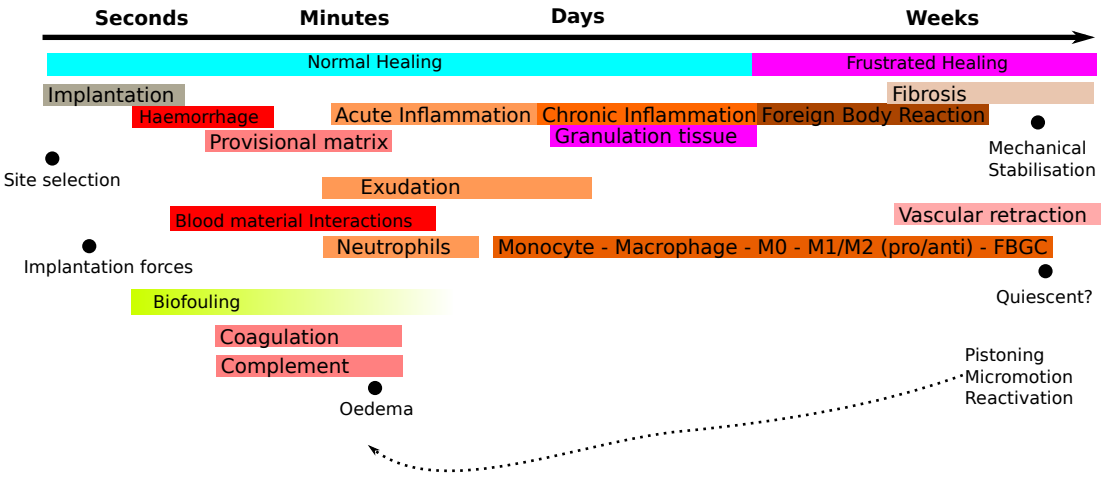


Figure 2.1: Phases of the immune response, after injury/implantation, show significant overlap.

in inflammation and have been shown to influence macrophage behaviour, in particular polarisation, influencing outcomes of the foreign body response[17,18,19].

2.1.2 Injury

Concurrent with implantation

Injury occurs where there is significant disruption to tissue architecture, triggering an immune response. Injury is characteristic of macroscopic implantation, acting as a trigger for subsequent immune processes. Implantation, implies the creation of a defect in tissue, this may be to access a potential or real anatomical space, but in most scenarios the implant is placed into this tissue defect, displacing surrounding tissue and forming an interface between artificial material and tissue that will subsequently form an implantation bed[20]. The response to implants is highly dependent on size[21] and shape[22,23]. However, all implants larger than microscopic[24,25,26], will initially cause vascular disruption, lymphatic disruption, and a variable amount of cell death by mechanical destruction or damage. Parenchymal (organ function) tissue will also be damaged and in neural applications, neuronal processes may be cut[27] causing local loss of function.

2.1.3 Blood coagulation

Seconds to minutes after injury

The coagulation of blood is one of the mechanisms through which blood flow is stopped

(haemostasis). The other being the passive elastic and active muscular, contraction of damaged blood vessels. Blood is a complex organ consisting of proteins and lipoproteins, other circulating molecules, red and white (immune) blood cells and platelets. The phenomenon of blood coagulation proceeds via multiple pathways of cascading signal amplification through blood factors, with several triggers (see Section 2.2). When blood is circulating normally through the vascular system and in the absence of disease, triggering mechanisms for this process are suppressed. Upon implantation both the extrinsic and intrinsic pathways can be activated[28]. Foreign materials trigger the intrinsic pathway by contact activation depending on properties such as wettability and surface charge[29]. The extrinsic pathway, by contrast, is mediated by factor III (tissue factor). Factor III is released from tissues and blood vessels damaged by injury[30]. Activation of the extrinsic pathway is not specific to implantation. The net result of this process is the conversion of the blood circulating fibrinogen to fibrin. Fibrin filaments produce a network with blood cells and platelets, in the injury site and on the implant, forming a clot.

Factor XII (Hagemans factor) forms the start of the intrinsic contact activating pathway. It is activated to factor XII_a by negatively charged surfaces, such as biomaterials. Positively charged biomaterial surfaces may also activate factor VII on the extrinsic pathway, bypassing tissue factor[31].

2.1.4 Provisional matrix formation

Minutes to hours after injury

The formation of this initial layer of proteins and cells at the site of implant is termed the provisional matrix. It is this structure that forms the basis for later remodelling by immune cells. Within the matrix, immune cells, platelets and the complement system produce chemical signals that attract further inflammatory cells and fibroblasts to the implantation site.

Within the complement system all three activation pathways have been implicated through direct interaction with the surface and with IgG from blood. Positive feedback loops are then started and complement products begin to attract immune cell migration and activate others[32]. Damaged cells release a variety of products that stimulate immune cells, these produces are collected under the terms damage-associated molecular patterns (DAMPs) or alarmins[33,13,32]. These interconnected sets of chemically mediated signals

also causes increased vascular permeability and blood flow to the area, further aiding immune cells to infiltrate from the blood. Fibrin fibres become further cross-linked, stabilising the network, which also contains cell attachment proteins allowing immune cells to navigate into and through the matrix. The matrix is ultimately resolved in subsequent steps by either fibrinolysis or remodelling to connective tissue. The cell adhesion protein fibronectin present in blood plasma is incorporated in the matrix and provides attachment sites for immune cells that arrive subsequently[34].

2.1.5 Acute inflammation

Minutes to hours after injury, may last days

In the acute phase of inflammation, immune cells and in particular neutrophils appear at the implant site, closely followed by monocytes that differentiate to form macrophages. These cells or their precursors move from the blood and surrounding tissue following chemical gradients emanating from the provisional matrix. Other cell types participate in the immune response, however neutrophils and macrophages[19] dominate in terms of number and influence and therefore are considered central to the immune reponse to biomaterials.

Both neutrophils[35] and macrophages[36] migrate to the implant site and attempt to consume foreign material by phagocytosis along with releasing enzymes in response to interaction with a biomaterial surface.

2.1.6 Chronic inflammation

Days to weeks after injury, may persist for years

Macrophages dominate this phase of inflammation. Macrophages release a number of products[37,38] that direct further inflammation, degrade extracellular matrix (ECM) proteins, produce reactive oxygen species[39], and various chemical signals that stimulate different behaviours at each stage of healing. The ECM is continuously remodelled by degradation and synthesis of matrix proteins during this stage[40]. Frustrated attempts to phagocytose the implant material result in macrophages fusing to form foreign body giant cells (FBGC)[41], which often become permanently resident on the implant surface. Macrophage and FBGC numbers begin to dwindle from day 7 to 30, while the population of fibroblasts increases[42].

2.1.7 Granulation tissue

Appears 3-5 days after injury

Angiogensis is the growth and development of blood vessels. Guided by fibrin material within the provisional matrix, capillary tubes grow from pre-existing vascular structures through the action vasculular endothelial cells. Fibroblasts activate and migrate, laying down collagen fibres that replace the provisional matrix. This leads to the development of a fibrous capsule. During wound healing a sequence of progressive replacement of provisional matrix fibrin with fibronectin, then fibronection/collagen(granulation tissue) and finally primarily collagen proceeds[43].

2.1.8 Foreign body response

Weeks to Months after injury

The FBR is an effect of frustrated healing[44]. Particular processes designed to regenerate damaged tissue are abandoned in favour of replacement of tissue with a fibrous tissue. The response is also characterised by:

- Sustained inflammation
- Continued presence of inflammatory cells
- Formation of a fibrous capsule
- Atrophy of vascular networks, withdrawal and isolation
- Contraction of fibrous capsule
- Possible calcification of capsular material

With the continued presence of foreign material, inflammatory triggers are maintained through release from macrophages and parenchymal cells that by failing to adhere to the implant surface destroy themselves[45,46]. Fibroblasts: cells that synthesise and maintain the ECM, produce an increasingly dense layer of fibrous collagen. This capsule is, primarily, composed of collagen fibres that are often highly oriented, encircling the implant[47].

2.1.9 Quiescence & reactivation

Providing that the stimuli promoting inflammation gradually decline then activity of surface macrophages and FBGC's similarly reduce their activity and eventually become quiescent. Multiple events can reactivate these cells, for example injury related to a mechanically unstable implant[48,49] or degradation of the implant material[50]. Periods of quiescence punctuated by reactivation may occur cyclically.

2.1.10 Effects of disease

Immune reaction can be modulated by the presence of disease, which may increase or decrease the severity of the reaction. For example rats with induced diabetes produce capsules of reduced thickness and lower macrophage activation compared to healthy controls[51]. Immune reactions are also modulated within tumours. Tests of responses to highly immunogenic cotton[52] and, more recently for several common materials used in biosensor fabrication[53], show a reduced reaction in tumour tissue.

2.2 Biofouling

Biofouling, the adsorption of biological material onto implanted surfaces, has been associated with influence on the outcome of immune reactions. In the context of implanted materials, biofouling is virtually synonymous with protein adsorption and so unless otherwise specified, the two terms with be used interchangeably through the remainder of the thesis.

Protein adsorption mediates biomaterial surface interactions with immune cells, augments cell attachment, triggers signalling cascades (coagulation and the complement system[54]). Hydration (wetting) is the first event that occurs on a surface upon submersion into a biofluid, which invariably follows implantation. A layer of water is deposited, potentially displacing gaseous and other environmental adsorbates[55]. This water film forms the structure that is subsequently displaced or modified by the arrival of biomolecules.

Biofouling in implant applications usually refers to protein interaction, but other dissolved chemical species can also act as adsorbates. These include amino acids, dissolved salts, other small molecules like apoliproteins[56] through to cells (particularly bacteria) and

even multicellular organisms (in the maritime application). The extent of influence of non-protein biomolecules on immune response is unclear.

For planar surfaces adsorption is the primary mechanism of interest. Absorption phenomena also occur in porous materials[57], particularly for proteins with mass lower than 15kDa. Protein-surface interactions have a significant influence on the development of the immune/healing response and FBR described in Section 2.1. Adsorbed protein layers with densities and thicknesses, on both polymers and crystalline solids, have been measured in the 0.6 ng mm^{-2} to 2.5 ng mm^{-2} and 1.5 nm to 9 nm ranges respectively[58,59].

2.2.1 Adsorption phenomena

Proteins display a bewildering array of behaviours during interaction with surfaces and a non-exhaustive selection of phenomena are shown in Fig 2.2. The multiple mechanisms of interaction for a single protein, and even on model surfaces, are not universally agreed upon, at least in terms of their precedence[60,61]. Interpretation and comparisons of literature results are also made difficult due to a wide variety of different measurement modalities employed. Complexity is also introduced due to the number of interacting components. Blood, which forms the biofluid initially interacting with most macroscopic implants, contains over 1000 different proteins, albeit distributed over several orders of magnitude in concentration under normal physiological conditions[60].

The phenomena observed to date of protein interactions on a surface extend beyond simple adsorption. Multilayer formation, jamming and screening, may all result in alterations to the efficiency of adsorption[62]. Individual proteins may also occupy multiple adsorption sites[63]. Subsequent dynamic interactions of proteins that can occur after adsorption can lead to reorganisation.

A common heuristic, concerning the conformation of proteins is that in solution they will exist at a local free energy minima[64]. This manifests with most hydrophobic side groups becoming buried in the core of the protein while hydrophilic amino acids will migrate to the exterior, interacting with the surrounding hydration shell[65]. This can be disrupted by interaction with a surface. It the surface is hydrophobic, for example, then conformational change will occur to present hydrophobic groups to the interface. If this reduces the interfacial tension of the surface sufficiently then adsorption may be essentially irreversible[66].

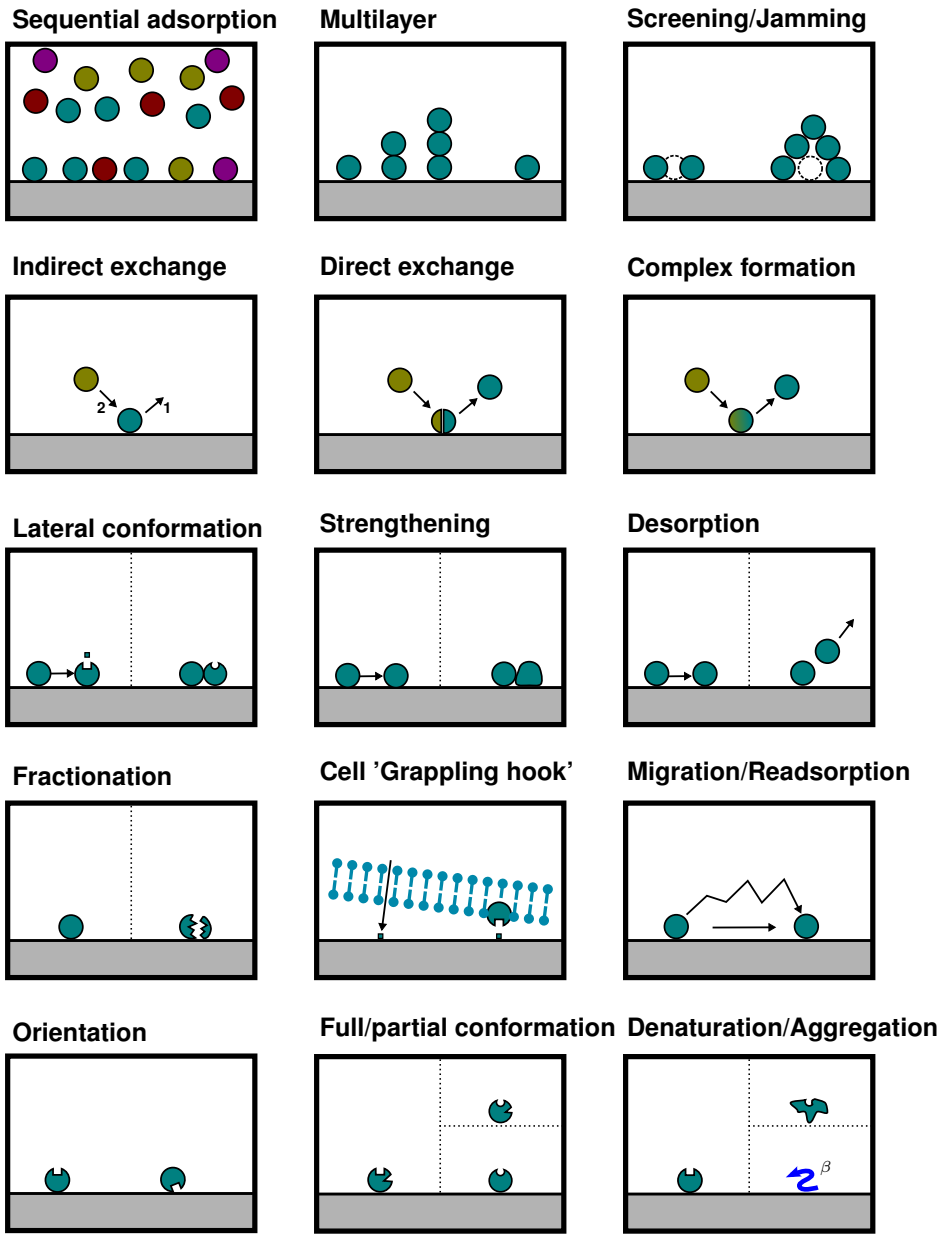


Figure 2.2: A number of phenomena have been described following protein interaction with biomaterial surfaces.

Conversely on hydrophilic substrates water can compete for adsorption sites so continuous exchange consisting of adsorption and desorption events can proceed[67,68].

Once adsorbed the strength of the interaction may increase as the protein can be multivalent in its binding sites[69]. This could occur through lateral transport of the bound protein across the surface[70] or via lateral interaction between proteins[71]. Adsorbed states may be much different from the bulk with conformational changes ranging in extremity from biologically equivocal (maintaining function) to full denaturation[72]. This can culminate in full loss of tertiary structure with aggregations of β sheet like proteins forming[73] or fragmentation of primary structure[74]. Lateral interaction and surface packing are dependent on solution concentration with high concentrations of proteins leading to looser layers as each molecule can claim future adsorption sites and is spatially limited in its capacity to increase adsorption strength by conformational change[75]. Proteins supporting cell-material interactions may be expressed by a cell already in contact with a surface[76].

Adsorption may occur preferentially in an orientation that does not present the active site to the solution side of the interface. This has been demonstrated in adsorbed protein films by probing using ToF-SIMS, which allows analysis of the distribution of amino acids released from the solution side of the adsorbed film[77]. Proteins may coexist in multiple adsorbed conformations following some surface dependent distribution[78] and with dynamic fluctuation occuring over seconds[79]. Proteins often have multiple functions and adsorption induced conformational change can interfere with some of these, while others are preserved[80]. A number of important protein adsorption phenomena are shown schematically in Fig 2.2.

As a result of this intractability and despite the emergence of heuristics, rational biomaterial design on the basis of control of protein biofouling remains illusory. When taken with the fact that the outcomes of adsorption processes interact in non-trivial ways with the complex machinery of the immune system it is easy to see why the design of biomaterials remains fundamentally empirical in nature.

2.2.2 Vroman effect

Proteins begin to arrive at a surface via diffusion through the interphase milliseconds after hydration, influenced by various biophysical properties. The order of protein arrival at a surface may also interact with the competitive exhange mechanisms described above influencing the evolution of the adsorbed protein film. Small molecular weight proteins arrive

first, especially those that minimise coulombic repulsion and possess an isoelectric point around pH 7 and are later displaced by larger (later arriving) proteins if they are better able to minimise surface free energy.

The eponymous *Vroman effect*[81] details an early observation that protein adsorption was a dynamic process in terms of evolution through time. Experiments used several model surfaces, including tantalum oxide. Consideration of the interplay of diffusion coefficients of common proteins, along with variation in thermodynamic favourability of adsorbate, leads to a view of the complex evolving nature of the interface.

Observations from – startlingly – simple experiments with blood-material interactions, requiring nothing more than a glass slide, microscope and a stopwatch were carried out. The results revealed that sequential displacement of five different proteins occurred over the span of the first minute of interaction with the artificial surface[82]. The relative surface concentrations of proteins of the resulting film may deviate significantly from the profile in the bulk.

Physical characteristics of the original five proteins studied by Vroman[82], along with a subsequently identified sequential protein (HMWK) are collected in Table 2.1 in order of exchange. Many of these play a significant role in mediating the immune response (see Section 2.2.3). As can be seen, proteins initially show a monotonic decline in diffusion coefficient and an increase in molecular weight with an inverse relationship to plasma concentration. Latterly these trends begin to break down, suggesting other properties, such as a more neutral isoelectric point in both factor XII and HMWK, becoming more influential along with time dependent effects.

Order	Protein	Molecular weight (kDa)	Diffusion coefficient (10^{-7} cm^2 s^{-1})	Isoelectric point (pH)	Plasma concentration (mg L^{-1})
1	Albumin	66.3[83]	6.1[84]	5.974[85]	40000[86]
2	IgG	160[83]	4.0[84]	5.5-6.7[87]	12390[88]
3	Fibrinogen	341[83]	2.0[84]	5.593[85]	270[86]
4	Fibronectin	460[60]	1.78[89]	5.432[85]	47[86]
5	Factor XII	80[90]	5.0[90]	7.533[85]	0.001[86]
6	HMWK	280[91]	-	6.475[85]	90[86]

Table 2.1: Physical characteristics and order of Vroman proteins (human).

Beyond the initial (transient) Vroman phase an equilibrium will be reached, arrival and interaction with a surface is then often modelled by a assuming random sequential adsorp-

tion[92]. Here, proteins in the bulk solution have a finite probability, based on concentration and other factors, of interacting with the surface and undergoing adsorption/desorption.

The transport of proteins through tissue to an interface *in vivo* is governed by diffusion and advection and the structure geometry of the extracellular space. Tortuosity reflects a ratio of effective diffusion coefficients to free diffusion coefficients and is influenced by properties of the extracellular matrix. Mechanisms underlying include geometric effects of actual path of a diffusing species versus total distance travelled, dead spaces and hinderances related to interactions with charged structures, biological binding and direct obstructive barriers.[93]. For example the volume fraction of extracellular space in brain is 20%, with a tortuosity around 1.6 with the gap between neighbouring cells begin approximately 50 nm[93,94].

2.2.3 Adsorption examples

The proteins in Table 2.1 have particular significance as mediators of several biochemical pathways in the immune reponse.

Albumin represents more than 50% of all blood plasma proteins and is the first protein to interact on contact with surfaces. It is involved in transport of molecules in the blood and in maintaining colloid-osmotic(oncotic) pressure. Albumin, at sub-physiological concentrations has been found to adsorb, forming a 4.8nm layer, 8 times the concentration of an equivalent lamina in bulk solution[61]. Arvidsson *et al.*[95] found that 70% of adsorbed radiolabelled human serum albumin was displaced from silicon surfaces within one minute by other proteins when introduced into solution. Titanium and (particularly) aluminium surfaces however, retained the majority of the albumin film for serveral hours. The authors also noted that the point of zero charge PZC of the materials corresponded with an expected electrostatic force between albumin and the surface producing net repulsion on silicon, a weaker repulsion on titanium and attraction on aluminium[95]. Albumin preferentially forms a saturating monolayer on the polymer Parylene-c but adsorbs at lower density on SiO_2, where it can be outcompeted by fibronectin in binary solution[58]. Cell attachment is low on albumin adsorbed surfaces when the solvated conformation is maintained and when adsorbed proteins that are attachment conducive, like fibronectin, are masked. Albumin

can, however, support cell attachment when conformation is disrupted, such as on fluoropolymers[66]. The potential extremity of time dependent effects was illustrated in another study[96]. Platelets can bind to adsorbed albumin if significant denaturation has occurred. Increases in platelet attachment were found on two SAM surfaces that were incubated at 37°C for six months. This change in biological function of the adsorbed layer corresponded with alterations in the secondary structure of the protein. Long-term prevention of desorption has also been achieved on the same surface via electrical stimulation[97]. This time scale extends well into the presumptive final FBR stage of the immune response to biomaterials. This suggests that the first protein to arrive at the interface could be dynamically contributing to its biological properties well after all detectable immune responses have fallen to minimal levels.

Immunoglobulins are a class of antibodies that bind to foreign material and present binding sites that activate and direct immune cells. The coating of materials in Immunoglobulin-G (IgG) is referred to as opsonisation. Depletion of igG from serum in contact with a dimethylsilane surface had a much larger influence by reducing macrophage interation and FBGC formation compared with removal of RGD containing proteins fibronectin and vitronectin[98]. Lutanie *et al.*[59] describe affinity of anti-IgG antibodies to IgG when adsorbed directly from solution but no activity when IgG replaced a pre-existing albumin protein layer by competitive exchange. The two fragments of the IgG protein behave differently from each other on adsorption when part of the intact protein. This behaviour is again different if the fragments are adsorbed seperately. This phenomena has been associated with differences in surface hydrophobicity of the two fragments[59].

Fibronectin is a component of the ECM that provides binding sites for cell attachment, interacting with cell membrane bound integrins, shown schematically in Fig 2.3. Simulation of fibronectin conformation on charged surfaces implies that the structural rearrangement may be subtle or involve global shifts in secondary and tertiary structures and that this situation can be influenced by surface charge[80]. Orientation on the surface was also necessary to expose an RGD binding domain. The time scale of single molecular behaviour of fibronectin adsorbed on glass, measured by FRET showed multiple events corresponding to conformational shifts/change occurring on the timescales of tens of seconds[79]. Fi-

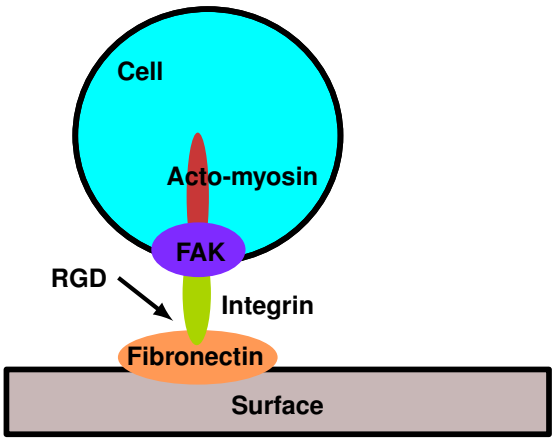


Figure 2.3: Simplified representation of cell adhesion mechanisms.

bronectin conformation, surface favourability and biological function are dependent on surface properties, including wettability[99]. As an example of partial denaturation of a multivalent protein: fibronectin conformational state, influenced by surface charge, can affect cell behaviour through signalling pathways that are independent of cell adhesion (integrin binding) functions[100].

Additionally, multiple adsorbed fibronectin conformations can simultaneously exist. These represent compact as well as more more extended forms associated with greater cell attachment[78]. Fibronectin has multiple domains with different functions. Adsorbed fibronectin has been shown to maintain integrin binding properties but lose the ability to perform a second function triggering a signal-transduction pathway[100].

Fibronectin is often outcompeted by albumin[101]. Pegueroles *et al.*[75] showed in a sequential adsorption experiment on TiO_2 that fibronectin adsorbed, at very low concentrations, on top of pre-adsorbed albumin. However, in the opposite scenario albumin was more able to displace pre-adsorbed fibronectin. The authors argued that this was not due to increased affinity of albumin for the surface but emerged from the smaller molecular mass of albumin and the associated advantages to transport that this entails.

Factor XII is involved in intrinsic pathway of blood coagulation. Interaction with negatively charged surfaces cleaves the protein, triggering the signalling cascade[74]. Procoagulant properties are undesirable in vascular implants due to increased risk of thrombus formation. Activation of the factor has been descibed by contact with denatured or misfolded proteins, including those induced by surface adsorption[102], while competition for adsorption sites limits activation on certain materials[103].

2.2.4 Measurements

- Radiolabelling (^{125}I)[59,104]
- Neutron reflectometry[71]
- Solution depletion[61]
- Solution spectroscopy[71]
- Desorption after rinsing[101,76]
- Ellipsometry[105]
- QCM[75,106]
- Field effect transistor[106]
- STReM[107]
- Differential scanning calorimetry[108]
- Circular dichroism[107,109]
- Fluorescence (FTIR)[73]
- Fluorescence (FRET)[79]
- ToF-SIMS[77,66]
- AFM[71,97]
- AFM-functionalised[110]
- SPR[111,106,112,113,76]
- Dual polarisation interferometry[58]
- Electron holography[114]

Figure 2.4: List of measurement techniques used to quantify biofouling

Measurement of protein adsorption can be achieved via a number of methods. Protein exchange and Vroman-like effects are often investigated with binary protein solutions[63]. These experiments allow competitive dynamics along with thermodynamic favourability to be probed, for example by reversing the order of arrival at the interface.

Many methodologies require colloidal suspensions of a biomaterial rather than planar surfaces[115] and so may be unsuitable for electrical stimulation expermiments. Trade-offs exist in terms of accuracy and the properties that can be measured[61]. For example loosely bound outer proteins in a multilayer will influence the resonant frequency of a quartz crystal microbalance (QCM) much less than those adsorbed directly to the surface possibly leading to viscoelastic effects and an underestimation of quantity[75]. Similarly, immune labelling techniques may result in underestimates of absolute adsorbate mass if, for example, a binding site is inaccessible. Although such techniques may, nevertheless, still accurately reflect the biological performance of the film. Some of the adsorption quantification and characterisation methods are listed in Fig 2.4, many of which have been reviewed for comparison[116].

2.2.5 Biophysical basis

The complexity of biofluids cannot be overstated, and this complexity carries over into understanding the behaviour of proteins and cells at biomaterial interfaces that determine the immune response to implanted material. However, interactions between the constituent

parts: surface, solvent(water), electrolytes, organic molecules, proteins, cells, matrix are all driven by intermolecular forces, and some observed phenomena can be understood in terms of thermodynamics[117].

The region of an electrolyte solution near a surface does not have the same properties as the bulk solution where electroneutrality, homogeneity and isotropy dominate. The situation is anisotropic and may hold a locally net charge influenced by charges bound to the surface.

Thermodynamic

Protein adsorption energetics include solvation, denaturation, entropic and enthalpic effects[118]. Enthalpy of adsorption, at least to hydrophobic surfaces is positive due to conformational changes[108].

The hydrophobic interaction is an entropic force. In aqueous solutions, it is driven by the tendency of water due to it polar nature to form a hydrogen bonded network[119,120]. Interaction with a surface constrains the molecular degrees of freedom reducing configurational entropy. The change in free energy of the protein adsorption and the entropic hydrophobic force competes against surface dehydration to determine the favourability of adsorption. The result is often that larger molecules are driven to the surface. These forces can have 10 to 100 times stronger attraction than dispersion forces between non-charged surfaces in water[121]. Proteins therefore act as a biosurfactant - reducing interfacial tension[60], indeed it has been observed that detergents can outcompete and displace the adsorption of proteins[111,122].

For a single component system, equilibrium is reached when the electrochemical potential of the adsorbed and bulk concentrations are equal. It is often found that if adsorbed concentration is greater than unity, individual proteins are adsorbed in excess of their bulk concentration. Additionally, adsorption often continues beyond a complete monolayer, implying multilayer protein films build on surface bound proteins, which provide adsorption sites for subsequent molecules that may be more loosely bound[61].

Many proteins, even in bulk solution would be at a thermodynamic minimum in a denatured state. This situation obviously does not occur in biological systems where protein stability is preserved through kinetic barriers, partially related to the interaction with water.

These barriers are removed or lowered in the adsorbed state, allowing proteins to transition to denaturation. This process can also involve inter-protein interactions and significant disruption of protein secondary structure[26]. Transitions between conformational states, partial denaturation and aggregation represent a progression towards reduced free energy made feasible by lowered kinetic barriers consequent upon adsorption. These are shown schematically in Fig 2.5.

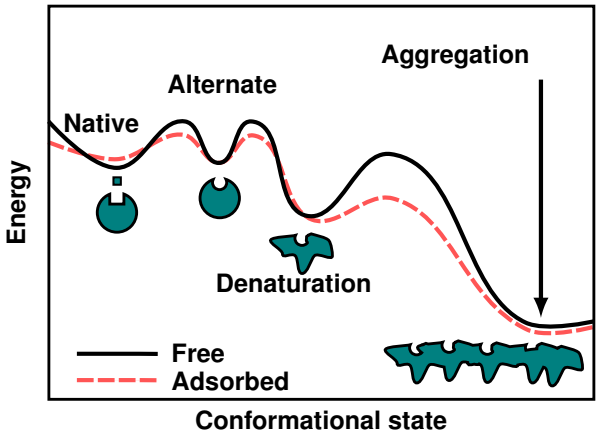


Figure 2.5: Schematic showing potential energy and kinetic barriers to protein conformation, denaturation and aggregation.

The ionic distribution near an interface also creates a region where the local pH and ionic strength differs from the bulk[123]. An electrical double layer (EDL) is formed by the response of charged molecules, ions and molecules possessing a dipole moment. When present in an aqueous solution they can become specifically adsorbed to a surface in response to an electronic potential. This produces a surface charge on the solution side of the interface. Over a short distance, and to maintain solution electroneutrality, these ions are screened by a cloud of counter-ions, which are ultimately continuous with the bulk solution. Surfaces become charged by a number of mechanisms[117], related to surface chemistry or adsorption. However, double layer formation is also sensitive to electronic conduction and polarisation of the substrate. The ability to store charge has resulted in an alternative name for the structure as a capacitive double layer. The capacitance of double layers are often modelled as constant phase elements, representing the non-linear behaviour of the capacitance during charging and in response to AC signals[119]. The exact composition of the double layer is the subject of multiple models[124,125]. At equilibrium, the ions within solution must all possess the same chemical potential and the counter-ions

cause significant screening of the surface. The Poisson-Boltzmann equation allows the prediction of profiles of both ionic concentration and electrical potential as a function of distance from the material surface. The debye length, defined as the point where potential drops to 37% of its original value (e^{-1}) in physiological solutions is around 1nm[126], despite this electrostatic effects can extend significantly further into solution (>50 nm)[55]. Pressure between double layer is generated by osmotic/entropic not electrostatic effects and is responsible for repulsion between opposing bodies with like charged double layers[117]. It has been shown that cells with long projections on their surface can overcome local inter-surface potential to reach distances where the totality of all intermolecular forces is attractive[127]. This is known as the *Elbow effect* and is illustrated schematically in Fig 2.6.

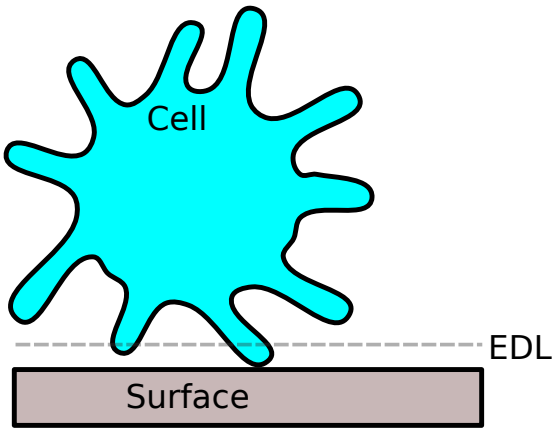


Figure 2.6: The elbow effect. Electric double layer (EDL)

Intermolecular forces

While many systems studied in surface science (colloids for example) are dominated by one or two types of interaction, four or more intermolecular forces can significantly contribute to the outcome in biological systems. These relevant intermolecular forces/potentials arise from several distinct physical sources and operate over differing distances[117]. Van der Waals (VdW) or dispersion forces involve dipole interactions which can be divided into London, Debye and Keesom interactions depending on the combination of spontaneous or permanent dipoles in the interaction. These short-ranged forces are almost universally attractive in aqueous solutions. Acid-base interactions result from electrostatic interaction following proton exchange. These may dominate the interaction when present and their strengths determine how tightly bound water is to the surface. While electrostatic

effects follow from fixed surface charge or dipole orientation and the effects on the solvent medium. Electrostatic (often coulombic) forces are significantly screened at physiological ionic concentrations, but still long range (>50nm)[55].

Steric effects arise under conditions when electron shells of approaching molecules overlap a manifestation of the Pauli exclusion principle. Engineering these effects to overcome other attractive potentials, that favour adsorption, is a strategy employed to create material with anti-fouling properties[110]. Conversely, dense or highly branching molecules can counter the intersurface repulsive force arising from double layer interactions leading to the elbow effect[128]. Forces, arising from electrostatic (double layer), acid-base and van der Waals interactions are all influenced by the ionic strength and valences within a solution[129,130].

There are varied opinions from the literature as to the relative weighting of the contributions from each intermolecular force to the adsorption process of proteins. Some authors claim electrostatic interactions are particularly significant[123,131], while others ascribe little role[61]. Others argue that the most important forces are steric[121], dispersive[72], or that hydrophobic interactions are key[76]. The picture is obviously complicated by the variation in protein structure across the many proteins that are potentially involved in biofouling. Additionally, evalulation of adsorption by many different methodologies across a range of surfaces, with disparate chemical and physical properties also adds to this complexity.

A feature of these forces are differences in variable distance dependence so when combined regions of net repulsion and net attraction develop at varying distances from the interface. As a result multiple minima can exist (depending on environmental conditions) where particles can be stably held. The combined effects of dispersive, electrostatic on intersuface potential, can be modelled using DLVO theory, with acid-base interactions also incorporated into an extending form[132]. This has been used to predict cell interaction with surfaces[127]. The presence of a secondary minima close to the surface explains biological obervations such as rouleaux formation[126]. This is a stacked cell-cell attachment often seen in red blood smears. This phenomena shows that cells may interact with a surface physically before any chemical interactions occur with, for example, adsorbed proteins.

DLVO theory does not include other relevant forces such as: solvation, entropic(hydrophobic), hydration and steric are not described by DVLO theory[117]. The presence of multiple minima

and counter-ion regions means that proteins interacting with a surface do not form a 2D structure but are better thought of as a 3D interphase that occupies the space immediately adjacent to the interface on the solution side[61].

Another consequence of multiple minima is that two processes: the terms cell attachment and cell adhesion, which are often used interchangeably in the literature, are distinct processes. They are usually considered to occur in sequence after the cell is brought into *contact* (several tens of nanometres) with a surface. The former refers to the trapping of cells (or more accurately a part it's surface) in a potential well near the surface of a structure, whether artificial or biological in origin[60]. Cell adhesion occurs subsequently and is characterised by the formation of chemical bonds or protein-protein interactions between cell surface receptors and surface binding sites[133]. In this sense, cell attachment is a physiosorptive process. Whereas, adhesion is chemisorptive, which includes the ligand-receptor interactions through which ordinary cell-matrix interactions occur. Despite this distinction, once anchor points are established, regardless of their physical origin, cells can spread at a biomaterial interface. Internal cytoskeletal features are used to increase the surface area of contact and can be coordinated to produce motility of the cell over the surface. Cell migration forms the basis for embryological development, wound healing and cancer metastasis. Cell attachment is also the commonly used term when quantifying cell surface interaction as usually no evidence is gathered in explicit support of adhesion. As such this the term attachment, using the looser definition, is used throughout the remainder of this thesis.

2.3 Consequences for implants

The combined effects of the FBR and biofouling can result in multiple deleterious effects on sensor function. These effects include drifts in sensor accuracy, mechanical or chemical destruction of sensors or stimulating implant associated disease. Sensor accuracy may be reduced, regardless of the modality of the transducer: optical[134,135], electrical[136] and chemical[137]. This is often a consequence of the fibrous capsule. Encapsulation thicknesses range from several µm to mm[23,42,138,139,140,141]. However, capsular thicknesses in the range 30–800 µm are typical[142,143,139]. This may alter the transport properties of

molecules to the sensor surface. For example, McClatchey *et al.*[137] found that glucose diffusion to a commercial oxygen sensor took less than a minute *in vitro* but this delay was increased to over 20 minutes in an *in vivo* environment, attributable to the presence of a FBR, particularly the encapsulation tissue. Alterations in the vascular density of the surrounding material are also observed[144,145,140]. Cell and protein interaction with sensor membranes may impede diffusion of analytes[146] and cell metabolism can adjust gradients of analyte concentration near a sensor surface[147]. Protein biofouling can also interfere with electrochemical sensors[148] After an interval of settling time after implantation the sensitivity of sensors may actually improve[149]. Dungel *et al.*[150] report a peak in sensitivity of a glucose sensor 7 day after implantation, followed by steady decline. This effect is likely related to transition between acute and chronic phases of the FBR.

Electrical impedance of encapsulation tissue is also higher than normal tissue. This can reduce ability to read or write to neural tissue[136]. Resistive components are related to collagen fibres in the capsule with resistivities around $500\,\Omega\,\mathrm{cm}^{-1}$[139], but significant anisotropy up to 10:1 have been reported[136], due to orientation of the fibres relative to the implant surface. Reactive components of impedance detect the presence of cells, at least up to several kHz[151] and can be used to distinguish between different types of immune reaction.

Formal quantification of FBR has been proposed through healing scores[152,153,42]. These are carried out on tissue surrounding explantated implants and use histological evaluation to measure protein/fibrin accumulation, immune cell quantity and type, and capsular properties like collagen thickness and density. In blood contacting devices, re-endothelialisation is an important factor in success[154]. Active monitoring of the immune response has been carried out using electrical impedance spectroscopy[155,156,157], along with piezoelectric[158] and strain[159] sensors.

2.4 Electrically active biomaterials

Active biomaterials and, in particular, electrically stimulated surfaces, that are described in this section, may be achieved by a number of mechanisms and seek to realise one or a combination of goals. For example, the prevention or removal of protein biofouling may be

desirable on sensor transducer membranes. In other applications, for example neural prosthetics close electrical association and minimal disruption of normal anatomy is sought[136]. In these cases the modulation of FBR or promotion of healing through control of protein adsorption or cell-material interactions is desirable. Influence over cell phenotype by differentiation or controlled cell migration and self-patterning may also be useful in certain applications.

As will be described, some surfaces are equipped with biological recognition elements: peptides, proteins and other functional sequences. Other materials rely on working with the biological materials they are presented with after implantation and wetting. Many studies to date rely on primarily *in vitro* work. Where *in vivo* translation has been attempted, this is noted. In fact, some works presented here for the purpose of describing their mechanism of action, may have originally been intended to create research tools or aid in diagnostics rather than have application *in vivo*

Electrical stimulation aimed at generating electric fields within tissues have also been studied to investigate effects on the migration of cells through electrotaxis[160,161] and dielectrophoresis[162]. Promotion of wound healing[163] and control of the FBR[164,165] have also been examined. However, these and similar approaches are not reviewed in depth as the electric effects were neither confined to the surface nor to the capacitive regime.

Active biomaterials employing alternative stimuli: ionic[166], thermal[167,168,169], light[170], vibration[171,172,173,174] have been proposed. A growing literature using magnetic stimulation and the magnetoelectric effect[175,176,177,178,179,180] also exists. Biological influenced realsied through adjustment of surface mechanical properties have also been explored[181]. Most surfaces investigated are planar, as this is how successful approaches would be incorporated onto the surfaces of implanted devices. However, truly 3D structures, including bioelectrodes are also being explored[182].

Electrically stimulatable or switchable biomaterials are reviewed below. Initially, they are categorised based the reversibility of the actuation. Subsequently, those approaches that exploited capacitance, and are therefore most relevant to this thesis, are divided based on the means by which surface charge was controlled.

2.4.1 Irreversible

As a minimum requirement for an active biomaterial, stimulated by electrical means, some property of the interface must be altered after exposure to a biological environment: *in vitro* or *in vivo* . Multiple approaches meet this requirement by virtue of having a single actuation mechanism that occur irreversibly. Of these, some have limited control in terms of magnitude and so only a single decision can be made: when to actuate. Despite this, materials may be designed in such a way that regions can be addressed individually and high spatial accuracy is possible[183]. Electrical stimulation is used primarily to actuate the mechanism rather than to generate fields or surface charge to influence biofouling and/or cell-surface interaction.

Surface assembly monolayers (SAM) can be functionalised onto materials, including electrodes. SAMs with a variety of headgroups can be functionalised onto surfaces. These may be linear or be highly branched structures with a wide array of terminal groups that confer different chemical properties. The monolayer nature of SAM also means that surface chemical properties can be isolated from bulk properties, allowing controlled comparison of surface response[184].

Polyethylene glycol (PEG) is a polyolefin that has been widely studied as an antifouling surface that may be functionalised onto metallic surfaces and hydrogels. Rejection of protein adsorption appears to stem from steric replusion[185] resulting in adsorption in the $\mathrm{ng\,cm^{-2}}$ range. This is three orders of magnitude lower than that found on bare metallic surfaces, like gold[67].

These materials have been used to explore the effect of different chemical properties on biomaterial performance. Using large chemical libraries surveys for anti-fouling properties led to the generation of heuristics for desirable chemical characteristics: *Whiteside's rules*. These rules provide the chemical characteristics required for a particular SAM headgroup to effectively resist protein fouling, bacterial attachment and promotion of mammalian cell spreading[76,113,186].

Brute-force approaches, reminiscent of drug discovery, which employ micro-arrays and microfluidics, experimental design, material libraries and automated analysis of experiments in a high-throughput manner can be used to produce large datasets of systematic exploration of biomaterial performance[187,188].

Techniques have been described for altering surfaces after SAM deposition to control protein and cell distributions prior to incubation. For example, scanning electrochemical microscopy was used to generate hypobromous acid, removing SAM locally[189,190]. This approach is impractical to implement dynamically in an *in vivo* environment but does demonstrate the feasibility of electrical modulation.

To achieve *in vitro* actuation, ethylene glycol based anti-fouling SAMs were electrically removed from an electrode[191]. Cells were subsequently able to attach on the newly exposed gold electrode, albeit relying on the native biocompatibility of the electrode material. Subsequent application of pulsed currents to newly exposed electrodes can be used to delay or inhibit the colonisation of the surface[192]. Removal of PEG surrounding collagen – an uncharged protein – coated ITO electrodes was achieved without removing previously attached cells[193]. It is thought the protein acted as an insulator and a similar effect has been produced using a patterned photoresist polymer[194]. The same protection against detachment has been reported even when the ITO electrodes were uncoated[195]. Presumably, proteins were adsorbed directly from the cell culture medium and were playing the same role as the collagen.

An improvement on this approach involved the switching of an antifouling SAM surface, functionalised on an electrode, to become cell conducive after exposure of adjacent cytophilic regions to cells *in vitro*[196]. In this case the switching allowed either a second batch of cells to attach or original cells to migrate out from patterned areas. However, the switching process involved both the application of potential to oxidise the SAM and also reaction of an externally supplied RGD peptide with the surface, making it inappropriate for *in vivo* application.

Bypassing this intermediate step was achieved through an alternative SAM that exposed aldehyde groups upon electrochemical decomposition[197]. This permitted non-specific binding of proteins (via amine reaction) from solution, allowing cells to migrate away from patterned islands. Cells have also been controllably detached by incubating on a SAM containing the cell integrin binding peptide sequence RGD[198] or surface bound hydrogel[199]. Yeo *et al.*[200] extended this by using attaching an RGD peptide to gold using two different linkers. These could be decomposed releasing the RGD and detaching any cells. The linkers were removed by application of potentials of opposite polarities meaning detachment

could be achieved on different regions of the same electrode independently.

High spatial density control could also be achieved via individually addressable electrodes. Wirtz *et al.*[183] were able to locally detach subcellular regions of individual cells using this approach.

SAMs can provide surfaces combining high biospecificity with spatial fidelity and precise actuation. Despite the utility of SAMs as experimental surfaces and in other biotechnological applications there are several drawbacks to their application *in vivo* . One issue with some SAM's is rapid conversion into other products once exposed to biological solution[76]. Further, they often possess poor stability, particularly beyond initial exposure to *in vivo* environments. For example, *in vivo* , PEG readily oxidises changing the terminal group[186]. In *in vitro* solutions, other thiolated surfaces can last for several weeks before oxidising and finally desorbing[201]. By contrast, *in vivo* lifetime can be reduced to less than a day, especially when functionalised on electrodes[202].

Other methods for producing irreversibly switchable surfaces, using conducting polymers, have a also been explored. Persson *et al.*[203] fabricated a PEDOT electrode with a superficial layer that could undergo electrochemical dissolution, releasing attached cells. Cultured cells showed expression profiles suggesting little to no cell damage occcurred from the detachment process. Approaches such as this cause the release of solute into the neighbourhood of the surface, so the immunogenic effects would need to be assessed for *in vivo* application. In an interesting inversion of the concept of biofouling, the surfaces themselves can become sources of protein. Zhu *et al.*[204] co-deposited two proteins: BSA and heparin into a polypyrrole(PPy) layer on top of an ITO electrode. Reduction and oxidation of the PPy, adjusted the local pH inside the polymer causing one or other of the proteins to develop a net charge. This caused electrostatic repulsion to drive the heparin or BSA into solution. The proteins became available near the interface and resulted in differing effects on preosteoblast cell proliferation and differentiation. The authors do admit that this approach required careful selection of proteins for mass, charge and isoelectric point to enable addressable desorption, so may no be applicable to any protein pair.

2.4.2 Reversible

The ability to dynamically alter a surface in a reversible manner, generates scope for dynamic interventions, across multiple time points, during the immune response. For example, periodic or event driven switching in response to measurements of FBR development. Two main categories of reversible surfaces are described here: conformational shifts and redox reactions. Switching may be monostable[205] or bistable[206,207] with respect to applied stimulation.

For conformational change SAMs are again employed. In this example, multiple molecules are applied together to make a mixed surface. Spacer molecules fill in the gaps between active molecules and are sized such that the binding site of the active molecule can be buried on change of conformation. Multiple examples demonstrate the reversible switching of biotin terminated SAM alter the binding ability of neutravidin in response to applied potential[208,209,210]. In contrast to the SAM work described in Section 2.4.1, switching did not remove or decompose the SAM but instead the conformation of the molecule altered to protect the binding site by collapsing towards the surface. In this way access to the binding site were sterically hindered. Removal of stimulation allowed the molecule to return to an extended configuration. In this case, the binding pair had very high affinity and would bind irreveribly, but binding can be delayed. The molecular construction of the SAM may also be designed in such a way that the on and off states both require application of potential to the electrode of opposite polarities[208]. The biotin system described is a proof of concept. A more relevant example used the RGD sequence. Lashkor *et al.*[211] used an RGD containing SAM, access to which could be blocked by conformational shift driven by application of a potential. This rendered the surface cytophobic, however if the potential was removed then cell attachment would return to positive control levels within an hour. This setup was inverted by Ng *et al.*[212] by using charged spacer molecules that were longer than the RGD sequence - creating a default off state. Spatial patterning of mixed SAMs with oppositely charged spacers created patterned surfaces that could be rendered conducive to cells by applying different polarities. Unfortunately in neither of these works[211,212] could cells be successfully detached via switching the surface back to its cytophobic state.

The conducting polymer PPy can undergo reversible redox reactions resulting in alterations to multiple biocompatibility related properties, including surface charge. Polypyrrole

(PPy) is a polycationic polymer, that is electrically conductive when oxidised, and reversible redox reactions can induce surface charge[213]. Electroneutrality is maintained by the addition of anionic dopants, which can also be selected to adjust other material properties or introduce ancillary effects on switching[214]. Controlled release of dopants is possible in response to oxidation, including potential induced drug release[215]. The PPy surface may also be functionalised. For example, Li *et al.*[216] showed reduced protein adsorption and evidence of blood coagulation by the combined effects of heparin functionalisation and electrical stimulation. The generation of nano-scale projection on the surface of a doped PPy film provided an additional mechanism of interaction with biological material - surface topography[217]. Morphology of finger-like PPy structures altered in response to redox state. Proteins were found to adsorb preferentially on reduced surfaces and bacteria attachment inhibited on reduce sites. Additionally, electrical stimulation was, however, only applied prior to experiments. Increase in cell attachment of cells from the PC12 line along with increase in neurite length have been observed on PPy films, using distinct dopants, stimulated with DC[214] and AC[218] potentials. Baumgartner *et al.*[219] found that cell viability was lowered on oxidised surfaces, which they attributed to inaccessiblity of binding sites within adsorbed IL-3 protein. Wong *et al.*[205] demonstrated that cell attachment supported by prior coating with the protein fibronectin could be diminished by reduction of the PPy film. However, the surfaces showed no change in fibronectin concentration, implying a conformational shift was responsible. The addition of dopants on formation of PPy provided a mechanism for the tuning of the surface towards hydrophilicity or hydrophobicity, thus influencing protein adsorption[68]. Doping with taurochloric acid (TCA) allows electrical stimulation of PPy to cause the hydrophobic or hydrophilic face (of TCA) to be exposed on the surface. This has been exploited to influence protein orientation, cell adhesion and spreading[206]. Similarly, TCS doped PPy wettability switching induced adsorption and beta aggregation of amyloidβ protein on when the surface was switched hydrophopic[207]. Protein release could be stimulated by subsequently switching back to a hydrophilic state.

Poly(ethylenedioxythiophene) (PEDOT) is another electrically conductive polymer that has risen to prominence in biological applications due to a high charge injection capability, good biocompatiblity and ability to participate in low impedance measurements of tissue electrical activity, particularly in neuroprosthetic technology[136].

Wan *et al.*[220] generated a gradient of reduction and oxidation on the surface of a PEDOT:PSS coated electrode. After stimulation, cells showed non-uniform distribution of cell attachment and of protein adsorption. Interestingly, the distribution of the adsorbed protein: fibronectin, which would be expected to induce attachment was adsorbed at higher concentrations on reduced PEDOT, while cells favoured the oxidised state. Subsequent work provided a possible explanation[221]. Using FRET to investigate protein conformation revealed that fibronectin adsorbed on the reduced material had a significantly extended conformation compared to that adsorbed on oxidised surfaces, likely influencing biological behaviour. Albumin has also been found to adsorb at lower densities and with less resistance to oxidised PEDOT, which similarly better supported cell attachment[104]. A general observation[69] that protein adsorption, conformation and subsequent cell attachment and *in vivo* biocompatibility are attributable to material wettability is consistent with these observations. In contrast to the previous examples[220,221], where stimulation was applied prior to biological exposure, electrical stimulation has also been maintained during cell and protein-surface interactions[104,222]. ElMahmoudy *et al.*[222] also applied an electrical gradient, although in this case across a microchannel patterned layer of PEDOT:PSS. The microchannel layer aided in constraining cell migration and the velocity of migration was a function of the level of oxidation/reduction of the material at a particular point.

By adding to a polythiophene derivative, a dopant that was able to bind to sialic acid, which is found on cell membranes, Hao *et al.*[223] were able to capture cells on the surface of coated ITO nanowire electrodes. Cells could be released via electrical de-doping of cell binding sites. Capture was reversible and even could be repeated over multiple cycles.

2.4.3 Capacitive

Capacitive approaches alter surface properties, like surface charge, through dielectric, double layer, ferroelectric and pseudocapacitive phenomena. Prevention of charge injection and faradaic processes reduces the deleterious effect of redox reaction products[224]. In the ideal case, biological interactions with the surface are purely a result of the consequences of polarisation of the interface. Low or absent electrochemical currents will not directly influence tissues, cells nor trigger electrotactic mechanisms. Two methods of limiting electrical switching to the capacitive regime, described here are material properties or

active control (via electronic circuitry). The proposed mechanisms by which electric fields interact with cells are many and varied[225,226,15]. However, when confined to the influence of surface potential/charge in some cases cells are responding to changes within an adsorbed protein layer but have also been shown to be capable of direct sensing. At least two mechanisms have been demonstrated for this transduction: calcium channels and a protein kinase pathway[227].

Active

Koyama[228] controlled the DC surface potential of an ITO electrode and found that adsorbed collagen and polylysine were desorbed at both positive and negative polarities relative to an Ag/AgCl reference. Cells were attracted to previously desorbed electrode surfaces under positive potential and crowded onto small SiO_2 control regions on application of negative potential. Cells could also be controllably detached from the surface on application of an AC signal.

Dargahi *et al.*[97] controlled the surface potential of a gold electrode incubated with the extracellular matrix protein: fibronectin. Applied potentials were kept within an electrochemical window where charging was capacitive (affected the double layer). Both positive and negative charged surfaces caused differing conformational shifts in the fibronectin, with negative surfaces adopting conformation more conductive to cell attachment. This conformational shift in fibronectin involved conversion to a fibrillar form. Fibronectin adsorbed preferentially to the negatively charged gold surfaces and exhibited a much reduced desorption profile over several weeks. A similar pattern of increased adsorption to pulse stimulated gold, and also pyrolytic carbon, surfaces was observed across several blood proteins[229]. Again, adsorption quantity was increased on negative surfaces. Both materials exhibited higher adsorption of blood derived proteins on positively charged surfaces. Simulation of the globular dimeric form of fibronectin, within an electric field on hydroxapatite (bone-like material), predicted that adsorption processes are primarily driven by electrostatic means[80]. At both polarities, electrostatic interactions were strongest at lower field strengths. This interaction, along presentation of the RGD binding domain, were predicted to reduce monotonically as the applied potential increased. Kotwal *et al.*, on the other hand, found that immediate stimulation after exposure of a PPy film to fibronectin

at a controlled potential enhanced the outgrowth of neurites. However, when stimulation was delayed in the presence of fibronectin no such change was detectable. This picture is further complicated by the fact that adsorption to a charged electrode can also be influenced by alterations in charge driven by pH fluctuations[231] changing net protein charge, a situation that readily occurs *in vivo* .

Control of bacterial attachment has also been investigated using similar techniques, but with notable differences in behaviour. Preferential attachment to negative electrodes is seen[232,233], in contrast to mammalian cells, which tend to favour positive surfaces[234],although differing, reversible, morphological change in attached cells have been observed at both potentials[235]. This highlights the differences in the attachment process between animal and bacterial cells. While not fully understood it is likely related to the evolution of bacteria to directly interact with surfaces in the environment. This is contrasted with animal cells that require a scaffold or ECM. Caution must therefore be employed when comparing the two bodies of literature. The same pattern has also been shown with 1 kHz AC signals on carbon nanotube electrodes in the capacitive regime, the proportion of killed cells was also higher on positively biased signals compared to negative[236]. Despite the phylogenetic distance between bacteria and animals, these results are notable as bacteria possess a negative surface charge. This suggests that the physico-chemical interactions leading to attachment extend beyond elecrostatic. Gall *et al.*[233] postulate that conformational change on the surface of the bacterial envelope may lead to steric hinderance that may be the cause of failure to attach to positively charged surfaces.

Bipolar electrochemistry is a novel approach which enables a wireless creation of a dipole charge on an electrically isolated material submerged in conductive media between two conducting electrodes. This induced charge can cause redox reactions and water splitting to occur, along with ionic intercalation in the material surface[237]. It has been proposed that these reactions combine with the electrotactic effects of ionic currents are responsible for changes in the behaviour of attached neural cells[238].

Guette-Marquet *et al.*[239] applied a controlled potential to commercial carbon electrodes and demonstrated that an applied surface potential (400 mV vs a silver pseudoreference) enhanced cell attachment of two cell lines over OCP. This was contrasted with drastic reduction of attachment at ±200 mV and 0 mV. The authors explained this result with ref-

erence to a PZC at 200 mV, meaning that only the high potential experiment created a positive surface charge. The authors advocated for literature reporting of controlled surface potentials using 3-electrode setups and cautioned that applied positive polarity, especially if uncontrolled as is common in the two electrode setups, does not equate to positive surface charge. This suggests consideration of the means by which the electrical state of a surface have been characterised must be employed in interpreting electrical setups. Especially where surface charge would be expected to vary across the substrate.

Passive

An alternative to controlling actively is to rely on the physical construction or material properties of the biomaterial to maintain the interface within the capacitive regime. This can be achieved by employing dielectric materials: which are capable of polarisation in response to an applied electric field.

Metal oxides based on titanium and tantalum have been investigated as capacitive replacements for conductive metals like platinum and iridium that are commonly used as bioelectrodes for intracortical stimulation[240]. However, when stimualating neural tissue, recruitment is desirable in cells that are distal to the electrode, which in turn requires high charge injection capacity[27] Capacitor electrodes are consistently outperformed by traditional conductive electrodes operating within safe limits[240].

Piezoelectric materials link mechanical deformation to voltage generation within the material. Many biological tissues possess piezoelectric properties, which have been associated with driving healing processes[241]. Biomaterials often seek to mimic the fields generated by endogenous sources in response to mechanical loading[242]. Polarising these materials can be performed before implantation, resulting in a biological influence[243].

Ferroelectric properties of these materials can be used to introduce a baseline polarisation. This is subsequently altered through mechanical activity to encourage biological effects, like healing. Mechanical stimulation *in vivo* can originate endogenously through body motion and loading, or at the local level by traction forces applied by attached cells. Exogenous stimulation can also be supplied, via ultrasonic energy[244] for example. Further examples of piezeoelectric polymers and their influence on cells when formed as nanofibres have been reviewed[244].

PZT piezoelectric surfaces have been used to detach adsorbed protein films, with[124] and without[245] addition of solution stirring. Three independent detachment mechanisms were are theoretically available: mechanical vibration, acoustic streaming and electrostatic effects[124]. However, the experimental setup used by Johnson *et al.*[245] successfully removed protein from an electrically isolated polyurethane layer, suggesting that the former of the two mechanisms dominates. The most common piezoelectric material studied is PZT, however this material can leach cytotoxic products when implanted, leading to an increased interest in alternative ferroelectric and polarisable materials: bioceramics[246].

Poly(vinylidene fluoride) (PVDF), is a fluoropolymer with electret and piezoelectric properties that make it useful in a number of technologies, including biomaterials[247]. Polarisation via electrospinning produced surfaces close in surface potential to the attaching cells, which increased cell proliferation to equivalent levels to tissue culture polystyrene (TCPS)[248]. Interestingly, positive and negative polarised surfaces both had negative surface potential with higher potential on negative polarised states due to accumulation of positive co-ions within the double layer, moving the potential from a negative OCP. Electrical polarisation of sheet PVDF also had the same effect, with negatively charged surfaces promoting stem cell differentiation[243]. When chemical surface modification was applied to polarised and unpolarised PVDF, both effects influenced neurite growth and differentiation, but the electrical effect was more influential on measured neurite spreading[249]. Aebischer *et al.*[250] implanted PVDF tubes into peripheral nerve regeneration model and found that material that had been polarised, using high voltage, before implantation causes more myelination in healing nerves compared to unpolarised controls. Polarised PVDF tubes have been used to stimulate nerve regeneration *in vivo* . Polarised tubes generated more signs of regeneration than unpolarised with greater effect seen with positive polarity[250]. Surface charge in the $\mathrm{pC\,cm^{-2}}$ range are generated with[251] with mechanical motion *in vivo* generating additional dynamic effects, although in an uncontrolled manner.

Many other materials can be polarised prior to incubation with cells and, albeit non-dynamically, leading to a variety of biological effects. Zhang *et al.*[252] polarised a sodium niobate crystal and abolished the polarisation locally using laser irradiation. Albumin and fibronectin adsorption was higher on the positive polarised surfaces compared with non-poled. Cell attachment, spreading and migration were also enhanced. The surface po-

tentials varied by 100 mV. The latter is an example of heterogeneity in surface charge to induce biological effects. A related homogenous approach was taken by Li *et al.*[253] who also found improved cell spreading on both polarised faces of lithium niobate crystal, with a large favourability for osteogenic differentiation for the positive crystal face. This dependence on polarity was further confirmed by Singh *et al.*[254], who polarised multiple electrets using a high temperature process showed that viability of mammalian cells were enhanced on polarised surfaces but particulary positive. When bacteria were cultured, viability was significantly lowered on negative polarity surfaces, which the authors attributed to electrostatic repulsion between the negative cell surface potential and the biomaterial.

Polarised heterojunction formed of gallium nitride on aluminium gallium nitride was able to promote differentiation on bone stem cells and stimulate bone formation in an *in vivo* model[255]. Similarly, Ning *et al.*[256] created patterns of material phase, generating electric fields on the surface of TiO_2. These fields were also able to cause differentiation *in vitro* and stimulate bone growth when implanted *in vivo* . Further examples of electrically polarised materials, with electret or piezoelectric properties, have been reviewed[55]. However, this review does not contain any examples of dynamically applied polarisation after exposure to an *in vitro* or *in vivo* environment but does inform on the mechanisms and extent of influence polarised surfaces can be expected to achieve.

A more dynamic approach was taken by Kapur *et al.*[257]. In this work, the fluoropolymer FEP or polystyrene were used to cover a high voltage electret. Assessments of the behaviour of chick embryonic fibroblasts and proteins were then made in contact with these surfaces. Orientation of the cell body was significantly constrained at higher values of surface charge density beyond a well defined threshold. Protein adsorption showed different profiles as a function of increasing positive or negative charge density. At positive charge densities protein adsorption increases monotonically, whereas when the surface was negative adsorption rose initially to a higher peak then precipitously declined.

The same authors also subsequently created 3.3 µm titanium electrode strips overlaid with a layer of SiO_2 and spin-coated polystyrene. When voltage (up to ±75 V) was applied in a dipolar manner to alternating electrodes up to 53 pC cm^{-2} surface charge density was generated[258]. This resulted in both spreading and increased activation of human monocytes when challenged with an inflammatory promoter compared with uncharged controls.

The use of passive capacitive charging is probably the least explored approach to active biomaterials. In principle, this approach would appear to be less sophisticated than using active control not least as larger applied fields are required to produce equivalent levels of surface potential/charge. However, the advantages of this approach include access to ferroelectric phenomena, allowing polarisation to be fixed even in the absence of an applied field. Additionally, surface charge states may be reachable that would be otherwise inaccessible, or their effects masked by coincident electrochemistry, on conventional electrodes.

2.4.4 Literature analysis

Details from the reviewed literature are presented in Tables 2.2 & 2.3. A number of common strategies can be observed related to the use of SAMs and conductive polymers as the cell contacting layer. For the underlying electrodes, gold (Au) and indiumn tin oxide (ITO are the most commonly used. As mentioned above the level of electrical characterisation can be crucial in interpreting the behaviour of cells and proteins in response to the stimulated surfaces. The timing of when stimulation is applied is often delayed until after cells/proteins have been incubated. In other cases stimulation is applied throughout the experiment or prior (Pre) to introduction of cells/proteins. Where possible the level of characterisation has been listed. In order of precedence they are: σ, ϕ, $\overrightarrow{E}$, V and $\overrightarrow{j}$. Surface charge (σ) is the most accurate value for determining the electrical state of the interface as it is independent of the ionic content of the solution and can be used to compared across experiments and to values of biological structures, such as cells and proteins[55]. Calculation of this value often requires differential capacitance measurements of a surface[97]. The value for surface potential (ϕ) can be accurately calculated if applied potential is measured relative to a reference such as Ag/AgCl. However, depending on the value of the PZC and the polarisation of the interface, surface potential polarity may not give any indication as the polarity of surface charge or the direction of equilibrium of surface bound redox processes. The electric field ($\overrightarrow{E}$) gives very little information about the state of the interface but does require knowledge of the geometry of the electrical setup. Finally, applied voltage (V) and current density ($\overrightarrow{j}$) or current (i) assume the least information about the experimental setup or state of the interface, but can be used to provide repeatable comparisons within

the same setup.

Measured biological properties include cell attachment, detachment, migration, differentiation, proliferation and gene expression. Protein adsorption and desorption are also tracked, along with conformation and biological function. In general, strategies reported have favoured control of cell and protein attachment/adsorption versus detachment/desorption, implying that augmenting biological behaviour of pristine surfaces is easier than once biological interactions begin to proceed. The proteins used in the studies mostly come from a small pool (albumin, fibronectin). Conversely, the cells types used are drawn from a wide variety of primary and immortalised cell lines that originate from a diverse range of organs and tissues. This inconsistency reduces the efficacy of comparisons made across the body of literature. Very few examples of *in vivo* studies are present in the literature surveyed above, so less can be said about the potential efficacy of any of the proposed approaches. The reasons for this is partially that much of the literature is specifically aimed at *in vitro* applications for diagnostics or tissue engineering, rather than deployment on the surface of medical device.

Stimulation				*in vitro*	*in vivo*	Ref
Electrode	**Electrical**	**Timing**	**Protein**	**Cells**		
Steel(316) PEDOT CNT	$\overrightarrow{E}$	initial interval		attach/neurite outgrowth/expression (NB-39-NU)		27
Au	σ	throughout	adsorb/conformation (Fn)	attach (HUVEC)		97
ITO	ϕ	throughout	desorb (collagen)	attach/detach (PC12, HeLa, dermal fibroblast)		228
Au SAM	ϕ	delayed	pre-incubation (Fn)	attach (3T3)		196
Au SAM	V, $\overrightarrow{E}$	delayed	adsorb (Serum,Fn)	attach/migrate (BCE)		191
Au SAM	ϕ	delayed	pre-incubation (Fn) adsorb (non-specific)	attach/migrate (3T3)		197
Au SAM	ϕ	delayed		detach (3T3)		183
ITO hydrogel	ϕ	delayed	pre-incubation (collagen)	detach (rat primary hepatocytes)		199
ITO PEG	ϕ	delayed	pre-incubation (collagen)	attach:co-culture (primary hepatocytes, fibroblasts)		193
ITO PEG	ϕ	delayed	pre-incubation (collagen)	attach:co-culture (HepG2, HSC)		195
ITO PEG	ϕ	delayed		attach/neurite outgrowth (NG108)		192
ITO SU-8 PEG	$\overrightarrow{j}$	delayed		detach (chondrocytes, MSC)		194
PEDOT	ϕ	delayed		detach/expression (T24)		203
PPy	-	-	pre-absorbed, desorb (BSA,Heparin)	attach/proliferate/differentiate (MC3T3)		204
ITO PEDOT	V	throughout	pre-incubation/conformation (Fn)	(3T3)		221
PPy	V	-	adsorb/desorb (Fn, PAS, BSA)	attach/spread/detach (MC3T3-E1)		206
SAM - mixed	ϕ	delayed		attach,migrate (BAEC, HL60)		212
ITO PPy	ϕ, $\overrightarrow{j}$	delayed		neurite outgrowth (PC-12)	Lewis rat(s/c,i/m) - unstimulated	214
ITO PPy	ϕ	delayed	pre-incubation (Fn)	attach (BAEC)		205
Au PPy	ϕ	throughout	pre-incubation, conformation (IL-3)	attach (FDC-P1)		219
Au PPy	$\overrightarrow{j}$	delayed		neurite outgrowth (L929, PC-12)		218
Ti PPy	ϕ	Pre	adsorb (BSA)	attach (S. aureus)		217
Au SAM	V	throughout		attach (RAW 264.7)		211
Au SAM	ϕ	throughout	adsorb (neutravidin)			209
Au SAM	ϕ	throughout	adsorb (neutravidin)			210
Au SAM	ϕ	throughout	adsorb (neutravidin)			208
ITO PPy	ϕ	throughout	adsorb/conformation (amyloidβ)			207
ITO PEDOT	$\overrightarrow{E}$	throughout		migration (BAEC, hCMEC)		222
ITO PEDOT	V	Pre	adsorb (Fn)	(3T3-L1, MDA-MB-231)		220

Table 2.2: Comparison of electrically active biomaterials literature.

Electrode	Stimulation: Electrical	Timing	*in vitro*: Protein	*in vitro*: Cells	*in vivo*	Ref
ITO polythiophene	V	delayed	desorb (sialic acid)	detach (MCF-7)		223
ITO	ϕ	throughout	desorb (collagen)	attach/detach (HeLa, PC12)		228
ITO	V	delayed	adsorb (serum)	attach/spread (rat bone marrow cells)		259
Pyrolytic carbon	ϕ	throughout	adsorb (serum)			229
Au SAM	ϕ	delayed		attach/detach (M. hyrdocarbonoclasticus)		232
ITO	ϕ	throughout		attach/detach Multiple bacterial species		234
Au	ϕ	throughout		attach (P.fluorescens)		233
CNT	V	throughout		(Pseudomonas putida)		236
hydrogel graphene	$\overrightarrow{E}$	intermittent	adsorb (BSA)	attach/differentiation/expression (mBMSC)		260
PEDOT	V	throughout	adsorb (albumin)	attach c17.2		104
PPy PEGMA heparin	i	throughout	adsorb (BSA, BFG)			216
Au	ϕ	throughout	adsorb (BSA)			231
Au PPy	i	throughout/delayed	adsorb (Fn)	neurite growth (PC-12)		230
carbon electrode	σ	delayed		attach/proliferate (RAW 264.7)		239
PVDF	V, i	Pre	adsorb (Fn)	differentiation (hASC)		243
PVDF/TrFE copolymer	V	Pre/throughout			Albino rat (i/m) - regeneration of transected sciatic nerve	251
PVDF	σ	Pre/throughout			mouse (i/m) - regeneration of transected sciatic nerve	250
PVDF	ϕ	Pre/throughout		attach (MG63)		248
PVDF, FEP	V	Pre		differentiation/neurite outgrowth (Nb2a)		261
TiO_2	ϕ	Pre		attach/proliferate/expression (BMSC)	Rat femoral defect	256
$LiNbO_3$	-	Pre		proliferation/spread (rBMMSC)		253
$Ka_{0.5}Na_{0.5}NbO_3$	ϕ	Pre	adsorb (albumin, Fn)	attach (MC3T3)		262
GaN/AlGaN	ϕ	Pre		attach/differentiation (BMSC)	Sprague Dawley rat - femoral bone defect	255
$Ka_{0.5}Na_{0.5}NbO_3$, electrets	V	Pre		attach (MG-63, SAOS2)		254
PZT	ϕ	throughout	desorb (BSA)			245
PZT	σ	throughout	desorb (BSA)			124
FEP, PS	σ	Pre	adsorb (serum)	(chick embryo fibroblasts)		257
Ti PS	σ	throughout		attach/spread (human monocytes)		258

Table 2.3: Comparison of electrically active biomaterials literature – continued.

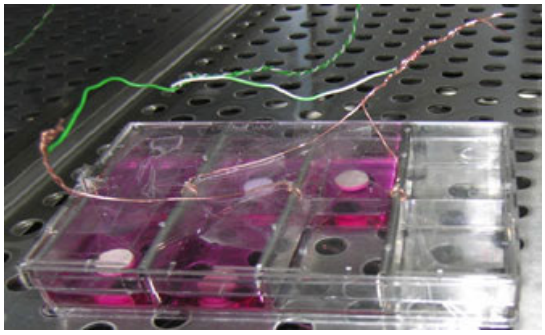
2.5 Platforms for electrical stimulation

Descriptions of the assembly, and practical realisation of protein and cell interaction experiments in the literature are scant. Only a small number of the publications reviewed in the Section 2.4 provided any such detail on the platform used to acquire the results presented[228,222,209,263,264,265,266,259,258,192,221,198,104,267,268,183,239].

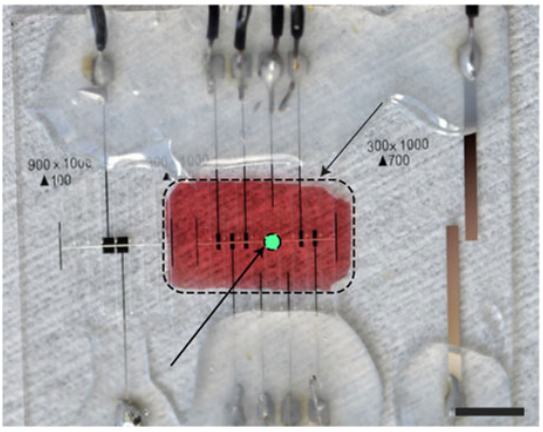
The most common electrode materials were gold and indium tin oxide (ITO). Gold is used due to corrosion resistance and ability to be functionalised with SAMs through thiolation. ITO is often selected as an electrode material for cell and protein interaction studies[269] due to its relatively high optical transmission and conductivity, although oxides of zinc and tin can also meet these criteria[270]. As can be seen in Table 2.2, these electrodes can also be overlaid with monolayers, hydrogels and various conductive polymers.

Some studies used or modified commercially available devices[265,239], whereas others were fully bespoke[209,267], contain specialised structures to, for example, investigate *ex vivo* nerve conduction[264]. Several incorporate laboratory plasticware[259,263,258], in order to retain culture medium over the substrate. Addition of ancillary components, such as PCBs, allows electrical connections to be brought out from the substrate to external instrumentation[265]. Micropatterning of the substrate permits finer spatial control over the stimulation applied[228], in some cases to the level of multiple individually addressable sub-cellular electrodes[198]. However, access to the full range of semiconductor and MEMS fabrication technologies can only be accessed through the use of silicon (or other) wafers as the substrate[258].

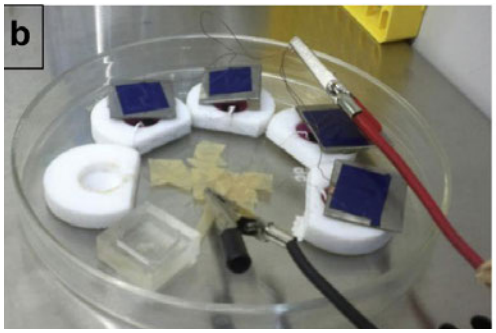
Notably, no single platform possessed all of the above properties and features. Example images of platforms are reproduced from the literature in Figs 2.7 & 2.8 and schematically in Figs 2.9 & 2.10.



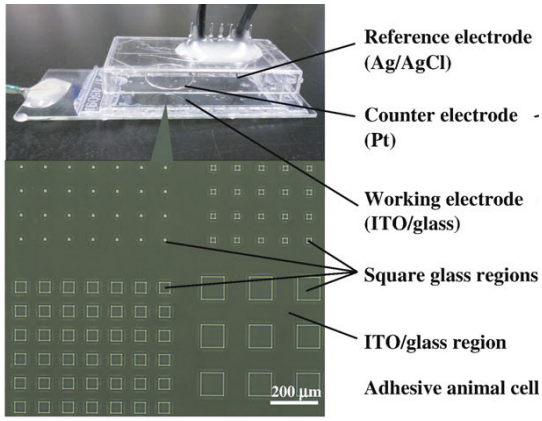
(a) Adapted from[263] (Fig 2a).



(b) Adapted from[264] (Fig 3b).



(c) Adapted from[268] (Fig 1b).



(d) Adapted from[228] (Fig 1).

Figure 2.7: Platform literature examples: images.

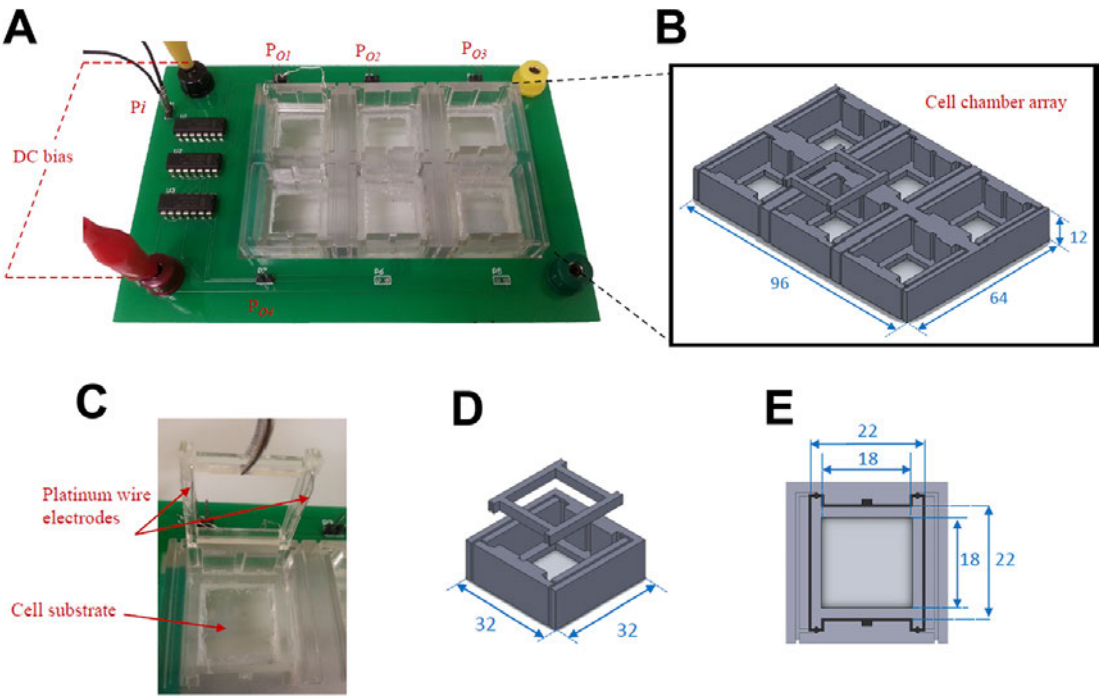
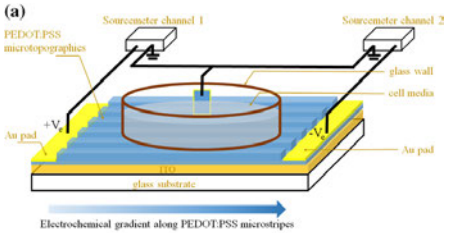
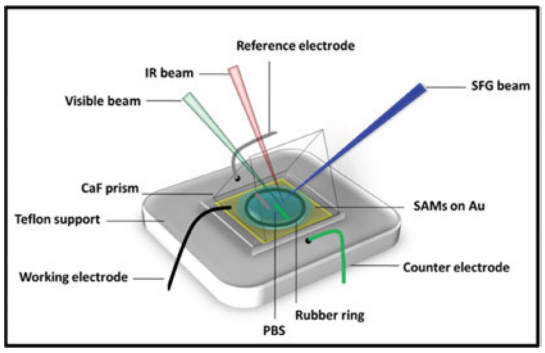


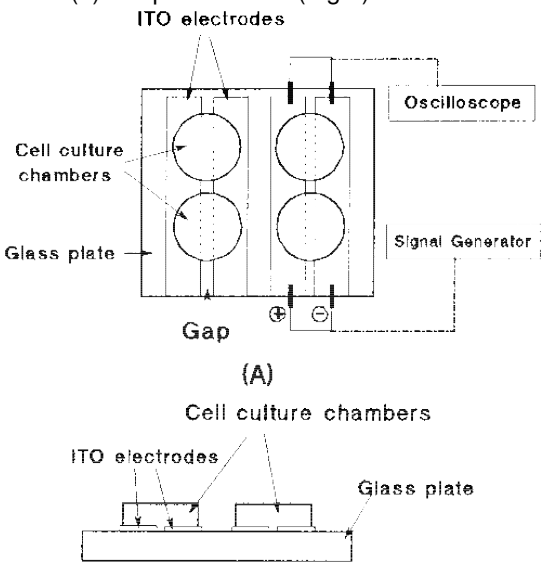
Figure 2.8: Platform literature example: multi-well stimulation device. Adapted from[265] (Fig 7).



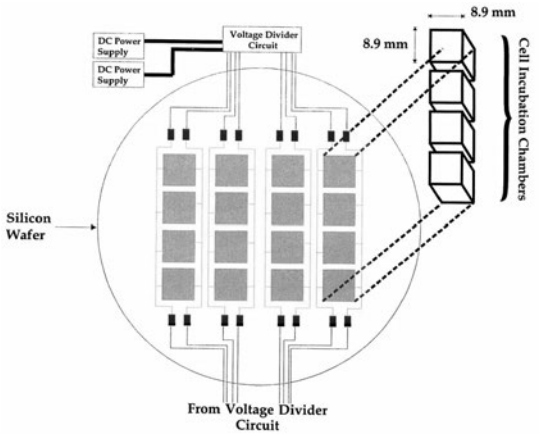
(a) Adapted from[222] (Fig 2).



(b) Adapted from[209] (Fig 2).

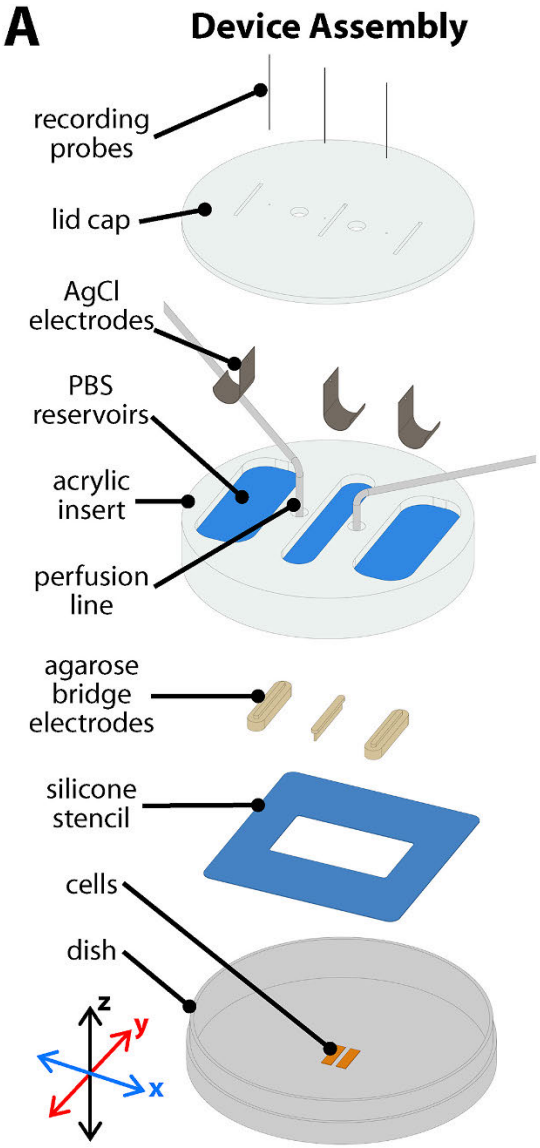


(c) Adapted from[259] (Fig 1).

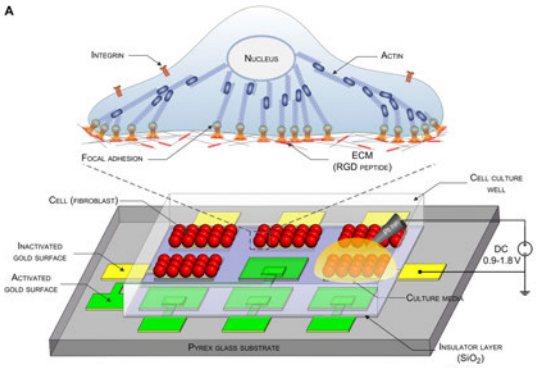


(d) Adapted from[258] (Fig 1).

Figure 2.9: Platform literature examples: schematics.



(a) Adapted from[267] (Fig 1A).



(b) Adapted from[198] (Fig 1).

Figure 2.10: Platform literature examples: schematics - continued.

2.6 Conclusion

This chapter gave a broad overview of the twin issues of the FBR and biofouling, along with their consequences for implanted devices. Detail of biophysics and pertinent examples were included, where appropriate, to develop insight into the rationale behind active biomaterials.

The immune response was first described, including the interaction with biomaterials, key cell types and approximate timings of their involvement. In particular, the reliance on cell-material interactions and associated survival of immune and other cells in contact (and in proximity) to the surface.

The phenomena of protein adsorption biofouling was discussed, in terms of the wide array of interactions that can occur for individual proteins, within the adsorbate and that govern the exchange processes that determine the evolution of the protein film. The biophysical basis of protein adsorption was touched upon along with some examples of how these effects manifest and produce different biological effects on different biomaterials.

The necessity of active biomaterials, in the search for improved biocompatibility, was argued for with reference to the complex dynamic nature of both the immune system and protein adsorption. Such materials can be actuated by a number of different stimuli, however electrical stimulation has a number of advantages, including precise control spatial and temporal aspect of stimulation, along with magnitude that can be achieved via available electronics and fabrication methods.

An in-depth review was made of the electrically stimulated surface and biomaterial literature. Methods of producing irreversible actuation were described and contrasted with higher utility reversible means. Capacitive charging of biomaterials, which restricts control of surface properties to electrostatic (double layer) charging, was reviewed. The effects of electrical parameters, including polarity, were compared and those characterising the surface were ranked, with surface charge then surface potential being the most reliable. A much less explored mechanism of capacitive charging, using passive material properties, was surveyed, revealing potentially interesting phenomena.

Descriptions of experimental platforms were assembled and used to collate a set of features that are desirable for carrying out investigations in this area.

Chapter 3

in vitro device platform

Introduction

In order to investigate the interaction of biomaterials with electronically adjustable material properties, platforms were needed to allow prototype devices to be moved from the concept through fabrication and to experiment.

There are several requirements of devices, to investigate of electrical manipulation of biosurfaces. Devices with variable material properties were required to allow experimentation on biological fluids, cell cultures, and to facilitate biophysical investigation of surface interaction. For work attempting to bridge the translational gap for biosensors and other devices, a mechanism was required to minimise the overhead associated the logistics and practical implementation of electrical stimulating cells and tissues. This would allow quick and flexible movement from concept to prototype and *in vitro* to *in vivo* study.

The aims that drove the specification of these devices were to combine multiple desirable features of platforms reviewed in in Section 2.5. These included a reconfigurable fluid contacting surface with high a relatively high number of electrical contacts to allow the application of potentials and reading and writing of signal to from biological material, ideally using a substrate compatibility with semiconductor fabrication processes. Additionally, broad comparability and interoperability with standard laboratory consumables and instruments and protocols was sought.

This chapter describes the development of the first of two platforms that share some common design features. The first was designed to allow biological fluids to be brought

in contact with a surface and to features that could be electrically connected to external circuitry, for the purposes of electrical interaction or sensing with cell culture models or for biophysical experiments. The major components of this platform are shown schematically in Fig 3.1 The second is described in Chapter 5 and is a modification to allow contact with an *in vivo* model. Ancillary test structures that were used to develop the processes for both platforms are also described.

The design and fabrication of these platforms heavily utilised common processes used for the production of semiconductor devices and required very little additional development of established recipes. However, to create interoperability with the biological laboratory consumables, several non-standard processing steps were required. Emphasis is paid to the development. The advantages and pitfalls of these processes are described in this chapter. Two key process steps were the formation of a high-κ dielectric layer from tantalum pentoxide via anodisation and the deposition and characterisation a fluoropolymer layer as the final surface of the device. As the combined effects of the these processes, were key to testing the hypothesis function of the devices.

3.1 Platform design

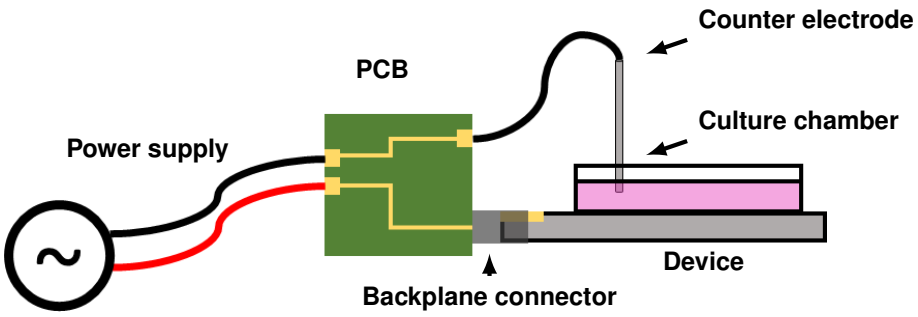


Figure 3.1: Schematic of the *in vitro* platform setup. Electrical signals are routed from an external power supply, through a PCB and into the die through a backplane connector. Cells within cell culture solution are brought into contact with the electrified surface, contained within a culture well.

To enable electrical interaction with cultured cells and biological solutions a strategy was applied of submerging an entire region of the substrate and routing interconnects out to an unsubmerged contact region to make external electrical connection. This was as an alternative to interconnect bonding electrical connections and potting to protect against

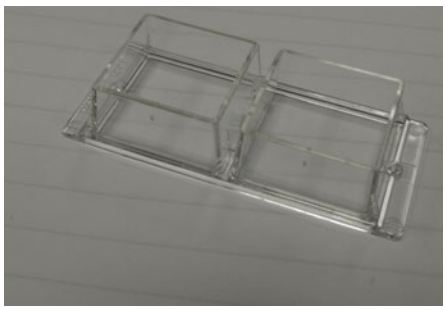


Figure 3.2: *Nunc Lab-Tek* chamber slide. Permanox® TCPS chamber separated from the slide prior to splitting yielding culture wells.

liquid environment. This approach simultaneously minimised process steps and limited the number of additional materials in contact with the solution, beyond those comprising the substrate under investigation, to two.

In this platform, a culture well *Nunc Lab-Tek* (ThermoFisher) formed from TCPS was used to create a reservoir of culture media over the electrically active area, Fig 3.2. Interconnect lines, fabricated onto the substrate, facilitated the electrical connection between the reservoir area and a high-speed backplane connector *HSEC-8* (Samtec inc.). The connector had been previously been successfully applied to lab on chip/microfluidic applications[271]. The connector was designed to make contact to a row on each side of the backplane. In this application only the top row was used to make connections to the die. On the opposite side of the die a series of larger contacts were placed to be used for ancillary connections or as test points. The specifications of the platform are given in Table 3.1.

Property	**Value**
Dimensions	25 mm x 75 mm
Culture area	4 cm^2
Media capacity	1–2 mL
Electrical connections	30
Ancillary connections	10
Assembly time	120 minutes
Sterilisation	autoclave
Wafer yield(100 mm)	3

Table 3.1: Specifications of the *in vitro* platform.

3.2 Device design

A cross-section of the microfabricated portion of the proposed device is shown in Fig 3.3. Figure 3.4 shows the processing steps along with the developing wafer cross-section.

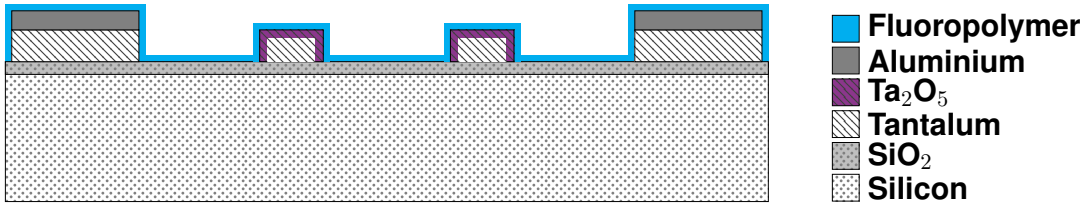


Figure 3.3: Device layer stack showing patterned electrodes of tantalum with an oxide layer coated in a hydrophobic polymer layer. The contact area tantalum has an overlying layer of aluminium.

3.3 Mask design

Two emulsion masks were fabricated from designs created using CAD software *KLayout*[272]. The first was used to define the tantalum electrode layout along with establishing dicing lanes, while the second was used to define the aluminium deposited over the tantalum to facilitate external contacts. Three different chip designs were created for each layout, Fig 3.5. The key features of the *in vitro* platform design are shown in Fig 3.6. These featured different electrode configurations in the active area. Interconnects from each electrode were brought out to two redundant electrode setups, one for the backplane connector and the other for a larger set of connectors that were used as test points. Dicing lanes were created with the intention that the estimated kerf (100 µm) of the dicing saw, would bring the total width of the die within the width as specified for the backplane features on printed circuit boards designed to interact with the connector. Consideration was also given to tolerances for angular and lateral misalignment detailed in the datasheet[273] along with metallic contact width and inter-contact spacing. The three electrode configurations were a large planar electrode, strip electrodes and wire electrodes. The planar electrode covered the entire active area (in contact with biological fluid in operation) of the die. The strip electrodes were 1000 µm wide with 1000 µm spacing of SiO_2 running the full length of the active area and were connected to an individual test point and redundantly to three neighbouring backplane contacts. The dimensions were chosen to provide elec-

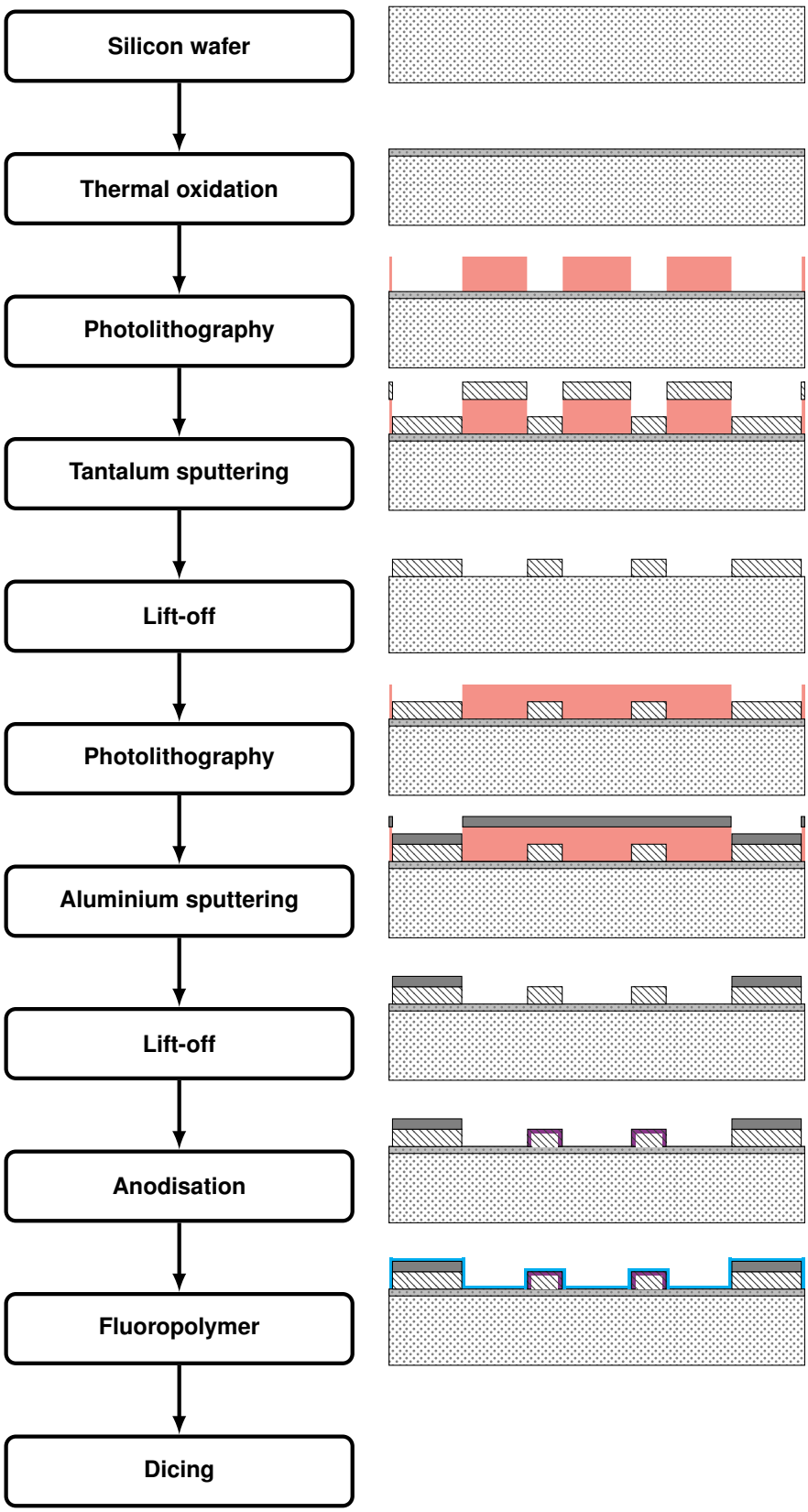
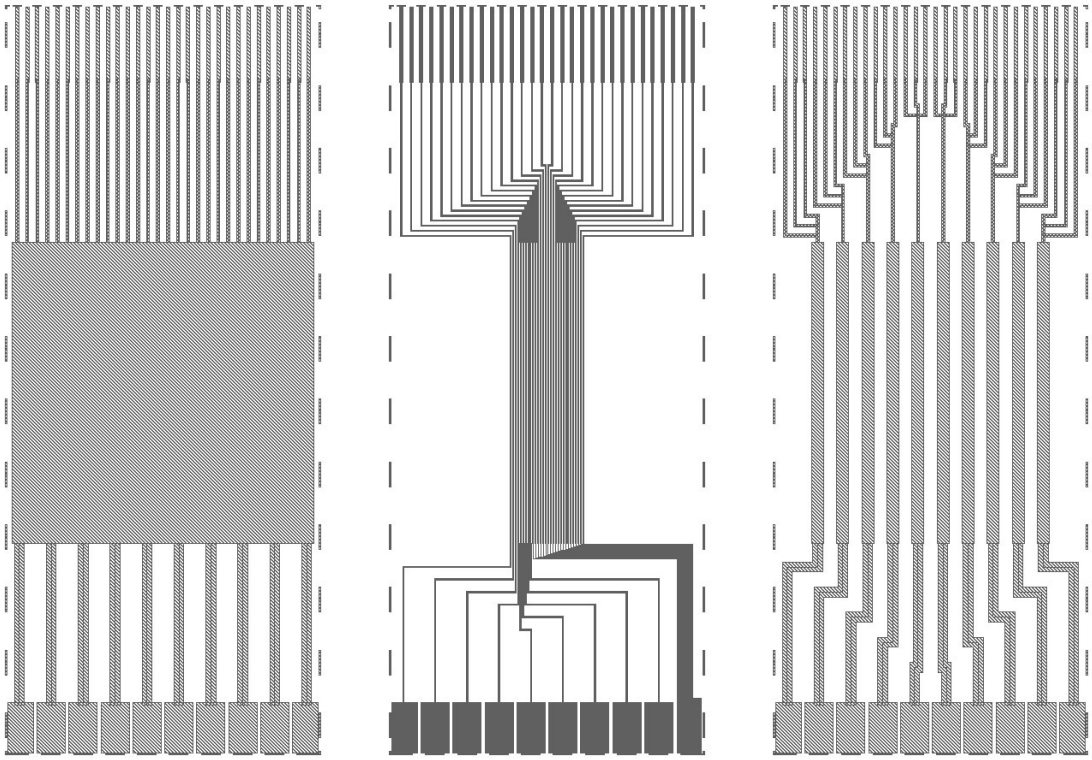


Figure 3.4: Microfabrication steps to produce the *in vitro* platform.



(a) Planar: (24x24mm) (b) Wire: 100 µm (c) Strip: 1000 µm

Figure 3.5: Three different electrode layouts following compatible with the *in vitro* platform.

trodes that would cover the entire culture area (planar), or allow occupation of multiple cells (1000 µm). The 100 µm (wire) electrodes were designed to allow adjacent analysis of cells on different electrodes or that spanned electrode boundaries. This approach made use of surplus contacts and maximised the probability of good electrical connection until the reliability of the connector-wafer connection could be established. Interconnect electrodes were 100 µm wide with a 100 µm spacing and were connected individually to a backplane contact each. With a total of 30 interconnects there were insufficient test points so the initial 9 were connected to test point contacts and the remaining test point was a pseudocontact, Fig 3.7. This was designed to allow electrical connection with to multiple interconnects simultaneously that was used during anodisation.

3.4 Silicon wafers

100mm p-type <100> plane wafers were acquired from *Si-Mat*, it was possible to fit three device designs per wafer at this wafer size. As all devices were constructed on top of a

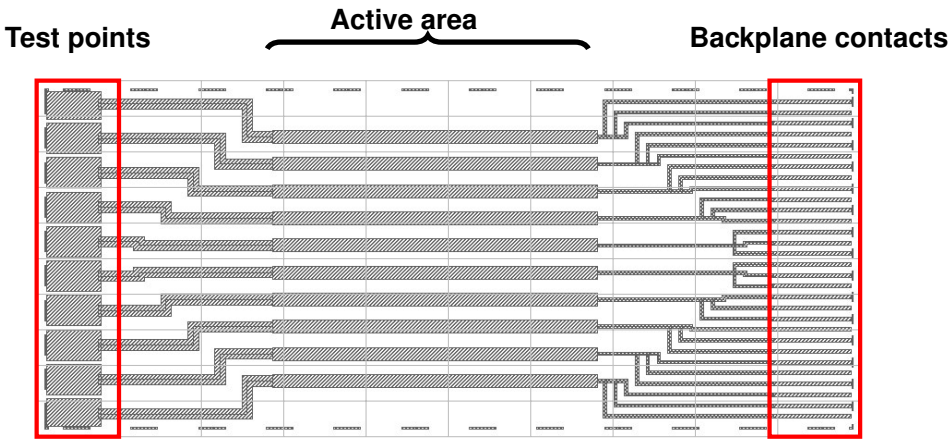


Figure 3.6: Key features of the fabricated components of the *in vitro* platform.

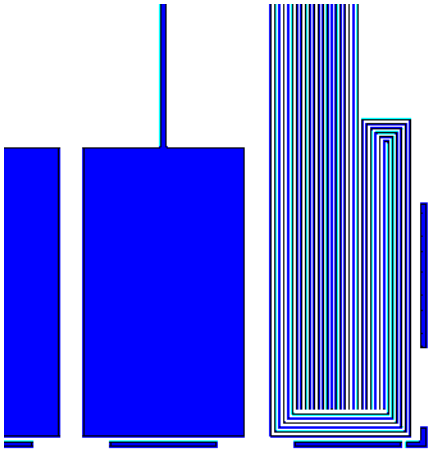


Figure 3.7: Pseudocontact in the 100 µm electrode design to allow rapid anodisation of individual electrodes without shorting.

layer of insulating SiO_2, the doping type and concentration were not a concern. Similarly the crystalline orientation of the wafer was judged to be arbitrary and so the specification of doping was based on cost and availability.

3.5 Thermal oxidation

Wafers were loaded into a quartz boat and placed in an oxidation furnace. A 1 µm film of SiO_2 was grown by wet thermal oxidation 1100 ℃ to act as electrical insulation between subsequent conductive layers and the bulk silicon substrate.

3.6 Photolithography

Wafers were cleaned by exposure to oxygen plasma for 30 minutes in a *barrel asher*. Wafers were then primed with the adhesion promoter HDMS for 10 minutes then coated with AZ nLof 2035 negative photoresist using a spin coater *POLOS*^{TM} at 500 rpm for 10 s, then 3000 rpm for 60 s. This was followed by a softbake at 90 ℃ for 5 min. The photoresist was patterned by exposure in a manual mask aligner (Karl Suss) using the emulsion mask. When creating the initial layer the mask pattern was visually aligned to the wafer. On subsequent layers alignment marks were used to align to the previous layers. Wafers were post-exposure baked at 110 ℃ for 90 s then allowed to cool to room temperature. Patterned wafers were developed using a double puddle technique in TMAH developer *AZ 726-MIF*, rinsed in DI water, dried with N_2 and stored until the deposition process.

3.7 Electrode Deposition

Tantalum was deposited by sputtering a *Plasmalab 400* sputter system to produce a nominal 300 nm film. A lift-off process was then carried out by submerging the wafer in resist stripper: 1-methyl-2-pyrrolidone (NMP) *Microposit remover 1165*. The solution was heated to 60 ℃ and ultrasonic agitation applied in a water bath, until all the negative photoresist and the unwanted metal on top of it was removed. Wafers were then rinsed progressively in acetone, isopropyl alcohol and deionised water and dried with N_2. Fig 3.15 shows the

thickness distribution across a wafer by profilometry measurements of unanodised tantalum test structures. Profiles were measured using a *Dektak XT* (Bruker corporation) profilometer. Thickness was taken to be the average step height of the levelled profile.

3.8 Contact deposition

In order to form mechanically robust contacts and promote electrical connection, aluminium was deposited over the tantalum in the contact region. To deposit an additional metal layer over the contacts, the above process was repeated, exchanging the initial mask for a second emulsion mask that contained only the contact areas and an aluminium sputtering recipe was selected. This process recipe included a pre-deposition argon milling step to remove any natively formed oxide and produce a low impedance inter-metallic interface. This second mask was aligned to the previous layer using alignment marks that were included in the first layer. A 300 nm layer of aluminium was deposited and patterned by lift-off as above.

3.9 Anodisation

To create the high-κ dielectric layer, prior to fluoropolymer coating and dicing. Tantalum pentoxide (Ta_2O_5) was formed by anodisation of sputter coated tantalum thin film electrodes. To produce anodised tantalum the metal is placed under potential in the presence of an acidic solution. A layer of oxide subsequently forms and becomes thicker. The solution was prepared as a gel to facilitate localised anodisation, by confining the extent of gel placement to select areas of the substrate.

For the *in vitro* devices, regions of tantalum comprising the active area were anodised at a constant potential of 30 V with a 100 mA current compliance. An anodisation apparatus was assembled incorporating a programmable power supply that allowed current measurement during anodisation and characterisation of the process. Anodisation test structures were created to characterise this process, in particular with regard to anodisation time, these are described in Section 3.10. Equation 3.1 shows the ideal stoichiometric half-cell oxidation reaction for tantalum.

$$2\,Ta + 5\,H_2O \longrightarrow Ta_2O_5 + 10\,H^+ + 10\,e^-(Ta) \tag{3.1}$$

3.9.1 Anodisation setup

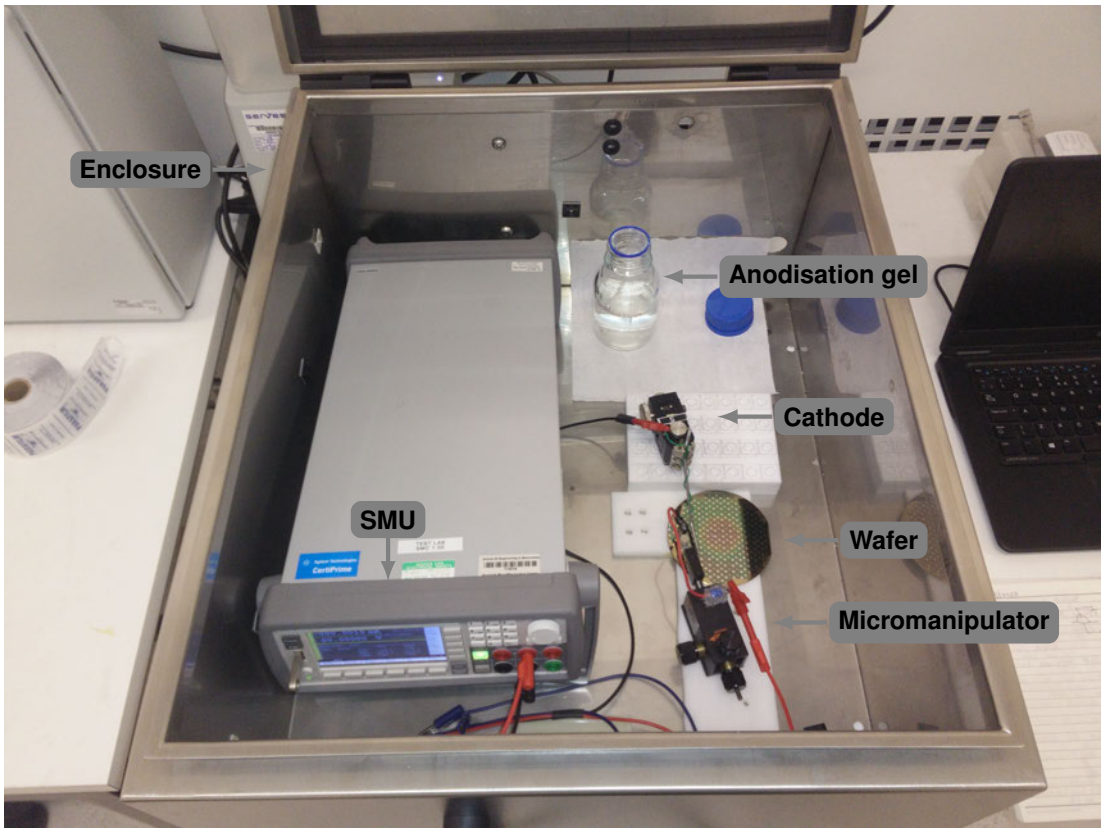


Figure 3.8: Anodisation setup.

Anodisation was carried out at the electrode level under clean room conditions, prior to dicing. The apparatus included a programmable power supply *B2900 precision source measure unit (SMU)* (Agilent) and several modified micromanipulators allowing precise connection to the anode and cathode. An earthed metal cabinet was used in lieu of a Faraday cage to shield from and reduce external sources of noise from affecting measurements during low current phases of the anodisation process. The wafer to be anodised was placed inside the cage along with the a SMU and the cage was connected to the power supply earth. Figure 3.8. Anodisation gel stock was mixed and a volume placed by pipette sufficient to cover the area to be anodised. The gel viscosity aided in controlling the boundary of dispensed material. Electrical contact (Fig 3.9) was made via a micro-

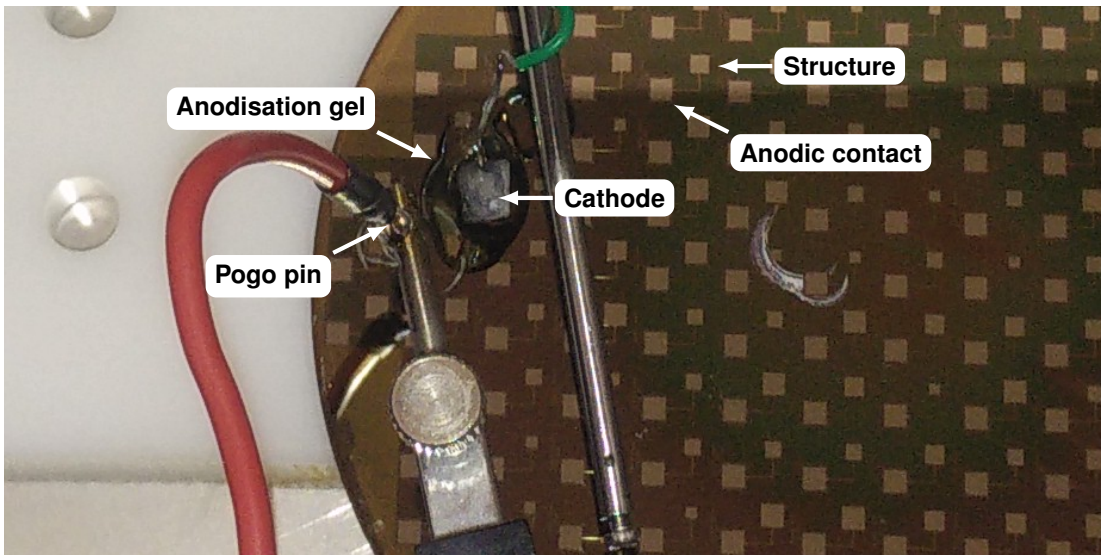


Figure 3.9: Closeup view of the anodisation setup. A test structure has been connected to to the anode via the pogo pin the structure to be anodised is covered in gel in contact with the copper cathode. All other areas of the wafer have been masked with photoresist.

manipulator modified to carry a flat contact 2.54 mm diameter pogo pin with flat head (RS Components Ltd). Cathodic connection made via a copper electrode - attached to a micro-manipulator arm - that was brought into contact with the anodisation gel [1]. A configuration file, designed to set up anodisation, was loaded into the SMU and modified to select a specific anodisation potential. On starting the program, the SMU recorded for a period of 5 s with no potential applied. This allowed the cabinet to be closed and an external timer started. The SMU then applied a previously selected potential to the sample with a 100 mA current compliance. The potential was held for 300 s at which point the anodised current had fallen to negligible levels. Finally, the potential was disabled and a measurement file written, which contained sampled current with respect to anodisation time. At the end of a session, the anode contact was carefully raised from the surface of the wafer and the cathode contact removed from the gel. Components and surfaces contaminated with gel were cleaned and neutralised using deionised water, then dried with a nitrogen gun. Table 3.2 shows the range of anodisation voltages applied to the structures. The thickness of the resulting film could be qualitatively assessed through thin film interference that results in a thickness dependent colour. Fig 3.10 shows the variety of oxide film colours within representative structures, the colours have been extracted and ordered by anodisation potential.

[1] The anodisation gel recipe was replicated from previous work detailed in[274].

A gradual progression from pale yellows, through brown, to indigo and blue as a function of anodisation potential. This progression can be used for thickness determination[275] in a similar manner as that for silicon oxides

In the 100 µm design of the *in vitro* devices, 9 of 30 electrodes electrodes were connected to individual contacts for anodisation. The remaining 21 were brought out to a pseudocontact, shown in Fig 3.7. This allowed multiple structures to be anodised under the same conditions simultaneously while remaining electrically isolated through the backplane connection, thus avoiding additional etching steps. The geometry was designed so that all structures could be contacted allowing for lateral misalignment of the pogo pin. This approach was shown to perform well during anodisation of devices, allowing all 21 wires to be anodised simultaneously.

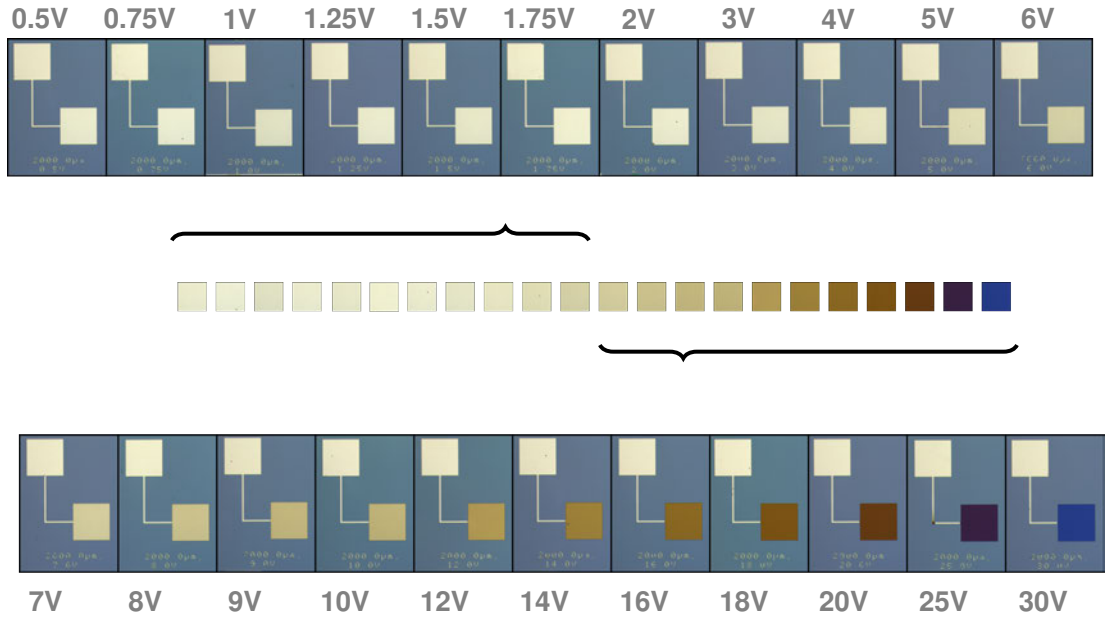


Figure 3.10: Tantalum pentoxide film colours sampled from microscopy images of test structures, arranged according to anodisation potential.

3.10 Anodisation test structure

Figure 3.11 shows the measured current versus time curves of example test structures anodised at a constant applied potential. As can be seen currents drop to negligible levels by around 10 seconds of the potential being applied, indicating the vast majority of electrochemical oxidation of Ta to Ta_2O_5 formation occurred over this time. The initial currents

shown as a function of the potential, shown in Fig 3.12 demonstrated an ohmic response. However the power supply was programmed to apply the potential to the structures for 300 seconds, this additional time, was designed to take into account a levelling process within the developing film where the potential developed across thin areas was higher than in thicker regions. This ultimately results in the oxide layer converging towards a uniform thickness. Extended process time also allows oxygen transport through the dielectric layer.

In the literature, such "soak" times of up to an hour have been reported[276]. However, anodisation times at this length were were not deemed practical given the constraints imposed by the device design. In particular, devices were anodised individually at differing voltages and the design software was written to deliberately distribute replicate structures across the wafer. This prevented electrically connecting structures that would due to receive the same anodisation treatment in exchange for producing data on cross-wafer uniformity.

To investigate the effect of longer anodisation times. Anodisation curves (Fig 3.13) over a longer period (30 minutes) were collected for three *in vivo* devices produced on a single wafer, these structures are described in Chapter 6. This further characterisation work of the anodisation process has been placed in this chapter to avoid repetition, due to sufficient similarity of the anodisation process between the two platforms.

In this situation, aside from the longer soak time, only two voltages were compared: 5 and 10 volts, with current shown as solid lines in the figure. In order to assess the soak time requirements, a second axis was added and the cumulative sum of the charge passed into the electrode was calculated. A piecewise constant interpolation of current samples across the sample period (Δt = 10 ms) was used to approximate a continuous current function. These values were then summed over all samples up to that time point to complete the numerical integration of the cumulative charge forced through the tantalum electrode (dashed line). When the raw data were examined many samples dropped below 0 A into negative values in this soak phase. This was interpreted as the signal being beneath the noise floor of the SMU. The data were therefore clipped to 0 A if negative, as otherwise the result was an non-physical cumulative negative charge. Further, the anodisation program in the SMU was designed to measure for 10 seconds before applying voltage yielding current values around –3 µA. Assuming this was a systematic error in the measurements, the

mean current over the initial measurement period was used to apply a correction to the anodisation currents (dotted line).

For tantalum test structures, profilometry measurements were carried out over the surface of the wafer both before and after anodisation. The measurement program was generated alongside the layout design allowing measurement and data recording to be automated. This allowed, in principle, for the alteration in thickness caused by the growing film to be measured. All anodised structures would be expected to present a positive change in absolute thickness between measurements. The measurements (Fig 3.14) show a distribution around zero thickness change. No significant difference between between unanodised structures and anodised structures was detectable. It was concluded that the film thickness was beneath the measurement resolution and repeatability of the instrument. Fig 3.15 shows the absolute thickness across the wafer of tantalum film deposition, by using step measurements of each structure and its wafer location. A horizontal band where structures measured 15–25 nm thicker than regions of the wafer edge that were adjacent and opposite the major flat, is easily distinguished. This is most likely attributable to spatial non-uniformity in tantalum metal sputtering process.

Test structures to measure capacitance of the anodised tantalum film were generated using a script written in Python. Structures consisted of four electrode sizes. Structure annotations were used to track the size and also the anodisation conditions applied to each structure. Structures were arrayed over the surface of a 100 mm wafer, alignment marks were injected into the design by assembling the coordinates of each structure into a spatial tree data structure using the Scipy scientific computing library[277]. Test structures were selected based on nearest neighbour calculations using this tree to supplied coordinates of preferred alignment mark locations. Alignment mark generation was toggled on these structures alongside a direction argument. An example of the construction of the structures is illustrated in Fig 3.16. Figure 3.17 shows the extension of the anodisation mask outside of the region to prevent shorting between to the two contacts. The revised absolute coordinates of alignment marks were annotated onto the wafer and written to file. Test structures were measured using a Keithley 4200-SCS parameter analyser connected to a Everbeing EB-8 analytical probe station.

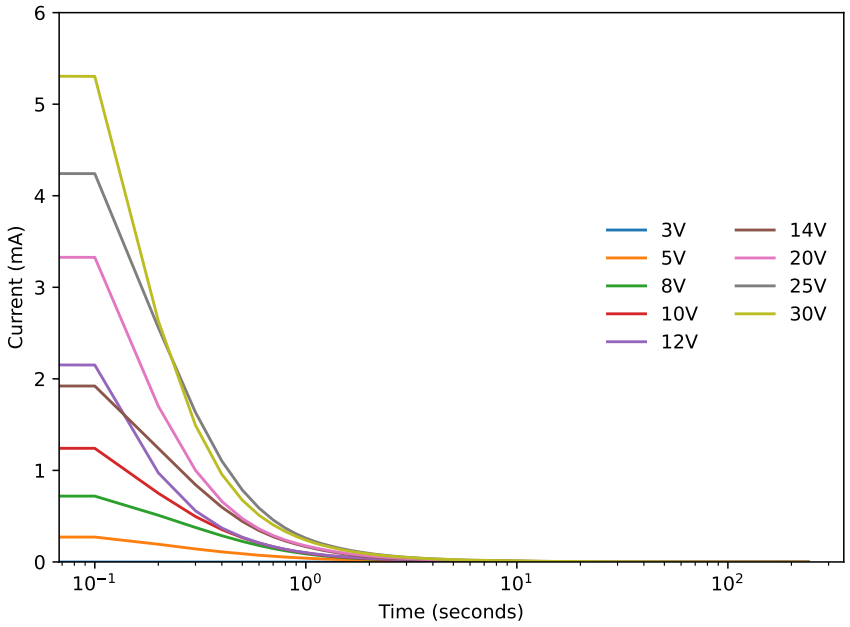


Figure 3.11: Anodisation curves of the Ta_2O_5 capacitance test structures as a function of applied constant potential.

Parameter	Value
Plate side (µm)	1000 µm, 1414 µm, 1732 µm, 2000 µm
Anodisation voltage (V)	0.5,0.75,1.25, 1.5, 1.0, 1.75, 2.0, 3.0, 4.0, 5.0, 6.0, 7.0, 8.0, 9.0, 10.0, 12.0, 14.0, 16.0, 18.0, 20.0, 25.0, 30.0

Table 3.2: Tantalum capacitance test structures, four plate sizes were generated for anodisation to varying voltages. The 2000 µm structures were actively anodised and used for characterisation.

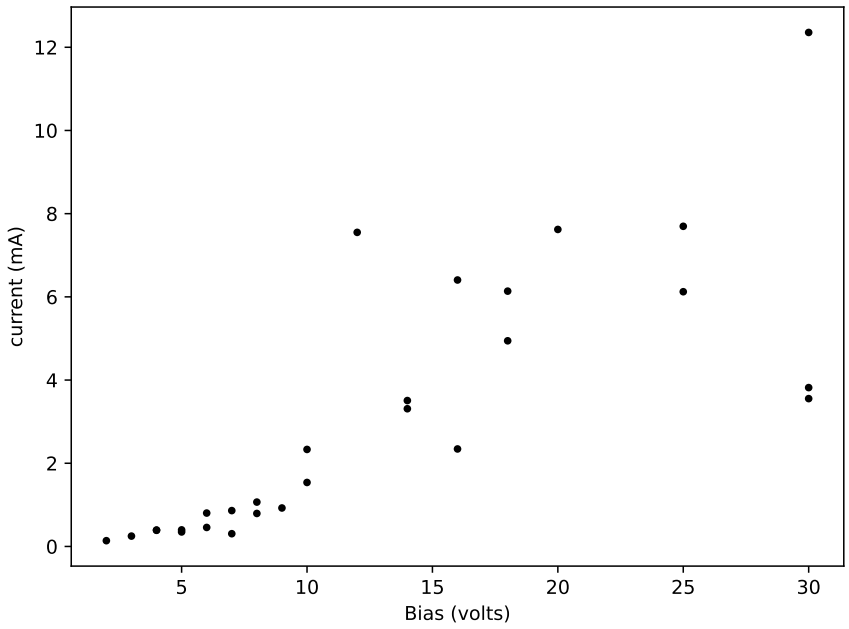


Figure 3.12: Initial measured currents during anodisation of test structures as a function of applied constant potential.

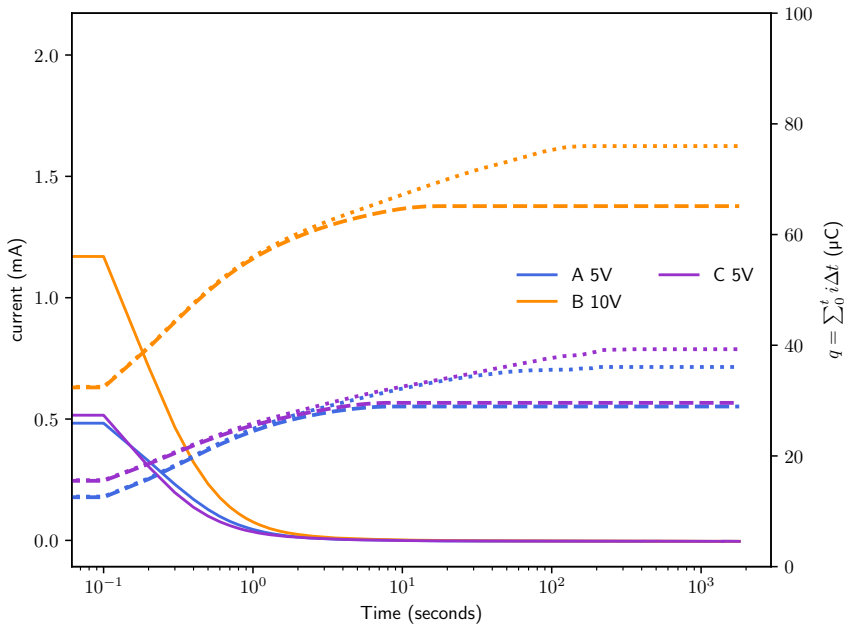


Figure 3.13: Anodisation curves (Solid lines) of three Ta_2O_5 *in vivo* devices (discussed in Chapter 6) from a single wafer. Two devices anodised at 5 V and one device at 10 Vs, all devices anodised for 30 minutes. Dashed line shows the cumulative charge on each device calculated by numerical integration. Dotted line shows cumulative charge after current offset correction.

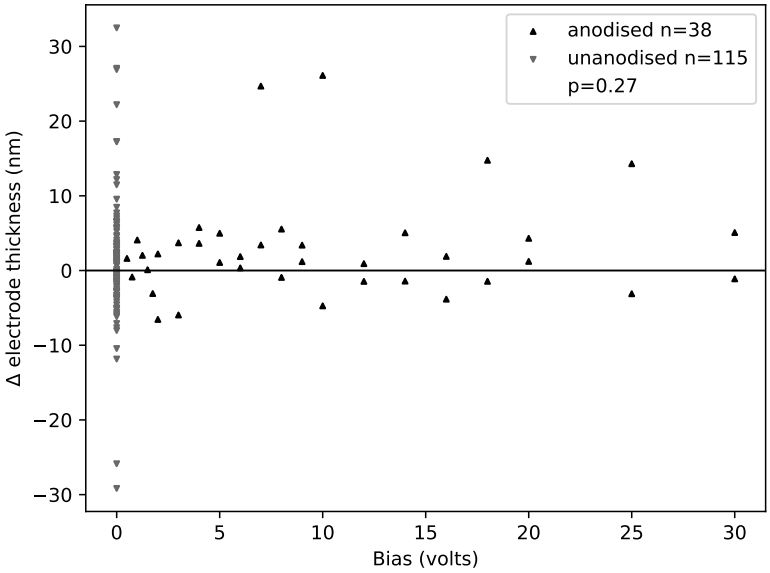


Figure 3.14: Change in height of tantalum electrodes in capacitance test structures, after anodisation generates a film of tantalum pentoxide, compared with control measurements of unanodised structures. Automated profilometry measurements.

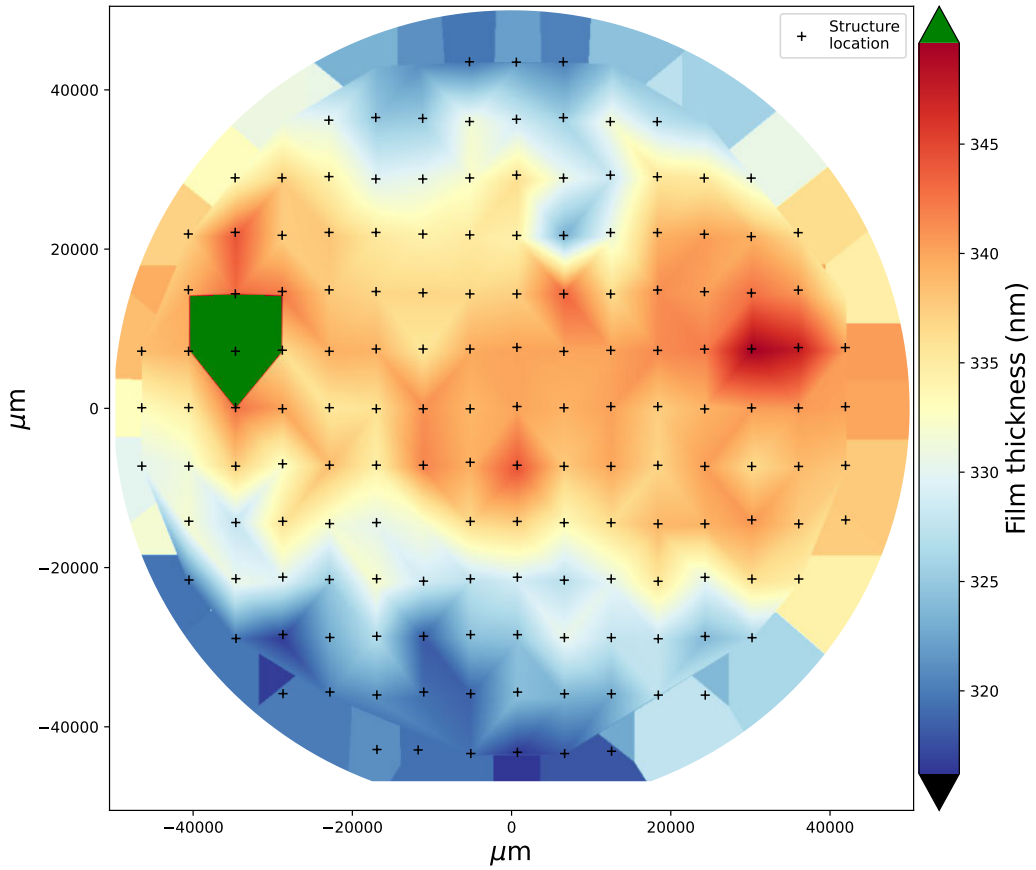


Figure 3.15: Thickness of unanodised tantalum film of each structure by automated profilometry measurement. Figure uses bi-linear interpolation between data points and extrapolation to the wafer edge using nearest value.

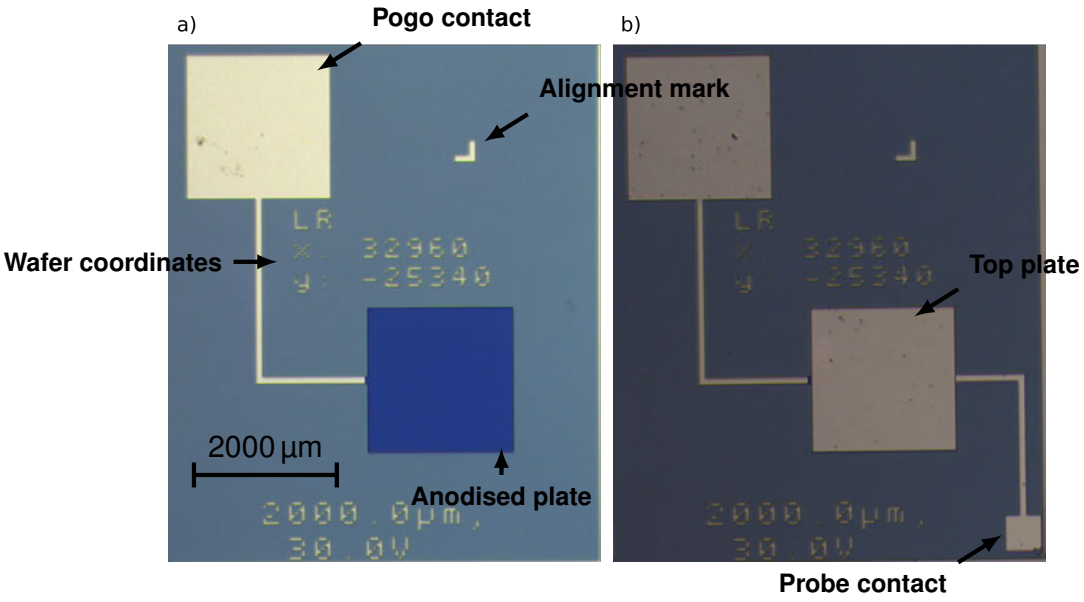


Figure 3.16: Example capacitance parametric test structure 2000 µm plate side, anodised to 30 V with LR alignment marker toggled. a) After anodisation, b) After deposition of the top plate. Top left contact designed for Pogo pin, bottom right designed for probe needle under magnification.

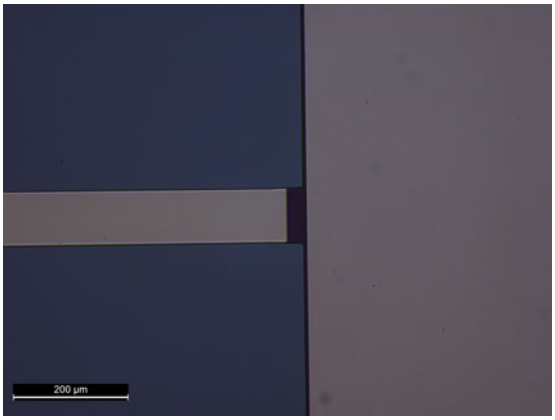


Figure 3.17: Anodisation gel is masked via photoresist window creating clear demarcation of oxide growth. The window was outset from the plate in the design to ensure the entire plate was anodised.

3.11 Fluoropolymer Layer

A thin fluoropolymer layer was deposited as a final layer on the surface of the devices, this had a dual role. Firstly, to control the surface energy of the cell contacting surfaces by creating a low energy interface creating conditions that could be expected to produce reliable biocompatibility outcomes. Secondly, to form a chemically uniform surface, independent of the underlying substrate allowing regions adjacent to electrodes to act as a control in cell adhesion experiments that are described in Chapter 4. Two spun fluoropolymers Teflon-AF (*Chemours*) and Cytop® (*AGC chemicals Inc.*) were tested alongside and another deposited by CVD octafluorocyclobutane (C_4F_8). Cytop® was chosen for *in vitro* devices used in the *in vitro* experiments, while C_4F_8 was used in the *in vivo* devices (see Chapter 5).

3.11.1 Deposition

A solution of Cytop® CTL-809M was diluted to 1% using Cytop® diluent *CT-SOLV-180* (*AGC chemicals*) and spun at 500 rpm, 10 s; 3000 rpm, 60 s to produce a 20 nm thick film. Reduced volumes of Cytop® per wafer were achieved by using a dynamic dispense with a micro-pipette on ramp up. The spun fluoropolymer layer was assessed using reflectometry and AFM.

3.11.2 Contact angle measurements

Alteration of the surface energy that was produced by film deposition was quantified using contact angle measurements. The sessile drop method[117] was employed, using a goniometer.

Deionised water was deposited in 5 µL droplets from a micropipette onto the surface. Droplet volume was selected to ensure the influence of surface tension dominated over gravitational forces on droplet shape as measured by the Bond number[278]. Immediately after depositing the droplet, an image of the droplet was brought into focus and an image was captured. Analysis of these images was subsequently performed to extract contact angle using an implementation of the LB-ADSA[279] algorithm, available as a plugin for the image processing software: ImageJ[280]. A mean angle was found from measurements on

Material	Treatment	Contact angle		γ C
		Measured	Literature	
SiO_2	Thermal oxidation	37.1°	-	-
SiO_2	after O_2 Plasma	62.0°	-	-
Ta_2O_5	Anodisation	47.8°	-	-
Teflon 1600	Spin Coated on SiO_2	124.5°	104°[281]	15.7 mN m^{-1}[281]
Teflon 1600	Spin Coated on Ta_2O_5	128.7°	105°[281]	15.6 mN m^{-1}[281]
Cytop 1%	Spin Coated on SiO_2	111.7°	112°[282]	19 mN m^{-1}[282]
Cytop 1%	Spin Coated on Ta_2O_5	112.9°	112°[282]	19 mN m^{-1}[282]
C_4F_8	PECVD on SiO_2	115.5°	176.2°[283] [a]	31.5 mN m^{-1}[284] [b]

[a] *Plasma deposition in a mixture CH_4 and He*
[b] *deposition on SiCOH*

Table 3.3: Static Contact angles of candidate fluoropolymer layers on different substrates compared against bare substrate, Measured contact angles are provided alongside literature sources of contact angle and surface energy calculations where available.

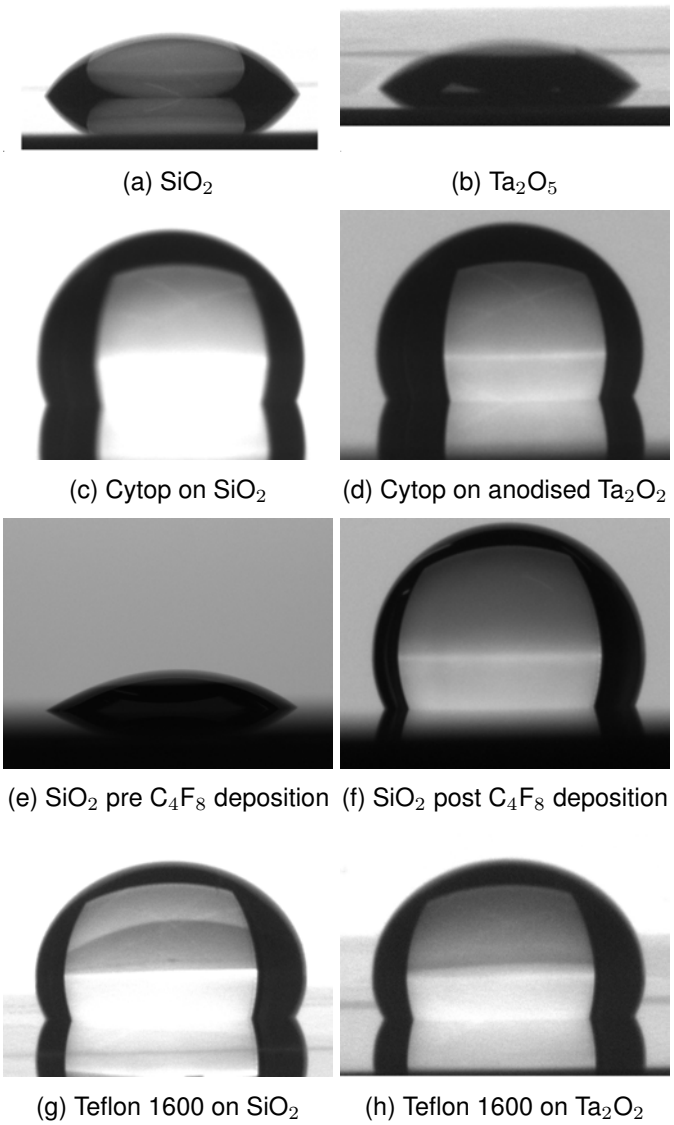
both sides of the droplet image that estimate a tangent line at the intersection of the droplet surface with the substrate.

Using the surface tension of water allowed an estimate of surface energy of a polymeric coating. Figure 3.18 shows comparison contact angles between of several fluoropolymers on a variety of substrates. Table 3.3 shows the calculated contact angles on differing substrates. The Cytop® surfaces show a difference of less than one degree. This is in contrast to surface energy disparity of the underlying substrates which show a 15° difference (SiO_2 and Ta_2O_5) in native substrate contact angle.

3.12 Atomic force microscopy

AFM was employed to assess the polymer coatings using a *Digital instruments D5000*. An example 2D scan is shown in Fig 3.19. This was taken over a region that included a manually introduced defect. A height profile could then be extracted across the step created at the boundary of the defect. This enabled a measurement of film thickness to be made, validating the process parameters for fluoropolymer spin coating.

Surface roughness of the polymer films overlying the different underlying substrates: Ta_2O_5, SiO_2, Ta, Al were also compared via AFM. In this case, samples were measured using tapping mode, over a 5 µm^2 region. This resulted in a data 512^2 sample array each containing height and phase information for each sample. Three replicates were taken for



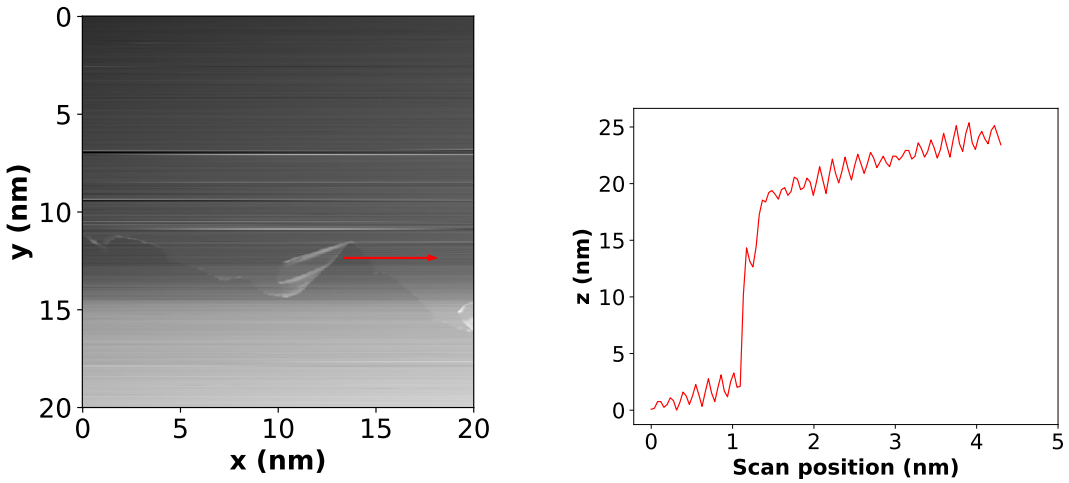
(a) SiO_2 (b) Ta_2O_5

(c) Cytop on SiO_2 (d) Cytop on anodised Ta_2O_2

(e) SiO_2 pre C_4F_8 deposition (f) SiO_2 post C_4F_8 deposition

(g) Teflon 1600 on SiO_2 (h) Teflon 1600 on Ta_2O_2

Figure 3.18: Droplet morphologies allowing water contact angle measurements and surface energy calculation on varying substrates.



(a) (b)

Figure 3.19: a) AFM scan data of nominal 20nm fluoropolymer layer spin coated onto a SiO_2 wafer. b) Height profile extracted along the line(red) allowed measurement of film thickness.

each material across two devices originating from different wafers [2]. Data was analysed using the open-source scanning microscopy processing software Gywyddion[285]. Figure 3.20 shows the surface roughness collected for each of the substrates.

3.13 Dicing & storage

Wafers were diced using a DAD640 *DISCO* semi-automatic dicing saw. Separated devices, despite their relative size could be removed from the dicing tape without incident.

3.14 Ancillary platform components

3.14.1 PCB

The PCB used to make connection to the devices was mounted in a project box with external connectors and the HSEC-8 connector exposed. Electrical connection between the PCB and power supply was achieved via a cable fabricated to with appropriate banana connectors on each end that could be routed from the external power supply via a feed through grommet in the cell incubator to the PCB.

[2]Scans were performed by Dr Camelia Dunare. Preparation of the samples and data analysis were carried out by the author.

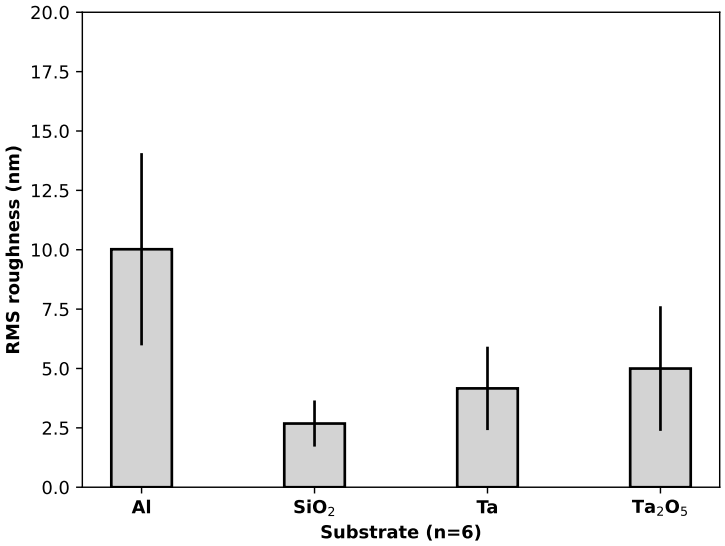


Figure 3.20: AFM roughness calculated across two unused devices. Roughness is calculated of the polymer layer overlying the different substrates.

3.14.2 PCB design

A printed circuit board was designed as a breakout board in order to allow electrical connections to be made to both the *in vitro* and *in vivo* devices. The design of this board had several functions to make the fine 0.8 mm pitch connections accessible to direct power and signal connection via header pins. To act as the basis for future specific circuit boards or to allow application specific daughter boards to be attached. Printed circuit board layouts were created in the PCB design software KiCad(v 4.05), using a footprint library supplied by (SAMTEC). Printed circuit boards and solder stencils were manufactured by Newbury electronics Ltd. Components were populated onto the board using a combination of reflow and manual soldering in the electronics teaching labs at the University of Edinburgh. Figure 3.21 shows the board installed on a 3D printed mount. Each of the upper pins on the upper row of the connector are broken out, jumpers can be used to connect each pin to either '+' or '-'. The header groups are spaced on a 0.254mm pitch allowing daughter boards to be prototyped and attached, extending functionality.

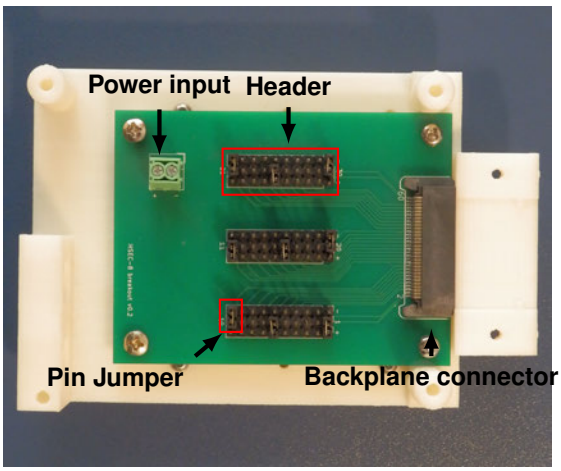
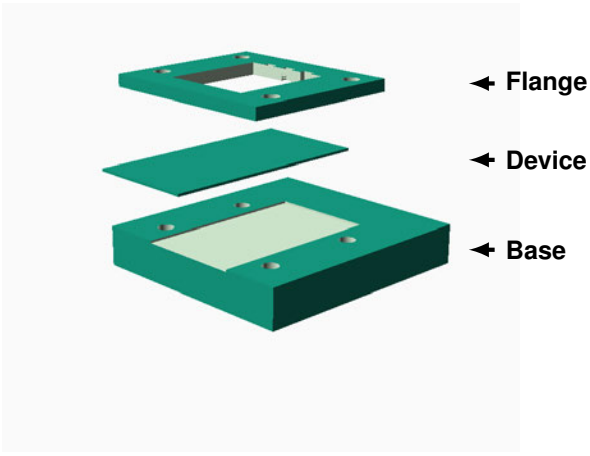


Figure 3.21: PCB breakout board for the HSEC-8 connector mounted in PCB 3D printed holder.



(a) Well frame comprising a 3D printed base, laser-cut flange to hold the well reservoir onto the device.



(b) Laser-cut lid with counter electrode pass-through.

3.14.3 Well assembly and holder

The well assembly was composed of several components: a base created from 3D printed ABS using a *Stratasys uPrint* FDM 3D printer, a laser-cut acrylic well frame and a laser-cut replacement for the double well lid. Figures 3.22a and 3.22b show the design of the 3D printed components. These were designed to interact with a single well from the two-well chamber slide, cleavage of the wells could be achieved by creating a score line with a scalpel. Cleavage was also tested with a laser, which could be performed successfully given the correct power and feed rate settings. An example of a final assembled device ready for connection is shown in Fig 3.23.

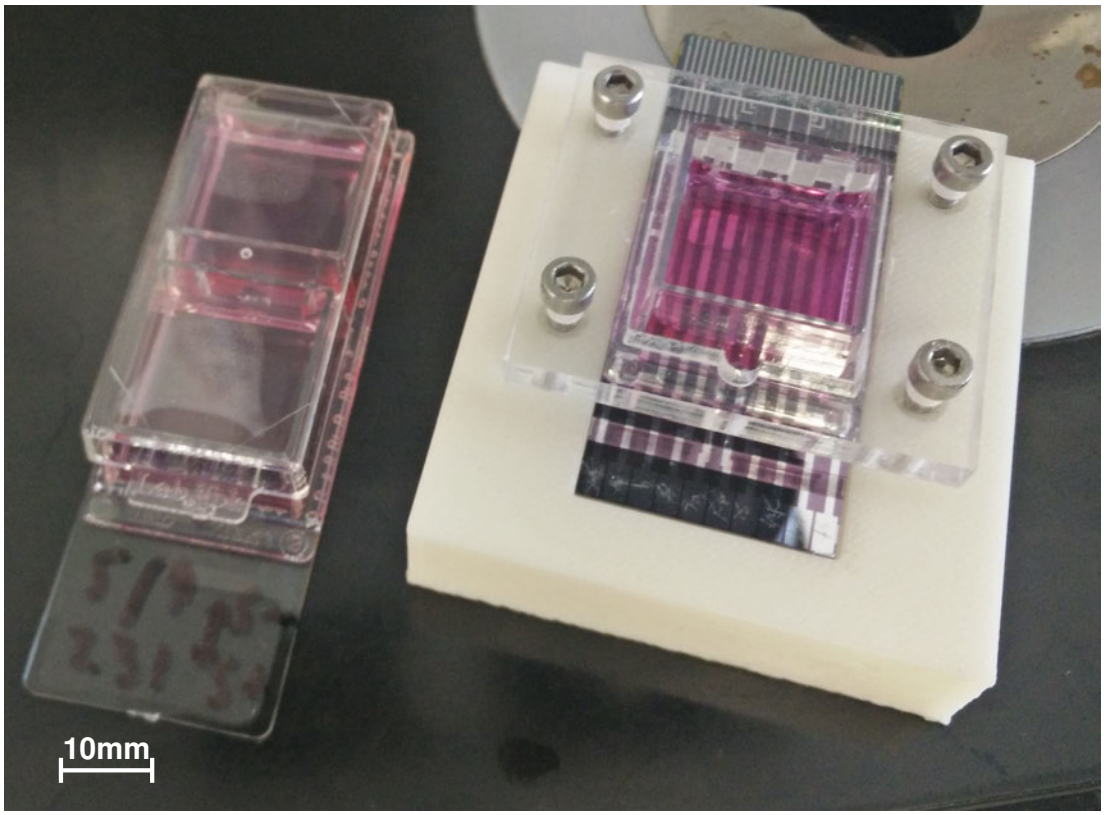


Figure 3.23: Comparison of original two well chamber slide (left) and setup for electrical stimulation (right).

3.14.4 Power supply and connection setup

A power supply, TOPS1 - stabilised power supply (*Farnell*) was used to charge device surfaces during the experiments. A suitable cable was fabricated to connect the power supply to the PCB. The cable contained a +ve, -ve and earth connection, the latter could be used to ground the cell incubator used in the experiments described in Chapter 4.

3.15 Discussion

The developed platform was easily fabricated, assembled, could reliably retain biological fluids and was suitable for use in a biological laboratory. The design ensured ease of fabrication, as relatively few processing steps were required for the base design. This was combined with low costs of raw materials, relative to comparable laboratory plasticware, provided the availability and access to process equipment can be assumed and therefore neglected in the cost.

The use of emulsion masks allowed the photolithography designs used in this work to be fabricated in the university cleanrooms and were significantly cheaper than externally supplied chrome photomasks. This was true because of the limited resolution required to form the features on the designs used and the relative short mask lifetime required. Future designs may require higher quality photomasks, however as discussed in Chapter 5, maskless lithography provided another alternatives with advantages properties.

By designing the platform around standard microscope slides, integration with pre-existing laboratory plasticware, media volumes, incubation densities and many pre-established protocols, processing techniques and analytical instruments could be achieved. This allows the widest possible scope for translation of procedures and techniques to be used with an electrified substrate, while also permitting meaningful comparison of the results with the biomedical literature.

Other apparatus and microfluidic systems have been used to allow cell culture under electrical stimuation[286,287,228], often implementing some subset of features like use of back-plane connectors[271,288] to provide a reversible electrical connection, or the incorporating commercially produced culture chambers and microfabricated surface features into their design[228]. However, the novelty of the platform presented here derives from a combination of features: a general prototyping surface with electrical connections, an interface for daughter boards to extend functionality, a low material count, a sterilisable surface and compatibility with pre-existing biological protocols.

The device stack was designed to allow capacitive charging of the solution interface to test the biological effects of electrical stimulation. The approach follows from work used in electrowetting on dielectric (EWOD) research[289]. Electrowetting and capacitive stimulation

of cells and tissues do share similar physical mechanisms of action. In EWOD it is the energy storage of the the capacitor formed by the stack that is related to changes in contact angle. In terms of influence on protein adsorption and cell attachment it appears that surface charge density is an influential property[69,290,123,141]. The permittivity of any dielectric layer that could be used is assumed to be much smaller than the the capacitive potential of the double layer[291]. Fluoropolymers are chosen for the solution contacting layer because of their unique properties as biomaterials. With the ability to irreveribly adsorb proteins, they represent an extreme condition case of low wettability hydrophobic surfaces. As apparent wettability increases during electrowetting, biological interactions with a surface may also be similarly altered. In particular, a surface could behave more like that of a more wettable (hydrophilic) material. An equivalent circuit for the device in operation is shown in Fig 3.24. Here a positive voltage was applied to the polar capacitance of the Ta_2O_5 layer in series with a fluoropolymer (Cytop®) film. The parallel leakage resistance was assumed to be very high with virtually no current flow once the system was charged. The two double layers, represented in the diagram as constant phase elements.[274]

$$\sigma = \frac{\epsilon_0 \epsilon_r}{t} V \tag{3.2}$$

Where σ is the surface charge density, ϵ_0 and ϵ_r are the permittivities of free space and of the dielectric respectively, *t* is the thickness of the dielectric and *V* is the applied potential.

Equation 3.2 shows the calculation of surface charge density. Tantalum pentoxide films can support 80–140 µC cm^{-2} charge storage density and has been used *In vivo* for intracortical stimulation[240]. Higher charge densities could be reached, compared with alternative electrode materials, without reaching solvent limits and offgassing.

Alternate dielectric materials, including TiO_2 $BaTiO_3$ may also be used[289,240], however tantalum has one of the highest dielectric constants (25[289]) while simultaneously being very stable again temperature and corrosion.

When in use, the potential across tantalum capacitors is suggested to be kept within a

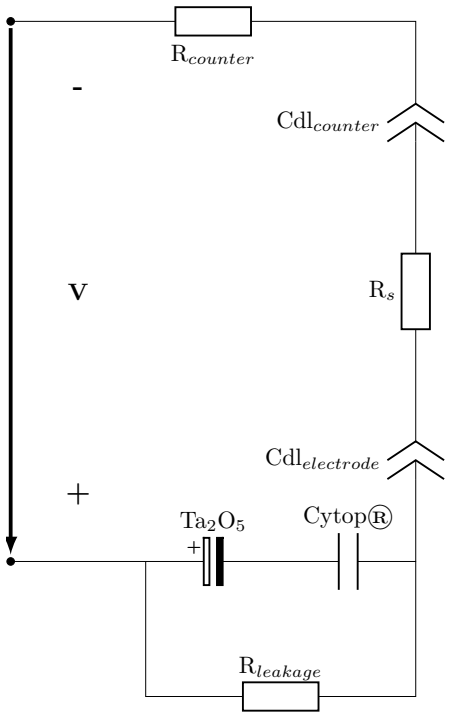


Figure 3.24: Equivalent circuit of device stackup.

range determined by a safety factor and based on anodic forming voltage. A figure of at most 80% of forming voltage has been suggested[240]. This would place an upper limit on the devices (which were anodised to 30 V) at 24 V.

Analysis of anodisation constants has found that dielectric constant is a function of forming voltage[292]. Leaving samples under continuous anodisation voltage has been suggested to create the most stable film. Soak times of up to an hour are often recommended[276]. In this work, ten minutes was deemed sufficient as the corrected anodisation curves seen Fig 3.13 had levelled off by this point. Additionally, the highest working voltage during the experiments would employ a very conservative safety factor, compared to the anodisation voltage. The effect of longer anodisation periods was analysed electrically and are shown in Fig 3.13. Multiple alternate deposition techniques and many other acids have also been using when forming Ta_2O_5 anodically[293], but large variations are seen in the quality and dielectric constants of the resultant oxide films.

The anodisation phenomena follows a Poole-Frenkel effect with oxygen migrating into the metal interface and tantalum metal moving out towards the solution causing the growing oxide film to extend from the interface[276,294]. This thickness change in the film was not measurable with profilometry as the magnitude was beneath the resolution of the instru-

ment.

Most of the anodisation current has been passed in the first few seconds after application of the fixed potential and was negligible by 10 s. However, when this current was integrated, (Fig 3.13, process lengths of at least 5 minutes appeared to be required for anodisation to slow sufficiently. Tantalum pentoxide electrodes for charge injection suffer from problems in creating adequate ratios of electrochemical surface area to geometric surface area. This is due to difficulty in fabricating porous or otherwise nano-roughened tantalum surfaces, in contrast to platinum[295296]. In this application, the interest was in the static charge developed on the surface of an overlying fluoropolymer layer that sets the chemical character of the interface. The advantages of a large surface area are removed as much of the charge is trapped inside inaccessible pores[136]. Overlap of double layers inside pores places a limit on the effect of increase surface area through porosity or roughness on the capacitance that can be achieved[297]. Deliberate roughening on the nanoscale in concert with the overlying layer could produce spatially heterogenous surface charge. The tuning of multiple independent surface properties has received some attention for optimising conventional biomaterials[188]. These approaches may also be applicable in active biomaterials.

Calculation of capacitance from the capacitive test structures was in broad agreement with prevous literature with 30 volt anodisation producing a dielectric with capacitive density of approximately 2 mF m^{-2}[274].

Parallel anodisation of the multiple individual electrodes using the pseudocontact that allowed a pogo pin spring-loading electrode to connect multiple structures simultaneously. At the cost of added processing steps, an alternative approach would be to temporarily short all electrodes together for anodisation and subsequently separate them back into individual structures via etching.

3.15.1 Fluoropolymers

The polymer film had several roles in the capacitive device. Crucially, it tuned surface chemistry and provided a mechanically more favourable surface from a biological point of view than bare tantalum would provide. In the case of the fluoropolymers there are also electrical effects that may operate independent of the surface chemistry. Surface

chemistry manifests as wettability, often quantified with contact angle measurements. The influence of the surface chemistry on an electrowetting application suggests that there is an dependence on the polarity of the terminal species[298]. Wettability may also be modified through surface treatment[299,300,301].

The fluoropolymers are characterised by containing carbon-fluorine bonds, which possess a high bond dissociation energy, ionisation potential[302], inertness, lubricity and hydrophobicity[303]. This bond is polar, but has low polarisability, resulting in an interaction potential that is primarily generated from van-der Waals forces[304].

The presence of electrolytes to aqueous solutions, as is the case with biological fluids, increases interfacial energy as a function of ionic strength. As a result, increased water contact angle with materials such as PTFE is observed. This is thought to mainly be caused by altered interactions (VdW and AB) rather than direct interactions with fluoropolymer surface[305].

In terms of protein adsorption, Teflon ® and untreated Polyethylene adsorbs in the region of 100[44]–250[26] ng cm^{-2} (although >1 µg cm^{-2} has been reported[306]) with a fractional coverage of 1.1 - implying surface packing and/or multilayer formation[26]. An alteration in kinetic barriers provided by the different environment of the surface can lead to extreme global shifts in protein conformational state, to the point of denaturation, when adsorbed on the surface of a fluoropolymer[26]. Such inertness is often attributed to often observed reduction of FBR *in vivo*[307], however protein dynamics on the surface tend to be less conducive to cell-material interactions, leading to poor implant integration in some situations and consequent promotion of FBR[48].

A layer thickness of 20 nm was used, this thickness had been employed previously to successfully create EWOD devices[274]. The relative permittivity of the Cytop® was lower than the tantalum dielectric and much lower than the double layer capacitance of any biological solution[291]. Electric fields can be generated across the polymer layer that are in excess of the dielectric strength of the material[274]. For Cytop® this is 900 kV cm^{-1}[282]. This produces a trade off between thickness and voltage requirements that has been addressed in the context of EWOD. An optimal thickness of Cytop® has been proposed at 12 nm, with thicknesses below 3 nm no longer producing the expected high water contact angles[308]. Many fluoropolymers[309], including Cytop® possess an electret property, meaning they can

retain polarisation after the stimulus has been removed. Cytop® has been produced with a surface charge three times that produced on amorphous Teflon[310], suggesting it may be the superior product for the application as a biomaterial. Annealing has been reported as a technique to improve the continuity of the spun fluoropolymer films. In this design the film, while it does contribute to the total capacitance of the surface if filling the role of chemical tuning, although surface defects may influence cell and protein attachment. Quantification of pinhole like defects and quantification would be beneficial. Samples used in the AFM (Fig 3.20) analysis were aged and had accumulated some particulate contamination before measurement, it is likely that any small discrepancies in the surface roughness between the SiO_2 and Ta_2O_5 surface arose from this contribution. The biological effect of the absolute and relative magnitude of the surface roughness on the biological results are discussed in Chapter 4 Section 4.13. Phase information is another possible measurement in characterise of polymer films, especially over differing substrates. However, this metric is more difficult to interpret than topography[311] because it arises from dynamic interactions between the surface and the probe tip.

Measurements of surface fluoropolymer coatings showed a reduction in interfacial energy. This process also created a chemical uniformity across the device independent of the substrate material. This along with characterisation of surface roughness reduced the effect of confounding variables in the following biological experiments.

Measurements of the alternative fluoropolymer surface Teflon™ showed a higher contact angle when measured than the manufacturer's literature. The measured film in this case was taken before application of a baking step where the film was raised above its glass transition temperature. The manufacturer states that this step is to drive off remaining solvent and produce a smoother film. It is postulated that the contact angle measured was a consequence of this roughness. Indeed, decreased wettability has been observed after artificially roughening Teflon[312], so a Cassie-Baxter wetting state may have been present, resulting in a temporarily superhydrophobic surface. Similarly, the value for C_4F_8 was significantly lower than the literature value, however this process included additional gases. The stability of the octafluorocyclobutane when exposed to solution is of concern for practical application. However, C_4F_8 copolymer films have also be shown to be stable in water for at least 8 weeks[313] suggesting that this material can be considered as an al-

ternative fluoropolymer layer to the spin-coated equivalents. Still further alternatives may exist in the deposition process: Teflon AF films produced by thermal evaporation showed higher charge stability with access to fewer discharge mechanisms, compared with Teflon FEP[314].

3.16 Conclusion

The *in vitro* platform developed in this chapter provided 4 cm^2 surface area available for culture, while the well could hold 1–2 mL of culture media or other solution. Thirty individual electrical connections were available for electrical connection to on-device structures. Multiple different electrode pattern designs were created. The facility for additional ancillary electrodes for example counter and reference in contact with the solution distant from the substrate has been demonstrated. The platform was integrated with a PCB that was designed to allow simple connection to a power supply or external instrumentation, connections were also exposed on the PCB through headers. These were placed on a standard spacing to allow daughter boards to be designed, prototyped and fabricated for future applications. Examples of which include signal generation, timed electrical stimulation and sensing. A single 100 mm wafer could yield three devices.

The devices produced possessed a tuneable surface chemistry that was independent of the electrode design and created a chemically and topographically uniform surface.

The platforms were easily assembled and reliably retained biological fluids. The devices were comparable in size to standard microscopy slides and could consequently be passed through standardised laboratory processes. The design produced a low cost platform, with ease of fabrication and requiring relatively few processes to fabricate the base design.

The platform was successfully utilised in an investigation of the electrical interactions with cell culture *in vitro* , described in Chapter 4. Both unstained incident light microscopy and fluorescent imaging after immunohistochemistry staining could be used to extract biologically useful information. The compatibility with procedures designed for laboratory plasticware permits future investigation of cell behaviour and morphology, ultrastructural adaptation, gene and protein expression that occur as a consequence of cell-surface interaction and direct comparison with results with the literature.

Chapter 4

in vitro experiments

Introduction

This chapter describes application of the *in vitro* devices developed in Chapter 3. This involved using the platform to support mammalian cell culture and was carried out at the Breakthrough unit at the Institute of Genetics & Molecular Medicine(*IGMM*). Two human cancer cell lines were used for experiments: MDA-MB-231 and MCF-7, both are breast cancer cells that are heavily represented in the literature[315]. Biomaterial interaction with tumour cells was also of interest as part of a project developing sensors to measure properties within solid mass tumours (IMPACT)[316]. Cell cultures were maintained via subculturing to provide cells for each experiment. These protocols along with those for fluorescent staining were used with minimal modification to demonstrate the compatibility of the platform with standard laboratory procedures. *In vitro* devices with 1000 µm (strip) electrodes were used for capacitive charging experiments as well as aluminium electrode experiments. These devices were designed such that when imaged a single (10x) microscopic field, could contain multiple cells in two distinct regions: an electrode region that could be capacitively charged and a non-electrode region that acted as a negative control.

Analysis of microscopic images served as the principle means of cell response quantification. An approach based on edge detection was developed that was compatible with the images obtained. Two complementary analyses were utilised. In the first, images of multiple fields were taken after a period of incubation with electrical stimulation, and a comparison of the two regions was made both within each field and across all fields. Second,

a hypothesis was explored that cellular dynamics, arising from cell detachment processes, would contain information about cell-surface interactions. This was achieved using time series measurements of single microscopic fields, after cessation of electrical stimulation. This process was termed 'Springback' as an analogy between release of cell-surface interactions - that are responsible for cell spreading - and the release of strain energy, stored within a material under elastic deformation.

In a separate experiment using the *in vitro* platform, aluminium electrodes that replaced tantalum were speculatively stimulated with 5 volts. A phenomenon was observed of alteration of the spatial distribution of cells when incubated near an electrochemically corroding electrode.

In the first part of this chapter the materials and methods are described, including description of the cell culture processes, setting up the apparatus for the experiments and the rationale and implementation of the quantification algorithms that were developed for analysis of the results. The results of cell stimulation experiments are then presented, starting with the capacitive charging followed by those that proceeded from an observation made about electrochemical corrosion of aluminium electrodes. This is followed by discussion and conclusions are then drawn, related to the capacitive charging hypothesis and the utility of the *in vitro* platform in investigating questions in this area.

4.1 Cell culture

Two immortalised cancer cell lines were used for the *in vitro* experiments: MCF-7 and MBA-MD-231. Both are adherent cells, their typical appearance is shown in Fig 4.1 and their properties are summarised in Table 4.1. Cells were cultured in Dulbecco's Modified Eagle Medium (DMEM) (*Thermofisher*) with low glucose and added pyruvate. The solution was supplemented with 20mL of foetal bovine serum (FBS), to provide growth factors and proteins, and 1mL of penicillin & streptomycin antibiotics was included - to suppress microbial activity. Cells were cultured in 250ml screw cap culture flasks (*Thermofisher*) under 120ml of culture solution.

Cells were incubated in a *Heraeus* cell incubator at 37℃ in a 5% CO_2 atmosphere. The culture media utilised a bicarbonate buffer to regulate the pH of the solution and manipula-

tion of the atmospheric composition during incubation (supplemented CO_2), was necessary for this process.

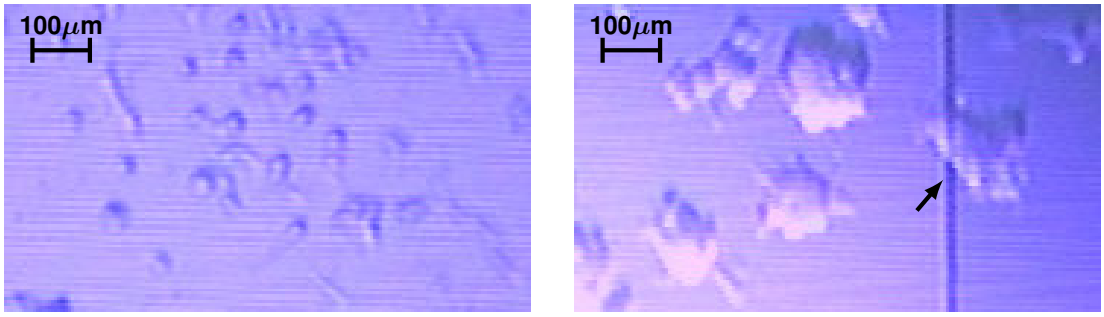
4.1.1 Subculturing

Subcultured cell cultures were used to supply cells for each experiment. The cell population was examined daily and the percentage confluency was estimated. A confluency of 100% would mean the whole surface was covered in a monolayer of cells that often exhibit contact inhibition - preventing further cell proliferation. When nearing 80-90% confluency, cells were released from their substrate, viable cells were counted and re-inoculated onto fresh plasticware. Cells required for experiments were also harvested at this stage and experiments were coordinated to coincide with subculturing. Culture media was exchanged with fresh solution at a standard interval (72 hours) to replenish consumed nutrients.

All materials were handled aseptically in a Class 2 laminar flow hood. Packaged consumables and gloved hands were wiped down with 70% ethanol before being used and on reintroduction to the laminar flow hood, if stored externally. To split a cell population, culture flasks were transferred from the incubator to a hood. The culture media was drained into a waste beaker containing chlorine tablets to render biological material safe prior to disposal. Trypsin enzyme solution was added to cover the cells and left for between 5 and 10 minutes with periodic light agitation of the flask to encourage cell release. This solution was then transferred to a universal container and the trypsin inactivated by the addition of fresh culture media, containing foetal bovine serum. A sample was transferred to a prepared haemocytometer, Trypan blue was added and live cells were counted under a microscope, ignoring any cells in contact with the lower left grid lines (south-east border exclusion). Cell count was used to calculate cell concentration, which was then diluted to a target concentration for culturing into the chamber slides and for seeding new culture. These were then labelled with the date, cell type and an incremented passage number and placed into the incubator. If required, cells were concentrated by centrifugation (2000 rpm for 5 minutes) and resuspended in a lower volume of fresh media.

Table 4.1: Key properties of the two cell lines used in the *in vitro* work.

Cell line	Characteristic	Histological origin	Cycle time (hours)	Source	Morphology
MDA-MB-231	Adherent	Adenocarcinoma	33.6 (25 - 41.9)[317]	Mammary gland	Fibroblastic
MCF-7	Adherent	Ductal carcinoma	50 (25.4 - 80)[317]	Pleural effusion	Epithelial



(a) MDA-MB-231 cells.

(b) MCF-7 cells.

Figure 4.1: The two cell lines: MDA-MB-231 and MCF-7 displayed distinct morphologies and diameters when cultured.

4.2 Preparing a cell stimulation experiment

To set up an electrical stimulation experiment, the well holder, flange plate and chamber lid, (see Figs 3.22a and 3.22b) were rendered aseptic using 70% ethanol, wiped down and placed into a laminar flow hood to dry. All other consumables, media, instruments and gloved hands were also cleaned with ethanol before being placed into the laminar flow hood. To assemble an experimental setup, a device was selected and placed into the slot on the holder, so that the backplane features extended beyond the end of the holder. A sterile well chamber was then opened and disassembled to retrieve a culture well. The original gasket was removed and the chamber was then cleaved by scoring with a scalpel along the flange connecting the two wells before separating. New gasket material - 3140 RTV coating (Dow Corning ®) - was loaded into a sterile 2.5 mL syringe and dispensed through a 21G blunt tipped needle. A continuous bead of material was run around the lower side the well flange. The well was then carefully lowered onto the device surface. The flange plate was placed over the well and fastened down to the holder using four M4 socket head cap screws. This compressed the uncured gasket material between the device surface and the well flange to create a seal. The assembled device was then set aside within the laminar flow hood to allow the gasket material to cure, according to the manufacturer's recommendations (>116 minutes), in an aseptic environment. A completed

assembly is shown in Fig 4.2.

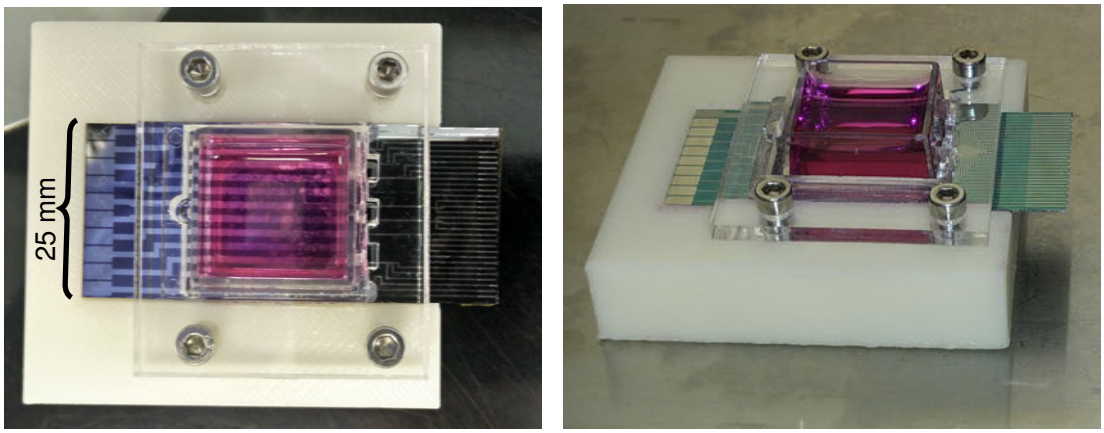


Figure 4.2: Assembled *in vitro* device with culture media.

The desired cell line was subcultured several days in advance to ensure sufficient surplus cells were available on the day of the experiment. A similar procedure was followed as for subculturing as described in Section 4.1.1. Briefly, culture media was disposed and the adhered cells were washed 3x with PBS to remove dead cells and proteins. Cells in the culture flask were then covered with pre-warmed Trypsin enzyme solution and placed in an incubator. After 5 minutes the flask was removed from the incubator and agitated, the enzyme solution was collected in a conical tube. The flask was washed several times DMEM to collect as many cells as possible, simultaneously diluting and inactivating the enzyme. The collected cell suspension was centrifuged and resuspended in a smaller volume of culture media. Cell concentration was established by counting a sample, diluted 1:1 with 0.4% Trypan blue, using a haemocytometer with south-east border exclusion. Cells showing uptake of Trypan blue were judged to be dead and excluded from the count. This concentration was then used to calculate a volume that contained 20×10^4 live cells. This volume was then drawn up into a micropipette for inoculation.

Immediately before inoculation, the device reservoir was washed several times with deionised water. This gave an opportunity to confirm the chamber was watertight. The chamber lid was similarly rinsed. Culture media sufficient to bring the total volume to 2 mL was added to the well, followed by the cell suspension. A 1 mL micropipette was then used to gently draw up and re-dispense some of the solution to distribute the cells uniformly within the solution. The chamber lid was placed over the well.

The assembled device was moved to the incubator and the backplane connector attached to the PCB. The electrical resistance between the PCB inputs and the test points on the device was measured to ensure a good connection. The power supply was connected to mains power and turned on. The open circuit voltage (OCP) was adjusted to the desired value using a multimeter and the power supply was then turned off again. The connecting cable was run from the power supply, through the rear port of the incubator and plugged into the PCB. The power supply was then turned on again and the voltage at each test point was confirmed relative to ground and the chamber counter electrode. As the test points were on opposite sides of the active cell area of the device from the backplane this confirmed that charge was present along the entire length of each electrode. After testing the incubator was closed and the cells on the device left for the duration of the 24 hour stimulation session. Testing was repeated before removal of the device for microscopic measurements, after the device was returned to the incubator and at the end of the experiment.

4.3 Microscopy

Device surfaces and unstained cultured cells were imaged using a *Navitar Micromate* microscope, equipped with a 10X *Mitutoyo* Plan Apo infinity corrected long working distance objective. This provided a 6.4 µm depth of field using incident light illumination supplied through a ring LED light source. Device surfaces were observed through the overlying culture media. Sensor data was encoded and output in s-video format. Images were saved using a USB capture card allowing individual frames to be acquired along with a timestamp either manually or periodically thereby enabling time-lapse imaging. The captured frames were 720x480 pixels using 8-bit per channel sRGB colourspace in lossless PNG format. The pixel pitch of the images produced by the microscope was 2.38 μm^2 per pixel, resulting in a 3.4 mm × 2.2 mm field of view. Some pixels around the edge of the resulting images were heavily affected by noise. The affected pixels were consistent and so were cropped out during analysis. The mask used for cropping the image is shown in Fig 4.3.

For each experiment and at every time point an image dataset was generated by scanning the substrate by moving the stage under the objective. Multiple fields were selected

at random across the device. This process created images where the relative position and quantity of the image occupied by each region varied. For time series imaging a new frame was acquired at five second intervals.

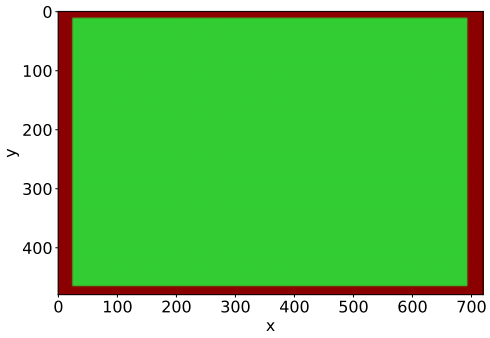


Figure 4.3: Image regions (red) are cropped out as part of the analysis, calculations are carried out on the remaining pixels (green).

4.4 Quantification algorithms

Image analysis was used to quantify the cell-surface interaction on the various substrates. A number of properties were hypothesised to be altered including: cell density, attachment, spreading and, survival. However, the resolution of the images and the lack of staining created constraints on the direct quantification of each of these that could be achieved.

Instead, a measure was developed that combined local cell confluency with attachment and spreading on unstained cells using incident light microscopy. This metric was then applied to quantify spatial changes in 'cellularity' (see Section 4.4.3) across microscopic fields and within labelled segments. This measure was complemented with distance calculation to quantify the spatial redistribution of cells across a device surface. Algorithms were then implemented to calculate these measures on different regions of the images.

4.4.1 Cellularity measure

Images were segmented and electrode and control regions were labelled and the resulting dataset was analysed using a custom Python script. The script loaded each image, converted to greyscale and the values were inverted. Edges were extracted using the Canny[318] edge detection technique. Briefly, images are blurred using a Gaussian kernel, gradients in the x and y directions were extracted by convolution of the image with a Sobel kernel and compared against a threshold to produce edges. A hysteresis step then used a lower threshold to include nearby pixels that presented a weaker response but were connected to pre-computed edges.

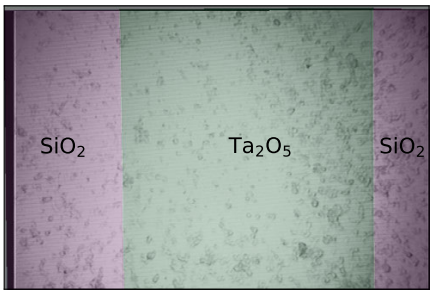
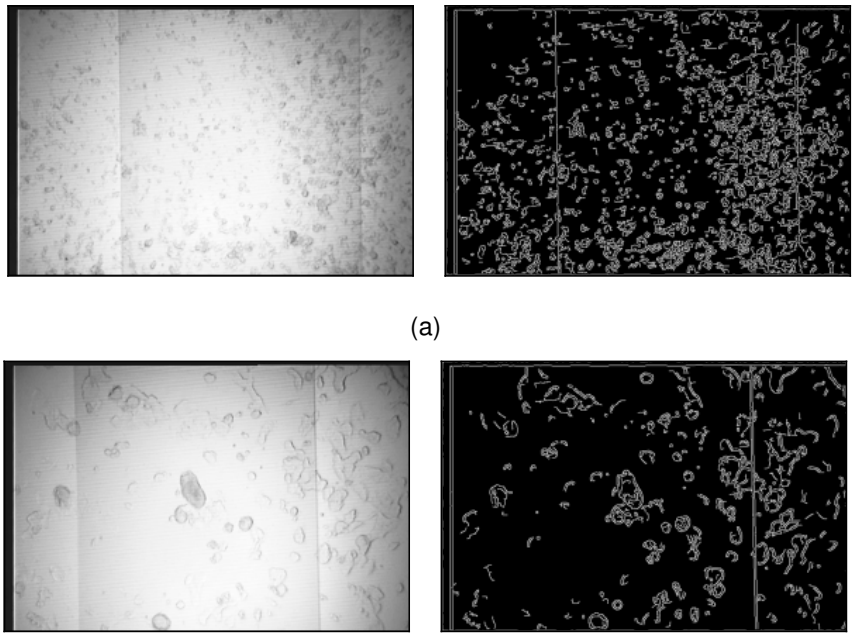


Figure 4.4: Example microscopy field showing labelled segments containing electrode (Ta_2O_5) and control regions (SiO_2).

4.4.2 Labelling

Images were labelled to create a segmentation using the open source software tool *Labelme*[319]. Electrode and control regions were demarcated using manually drawn polygons over each region and were named as SiO_2 or Ta_2O_5 as appropriate (Fig 4.4). For the aluminium experiments, electrode boundaries were marked with lines defined by two points and were labelled as: left and right, depending on where they appeared on the microscopic image. The coordinates of the shapes used to segment each image were saved to a JSON file by the software along with the image data with the same filename as the original image, which also contained the time that the images were acquired. These files could then be read and parsed by the analysis scripts.

4.4.3 Interpretation of Edge density



(a)

(b)

Figure 4.5: Examples of oringal frames and edge detection output: a) MDA-MB-231. b) MCF-7.

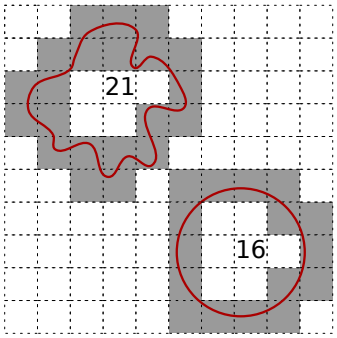


Figure 4.6: Interpretation of edge density. Example pixel array demonstrating a well attached(upper left) and poorly attached(lower right) cells. The outlines of the cells are shown as red lines and grey pixels represent computed edges. Cells are labelled with total number of edges that would be computed in each situation.

Edges in the image were created at large contrast changes that occurred predominantly at the boundary of unstained cells and were enhanced in the image due to the optical setup of the microscope, through phase-shift interference. The density of edges was defined as the ratio of edge pixels to the total pixels of a segment, expressed as a percentage. The edge density was correlated with two properties of the cell populated surface.

Firstly, cell density, which could be defined as cells per unit area or the confluency within a prescribed area. Secondly, cell spreading, which will increase the length of the circumference of the cell, due to attachment of ever greater cell surface area. This was caused by interaction with the underlying substrate. Figure 4.6 shows a schematic representation of this phenomenon. The outline of two cells are drawn overlayed on the pixels expected to be identified as edges. Alteration of cell shape from a minimal energy surface (spherical), was highly dependent on cell attachment. Different cell lines have varying tendencies to generate processes that alter the shape of the cell away from a spherical. This would also influence the number of calculated edges.

Cell density was controlled by inoculating all devices with the same number of cells along with a mixing step that aimed to create a uniformly distributed cell population, across the device. Due to the sensitivity of edge density to multiple properties of cells on surfaces the term cellularity was used in favour of cell density, spreading index or cell attachment.

4.4.4 Springback

Time series images of a single field were used to observe the dynamics of edge density after removal of electrical stimulation. Timestamps from the underlying image files were used to calculate the offset in seconds from the start of the measurement process for analysis. Sections of this series, corresponding to initial monotonic decline in edge density, were then extracted and a gradient determined via ordinary least squares regression. This rate was then used to compare dynamics across different experiments.

4.4.5 Aluminium electrode cell distribution

To quantify the cell distribution, a distance metric was developed for each calculated edge with reference to nearest point on the boundary of an adjacent electrode. The region of interest and the boundaries were labelled as described in Section 4.4.2.

Calculation

Distances in pixel space were converted to SI distance units using the pixel pitch. The metric used was the distance to the nearest point on the most proximal boundary using

the scalar rejection in pixel space of the edge vector and the boundary line vector. The coordinates of each edge are given in pixel values with an origin on the top left corner of the image (Fig 4.7). Figure 4.8 shows an example scenario for calculation of distance. Geometrically, this represents the scalar rejection (in pixel space) from a calculated edge, $\mathbf{e}$, to the line defined by two image annotation points: $\mathbf{p1}$ and $\mathbf{p2}$. Coordinates were first translated so that the origin coincided with the first annotation point.

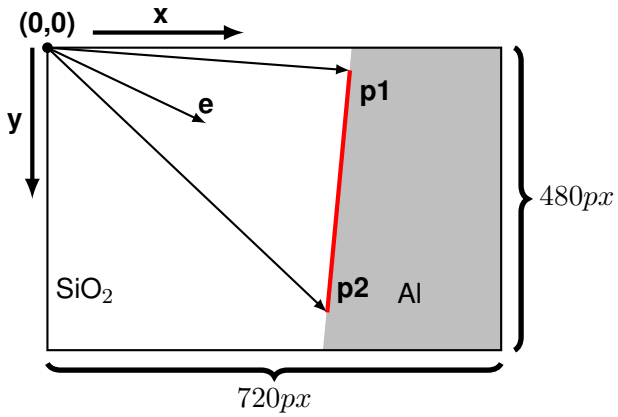


Figure 4.7: Example scenario for edge-electrode distance calculation inside a typical field. Image arrays have an origin at the top left corner of the image with the y-axis flipped in comparison to Cartesian convention. An example detected edge is shown $\mathbf{e}$ and an annotation line (red) follows the boundary of electrode regions (grey), defined by the annotation points $\mathbf{p1}$ and $\mathbf{p2}$.

$$\mathbf{a} = \mathbf{p2} - \mathbf{p1} \tag{4.1}$$

$$\mathbf{b} = \mathbf{e} - \mathbf{p1} \tag{4.2}$$

The scalar rejection, or distance of the shortest vector from $\mathbf{b}$ to a point on the span of $\mathbf{a}$ can then be stated as:

$$d_{\mathbf{pixel}} = \frac{\mathbf{a}^{\perp} \cdot \mathbf{b}}{\|\mathbf{a}\|} \tag{4.3}$$

where $\mathbf{a}^{\perp}$, the perpendicular complement of $\mathbf{a}$ is defined as:

$$\mathbf{a}^{\perp} = [\, -\mathbf{a_y} \quad \mathbf{a_x} \,] \tag{4.4}$$

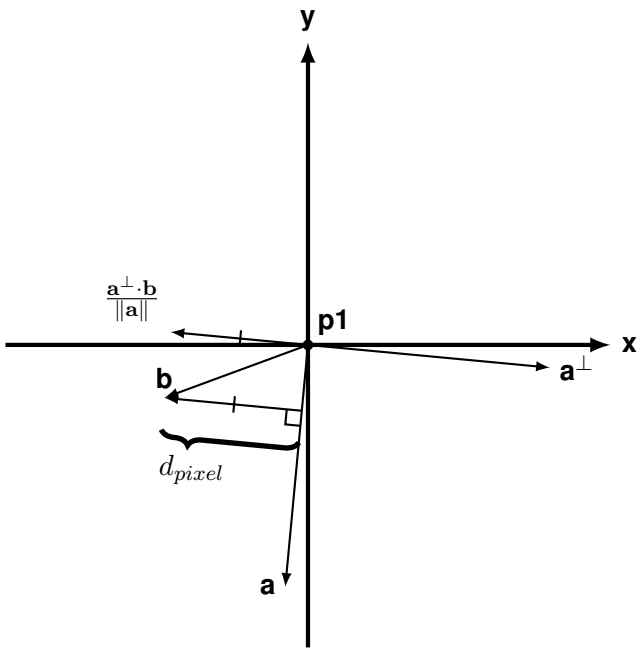


Figure 4.8: Edge-electrode distance calculation geometry. The length d_{pixel} is the scalar rejection of the the vectors $\mathbf{a}$ and $\mathbf{b}$.

Expanding to the components of the original vectors, the resultant formula was implemented in the analysis code:

$$d_{\mathbf{pixel}} = \frac{|(\mathbf{p2}_x - \mathbf{p1}_x)\mathbf{e_y} - (\mathbf{p2}_y - \mathbf{p1}_y)\mathbf{e_x} + \mathbf{p2_y p1_x} - \mathbf{p2_x p1_y}|}{\sqrt{(\mathbf{p2_x} - \mathbf{p1_x})^2 + (\mathbf{p2_y} - \mathbf{p1_y})^2}} \tag{4.5}$$

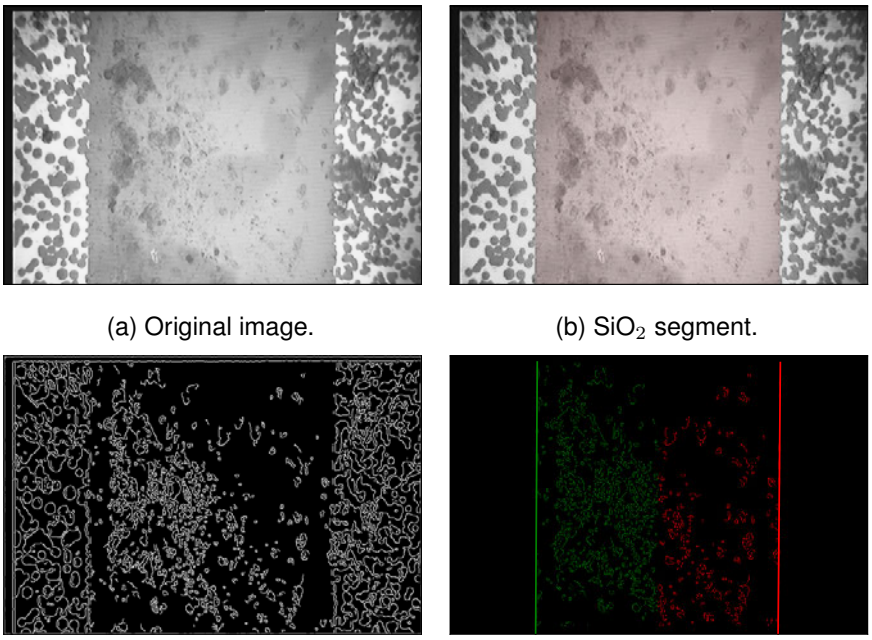
Note: the absolute value of the numerator was taken because the sign of the scalar rejection is dependent on configuration of the annotation points and the measured edge. Finally, the distance in microns was calculated using the previously established pixel pitch (Section 4.3):

$$d = d_{\mathbf{pixel}} \cdot pitch \tag{4.6}$$

Process

Figure 4.9 shows an example field and the intermediate steps in the detection process. As can be seen, edges were generally associated with most cellular structures visible on the device surface and were not generated by the electrode background. This process was repeated across all available fields, and accumulated into a single dataset, from which a

distance histogram could be derived. The width of the microscopic field allowed at most two electrode edges to be visible simultaneously. In these cases, both were annotated and the shortest of the both calculated distances was used for that edge. If the closest edge was not visible, the distance to the visible edge was calculated and then subtracted from the width of the channel (1000.0 µm). This meant all calculated distances were confined to an interval: 0 µm to 500 µm. An example of the output of this process can be seen in 4.9d where detected edges have been coloured according to the nearest electrode boundary.



(a) Original image. (b) SiO_2 segment.

(c) Edge detection. (d) Segment edges assigned boundary.

Figure 4.9: Example intermediate steps in image processing: a) Original image converted to greyscale. b) Segmented silicon region(pink), where cell detection will take place between two corroded aluminium electrodes. c) Output of the Edge detection algorithm. d) Edges cropped to segment coloured according to nearest electrode boundary (annotated) that act as a datum for distance measurement.

4.4.6 Luminance

Colour images were converted to greyscale via a perceptually weighted average of each colour channel. A mask was created for each dataset of all pixels that contributed to an edge and the complement of this set was used to select pixels that did not participate in an edge. The luminance was calculated by summing the intensities of these pixels for each image and normalising to the largest value in the set.

4.4.7 pH tracking

Colourimetric measurement, correlated with changes in the pH of the media, were used to track pH over the time series experiments. The pH of the DMEM culture media was indicated by the presence of a phenol red indicator, which can be used to quantify pH[320]. As pH was stabilised by the bicarbonate buffer, in concert with a higher CO_2 concentration, which was maintained within the cell incubator, the pH was maintained between pH 7.0 and 7.4. Removal of the media from this environment would result in a shift in the pH towards more basic indicated by a colour change from red to fuchsia. To take a measurement for each frame of the time series, images were converted into Hue saturation value (HSV) colourspace. The Hue component is a single value, representing the colour of each pixel. To calculate a single value for each frame a mask was constructed by taking the union of the edges for each frame over the entire time series. This produced a set of pixels (E) that were calculated as an edge in at least one frame in the dataset. This set was increased by calculating a binary morphological dilation using 12 by 12 pixel kernel ($E_{dilated}$). The complement of this set contained only non-edge participating pixels ($P = {E_{dilated}}^c$).

The HSV colourspace is often visualised as a cylinder with the hue component representing the theta value in cylindrical coordinates. To calculate a mean value of these pixels, the hue values (P_{hue}), which fell on the interval [0,1], were mapped onto [0,2π] and assumed to be points on a unit circle in the complex plane. The arithmetic mean of the real and imaginary components of this set of points was then calculated. The circular mean was defined as the argument of this new point in polar coordinates which could then be mapped back to original interval (Equation 4.7).

$$\overline{hue} = \frac{\operatorname{atan2}(\frac{1}{N}\sum_{n=1}^{N}\sin(2\pi P_{hue}), \frac{1}{N}\sum_{n=1}^{N}\cos(2\pi P_{hue})}{2\pi} \tag{4.7}$$

4.5 Statistical analysis

For each experiment, the distributions of calculated edge densities on each region were compared. As the variance of the electrode and control regions was not equal Welch's test[321] was carried out to assess whether there were significant differences between the

two populations of edge densities. To directly compare adjacent regions a paired test was also applied to each experiment. Here the difference in edge densities between electrode and control region was calculated for each field. Only fields where both regions had been segmented were included, this was the in the majority of fields across all datasets. In the paired test, an expected difference between the regions of zero was assumed, corresponding to a locally uniform cell distribution. A threshold for significance was set at $p<0.01$.

4.6 Staining and fluorescence imaging

Fluorescent staining enables a wide array of techniques and methods for quantification of cell behaviour and so it was desirable to demonstrate the feasibility of using this technique on the *in vitro* devices. A fluorescence protocol was applied to fixed cells attached to the surface of several devices after electrical stimulation experiments had been completed.

4.6.1 Fluorescence protocol

On completion of an electrical stimulation experiment, culture media was removed from the wells and they were washed twice with cold PBS dispensed slowly from a micropipette. Cells were fixed by exchanging PBS with 500 µL chilled acetone and incubating for 10 minutes in a chiller at 4 ℃. After fixation, excess acetone was removed and devices were air-dried and batch stored at –20 ℃ in a universal container until immunocytochemistry staining.

Immunocytochemistry: cells adherent to the device surface were washed twice for 5 minutes each with PBST using 1ml per well. Cells were then incubated with 3% H_2O_2 for 10 minutes. This was followed by repeated washings with further PBST for 5 minutes. 240 µL DAKO® blocking solution was added to the cells and incubated for 10 minutes in a humid container at room temperature.

Primary cytokeratin antibody: anti-cytokeratin antibody was diluted 1:50 in DAKO antibody dilution solution. A volume of 400 µL was added to each chamber and incubated in a humid container for 1 hour. Cells were then again washed three times in PBST for 5 minutes each.

Secondary cytokeratin antibody: the secondary anti-cytokeratin antibody was diluted

1:25 in DAKO antibody dilution solution and 400 µL was incubated with the cells for 1.5 hours. Cells were then washed three times with PBST for 5 minutes. The slides were dehydrated using industrial methylated spirits (IMS) for 5 minutes then allowed to air-dry in a dark container.

Nuclear counterstaining: nuclear visualisation media DAPI *Prolong Gold anti-fade* was used to stain the cell nucleus. 45 µL was added to a glass cover slip. The well chamber was removed from the surface of the device and the cover slip carefully placed over the cell containing region of the device. This was to prevent trapping air between cover slip and substrate. Nail polish was applied around the edges of the cover slip to seal the edges. The slides were stored wrapped in aluminium foil to protect from light at 4 ℃ until imaged by microscopy.

Immunocytochemistry and fluorescence staining in general are commonly used techniques for examining protein expression and other intracellular processes. Multiple structures are involved in actuating cell behaviour in response to surfaces and have been described in preceding chapters. Fluorescence microscopy is often used as an incident light microscopic technique. Therefore it was suitable for visualising cells and tissue structures on the *in vitro* devices, as they were based on silicon wafers that were opaque to visible light. Figure 4.10 shows cells that were stained after incubation on the surface of a device. Two stains were used simultaneously to highlight two different structures of the cell. An unmodified standard operating procedure was followed, and was successful. The two stains: DAPI and cytokeratin, highlight the cell nucleus and a component of intermediate filaments that are involved in maintaining the mechanical shape and in tissues are involved in the connection of the cell to connective tissues. Additionally, DAPI can be used to distinguish live and dead cells at the time of fixation. In the figure, three bright regions represent the nuclei of three cells. A fainter halo, surrounding the nuclei, represents the cytokeratin signal. The irregular outline demonstrates the successful attachment to the underlying fluoropolymer substrate. Alterations to this attachment are proposed to be a component of the measured difference between charged and non-charged regions of the substrate.

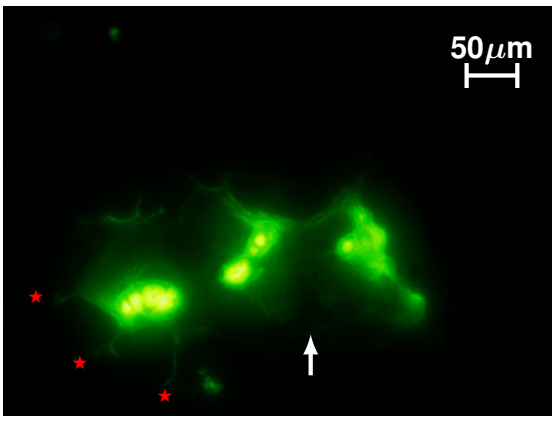


Figure 4.10: Fluorescence staining of MCF-7 cells on a device surface after incubation, using dual staining with DAPI and cytokeratin. Two of the cells have just completed mitosis (arrow), cells are attached to the substrate and cell processes/invadopodia (★) are visible.

4.7 Gasket and leachate test

A concern when creating a new combination of materials was the possibility of introduction of cytotoxic chemicals, either as part of the material or as breakdown product or residue from manufacturing. The original chamber slide around which the devices were designed contained a small piece of gasket material to create a watertight seal between the chamber wall and the slide. The gasket also allowed the chambers to be removed at the end of the experiment, permitting the slide to be processed. When assembling a device the well portion of the chamber slide was removed before the two chambers were split apart. Gasket material was then used to re-create the seal and the chamber was compressed onto the surface of the substrate with a screwed down flange and allowed to cure. The gasket material therefore, represented the only material that could contact the cell media that did not originate from a commercial cell culture device or was part of the experimental investigation. The gasket material used was 3140 RTV Coating (Dow Corning ®), with a stated cure time of 116 minutes[322].

In order to exclude gasket material as a contaminating factor a modified direct and indirect biocompatibility experiment was run[323]. Some gasket material was dispensed onto unmodified chamber slides to cover about one third of the surface. Both cell lines were exposed to gasket material using two different cure times in a direct and indirect test. The cure times were 2 hours and 72 hours before addition of cells and media. For the direct test, cells were incubated in contact with the gasket material for 48 hours. For the indirect

test, sterile media was incubated with the gasket material for 24 hours then transferred (along with any elution) to a fresh chamber and used to incubate cells for 48 hours. No difference in cell survival or morphology was evident on visual inspection at 24 and 48 hours of incubation in either the direct or indirect tests.

4.8 Cell survival on Cytop®

In the longest experiment cells were cultured for 96 hours on the surfaces under electrical stimulation. Cells in this and other experiments appeared viable at the end of the experiment. After fluorescent staining as can be seen in the example image shown in Fig 4.10 cells were actively attached to the underlying substrate with two cells that appear to be dividing. This demonstrated that cells were capable of interacting with the surface and proliferating through mitosis.

4.9 Electrical stimulation

Electrical stimulation experiments all used the same cell inoculation density. The electrode area was constant throughout, the capacitive charging experiments and all devices had Ta_2O_5 electrodes anodised to 30 V. The charge applied is set by the fixed voltage, supplied by the power supply. The polarity of this voltage was always positive on the cell contacting electrodes versus the counter electrode incorporated into the chamber lid which was set at ground potential.

4.10 Springback effect

The time series evolution of edge density was tracked within a single, randomly selected, field in several experiments. Images were acquired at five second intervals for up to two hours after removal from the incubator. Times are referenced in seconds from cessation of electrical stimulation and removal of the device from the incubation environment. Not all series were taken immediately as measurements were often interspersed with acquisition of multiple fields. As a result not all time series start immediately, but the offset to the start of measurements was known. The relative time allowed comparison of cell dynamics

between experiments, where the data overlapped. The series compare edge densities for each experimental region within each image. Additionally, the image luminance across both regions, the calculation of which was described in Section 4.4.6, is also shown in each series.

Edge density measurements appeared highly repeatable between samples and trends were larger than the local inter-frame variance allowing adequate monitoring.

Figures 4.11, 4.12 and 4.13 all show an initial a sharp decline in edge density almost immediately after removal from the incubator. In the control (Fig 4.11), this decline continues steadily over a 2 hour period of measurement. By contrast, more complex dynamics are observed on the fluoropolymer coated devices. In Fig 4.12 a subsequent peak was followed by a steady rise in edge density, this trend appeared to be mirrored in the data available for the MCF-7 cells in Fig 4.14 that covered the same interval around 1000 seconds.

Quantification of the reduction in edge density was achieved by extracting gradient information from an initial feature of edge density reduction consistent to all series examined. Intervals in the data - highlighted grey in the figures - were extracted and an average rate of change in edge density was computed by linear regression for each series. These gradients are presented in Fig 4.15, positive gradients would indicate progressive cell attachment. However, all gradients are negative, which is interpreted as cell detachment with the magnitude indicating the speed of the process. A notable contrast between TCPS and device Cytop® SiO_2 was observed: a shallower decline of edges on TCPS, over the sampled interval, compared with Cytop® surfaces (device). The edge density gradients on the internal controls of each 17 V experiment showed a shallower edge reduction from a lower absolute value on Ta_2O_5 compared with SiO_2. This was consistent with the edge density interpretation and with the cellularity results which showed a reduction on the Ta_2O_5 surfaces at this voltage. The reduced cell attachment resulted in a lower capacity for edge loss. Conversely, the field examined on the 5 V device showed a larger absolute edge density than the internal control. This scenario was present in around 50% of fields, although the mean edge density in this region were lower than the previous timepoint (see Section 4.11 they showed a higher edge density on the electrode. While the gradient may be partially a function of absolute density, the similarity of the SiO_2 gradients despite the differences

in absolute edges would tend to discount this, raising the possibility of a positive effect on cell attachment at lower voltages.

Figure 4.11 shows a discontinuity in the edge density at 885 seconds. This was also present in the luminance data and could be attributed to contamination by an external light source and so gradient extraction was limited to the preceding interval. The trend of luminance reduction over the sampling period was a result of the experiment being performed in the early evening when ambient light levels were reducing. The mean hue component of all non-edge participating pixels, across the images, of the TCPS series were plotted over the time series overlayed with a fitted curve in Fig 4.16. Shifts in hue were likely largely created by alterations in the phenol red component of the culture media. Phenol red is a pH indicator and the colour change observed was consistent with removal from the enriched CO_2 environment.

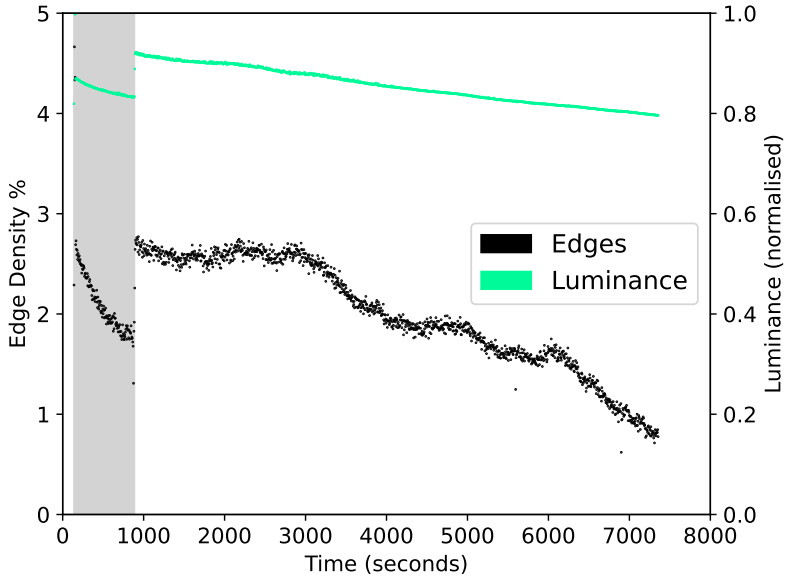


Figure 4.11: MDA-MB-231 cells cultured on Permanox®(TCPS) chamber slides after 48 hours incubation.

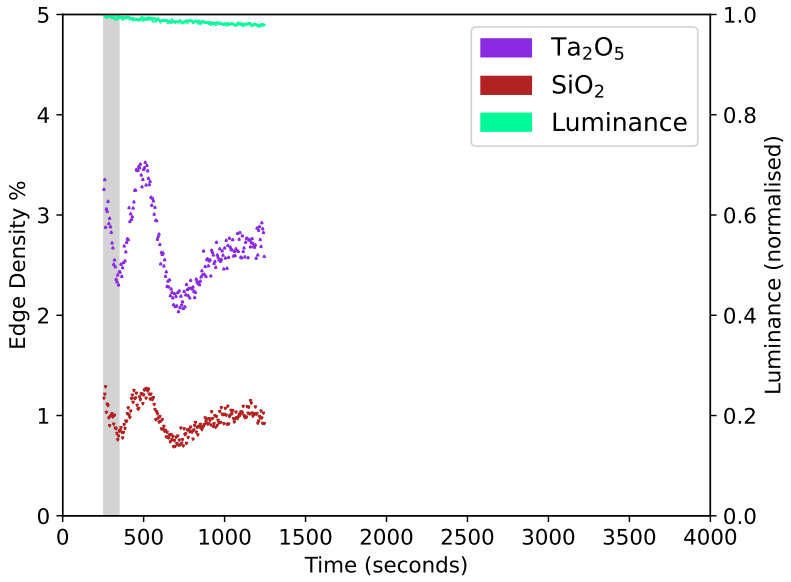


Figure 4.12: MDA-MB-231 cells stimulated at 5 volts after 48 hours incubation.

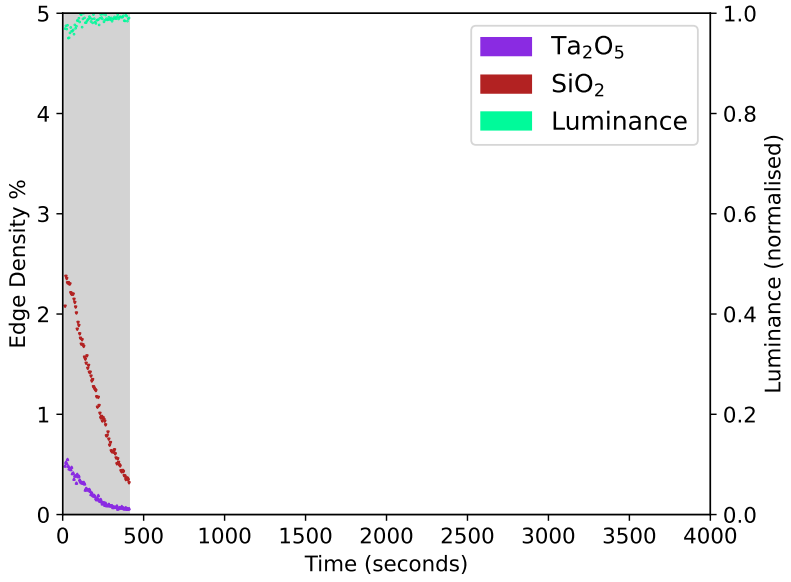


Figure 4.13: MDA-MB-231 cells stimulated at 17 volts after 48 hours incubation.

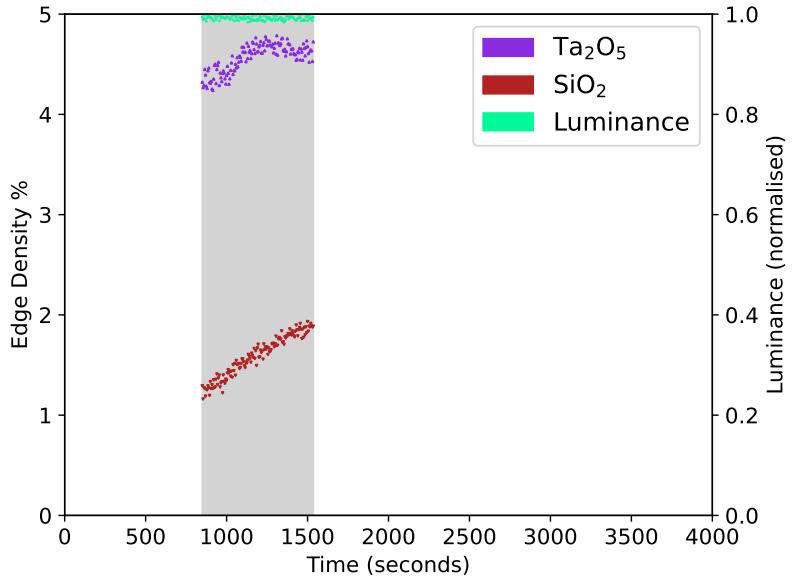


Figure 4.14: MCF-7 cells stimulated at 15 volts after 96 hours incutbation.

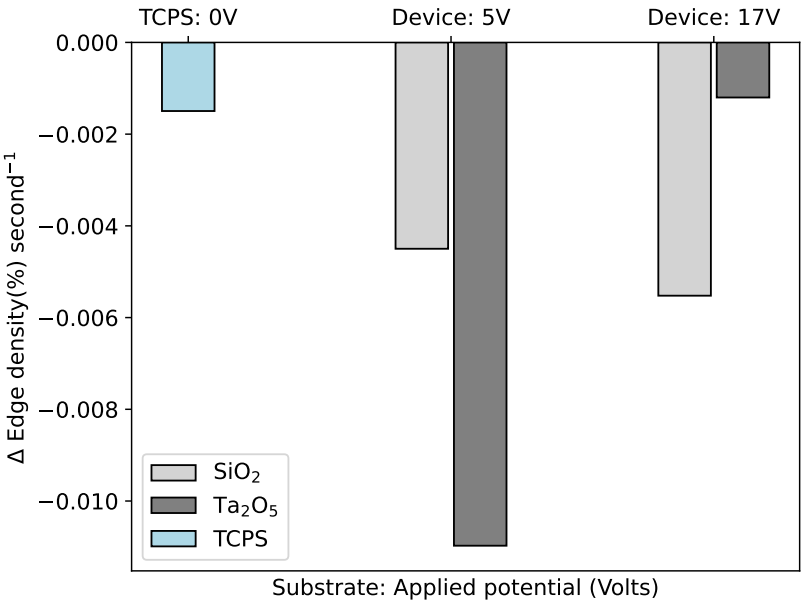


Figure 4.15: Rate of edge density decline in springback experiments, after removal from incubator and cessation of stimulation. Linear regression of data within highlighted regions in Figs 4.11, 4.12 and 4.13.

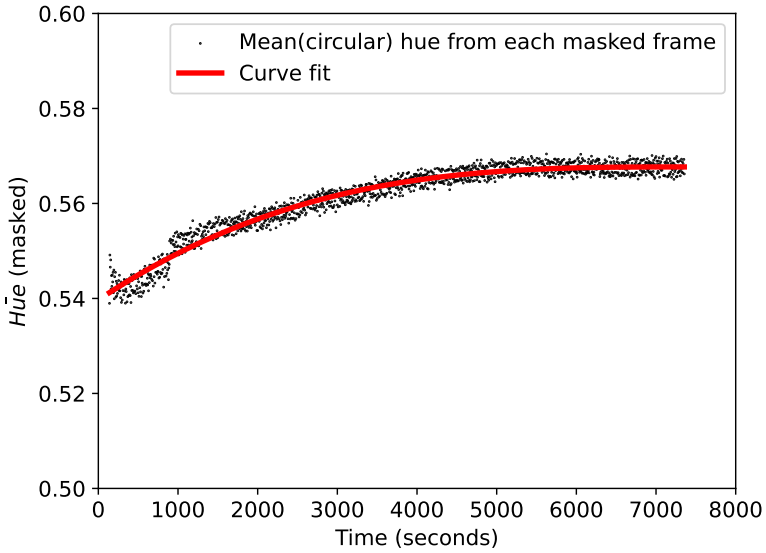


Figure 4.16: Mean hue(colour) for each microscopy frame of a TCPS (Permanox®) experiment after 48 hours of incubation. Time starts on removal from the incubator. Fitted curve (red).

4.11 Capacitive charging

Figure 4.17 shows the distribution of edge densities within each field calculated for electrodes and controls, with p-values and number of fields indicated in each group reported on the figures. The edge densities of most fields across the experiments were between 5% and 10%. Table 4.2 shows the total edge densities for each experiment, found by calculating the ratio of edges on electrode and control regions across all fields compared to their respective summed areas (in pixels). The mean of the population of edge densities calculated from each individual field is also given. In general, MDA-MB-231 shows a higher edge density across all experiments compared to MCF-7. The MDA-MB-231 cells on electrodes at the lower voltage level is 1% lower than the control. This difference rises to over 2% on the higher voltage experiment. Edge density increased at both electrode and control region between time points by (1.56% and 1.36%). This implies proliferation of cells on both surfaces while the increase in difference between the two surfaces suggest a disparity in behaviour. The 5 V stimulation at the second timepoint drops drastically on both surfaces, suggesting that there was an issue with the culture. However the opposite effect with edge density being higher on the electrode even at the lower level of absolute edge density. Densities were lower on the electrodes with the MCF-7 cells, however the two points saw a small decline in contrast to the MDA-MB-231.

The distribution in edge densities calculated from individual fields are shown in Fig 4.17. Electrodes charged at 5 V and incubated with MBA-MD-231 cells did not show statistically significant differences in the means of edge density compared with controls at 24 and 48 hours after inoculation Figs 4.17a and 4.17b. However, when charged to 17 V edge densities were significantly reduced at both time points compared with controls. The trend was also present using MCF-7 cells at 48 and 96 hours in electrodes charged to 15 V but did not meet the criteria of significance ($p<0.01$).

Table 4.3 shows the results of paired t-test comparisons between calculated edge density within fields where both electrodes and controls were visible. The 17 V MDA-MB-231 results were also the only statistically significant results under this paired analysis. However, it also allowed calculation of the number of fields across the experiments where the electrode density was reduced compared to controls, independent of the magnitude of the

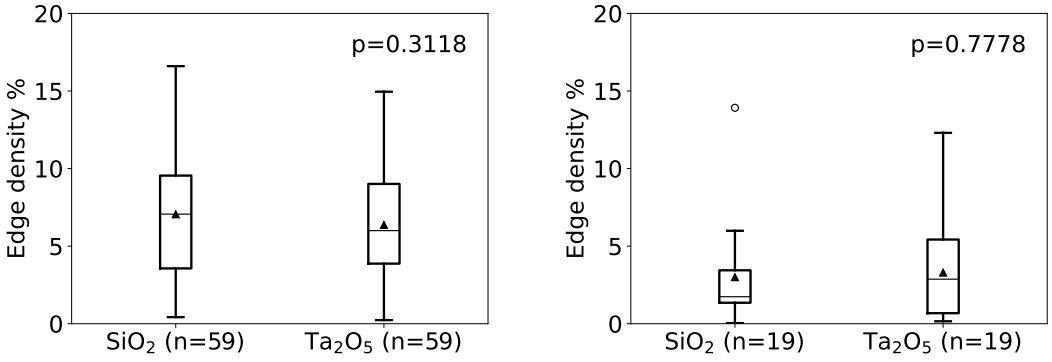
effect. While under 5 V stimulation the results were equivocal and consistent with the null hypothesis with the two points sitting close to 50%, the majority of fields examined for the MCF-7 cells showed a reduced edge density on the electrodes compared with controls at both time points (62% and 57%).

Cell	Volts	Time	Surface	Fields	Edge density (%)	
					Total	Mean
MDA-MB-231	5 V	24hr	SiO_2	59	8.05	7.05
			Ta_2O_5	59	6.97	6.37
		48hr	SiO_2	19	3.52	3.00
			Ta_2O_5	19	3.85	3.30
	17 V	24hr	SiO_2	75	6.78	6.70
			Ta_2O_5	75	4.69	4.59
		48hr	SiO_2	60	8.34	8.17
			Ta_2O_5	60	6.05	5.87
MCF-7	15 V	48hr	SiO_2	56	4.75	4.73
			Ta_2O_5	57	4.30	4.04
		96hr	SiO_2	53	4.20	4.35
			Ta_2O_5	53	3.61	3.80

Table 4.2: Summed edge densities across all fields compared with mean of inter-field edge densities.

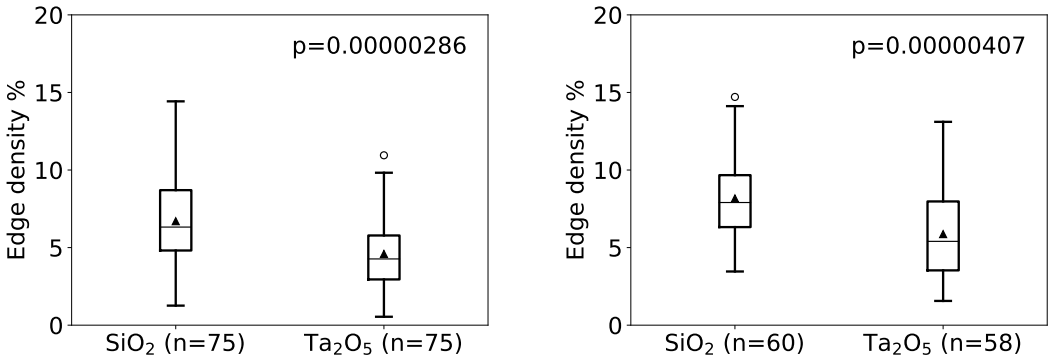
Experiment	Fields	Ta_2O_5 < SiO_2	p-value (paired t-test)
MDA-MB-231 Cells 5V 24hr	57	30 (52.63%)	0.172
MDA-MB-231 Cells 5V 48hr	19	9 (47.37%)	0.710
MDA-MB-231 Cells 17V 24hr	73	58 (79.45%)	0.000000008804
MDA-MB-231 Cells 17v 48hr	58	41 (70.69%)	0.000015871959
MCF-7 Cells 15V 48hr	56	35 (62.50%)	0.015
MCF-7 Cells 15V 96hr	52	30 (57.69%)	0.134

Table 4.3: Results of paired two-tailed t-test across segments from each experiments along with percent of fields where edge density of Ta_2O_5 segments were less than adjacent SiO_2(control) regions.



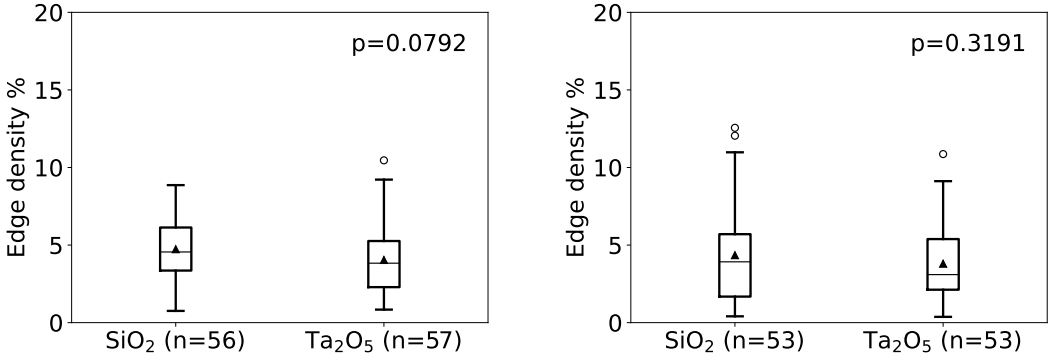
(a) MDA-MB-231 at 5 V after 24 Hours.

(b) MDA-MB-231 at 5 V after 48 Hours.



(c) MDA-MB-231 at 17 V after 24 Hours.

(d) MDA-MB-231 at 17 V after 48 Hours.



(e) MCF-7 at 15 V after 48 Hours.

(f) MCF-7 at 15 V after 96 Hours.

Figure 4.17: Edge density distributions on electrode and control regions in each experiment (▲: mean).

4.12 Cell distribution near an aluminium electrode

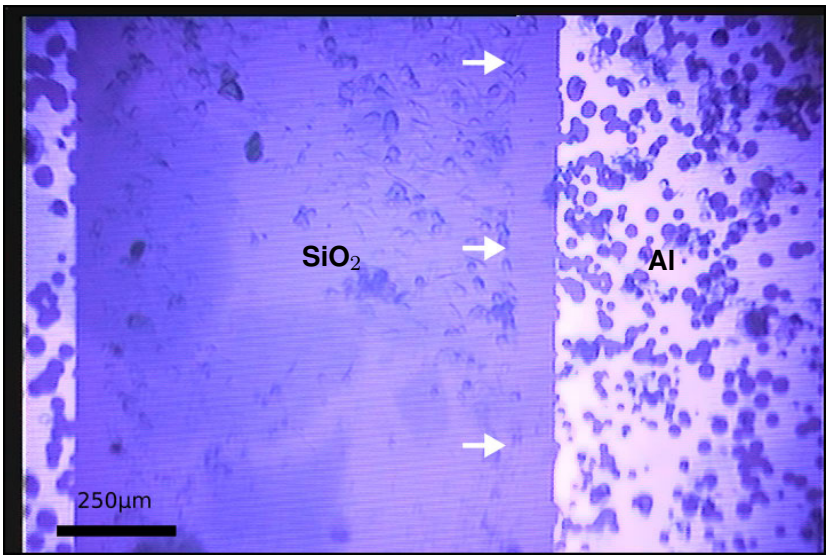
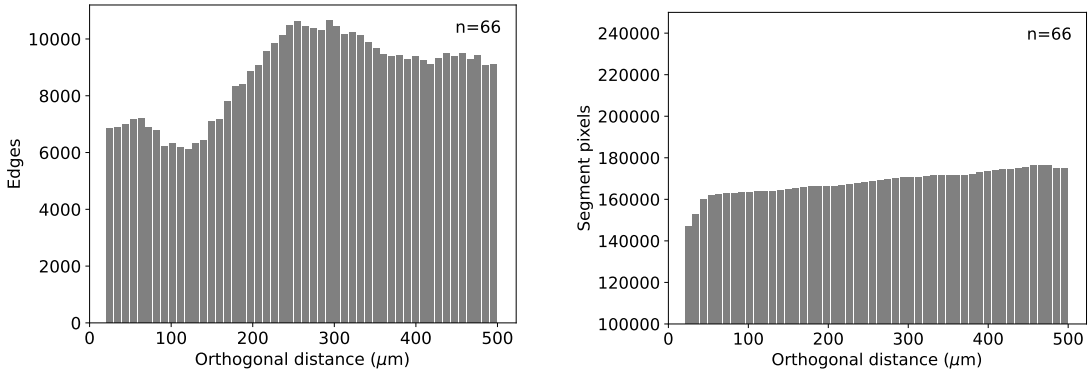


Figure 4.18: Example image showing typical distribution of cells on SiO_2. White arrows show an apparent line of where visible cells stop abruptly near the corroded aluminium electrode. The pattern is also visible near the opposite electrode in this image.

A 1000 µm strip electrode device (Fig 3.5c) with the Ta_2O_5 electrodes replaced with aluminium was used to examine the redistribution of cells under an elecric field. The device was inoculated with 20×10^4 MDA-MB-231 cells and was stimulated at +5 V, relative to the solution auxilliary electrode, for 24 hours. On examining the devices the electrode had suffered significant corrosion with a pitted, moth-eaten, appearance. The aluminium electrode was found along with a region, where a reduction in cell numbers was easily visible. This region was present consistently in virtually all fields examined and was always positioned close to the electrode. Cells on the electrode itself could not be readily distinguished. Figure 4.18 shows an typical field, with the cell deficit region labelled. An algorithmic quantification approach detailed in Section 4.4 was developed and applied to the fields to characterise this effect. Figure 4.19a shows a histogram calculated from the distribution of edges as a function of distance from the edge to the closest point on the nearest electrode. Unfortunately, the image fields did not contain a uniform number of pixels at each distance. The number of pixels as a function of distance is shown in Fig 4.19b. This meant that the absolute edge distribution was not representative of the underlying cell distribution. To correct this, edge density by distance was calculated by taking the ratio of edges and segment pixels. This is shown in Fig 4.20.

Moving away from the electrode edge (0 µm), the edge density reduces to a minimum at around 125 µm with a small local maximum near the electrode. There follows a steep rise in edge density, crossing the mean line at 225 µm to a maximum at 275 µm. Edge density then returns the mean value at 500 µm, which represents the middle of the control region, equidistant from each adjacent electrode. The total (mean) edge density aggregating all measured fields was 5.4 %. This is was in agreement with the densities measured on other experiments, which were also seeded with identical numbers of cells. This suggests that cells were re-distributed within the control region and that no cells migrated, or re-attached after removal from the electrode. The re-distributed cells on the control region appeared viable and unaffected by toxicity up to 48 hours from initial inoculation. This mirrors the other experiments where cells were observed to be viable and divide on fluoropolymer surfaces up to 96 hours. The technique used to inoculate cells onto the culture chambers should ensure a uniform distribution of cells. Indeed, such a distribution can be seen in Fig 4.21 after an identical analysis was carried out on a capacitively charged surface, after 24 hours of cell stimulation.



(a) Number of edges.

(b) Number of pixels.

Figure 4.19: Aluminium electrode: distribution detected edges and the number of pixels, across all fields (n=66), as a function of orthogonal distance in µm to the nearest point on electrode boundary.

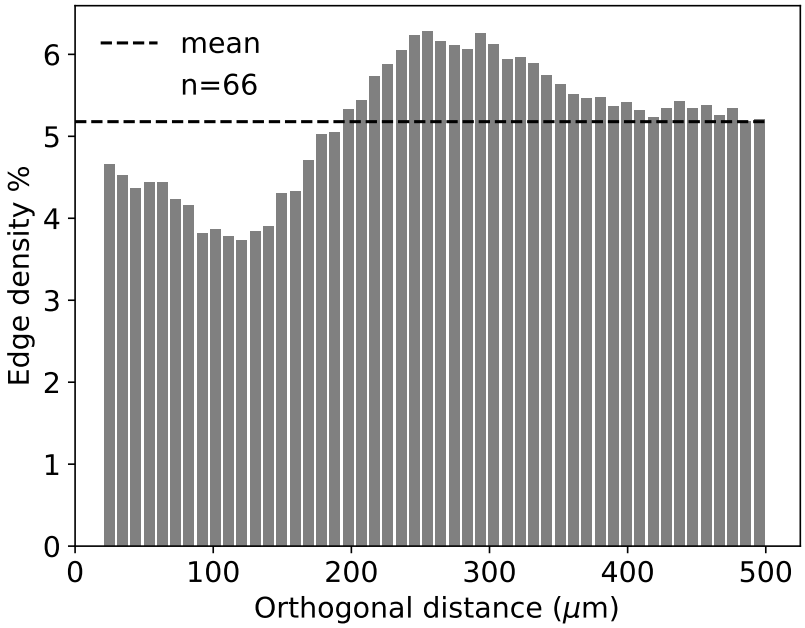


Figure 4.20: Aluminium electrode: edge density as a function of orthogonal distance in µm to the nearest point of electrode boundary.

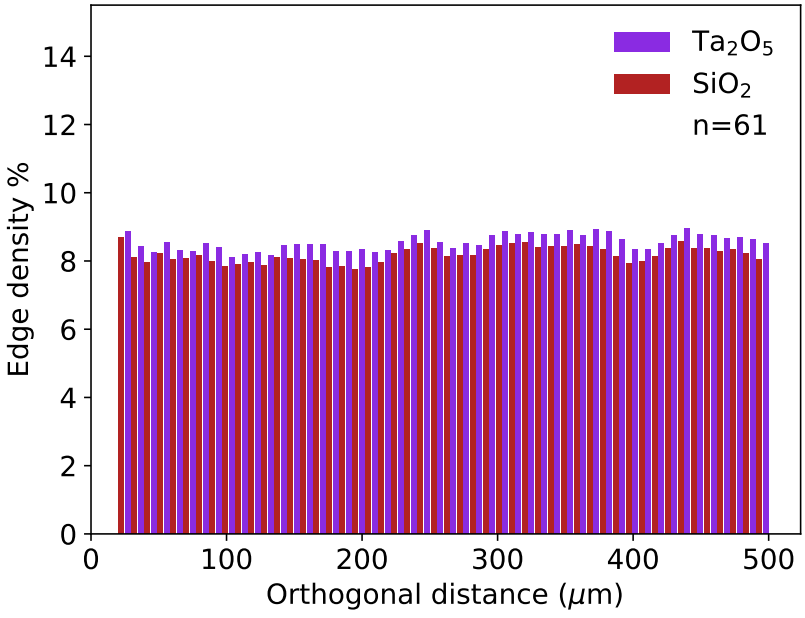


Figure 4.21: MDA-MB-231 5 V 24hr: edge density as a function of orthogonal distance to nearest electrode: approximately uniform on both the electrode and control regions.

4.13 Discussion

This chapter explored the utility of an electrical stimulation platform for investigating, in particular, the effect of capacitive charging on cells of two immortalised cancer cell lines. Cells from two cancer cell lines were cultured on the *in vitro* platform under electrical stimulation for up to 96 hours. Evidence was observed of reduced cell attachment, process formation and proliferation on a charged electrode compared with an uncharged control region.

There are, however a number of limitations to work presented, these will be addressed below. Insufficient devices were available to cover a range of applied potentials, including an independent OCP experiment. Likewise although statistically significant effects can be inferred from examination of multiple randomly selected on each device there was a lack of inter-device replicates. The measurement system has disadvantages that are expounded upon below, along with potential solutions. Complementary analysis including of cell fate would be advantageous, but have been shown to be possible using the platform. The construction of the device limited the polarity of applied potential. The electrical setup used an external potential applied between the functional electrode and an auxiliary electrode in solution. As has been noted in recent literature[239], this setup suffers from the disadvantage of giving little information about the developed surface potential, double layer structure, electret polarisation state and surface charge. While conclusions drawn from the result support the hypothesis about the potential utility of capacitive biomaterials based on this approach, a prerequisite of future work in this area would include electrical characterisation and more use of more diverse probes of the biological effects.

Experiments with no applied electrical stimulation (OCP) were carried out but insufficient images were collected to allow quantification. Cells on both commercial chamber slide and an Cytop® surface were clumped perhaps from inadequate trypsinisation. Additionally, at this stage fluorescent imaging was intended to be the main means of quantification of cell response, however unexpected issues with access to a functioning fluorescent microscope necessitated the use of microscopy approach that was adopted. The low and high voltage experiments, however, do allow the threshold for a measurable response, using the technique, to be placed between 5V and 17V stimulation. The devices were also designed to have internal control regions adjacent to each electrode region where the only

factor differentiating the surfaces was the potential applied.

In one cell type – MDA-MB-231 – stimulation at 5 V did not show any statistically significant difference between electrode and control regions, while 17 V did show statistically significant difference at two time points, Fig 4.17. These results were the same whether the calculated edges were aggregated or totalled across fields or under a paired analysis. The other cell type, MCF-7, did not appear to respond at 15 V, although the majority of fields presented a lower edge density on the electrode compared with control regions at both time points. This could be the result of differences in the biology of the two cell lines or to interactions of the cell morphology with the image quantification technique. Given the confirmation of uniformity of edges across the devices it is argued that this could be the result of a lowered cell spreading and/or poorer attachment of cells to the stimulated surfaces that is voltage dependent.

When the time series of individual fields, after removal of electrical stimulation, were examined as videos (not shown), the cells were seen rounding up and in some cases detaching individually or in clusters. The tracking of edge density over time was designed to quantify this for each surface. As can be seen in Fig 4.15, SiO_2 rates are similar regardless of stimulation voltages. They also differ from TCPS, suggesting that that information is being captured about differences in cell-material interactions of each substrate.

Interpretation of the edge density decline rates must be made with consideration of the absolute edge density and the presumed state of cell attachment. Comparing the Ta_2O_5 electrodes at the two voltage levels in Fig 4.15, the 17V field was typical in that initial edge density was lower than the control region (70% of all fields, Table 4.3) and therefore may have already been closer to a minimally attached state. This would explain the low rate of decline in edge density. The 5V field showed a higher absolute edge density on the Ta_2O_5 electrode compared to the SiO_2 control, this field was a typical as the opposite relationship when averaged across all fields, see Table 4.2. The edge density curves followed each other closely in this case, implying the dynamics were the same but that perhaps there was a non-uniformity in the number of cells on each substrate, The distribution of cells on these devices was shown to be initially very uniform. Across all fields at this voltage and time point (5V, 48hr) the Ta_2O_5 had a larger variance than the control. However the total number of fields included in the analysis was lower than the other experiments and total

edge density was largely reduced at this time point compard with the earlier situation. A significant difference in edge density was found collectively across all fields examined at 17V and on the timelapse the edge densities appeared to be converging (Fig 4.13. This implied that the reason for the difference in edge density was related to cell attachment and not absolute number of cells on each electrode.

4.13.1 Measurement and quantification

Edge density as applied to the results of cellularity experiments uses calculated edges as a proxy for both cell density and cell spreading see Fig 4.6. While it would be useful to have a value for edge density at 100% cell confluence in order to estimate a function mapping density to cell mass, the sensitivity of method can be confirmed by examining the internal consistency of the presented data. For example, by examining the circumstances of the springback and aluminium experiments. In the aluminium experiments, visible alterations in cell density are clearly being quantified through edge density. This is contrasted with the presence of a measurable springback effect where change in cell number within each field is negligible over the time period and environmental effects, such as luminance, temperature and pH, have been controlled for. As detachment can be observed at disparate time points in the series, it is suggested that edge density must also be sensitive to cell spreading.

In an effort to understand the influence of measurement uncertainty on the outcomes of the capacitive experiments, two sources of noise were quantified: temporal and spatial. Examining the scatter plot in Fig 4.11, edge density trends are subject to local inter-sample variance. In order to quantify this, data outside of the highlighted region (after 886 seconds) was examined. This data was not stationary, so a difference approach was employed between neighbouring samples. These processed data were stationary, with a distribution mean approaching zero. Spatial variation: the difference in calculated edges as the objective was translated across the sample was calculated using image fields that were taken close together in time and that partially overlapped in the region of the surface they imaged. These field pairs (n=41), which were drawn from multiple experiments were manually registered. The resulting transformation matrices were used for each pair to calculate a subset of corresponding pixels in each image. The differences between the calculated edge den-

sities between each pair was then found. The standard deviation in edge density on the temporal noise was found to be 0.067 % and spatial error in edge density associated with translating the microscope field over the same region of cells was 0.87 %. It should be noted that the registered images were taken at different times, so would be expected to also contain temporal noise. These values were much lower than the standard deviations of the edge density distributions found in the experiments that showed statistically significant differences: σ = 2.37,2.87,2.57,2.54 on the SiO_2 and Ta_2O_5 at 24hr and SiO_2 and Ta_2O_5 at 48hr respectively. This suggests that the main source of variance in the samples was due to inter-field effects, for example cell density and morphology. To qualitatively assess the effect these uncertainties had on the significant results the test statistics were recalculated with the standard deviations increased by both the calculated temporal and spatial quantities. This procedure did not abolish the statistical significance of the differences in edge density between the electrode and control regions, increasing confidence in the result. The sum of the error calculated, from spatial and temporal noise, was 36% of that found in these experiments. This suggests that improvements to the measurement system would improve the sensitivity of the edge density metric.

Manual segmentation of the images was initially considered as the dataset was not prohibitively large and the approach has been used successfully[324]. However the combination of resolution and artefact effects would likely have created significant inconsistency in the results. Treloar *et al.*[325] compared edge detection techniques for quantifying cell migration assays. This included the Sobel edge detection algorithm, of which the Canny edge detector, that formed the basis of the quantification algorithm used in this work, is an enhancement. Algorithmic approaches were found to be more reliable and repeatable than manual measurements. The authors did note a strong dependence of the calculated values on parameters used by the algorithm such as for thresholding and morphological operations. Systematic variation of the parameters of the edge detection algorithm was not carried out in this work. Instead, edges were qualitatively compared against the cell images to optimise the algorithm parameters.

Independent measurements of cell density and spreading would be valuable along with measures of cell morphology, which have particular relevance in cancer cells[326] and would complement spreading and provide more information on the cell-material interactions oc-

curring on surfaces of varying charge states.

Biomaterial responsive cell attachment, strength, proliferation and spreading have been shown to be positively correlated[327] for both MDA-MB-231 and MCF-7. This lends support to the validity of the cellularity metric employed herein. Despite this, higher value information can likely be obtained through separation of the contributory mechanisms, by improving image quality or employing complementary quantification methods.

Discrimination of cells within the images was good despite lack of staining. This can be attributed to the optical setup of the microscope, illumination was supplied abaxially from an LED ring light. This produced an oblique contrast effect, meaning that image intensity was influenced by phase effects[328]. This combined with absorption, reflection and diffractive properties of the cells and underlying surface resulted in large intensity gradients at the boundary of cells, the magnitude of which were used to classify edges.

Where cell segmentation could be carried out more sophisticated assessment of cell morphology becomes possible. For example, deviation of the perimeter of a cell from the circumference of a circle with same area - circularity - allows a simple assessment of elongation and attachment success[329,324]. Similarly, the feret diameter - the diameter of a circle with an equivalent area to that defined by a perimeter can also be used to characterise cell attachment[99,330]. Differences between morphological properties of the two cell lines have also been quantified, in the literature, through "bending energy" - a type of fractal analysis[326]. Other, more complex, shape descriptors and feature detectors based on image invariants that may also be applicable to analysing cell morphology[331].

A variety of intra-vital labelling techniques are available to allow the tracking of cell death and would make useful additions to stimulation experiments. Calcein AM (Invitrogen ™), a fluorescent reporter, is transported into live cells allowing tracking of cell viability[332]. Propidium iodide cell also quantifies cell viability[333]. However, many of these colourimetric tests use instruments that rely on light transmission, which presents issues given the opaque nature of the silicon substrate. Although in some cases custom implementations of the required instrumentation may be possible.

Ellipsometry as originally carried out by Vroman *et al.*[81], to identify their eponymous effect is compatible with these surfaces under electrical stimulation. Washing and recounting cell density has also been used as a means of probing the strength of cell attachment

to a substrate[324].

Electrical properties of cell-material interactions can also be used. Cell attachment displaces charge, which can be measured to give information about cell-material interactions occurring at the interface[334,335]. These systems operate by examining impedance changes that occur at a biosurface. Commercial systems for tracking cell spreading exist, for example the Xcelligence system (*Agilent*)[336,337] uses interdigitated gold electrodes to perform impedance analysis that can distinguish attachment, spreading and apoptosis of cells in special culture wells. This type of setup removes the issues associated with substrate opacity that occur with optical imaging but require charge transfer, which is incompatible with investigating capacitive designs.

The influence of capacitive charging on biofouling and protein conformation can only be indirectly inferred based on the results of this work and in context of the some of other electrically active biomaterials described in Chapter 2. Specific examination of protein interaction with capacitively charged would be revealing.

The issue of substrate opacity has been circumvented in other studies by using the transparent conductor (Section 2.5). However, this approach would not be compatible with the setup used in this work due to the presence of opaque tantalum metal. A transmissive structure (of tantalum) may be achievable using an alternative technique for deposition of Ta_2O_5, but the window of light transmission within the visible spectrum appears to be narrowed in films created with these techniques[338]. Many of the quantification methods described would require higher resolution imaging sensors with direct digitisation. Such images would be revealing as to mechanisms and differences between various cell lines in attachment processes, especially if combined with live, or timelapse, imaging throughout stimulation experiments. Variation in luminance affecting the images was measured and was found not to influence the stimulation experiments, but was not controlled for in the TCPS springback controls. The discontinuity in the TCPS springback experiment (Fig 4.11) shows that, while the trends are robust, the absolute value of edge density measurement is indeed a function of sample illumination.

4.13.2 Protein adsorption

Electrical stimulation was applied after the media (containing serum proteins) and the cells were added to the chamber. Delays were short, on the order of a minute or two after surface wetting, while the device was moved to the incubator. However, potentially irreversible adsorption processes start to occur within milliseconds of contact[61]. It is also generally understood from the Vroman effect that the adsorbed protein layer is dynamic in terms of its thermodynamic evolution and trapping at local minima is possible depending on the material. Indeed this process may be responsible for some of the dynamics seen in the springback experiments, Fig 4.12. Electrical stimulation almost certainly preceded any cell attachment processes after initial incubation and so a reorganisation of the protein film would have been possible in this interval. Therefore, it is possible that not only the presence of charge modifying surface properties but the timing is important and different outcomes may be expected by adding proteins to a pre-charged solution interface versus adding a protein solution to a surface which is subsequently charged. Surfaces are often coated in albumin so charging until after the albumin epoch, less than a minute after wetting, may have drastic consequences on the evolution of the biological response of the film. Albumin as was present in the culture medium in these experiments has been shown to be the dominant adsorbed protein film on fluoropolymer surfaces[66]. Albumin is the first Vroman protein and is present within the cell culture medium making up around 60% of proteins found in the bovine serum albumin constituent[339]. Competitive exchange of proteins on fluoropolymer surfaces tends to proceed very slowly and so incubated cells likely encounter an albumin coated surface on first contact with the electrode and control regions of the *in vitro* device. Conformational shifts to albumin that occur on adsorption have been shown be conducive to cell attachment in some cells[66] at least to a greater degree than when the protein is in its solvated conformation. The exact protein make up of the interface adsorbate is not known, or how charging affects the distribution of proteins or conformations that forms. A reasonable hypothesis is that cells are attaching to albumin and that alteration in surface charge are reverting the protein layer to a much less conducive form.

Another potential experiment would test the hypothesis that albumin protein interactions with the surface are responsible for the electrical stimulation results. Incubating cells using serum-free media and pre-incubation with purified protein solutions would allow com-

parison of the attachment rates and may provide some information about the importance of proteins in the cell interactions with these surfaces. The degree of denaturation/conformational change *in vitro* can be a function of protein concentration[108]. Although, assessment under physiological conditions are of particular importance for implant applications. Culture media formulations commonly use 5-10% serum protein solutions meaning protein concentration is a factor of 10-20x lower than *in vivo* . An attachment promoting enzyme deposited on a hydrophilic protein surface increased the strength of MDA-MB-231 cell attachment, as measured by resistance to washing. However, the strength of cell attachment became less important beyond 18 hours of incubation, it was speculated that this was due the MDA-MB-231 cells secreting endogenous cell-surface binding proteins by this point[324].

Analysis of the springback effect utilised regression analysis in regions where the changes were approximately linear. However, there is evidence that the dynamics on the fluoropolymer surfaces are not monotonic nor linear in these regions. This may be a manifestation of stimulated Vroman-like competitive exchange and other adsorption phenomena brought about by a sudden change in surface properties. The complex dynamics observed over the period after removal of electrical stimulation may be driven by cell-mediated alterations in surface adherent structures or purely as a result of the interface evolving towards a new equilibrium.

4.13.3 Protocol

In several cases electrical stimulation was broken for visualisation and devices removed from the incubator, examined then incubated under stimulation once more. The same trends were present at the next sampling period, implying that any effects of removal from the incubator, including the springback effect were reversible and results for the 17 V experiments were consistent across two time points despite the electrical stimulation being interrupted.

The design of the *in vitro* platform, especially the 'strip' electrodes not only allowed two regions to be examined within the same microscope field, but allowed the effects of fringe fields and influence on neighbouring unstimulated regions to be observed. This permitted the cell redistribution within the aluminium electrode experiments to be measured.

To establish a link between attachment/adhesion as a function of adsorption or of con-

formational mechanisms, measurements of attachment can be tested in a minimal serum environment. Adsorption can also be tested by surface characterisation via fluorescence, spectroscopy, or protein stains. The polarity of the experiments was kept anodic with reference to the anodised Ta_2O_5. This was to try and minimise faradaic reactions that would have occurred if the inner dielectric was electrochemically reduced as the oxide is electrochemically unstable under cathodic potentials[274]. Due to the presence of the composite dielectric the charge and assuming a parallel plate model the fluoropolymer surface would be expected to take on a negative charge with a positive counter-ion field within the double layer. The measured effect of reduced attachment on electrode surfaces is consistent with that seen in metal bioelectrodes that are kept within the capacitive regime[97] as well as biomaterials that possess a net negative charge charge under physiological conditions (see Section 2.4). A consequence of the limited access to the opposite polarity is that attachment favouring surface electrical conditions may be harder to achieve. This issue has also been considered in the dielectrowetting literature[340], with alternate dielectric layers particularly some ceramics such as barium-strontium titanate suggested, as these possess high relative permittivity and are capable of producing devices tolerant to both positive and negative potentials.

Reuse of surfaces would be a useful technique to conserve fabricated surfaces and may be possible. This would require that the surfaces can be adequately cleaned, intercalation does not occur and they remain unaffected by previous stimulation experiments. Great care would, however, be required in ensuring that all residual protein deposits were removed from surface prior to re-use.

4.13.4 Cell lines

The two breast cancer cell lines can be further differentiated from each other by examining additional properties. They are both used not only within cancer biology but increasingly within bioengineering applications, likely due to their ubiquity and ability to survive adverse environments. While both cell lines are derived from breast cancer, MDA-MB-231 cells are so-called 'triple negative' because they lack receptors for oestrogen. Both cell lines are adherent, however, there are differences in their anchorage dependence. MDA-MB-231 cells are not anchorage dependent for survival, whereas MCF-7 are much less resistant

to anoikis[333]. Cell detachment can also be produced in these cell lines by exposure to drugs[333]. MCF-7 cells are able to grow on C_4F_8 fluoropolymer (the same material was employed in the *in vivo* devices in Chapter 5) and preferentially forming invadopodia between coated silicon micropillars[341]. A closely related culture to MCF-7 can augment fibronectin production in response to substrate stiffness[342].Cells were able to generate processes, indicating some level ability to interact with the surface but possibly indicating anchorage starvation. Proliferation also occurred, perhaps unsurprisingly given the aggressive nature of the cell lines selected.

4.13.5 Springback

Examination of timelapse videos of these control experiments shows the detachment of the cells. The causes of the springback effect on TCPS and control regions of the stimulated electrodes is likely due to decline of temperature and shifts of pH, both resulting from removal from the incubator. Temperature was also not controlled in this case, after removal from the incubator. Effects of temperature on the cell-material interactions are well recognised to the practitioners of cell-culture and may be related changes to cellular function or within the surface adsorbed protein layer. Cell detachment on thermoresponsive culture surfaces has been related to reduced adsorption in both serum albumin and fibronectin[343] and protein conformation. Further, denaturation can be stimulated by thermal energy, potentially limited binding sites for cell membrane proteins. Reduced temperatures also appear to modulate intracellular structures, altering cell elasticity. Additionally, recession of cell processes and interference with the formation and function of cell-material structures have been described[344]. This implies that loss of adhesion anchors from the surface is at least a component of the temperature dependent springback effect.

Detachment and rounding of cells may follow from kinetics of desorbing or denaturing proteins providing anchor sites or may be driven by the cell. This could be through reduction of the cell's ability to maintain adhesion complexes or a behavioural shift favouring dismantling of cytoskeletal structures.

The two cell types appeared to differ in their response to the surfaces. A phenomenon that has been observed in other biomaterials, including those that were electrically charged[345].

Attachment of both MDA-MB-231 and MCF-7 cells is higher on glass surfaces that

had been processed by RIE etching to increase surface roughness[327]. Cell capture rate increased from less than 20% on 1 nm smooth surface to more than 80% on rougher surfaces (150nm). Cell attachment strength and cell spreading was also increased on rougher surfaces and focal adhesions were distributed more evenly over the surface contacting regions of the cell. Surface roughness measured by AFM on the fluoropolymer surfaces of the *in vitro* devices (Fig 3.20) was around 5 nm suggesting a poor adherence. However, the surfaces used in this thesis are not directly comparable as other mechanical properties vary, and are known to be detectable by cells, between polymers and harder surface like SiO_2[188] . Interestingly, on the same SiO_2 surfaces[327], MCF-7 cells showed slightly greater affinity for rougher surfaces at both low and high roughnesses compared to MDA-MB-231. It is again unclear if this effect is translatable to the lower elastic modulus less wettable surface of the fluoropolymer layer used in this thesis.

The springback effects suggests reversibility of the effects of stimulation. If surfaces revert to native properties when stimulation is removed then this may explain the differential response on stimulated and unstimulated surfaces. The re-establishment of the same trends between multiple time points and after interruption of stimulation for measurement, also allows the conclusion that biological detachment processes are also reversible and that cells can recover a previous state on a substrate once the environment becomes favourable again. An interesting investigation would be to characterise the springback effect under deliberate removal of cells from surfaces using trypsinisation.

4.13.6 Aluminium electrodes

The corroding aluminium electrode appeared to stimulate migration of the cells within the control region. Cells on the electrodes themselves were not accessible. It is unclear how much, if any, the pattern of corrosion was influenced by the presence of the fluoropolymer layer overlying the entire device surface. The pattern may be an artefact of pinhole defects in this layer. This phenomena has been noted by others working with spun amorphous fluoropolymers[274]. Two hypotheses for the cause of the cell redistribution are electrotaxis or chemotaxis.

A threshold range for electrotaxis, of MDA-MB-231 cells, has been suggested around 0.1–10 $V\,cm^{-1}$ for DC fields and electric fields $\approx$3.8 $\mu V\,cm^{-1}$, under AC stimulation (100 kHz)[160].

For MDA-MB-231 cells, directionality of migration reached a peak at $3\,V\,cm^{-1}$ DC ,but the velocity of electrotaxis continued to increase at higher electric field strengths[346]. MDA-MB-231 tend to migrate anodically, towards the positive electrode, in contrast with other cancer cells derived from other organs[347]. This is achieved by extending cell membrane processes towards the positive electrode. Mechanisms of action include: polarisation of a growth factor receptor and increased intracellular calcium[347]. Both of these processes are also important to metastasis in breast cancer. This is because electric field gradients form between tumour and healthy tissue, that may play a role in directing tumour invasion[346]. In the setup reported in this thesis, the cathode is far above the electrodes in the solution, essentially at infinity in terms of the effect on the field lines. The field strength felt by the cell within the SiO_2 region will therefore be much lower.

The composition of the cell culture media is given in Table 4.4. As can be seen, there are several chloride salts that make up the majority by mass of the solution. It is assumed that the major oxidation reaction of the aluminium is a two-step process involving an initial reduction of chloride at the electrode to form chlorine which then reacts with metallic aluminium to form aluminium chloride. As can be seen from the standard electrode potentials of both half cell reactions, this redox reaction is feasible under standard conditions even without the addition of potential on the aluminium electrode.

$$Al^{3+} + 3\,e^- \rightleftharpoons Al \quad \text{-1.66V}$$

$$Cl_2 + 2\,e^- \rightleftharpoons {}_2Cl^{2-} \quad \text{+1.34V}$$

$$2\,Al + 3\,Cl_2 \longrightarrow AlCl_3$$

This form of corrosion has been investigated on sputtered aluminium[348], particularly in acidic solutions[349]. The produced aluminium salt is soluble in aqueous solutions and happens to be cytotoxic as well as systemically toxic[350]. The mechanism of action appears to be the competition between Al(III) cation with protein cofactors, necessary for various biochemical functions, Mg^{2+} in particular. The wafer in this experiment was re-examined after 48 hours (data not shown) and demonstrated living cells showing that significant toxicity does not build up over this period.

To further investigate the change in cell population distribution near a corroding electrode, the platform could, with simple modification, be used to distinguish between electric current and toxic redox products by applying potential to one strip under cross-flow of fresh

culture media. These types of setups are commonly employed in galvanotaxis experiments[351]. If flow rates were selected to outcompete the diffusion of corrosion products (aluminium chloride:$1.72 \times 10^{-9}\,m^2\,s^{-1}$[352]) then the effects would reveal the relative contribution of electrical and chemical effects. Reversion of the cell profile seen in Fig 4.20 to uniform would be expected on the fresh media side of the electrode if the stimulus is a toxicity and maintained if the driving force is electrotactic. It is notable that mimimum region of edges is away from the electrode beyond a local maxima. It is possible that cells in this region are experiencing the effects of electrotactic, which would be directed towards the electrode and chemotactic away from high concentration gradients.

4.13.7 Cell properties

Cancer cells have been shown to gain abilities to move in amoeboid like fashion,[353] similar to the mode of migration some immune cells[37], this mechanism partially underlies the invasiveness and metastatic abilities of such cells. Collective motion is also possible and tends to dominate when the cell layers are approaching confluence. It is unclear how the non-uniform distributions of cells formed over the 24 hour period of cell incubation and what combination of passive or active cellular motion gave rise to it. An alternative means of cell redistribution can occur where cells detach to free-float in solution and subsequently re-attach at another location. There is a higher tendency to express this behaviour within the MDA-MB-231 than MCF-7[354].

Zhu *et al.*[355] has observed that a breast cancer cell line (4T1) collectively migrate towards the anode under a $1\,V\,cm^{-1}$ electric field[355]. The authors also provide evidence, from *in vivo* measurement of tumour endogenous electric fields that contributes to a growing recognition of the importance of electric fields within the tumour microenvironment and metastasis[353,356].

Tumour cells such as the two lines used here have a generally larger membrane charge than healthy cells. This surface charge is a major determinant of invasiveness of a tumour. The surface charge arises from net surface concentrations of charge. These charges are associated with surface acidic and basic groups that depend on pH dissociation constants. Dobrzyńska *et al.*[356] studied the electrical properties of both cell lines using electrophoresis as a function of pH. At physiological pH both MCF-7 and MDA-MB-231 cells have a

more negative surface charge density than fibroblasts at $-1.25\,\mu C\,cm^{-2}$. At pH 7.2 (middle of DMEM range) MDA-MB-2321: $-1.7\,\mu C\,cm^{-1}$ and MCF-7: $-1.9\,\mu C\,cm^{-2}$[356]. Improved cell attachment has been seen when the biomaterial surface potential is matched with that of the surrounding cells[248]. Association with a surface may also alter the potential of the cell[258], along with inducing local migration of cell membrane receptors. These discrepancies should be considered in analysing the behaviour of different cell cultures at surfaces purely due to charge. However, this charge cannot be viewed in isolation in the cellularity experiments. If direct double layer repulsion was the cause of attachment change, and in absence of differential response to the quantification method, then the more negative cells (MCF-7) would be expected to produce a larger response than the MDA-MB-231, the opposite of what was observed. It is therefore more likely that the attachment was mediated through surface adsorbed proteins.

Both cell lines used were cultured for several days, there is a difference between in cell doubling time between the two cell lines from the literature, with MCF-7 taking significantly longer to divide (see Table 4.1). Cells were noted to be capable of dividing on the surfaces through observation of mitotic cells on fluorescent stained surfaces, Fig 4.10. Edge density did rise on control surfaces and higher voltage electrodes between 24 and 48 hours of incubation. This is likely a sign of proliferation, but could also be related to increases in cell areas due to spreading.

Spontaneous detachment of cells cultured on fluoropolymer surfaces has been observed after several days of incubation[249]. It is unclear if this is associated with cell death, however it does suggest that continued cell attachment to these surfaces does not purely depend on biophysical mechanisms, but that cell behaviour is influenced by a time dependent sensing of the quality of cell-material interactions.

Ta_2O_5 capacitively charged electrodes, in contrast to aluminium, showed no obvious shifts in cell distribution away from uniform as exemplified in Fig 4.21. Thus any leakage currents if present, were beneath the threshold to stimulate electrotaxis. In this case the observed cellular phenomena must be explained by the capacitance of the interface and given the inertness of the overlying fluoropolymer, by charging of the double layer.

The debye screening length represents the point where double layer potential falls to $\frac{1}{e}$ or 37% compared to the interface surface. This distance is often take to represent the

maximum distance of electrostatic influence between bodies across a medium. In aqueous electrolyte solutions the distance is affected by the ionic strength of the solution. In pure water the debye length is around 1 μm. To calculate the value for the *in vitro* solution the ionic constituents of the culture medium were collected along with their concentrations and valence, shown in Table 4.4. Applying these data to Equation 4.8 gives a value for the distance of electrostatic influence from the surface of the device of 7.34 Å. This value is significantly smaller than the size of even a single small protein (albumin occupies approximately a cube 12 nm on a side[126]), implying that any influence on the cells is mediated not only by electrostatic interaction with a single layer of protein, but possibly a small part of an absorbed protein.

Source	Electrolyte	Subscript	Valence	Concentration (mmol L^{-1})
calcium chloride	Ca	1	2	1.8018018
	Cl	2	-1	1.8018018
ferric nitrate	Fe	1	3	2.475e-4
	NO_3	3	-1	2.475e-4
magnesium sulphate	Mg	1	2	0.8139166
	SO_4	1	-2	0.8139166
potassium chloride	K	1	1	5.3333335
	Cl	1	-1	5.3333335
sodium bicarbonate	Na	1	1	44.04762
	HCO_3	1	-1	44.04762
sodium chloride	Na	1	1	110.344826
	Cl	1	-1	110.344826
sodium phosphate monobasic	Na	1	1	0.9057971
	H_2PO_4	1	-1	0.9057971

Table 4.4: Electrolytes adapted from the full composition of Dulbecco's Modified Eagle Medium(DMEM) used in cell experiments. Source:*https://www.thermofisher.com/uk/en/home/technical-resources/media-formulation.48.html*

$$\lambda_d = \left(\frac{K_B T \epsilon_0 \epsilon_r}{\sum_{j=1}^{N} n_j s_j N_A (z_i e)^2} \right)^{\frac{1}{2}} \tag{4.8}$$

Where K_B is Boltzmann's constant, T is culture media temperature (310 K), ϵ_0 and ϵ_r are the permittivities of free space and of water respectively, n_j,s_j and z_j are the concentration, subscript and valence of the electrolytes from Table 4.4 , N_A is Avogadro's number and e is the elementary charge.

At higher values of surface potential, electrosorbed polyelectrolytes (proteins) would be expected to pass through conformational changes to more efficiently pack the surface with charged groups. Ultimately, as surface potential increases still further, these large partially charged molecules would be competitively exchanged for trivalent, divalent and finally monovalent ions[130].

Aleksandrova *et al.*[345] examined cells spreading on polarised Ta_2O_5 electrets without any coating. Cells spread on both polarised and control surfaces, but contained more processes on surfaces that were electrically treated. In the case of fibroblasts, proliferation and outward migration on electrically polarised samples was impeded, while other cell types had increased viability on these surfaces. This behaviour is typical of cells searching for better surface anchors (haptotaxis), where electrical polarisation gradients were created cells appeared to migrate into preferred regions. Enhanced metrics of cell-surface behaviour, such as cell spreading and surface process formation are likely not distinguishable by edge density alone, but clearly occur on electrically active biosurfaces, necessitating the need for improved imaging and quantification methods. Surface charges of approximately 5 µC cm^{-2} negative created by apriori electret charging on native Ta_2O_5 surfaces were found to influence cells[345]. This density is much lower than the 80–140 µC cm^{-2} charge storage that can theoretically be placed on the tantalum bioelectrodes[240] under dynamic conditions.

Measurements of capacitances of the strip electrodes in culture media give a value of 83 nF cm^{-2}, which would result in a surface charge density of 1.42 µC cm^{-2} at 17 V, 0.42 µC cm^{-2} at 5 V. These values are similar to densities achievable on electrets, except in this case charge can be applied dynamically. Both values are at the lower range in comparison to much of the comparable literature producing biological responses. However, they are significantly higher than the small surface charge density reported within the literature surveyed (pC cm^{-2}[258]). That value was achieved at a much higher voltage (75 V), showing that device construction can heavily influence the potentials required to interact with the biology. At 30 V anodisation significant leakage currents can be expected from 4 V reverse polarisation, severely limiting the ability to explore opposite charge densities. There is, however evidence of differing biological effects on a polarised fluoropolymer at positive versus negative charged surfaces[357]. Some alternative dielectrics that are not

polarised would be required to exploit bipolarity of stimulation.

4.13.8 Material properties

Several potentially relevant features of the fluoropolymer surfaces have to be considered. Many fluoropolymers also possess an electret property, a result of charge incorporation into the dielectric, generating a near permanent surface charge. Voltage driven charge trapping has been shown to lead to irreversible effects on contact angle change in electrowetting applications[309]. Fluoropolymer surfaces have been also been observed to spontaneously develop negative surface charge after immersion in pure water and other solutions[358]. In electrowetting applications this tendency manifests as an electro(de)wetting phenomenon - creating small increase in contact angle after application of voltage corresponding to either removal of trapped charge or balancing by further ionic adsorption. This behaviour is analogous to the potential of zero charge (PZC) on metal surfaces, which can influence the surface charge of the metal electrode being used for biological interaction[97]. This suggests that distinct cell and protein phenomena may exist and be accessible at both polarities at low, as well as high, potentials. Speculatively, this may offer explanation for discrepancy between the high springback rate (compared to control) seen at lower voltages in Fig 4.15. A wider range of applied potentials would establish if this was the case. The charge state of these materials can also alter over time when in contact with electrolyte solutions[249], meaning that pre-incubation of surfaces under various time/solution conditions prior to setting up electrical stimulation experiments may produce different results. If the fluoropolymer is maintained at sub-breakdown electric field strengths then potentially two static (electret and surface chemistry) and one dynamic surface charge are available. Charge trapping and electret effect outside of stimulation on the behaviour of the surfaces. Direct investigation would require direct measurement of surface potential using techniques such as Kelvin probe scanning microscopy and may also be detected by protein conformation experiments.

Cytop breakdown voltage is 9 kV/100µm[282], which at 20 nm is only 1.8 V. The tantalum layer has the higher capacitance so a larger potential will appear across the polymer layer. These layers have been shown to be beyond dielectric strength in devices of similar construction[274] and so permanent polarisation may be expected to have proceeded under the

stimulation conditions produced in this work.

4.13.9 Electrical

The voltages used were selected for two reasons to keep within the safety factor of the tantalum oxide film and on safety grounds as the incubator used was in a communal area. Higher voltages would be of interest to attempt to create surface charge densities within the electrochemical window of the culture solution. In the electrowetting literature, voltages around 100 V and higher are commonly applied before contact angle saturation is reached[274]. Similarly, high voltages have been used in the electret based approaches[345,258]. Using such voltages requires the use of safety interlocks and dedicated incubators. Additionally, lower voltages possess more interest from the point of view of ease of application, especially in implanted applications.

4.14 Conclusion

Two cancer cell lines were able to grow and survive on the surfaces and appear unaffected by the single additional material, used as a gasket, allowing the commercial chambers to function as a direct comparison and control against fabricated surfaces. Cells could be imaged unstained but were also successfully fixed, fluorescently stained and imaged, opening up many possibilities for further investigation of cell-surface interaction on charged surfaces and other microfabricated structures as well as alternative investigations of other biological effects.

The developed metric: edge density, was shown to be repeatable and a sensitive measure of cell density and attachment. Measurements of cell interaction with devices under a number electrical conditions were sufficient to extract meaningful biological data from unstained cells in culture. Additionally, through further data processing, multiple potentially confounding variables could be quantified.

Through electrical stimulation experiments, a trend of reduced cell attachment was observed on capacitively charged electrodes. However, this was only statistically significant at a higher voltage in one cell line (MDA-MB-231) at 17 V. The results were consistent across two time points and under a separate, paired analysis. When adjacent regions were compared, the trend was also observed in the majority of microscopic fields in MCF-7 cells at 15 V, whereas at 5 V in MDA-MB-231 cells adjacent fields were equivocal. This suggests that the effect was voltage dependent and it is speculated that differences in cell morphology across the two cell lines were responsible for a weaker signal in the MCF-7 cells under the developed metric. However, it is also possible that intrinsic differences in the biological mechanisms of cell attachment between the two cell lines influenced the outcome. Time series analysis implied that the dynamics of the cell detachment on the fluoropolymer surfaces showed a greater complexity than on standard TCPS surfaces. Comparison of electrode and control regions, supports the conclusion that higher voltages led to reduced cell attachment and it is also possible that a region of enhanced attachment exists at lower voltages. The results support the novel claim that cell detachment processes contain information about cell-surface interactions and may be complementary or act as a substitute, where direct observation of cell attachment is not possible.

In an independent experiment a second bioelectrochemical phenomena was observed using the *in vitro* platform, implying the versatility and potential wide applicability of the *in vitro* platform. Here, corrosion currents from an aluminium electrode appeared to be capable of adjusting the position of cultured cells on an adjacent uncharged region. In particular, there appears to be a 100 µm wide region starting about 130 µm from an electrode edge where cells are significantly reduced, followed by a more distant region of accumulation, implying that cell migration was stimulated. This phenomenon, if generalisable to *in vivo* environments, could present a mechanism to control cell interaction with working electrodes and other transducers, by including a nearby sacrificial electrode in the design. This could allow increased the accuracy of biosensors that rely on inward diffusion of analyte or that are sensitive to metabolism of analytes by surface dwelling immune cells(macrophages and FBGC).

Chapter 5

in vivo device platform

Introduction

This chapter describes the development of a device that was designed to allow electrical interaction experiments with an *in vivo* model, based on the chorio-allantoic membrane(CAM) found within chicken eggs. More detail about this organ and its use as a model in biology can be found in Chapter 6 . In this case the entire active area of the device was introduced into the egg membrane. Specifically, bringing microfabricated structrues, electrodes and sensors in contact with a tissue environment while exposing electrical connections to external instrumentation. Needle structures carrying electrodes were chosen for this purpose. A schematic shown in Fig 5.1 shows how the components of the platform interact to enable electrical stimulation experiments *in vivo* . Several features and processes used in the *in vitro* platform (Chapter 3) were conserved to produce a general platform and devices for electrical interaction studies with low packaging complexity.

However, the design differed in several ways from the *in vitro* platform. For example an on-device platinum counter electrode was added, and a silicon nitride passivation layer was used to protect interconnects. The silicon nitride was removed around electrodes, test points and backplane contacts by RIE and this layer replaced photoresist (used in anodisation test structures) as an anodisation mask.

Several processes were developed for this platform and will be discussed in this chapter. The requirements for a needle interacting with CAM tissue had little precedent and so all designs were created with parameterisation of the key features. To maintain this

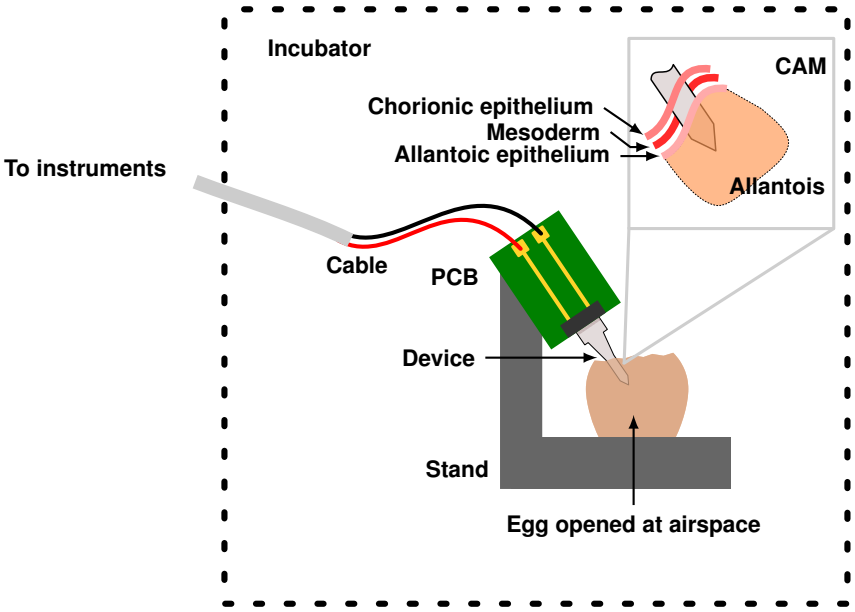


Figure 5.1: Proposed setup and electrical connection to the *in vivo* model through an *in vivo* needle device and PCB supported by a stand including 3D printed components.

flexibility, maskless lithography was adopted for all photolithography. As lift-off processes had not been optimised with the maskless tool, an approach based on a bilayer photoresist was developed. Test structures were developed to exploit intra-wafer process parameter variation capabilities of the maskless tool. The needle-like devices required an irregularly shaped die. A solution combining a through-wafer etch process with wafer dicing was developed. To efficiently develop these structures, software tools for electronic design automation (EDA) along with automated metrology and analysis, were created. While initially used to accelerate optimisation of the lithography processes the were subsequently generalised. Finally, an approach to make electrical contact with the devices and position both needle device and chick egg was developed using rapid prototyping.

All fabrication was carried out in the cleanrooms and laboratories at the Scottish Microelectronics Centre in the School of Engineering at the University of Edinburgh.

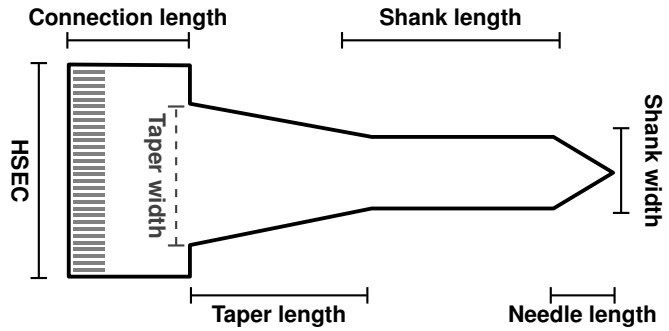
5.1 Parametric design

The overall design for the CAM devices is shown in Fig 5.2, each parameter (shown schematically in Fig 5.2a) was independently controllable and was generated from a Python script using the GDSII library *GDSPY*[359]. Adjusting any of these parameters modified the

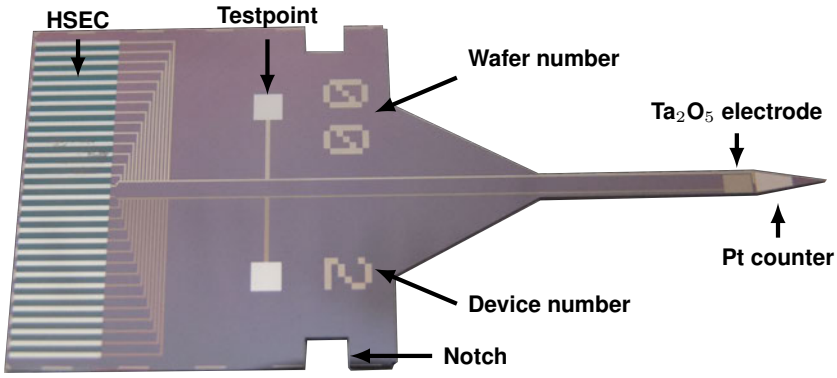
property itself, but also altered other derived structures across all layers of the design. For example adjusting the needle tip profile via the *shank width* and *needle length* parameters would cause recalculation of the geometry on layers defining the platinum and tantalum electrodes. This ensured the electrodes accommodated the new needle geometry and maintained a predetermined gap – itself a parameter – to the edge of the silicon region. The control parameters available along with the default values used are detailed in Table 5.1. Parameters included those related directly to research questions in the intended application of the devices but also to those to aid process development and optimisation. Parameters could be divided into two categories: Those related to the research question, such as the effect of needle width of the biological model, and others included to aid process development and optimisation. An example process parameter was width of the release etch. This had implications on the total required etch time but also on the ease of separation of final devices from surrounding waste silicon.

Parameter	Description	Device value	Test structure range
Shank width	Width of the shank of the needle	1750μm	centre: 1750μm, low: 400μm high:1750 μm
Shank length	Length of the needle shank to base of the tip	15000μm	3000μm
Taper length	Length of the taper between contact and shank	10000μm	2000μm
Taper base	Width of the taper between contact and shank	12675μm	5000μm
Aspect ratio	Defines the length of the tip based on the shank width	3.0	centre: 3.0, low: 1.0 high: 5.0
Release trench	Width of the DRIE release trench	300μm	300μm
Electrode inset	Gap enforced between the release trench and electrode material	100μm	20 μm
Identification	Annotation for each device with wafer number and device ID	Wafer: ##, Device: 0,1,2	000 - 999
Ancillary			
Connection length	Length of the body of the device containing contacts and test points	25375 μm	3000 μm
Interconnect width	Width of the contact-test point-electrode electrical connections.	300 μm	N/A
RIE offset	Enlargement of test point and electrode windows.	30μm	N/A
Marker width	Markers defining the dicing lanes.	100μm	100μm
Test pads	Toggles test pads on and off	Yes	N/A
Clip notches	Toggle clip notches on and off	Yes	N/A
Test pad side	Size of test pad	2000μm	N/A
Notch length	Dimension of dicing lane notch designed for device holding	2800μm	N/A
Notch width	Dimension of dicing lane notch designed for device holding	2000μm	N/A
Derived			
Needle length	Derived from: *Shank width* and *Aspect ratio*.	5250 μm	*Shank width* x *Aspect ratio*
Ta_2O_5 electrode area	Derived from: *Shank width*, *Aspect ratio* and *electrode inset*.	2.7 mm^2	N/A
Pt electrode area	Derived from: *Shank width*, *Aspect ratio* and *electrode inset*.	2.91 mm^2	N/A

Table 5.1: Description and values of parameters used to generate the *in vivo* devices and test structures.



(a) Parametric controls of *in vivo* needle devices.



(b) Fabricated *in vivo* needle device.

Figure 5.2: Schematic *in vivo* needle device with parameters and fabricated device.

5.2 Processes

The processes required to deposit the electrodes and release the needle geometry are shown in Fig 5.3 and Fig 5.4.

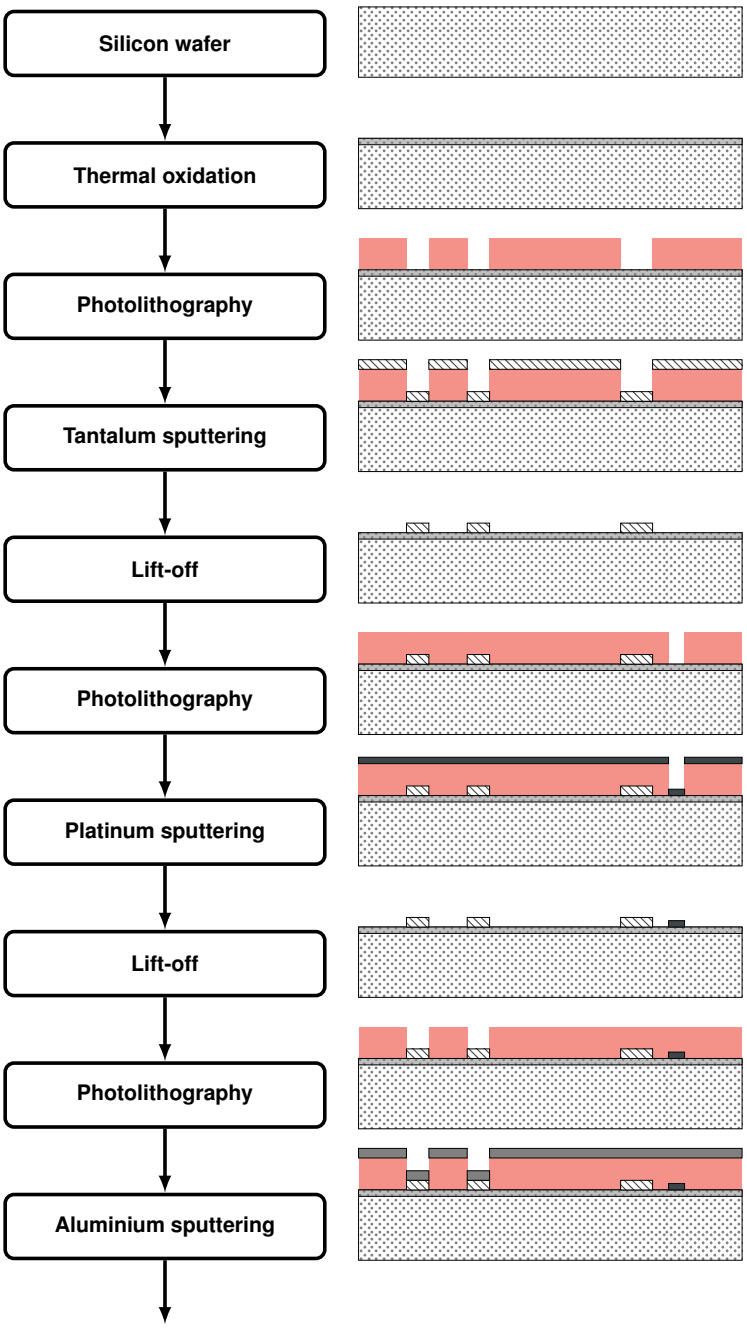


Figure 5.3: Microfabrication steps to produce the *in vivo* platform.

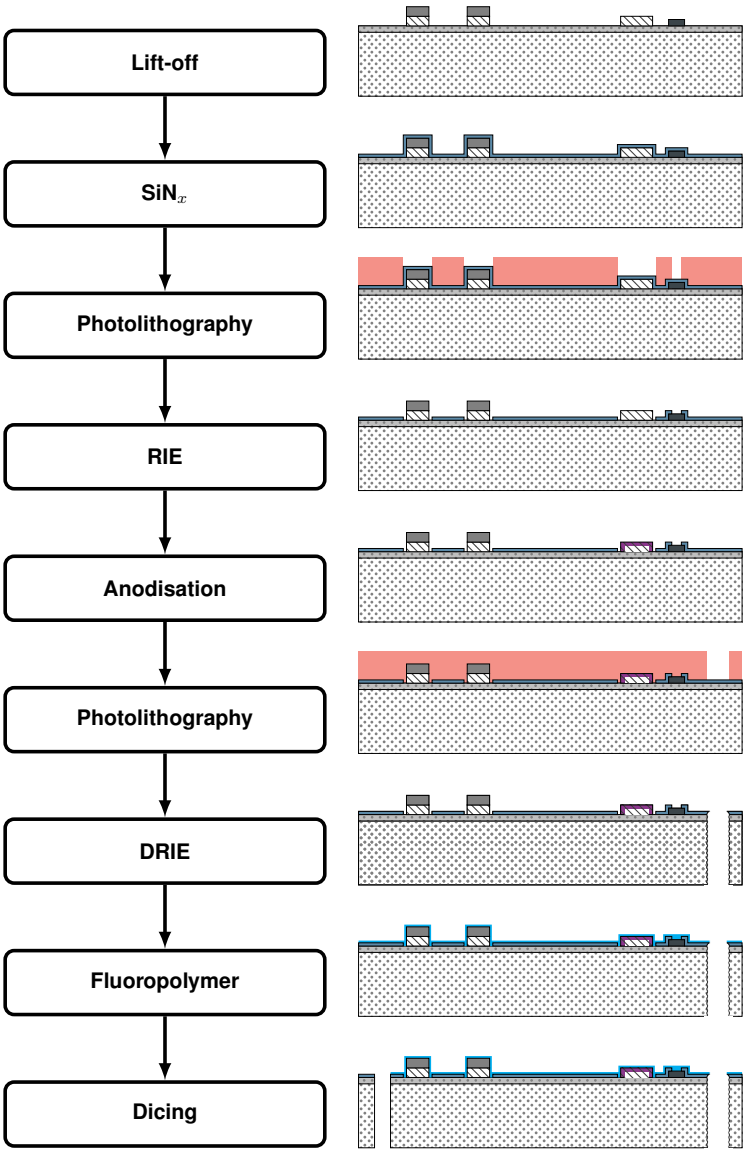


Figure 5.4: Microfabrication steps to produce the *in vivo* platform - continued.

5.3 Maskless photolithography

The availability of a maskless lithography tool allowed maximum exploitation of the benefits accrued from a parametric design. Silicon wafers 100mm in diameter with a 1 µm thermal SiO_2 layer were cleaned and dehydrated for 30 minutes in an oxygen plasma. Wafers were coated with a positive tone bilayer resist prior to maskless lithography. A maskless bilayer resist process was established specifically for this work, the development of which is described in Section 5.13.1. For the bilayer: *LOR 5B* (Microchem) was spin-coated at 3000 rpm and then soft baked at 180 ℃ for 5 minutes. A subsequent layer of photoresist *SPR 220-3.0* (Microchem) was spun directly on top of the previous layer and soft baked at 110 ℃ for 90 seconds. Wafers were exposed on an *DMO ML3* maskless lithography tool (Durham Magneto Optics) using a 1 µm resolution and 230 mJ cm^{-2} dose. All other quality settings were left at machine defaults. After exposure the photoresist was rested for 30 minutes as per the manufacturer's recommendations then post-exposure baked at 110 ℃ for 90 seconds. The pattern in the bilayer resist was developed for 90 seconds using a double puddle technique in TMAH (Shipley Microposit MF-26A). Wafers were then rinsed in deionised water and dried using a N_2 gun.

5.4 Metals deposition

After an initial photolithography step to define the desired pattern, a 300 nm film of tantalum was deposited by sputtering using a *PlasmaLab 400* sputter tool (SGC equipment). Unwanted parts of the deposited film were then removed by lift-off using NMP *Microposit remover 1165* combined with heat and sonication in a water bath.

The photolithography steps were repeated as for the tantalum for the platinum layer. A 100 nm thick platinum film was then deposited using E-beam evaporation. A titanium film (10 nm) was deposited before the platinum to improve adhesion to the underlying SiO_2. This film was also patterned by lift-off.

Aluminium was used as the final metal layer to define the contact region and test points. Aluminium was sputtered onto both the tantalum and platinum test point interconnects and contact region. A pre-sputtering argon milling step was included in the *Plasmalab 400* programme in order to remove any native metal oxide and ensure good electrical

conductivity at each of the inter-metal interfaces.

5.5 PECVD silicon nitride

A layer of SiN_x was deposited as a passivation layer, using a plasma enhanced chemical vapour deposition (PECVD) tool (Surface Technology Systems). The thickness of the deposited film was measured using reflectometry to be around 400 nm. The 'x' subscript in SiN_x refers to the non-stoichiometric nature of silicon nitride films generated using this process.

5.6 Reactive Ion Etching (RIE) window

Windows were then opened through the SiN_x passivation layer in regions around the electrodes, test points and contacts using reactive ion etching (RIE) *RIE* tool (JLS Ltd.). This process was performed using a single layer photoresist *SPR-220-3.0*. Optimisation to minimise process time was carried out by varying etch parameters across several test wafers and measuring the remaining film thickness, until complete material removal was achieved - data not shown.

5.7 Anodisation

The anodisation process for the tantalum electrodes proceeded in a similar manner as described for the *in vitro* devices (Section 3.9). In this case, however, the patterned SiN_x passivation layer replaced photoresist as an anodisation mask.

5.8 Deep reactive ion etching

Deep reactive ion etching (DRIE) was used to partially release needle structures and define the cutting edges using the Bosch process[360]. This process alternates a SF_6 etch step with C_4F_8 deposition to produce an anisotropic etch into silicon material. The etch location was controlled through a photoresist pattern. A thicker layer of photoresist was required, compared with previous steps due to the etch depth required and the selectivity of the etch

process. This was achieved using *SPR-220-7.0* (Microchem) photoresist to produce a high selectivity mask layer , initially set at 7 µm.

The DRIE tool used, *Plasmatherm Versaline DSE IV*, was set up to handle 150 mm wafers, whereas the product wafers were 100 mm. The product wafers were therefore placed on 150 mm wafers that acted as carriers. This gave the advantage that wafers could be processed up to the edges and etching through the wafer would not interfere with the chucking mechanism of the tool. Wafers were coated in photoresist and patterned to expose trenches to be etched. These trenches intersected the dicing lanes, allowing the combination of the etch and dicing to define the final geometry of the structures. The adhesive *Crystalbond™ 555 adhesive* (Aremco Produces Inc.) was applied to the carrier wafer on a hot plate at 55 ℃ and the product wafer was lowered onto the surface and allowed to temporarily bond. The assembly was then removed from the heat and allowed to cool. Wafers were then etched using a recipe requiring approximately 1 hour of processing. After processing, the wafers were again heated to allow separation of the etched wafer from the carrier. Residual adhesive was then removed from the etched wafer using acetone, followed by deionised water at 60 ℃. This was the penultimate processing step and immediately preceded dicing. An electron micrograph of a released needle prototype is shown in Fig 5.5.

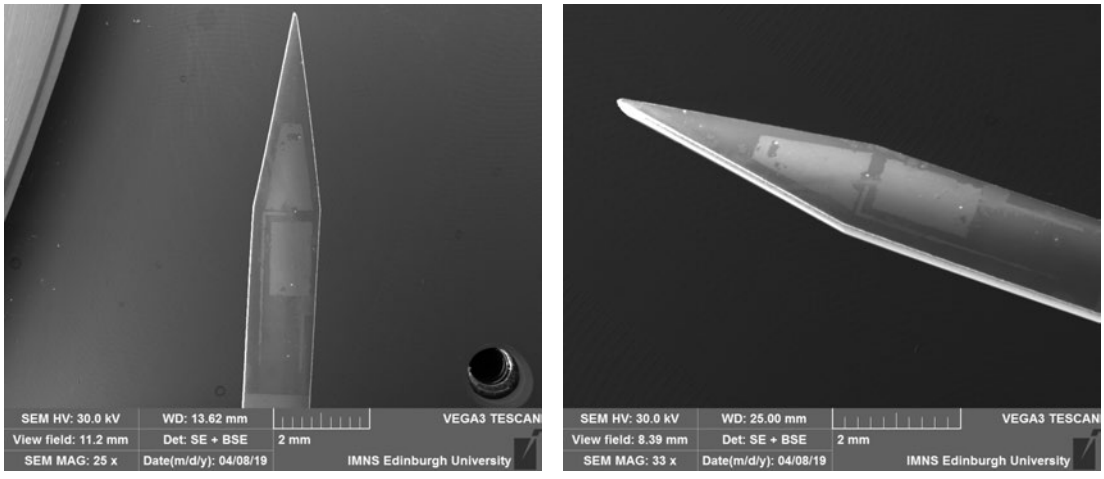


Figure 5.5: Scanning electron microscopy (SEM) image of a needle prototype showing sucessful DRIE etch definition of the needle structure but electrode damage due to inadequate etch mask selectivity.

5.9 Fluoropolymer

In the *in vitro* devices, a hydrophobic layer was deposited by means of spin-coating. With this device an alternative material, octafluorocyclobutane (C_4F_8), was used. This was deposited using CVD as part of the DRIE etch. A thin film was deposited by creating a long deposition step in the programme on the Plasmatherm deep reactive ion etcher. This step ran immediately after the end of the through-wafer etch process. The effect of deposition on contact angle in contrast to spin-coating can be seen in Table 3.3 and Fig 3.18.

5.10 Dicing

Wafers were diced using using a DAD640 *DISCO* semi-automatic dicing saw. The etch released regions of the wafer continued into the dicing lane (see Fig 5.7: arrows) creating an interrupted cut. Thus the dicing process fully released the needle structure while simultaneously defining contact region as described for the *in vitro* devices in Section 3.13. The diced wafer returned from this step mounted on dicing tape attached to a frame. Devices and waste material were then removed from the tape manually and stored.

5.11 Needle test structures

Test structures were used to examine the response of the *in vivo* model to implantation with passive devices composed of the same materials as that used for electrical stimulation. A parametric test structure was designed allowing control of the needle width, aspect ratio and the presence of metal electrodes. Each test structure also contained a 3-digit identifying label that could be related to a database of structure parameters that was generated alongside the layouts. A range of structures were created by varying parameters using a design of experiments approach, an example layout is shown in Fig 5.6. Values for structure parameters were derived using a central composite design (CC). An inscribed design (CCI) was used so that absolute parameter limits could be set when generating the design. This particular scheme embeds a factorial design with centre points to estimate variance that also contains interaction terms allowing optimisation. Released needle test structures are shown in Fig 5.7. The fabrication processes were identical to those developed for the

CAM devices described above. The parameters of the test structure were similar to those for the devices and are shown in Table 5.1.

5.12 Ancillary platform components

A stand was built to hold the needle structures at a given angle from the CAM surface. To achieve this the PCB was mounted to 3D printed components. This included a mechanism to precisely advance the needle tip using a screw adjustment on the rear of the stand. The components of the well holder were designed using the parametric 3D modelling language *Openscad*[361]. Annotated images of the 3D models are shown in Fig 5.8 and assembled in Fig 5.9. The holder was planned to work with a microscope stand (Dinolite MFR RK-06A), *RS Components*. The egg holder was created using a surface of revolution operation on a scaled profile that was extracted from an image of an example egg and featured a magnetic base.

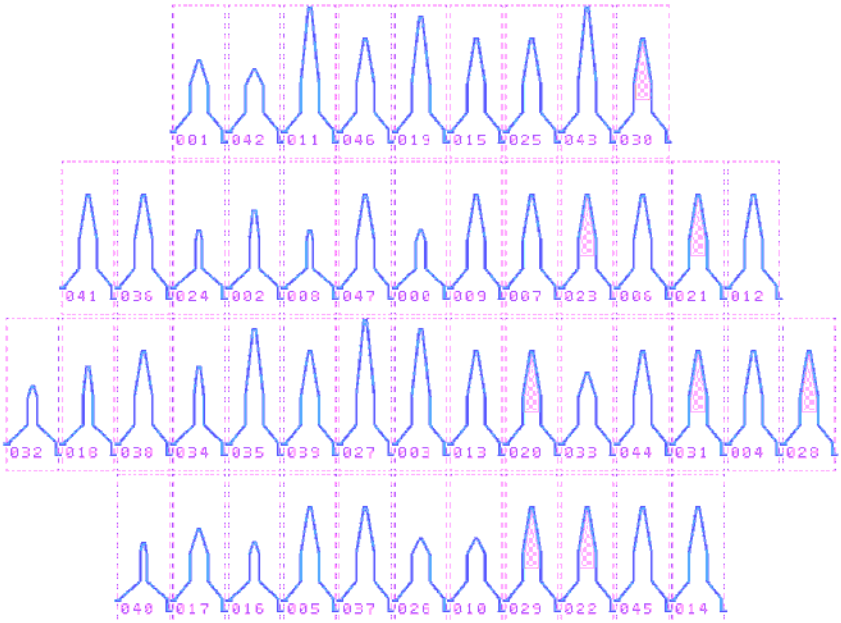


Figure 5.6: Wafer map of needle test structures generated from a design of experiments (DOE). Structures with tantalum regions toggled on were placed at surplus wafer positions after the experimental design had been satisfied.

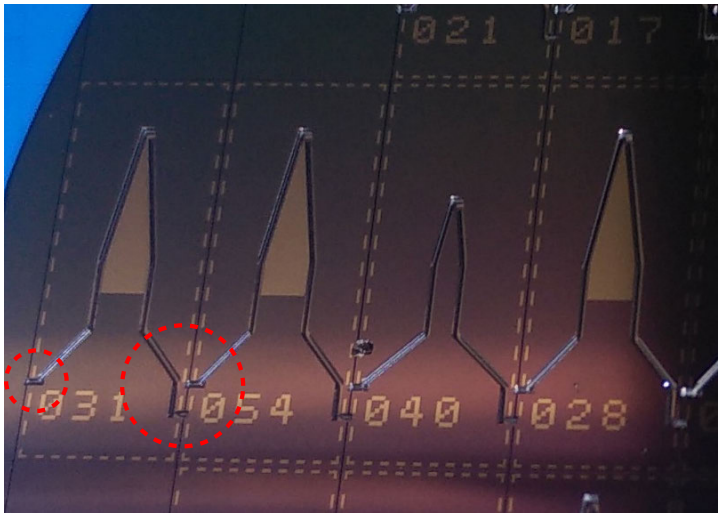


Figure 5.7: Needle test structures post-dicing, prior to manual release from dicing tape. Three identical structures and a structure generated with different parameters are shown. Junction of DRIE etch and dicing lane to complete release (red circles).

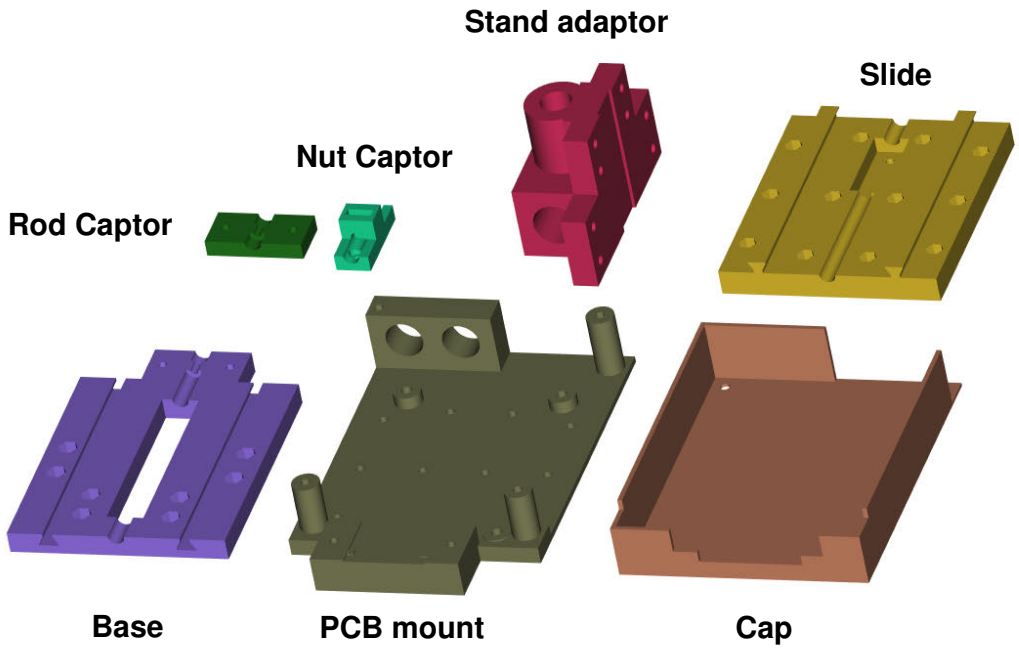


Figure 5.8: 3D printed holder for CAM devices. Interfaces with Dino-Lite microscope stand and allows controlled advancement of the needle into the CAM via screw thread.

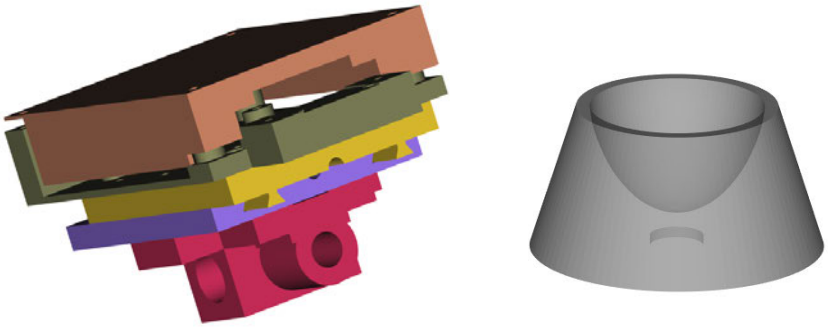
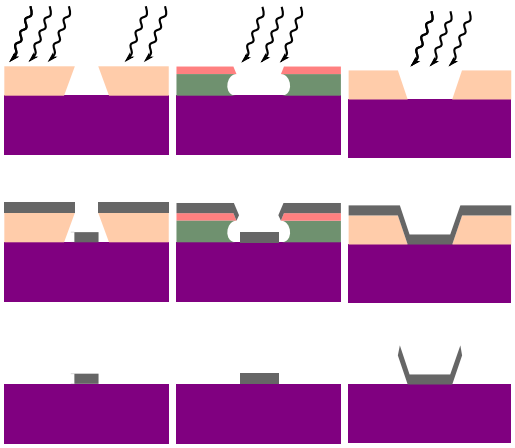


Figure 5.9: Assembled 3D printed CAM holder and egg holder



(a) Negative (b) Bilayer (c) Positive

Figure 5.10: Photoresist lift-off options: Rationale for using bilayer photoresist in maskless applications.
Top row: Location of light exposure to define pattern and sidewall profile formed.
Middle row: Response of a deposited thin film to patterned resist.
Bottom row: Patterned film after lift-off.

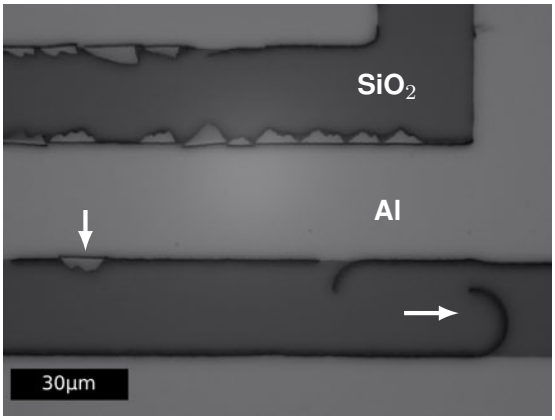


Figure 5.11: Lift-off failure of a patterned aluminium thin-film showing 'upstickers' (arrows).

5.13 Bilayer resist processed using maskless lithography

To keep the design of structures flexible and to allow creation of parametric test structures for CAM devices, all lithography steps on the CAM design were carried out on the maskless lithography tool. The critical dimensions of all parts were such that patterning of thin film metal could be achieved via a lift-off process. Lift-off processes normally require the use of negative resists that produce a negative side wall profile Fig 5.10a. However, these resists are cross-linked by light exposure, requiring the use of a light field mask, where non-feature areas are exposed.

On a maskless tool, patterns are transferred to the substrate by sequential exposure

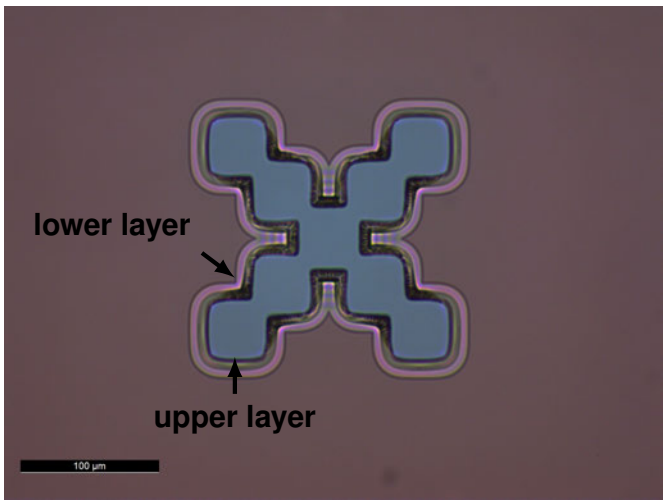


Figure 5.12: Example of maskless processing of a bilayer resist. Here the letter "x" is defined showing central exposure of the substrate for deposition, The positive sidewall of the upper layer and the negative undercut of the undeveloped resist peripherally.

of small regions. Using a light field approach thus leads to long exposure times. Additionally, the wavelength available for exposure (I-line) was not optimised for negative resists meaning that a higher dose was required further increasing exposure time. Conversely, the exposure dose and therefore time was reduced when using a positive tone photoresist. Positive photoresists are destabilised by light and as such a dark-field exposure allows only those fields containing features to be exposed. However, positive photoresists produce a sidewall profile (positive) that is inappropriate for lift-off processes. This is due to the high probability of film continuity from the resist to the substrate at a feature Fig 5.10c. When the resist is subsequently stripped, after deposition, metal "upstickers" (Fig 5.10c) often remain in the region of the sidewalls an example of which can be seen in Fig 5.11.

In a bilayer resist, a light insensitive resist is overlayed with a photoresist, in this case positive. When exposed, the top layer of photoresist becomes selectively soluble in developer and during development acts as a mask allowing the underlying layer to be isotropically developed in the same processing step, generating an undercut that replicated a negative sidewall profile (Fig 5.12), resulting in discontinuous film deposition. This process has advantageous properties of both positive and negative resists in that the exposure can be dark-field resulting in reduced exposure times, whereas the pseudo-negative sidewall allows clean lift-off.

Bilayer resists were investigated and found to produce an acceptable alternative to neg-

ative resists for maskless patterning for lift-off. The disadvantages of this process include the requirement for two consecutive spinning and baking cycles for each photolithographic step. Another disadvantage was that the Bilayer component (LOR series *Microchem*) is more expensive, compared to other photoresists.

5.13.1 Bilayer test structures

As the top layer of the bilayer stack was the only photosensitive component, the z-focus of the tool, along with the photodose, required optimisation. Photodose refers to the amount of light energy transferred to the photoresist during exposure. The focus was set using an automated routine in the tool that analysed a pattern projected onto the substrate. This focus value could be offset, prior to wafer patterning, for each individual structure. Figure 5.13 shows a linewidth test structure developed to optimise the exposure parameters for the bilayer lift-off process. The linewidth structure itself consisted of sequentially reducing alternating exposed and unexposed features (fingers). The design tested the ability of the tool to expose structures of reducing dimension, but was also sensitive to resist development time. This was because a fully undercut feature could be released from the substrate, and could either be removed or suffer extreme deflection during the rinse and drying steps, an example showing these outcomes can be seen in Fig 5.14. Structures were automatically generated and distributed across a wafer. However, instead of producing a single layout, each structure was generated as a separate file and referenced in a simultaneously generated tool configuration file. This allowed placement of each structure on a wafer at a predetermined location, and with a per structure dose and focus setting. Structures were imaged by automated microscopy using configuration files also generated when the layout was compiled. An opening below the finger structures was also enlarged to allow imaging so that the structures could also be imaged by oblique automated SEM.

A QR code was encoded as part of the structure, this contained a unique experiment number and associated parameters, Fig 5.13. These structures were included for redundancy features to track each structure while the software tools that were developed to generate and manage metrology were being validated. As the computer ultimately tracks and manages the location and experimental parameters of each structure these additional structures were intended to be removed in future iterations. The readability of the QR codes was tested by running a software decoding script, but some image processing was first required. Images were converted to greyscale and a threshold was applied. The difference in albedo between resist and substrate was sufficient to allow discrimination using a suitable threshold value calculated by Otsu segmentation[362]. This was followed by several morphological operations to remove noise. The final result produced an image that could

be decoded, an example can be seen in Fig 5.15. Variation of parameters in the image processing script was performed to optimise decoding success. After optimisation all QR codes within the dataset could be sucessfully decoded.

A wafer was prepared and patterned with bilayer photoresist as described in Section 5.3. Microscopy was carried on a Leica DM12000 M Inspection Microscope (Leica Microsystems). The microscope featured a motorised stage and objective selection, image acquisition was automated by supplying a list of structure coordinates. Acquired images were manually labelled using the annotation tool *Labelme*[319]. This consisted of a single line running right to left on the image through the middle of the features. All the remaining analysis was then performed automatically using a custom developed analysis script. The intensity of the pixels in each structure image (converted to grayscale) was extracted along the annotation line. Features were detected by cross-correlation of the intensity profile with a custom waveform, shown in Fig 5.16. This kernel was designed to produce a detectable signal at each feature that could discriminate between successfully formed features from those were either not formed due to patterning failure or lost during resist development. Figure 5.17 shows an example of a test structure along with the pixel intensity profile, (extracted along the labelled line), the correlated signal and the resulting classification. This classification is shown annotated onto the original test structure in Fig 5.18.

Fig 5.19 shows some results extracted from a bilayer test structure experiment. The smallest photoresist line feature that was extracted for each test structure, using the procedure described above was plotted against the exposure parameters (photodose and focus). A trend was visible where smaller structures were more likely to be produced at low photodoses and negative z-focus offsets (lower left quadrant of Fig 5.19. This contrasted with poorer results (larger features) at high doses and positive focus offsets(upper right). These results are consistent with the positive tone and structure of bilayer resists. In the case of focus offset the default focus plane would occur near to to the wafer surface, but the photoactive component was raised from the wafer surface by the initial layer. This along with the nominal thickness of 3 µm explains the improved performance at occurring around −4 µm. As the definition of the features requires exposure of neighbouring regions (gaps between fingers) reducing the exposure dose prevents scattering and other overexposure mechanisms interfering with the definition of small structures at the expense of accurate

scaling. These factors should be constrasted against small dark field features from the opposite side of the structure, where the opposite effects would be expected. These structures were not, however, measured, and would require a modified quantification algorithm. As a result, a trade-off exists in the formation of narrow line features or narrow gap features in the photoresist. These data were used to optimise the bilayer process sufficient to allow the development of the *in vivo* devices. An example can be seen in Fig 5.20, where definition of the platinum electrode prior to metal deposition, resulted in successful lift-off that did not require sonication to complete.

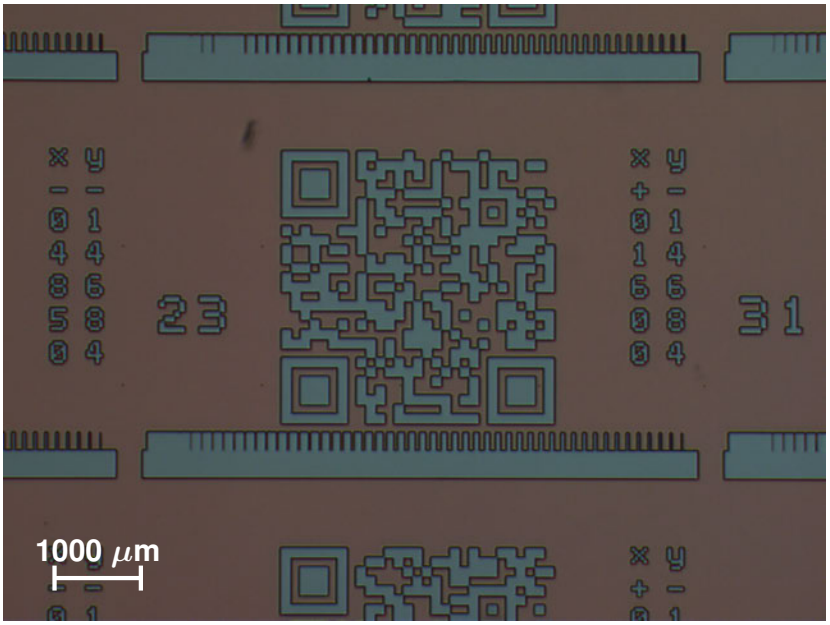


Figure 5.13: Bilayer linewidth test structure showing finger like features of gradually reducing dimension extending into a resist-free area, designed to allow oblique imaging of the structures.

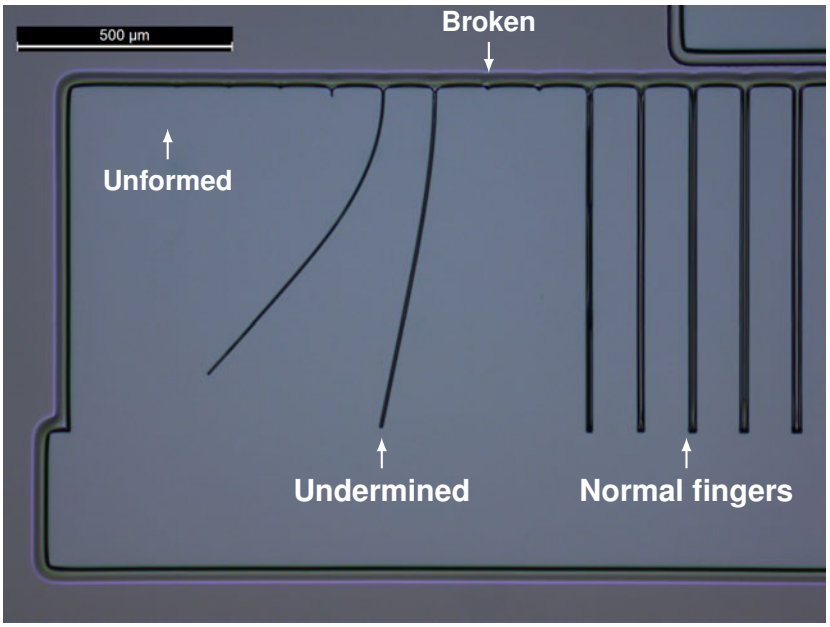


Figure 5.14: Absent features could result from two mechanisms: photolithographic or bilayer over development.

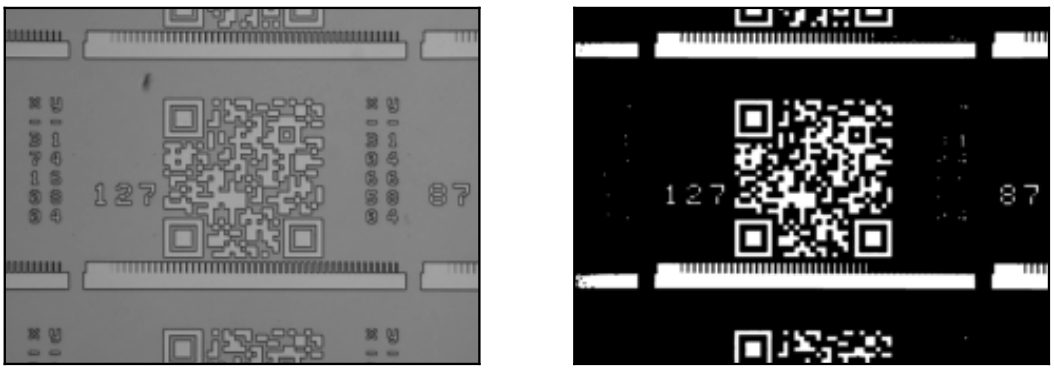


Figure 5.15: Original (left) and processed (right) bilayer test structure images to allow QR decoding and extraction of experimental parameters. The reader is invited to attempt to decode this QR code (index: 127, dose coefficient: 1.342, focus offset: –2.0 µm).

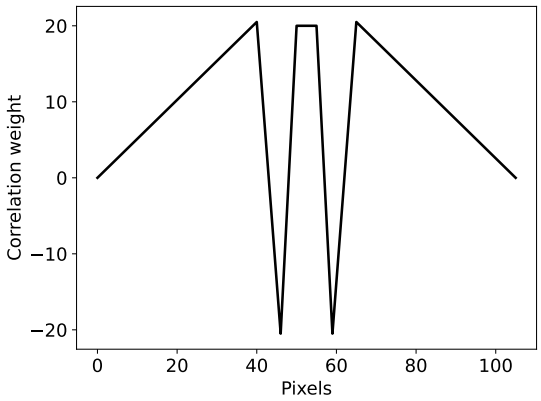


Figure 5.16: Kernel that is cross-correlated against the extracted profile to produce a signal that can be used for classification of the presence/absence of features.

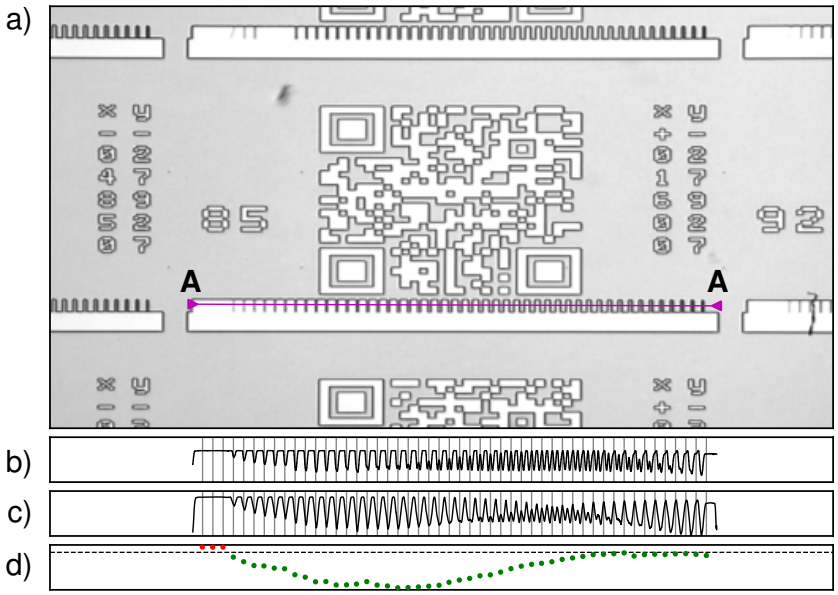


Figure 5.17: Example signal processing of bilayer test structure.
a) Pixel intensity extraction along **A-A**.
b) Extracted profile with calculated structure locations (vertical lines).
c) Profile cross-correlated with kernel shown in Fig 5.16.
d) Structures classified by thresholding.

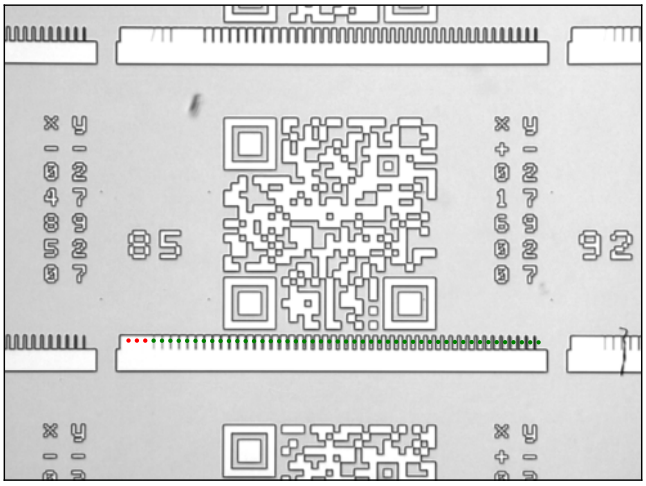


Figure 5.18: Example test structure showing the results of automated classification. Detections are green dots in the top image, failed detections are annotated with red dots.

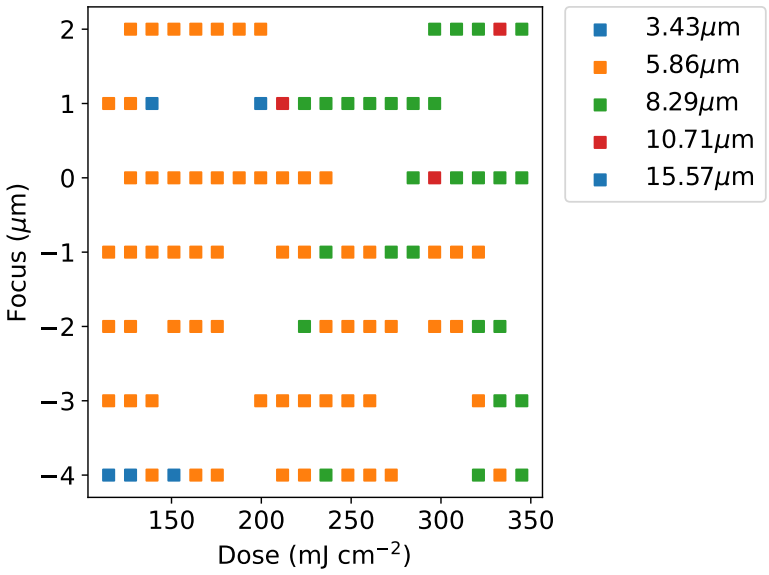
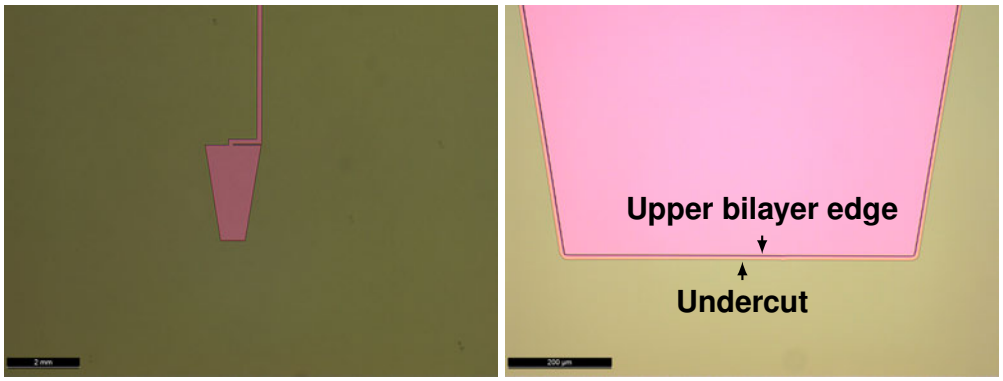


Figure 5.19: Results of bilayer test structure analysis. Each structure is labelled by smallest feature classified and plotted against photodose and focus offset used.



(a) (b)

Figure 5.20: a) Bilayer photoresist patterned for deposition of the platinum electrode. b) Higher magnification reveals the undercut resist profile.

5.14 Discussion

Functional devices and test structures were fabricated using the designs and processes presented in this chapter and used for the *in vivo* work presented in Chapter 6. Significant uncertainty about how the *in vivo* model would respond to implantation stimulated the use of automation tools. In particular, the use of maskless lithography created the flexibility to parameterise and explore the device design space. This parameterisation not only aided answering biological research questions but allowed concurrent process development.

In turn, the constraints of maskless lithography necessitated the characterisation and utilisation of bilayer resists that were suitable for lift-off processes. Bilayer resists were investigated and found to produce an acceptable alternative to negative resists for maskless patterning for lift-off. Software tools were developed to help optimise processes using automation and metrology. A linewidth test structure was developed, which allowed optimisation of internal process parameters of the maskless tool itself on single wafer experiments. Automation was employed to generate process parameter experiments and metrology, along with image and data analysis. Across design, layout, imaging and analysis, only a single step (labelling the structure in the image) required the author's intervention. This novel approach, when combined wth increasing availability digital manufacturing tools and automated metrology would facilitate accelerated prototyping of biosensors and other devices. Especially where the influence of design choices on interaction with biology can only be illuminated by an empirical approach.

The combination of plasma dicing and mechanical dicing can be used to create irregularly shaped wafer die. The DRIE etch process presented particular challenges with multiple failure mechanisms encountered, during process development. Carrier wafers were initially protected with a layer of photoresist and, subsequently with PECVD silicon oxide. However, both of these approaches presented issues. The photoresist would often foul on the chucking mechanism causing unloading failures and the silicon oxide surfaces would occasionally pit and holes would form to the backside interfering with a helium pressure differential that was maintained as part of the chuck mechanism. The larger area of SiO_2 exposed in this second situation also slowed the etch rate in the desired areas of the product wafer leading in some cases to consumption of the mask and sputtering and

re-deposition of metal across the wafer. This issue was eventually resolved by increasing resist thickness up to its maximum thickness, per the datasheet. In future work, an alternate approach is proposed: using quartz wafers as carriers due to the lower etch rate of SiO_2 and a photolithographically defined photoresist coverage on the carrier wafer with suitable exclusion from the edge in regions of the chuck.

Another alternative means to release needle-like structures defined using DRIE has been reported. In this paper, trenches were created that were not full thickness through the wafer and the backside ground until the structures were released[363]. This would remove the need for a carrier wafer as no through-etch would be created.

As an alternative to DRIE, Laser ablation dicing could be used. A wide range of laser types and wavelengths have been described with the advantages of enabling non-straight cuts and varying sized dies across a wafer[364,365].

Removal of the devices from the dicing tape proved challenging resulting in the destruction of several devices to fracture at this final step and despite great care being taken. The trench width of the etch process to define the shank and lancet of the needles was set at a default 100 µm to provide clearance, which appeared sufficient, but was also under parametric control in the design should it require adjustment.

While removal of dies from this tape is normally achieved via vacuum handling devices; the large, irregular shape with high aspect ratio features made applying a sufficient force, normal to the plane of the tape and sufficient to overcome the adhesion, difficult. Maintaining uniformity of this force over the whole structure, while preventing fracture inducing bending moments between the body and shank of the structure would also be challenging using this technique. However, lower adhesion tapes are available and may allow this approach.

Solvent release was considered but is not universally compatible with all materials and chemistries present in BioMEMS devices.

The combination of the dicing lanes (mechanical) and DRIE trenches (sometimes referred to as dicing streets), presents an interesting problem in terms of release of the structures from dicing tape. When generalised to shapes of arbitrary irregularity, potentially containing high aspect ratio features, the complexity of the releasing the structures increases. The simplest mechanical means considered is a roller with a radius selected

in order to remove structures from dicing tape progressively increasing the fraction of the structure that is self supporting. In this work, waste fragments were kept intact and there was a means to remove the devices starting from periperal waste fragments and working in towards the product. Higher complexity structures would possibly require additional dicing streets, added to the waste material, in order to prevent inter-fragment fouling during the release process. This process would have significant planning requirements and is reminiscent of recent interest in the engineering applications of origami[366].

A final factor, is that the fractures in destroyed devices were affected by the crystalline orientation of the wafer, the wafers used were <100> plane, which placed a weak axis perpendicular to the likely force applied. No other aspects of the design are currently dependent on this orientation and the selection was arbitrary based of cost. Wafers with different crystalline orientations (<110> or <111>) could be used or the design could be rotated relative to the preferred fracture lines on the wafer to improve resilience against bending moments.

A significant failure mechanism of implanted silicon needles has been recognised as deriving from focii of strain on electrodes and other surface features that protrude above the substrate[16]. This could be mitigated by planarisation in a similar process to multi-level metalisation[367]. This would bring electrodes level with the surface of the substrate. The opposite effect has also been proposed using masked DRIE to produce highly protruding microelectrode arrays on flexible substrates for neural electrical stimulation[368].

The platinum counter electrode is brought into contact with the deepest part of the tissue when implanted. Improvement to the electrochemical surface area of this electrode could be made by forming a layer of platinum black on the surface[369,295]. A photolithography step was included in the design of the needle structure to facilitate this but was bypassed in the current work. This utility of this modification could also be explored as part of future development of the platform.

5.15 Conclusion

Several novel processes were developed in order to create a platform compatible with a co-developed *in vivo* model, using chick embryos. This model is described in Chapter 6.

Devices based on a planar needle, and sharing several features with the *in vitro* devices, discussed in Chapter 3, were designed and fabricated for the initial purpose of electrical stimulation experiments in an *in vivo* model. In comparison to the *in vitro* platform, these devices featured both a working and counter electrode. In particular, the demonstration of release of large needle structures via combined DRIE etch and dicing presented the greatest challenges. However, several issues were successfully identified and partially addressed sufficient to yield some functional devices, but further optimisation work is required.

A recognition of uncertainties inherent in design for biological applications led to the adoption of maskless photolithography. This tool enables rapid prototyping of digitised designs and invited the development of novel software tools to parametrically generate, process and analyse designs.

This parameterisation not only to aided answering biological research questions but allowed concurrent process development. In turn, the constraints of the maskless lithography system employed, necessitated the development and characterisation of bilayer resists, suitable for required lift-off processes. A linewidth test structure was developed for this purpose along with software tools to allow optimisation of process parameters for the maskless tool, on a single wafer. The application of automation to generate test structures – following experimental designs was novel. The coincident control of process parameters, metrology and analysis of generated images, signals and other data, inspired work that partially formalised this approach[370]. Further, future, work in this direction is anticipated.

Multiple functional devices were successfully fabricated based on processes developed and the designs presented in this chapter. Smaller test structures were also developed to examine the biological of needle parameters on the outcome of needle insertion into tissue.

Chapter 6

in vivo model

Introduction

An *in vivo* model was required, compatible with the devices described in Chapter 5. This chapter describes the investigation of the feasibility of that platform in this model.

Chick eggs contain an extra-embryonic structure, the Chorio-allantoic membrane (CAM), shown schematically in relation to egg anatomy in Fig 6.1. This serves a function similar to the mammalian placenta, in that it facilitates respiratory exchange, storage of nitrogenous waste and calcium metabolism to support the developing embryo. The CAM has an extensive vascular structure and is capable of mounting an immune response. As such, it has been used as a model in many areas of biomedical science, including oncology, immunology, virology and, in particular, biocompatibility. CAM has also been used as an initial *in vivo* model for biosensors[155]. The CAM is composed of three histological layers with a total thickness around 80 µm[371,372], which becomes fully formed by day 6 (of 21 days) of development.

Genetically modified chick eggs were incubated for 14 days. In a subset, at day 7/8, a window was created through the shell and implants consisting of *in vivo* platform needle test structures were placed into the CAM. An unexpectedly high mortality rate was observed amongst these implanted eggs. Given the required implantation time to produce a measurable immune response, it appeared likely that producing meaningful results for electrical stimulation would be difficult until the reliability of the model itself could be stabilised. As a result, planned electrical stimulation experiments were instead replaced

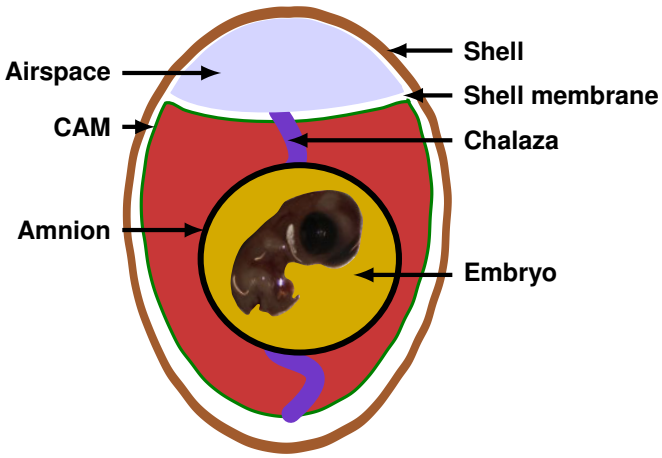


Figure 6.1: Major anatomical features of the CAM.

with an investigation of the practicality of using the CAM as a model for the purpose of bioelectronics research, along with an attempt to optimise the design of the *in vivo* platform. Statistics were recorded regarding: mortality rate under a number of experimental conditions, pathology, the viability rate of embryos and an evaluation of the accuracy of a commonly applied non-invasive technique, used to assess egg viability. Conclusions are drawn about the effect of opening, implantation and storage of eggs prior to experimental work. The incidence and distribution of common pathologies that resulted in mortality were also quantified. Techniques of live imaging and histopathology were successfully demonstrated culminating in the observation of an immune response of the CAM to implanted structures. These data were used to produce the first estimation method to compute the size of experiment (of this type) that would be necessary to achieve a required statistical power.

6.1 Egg collection

Eggs were procured from the Transgenic Chicken Facility, part of the National Avian Research facility, at the Roslin institute, Edinburgh. Macgreen eggs[373] were used. These eggs were obtained from genetically modified chickens that had been tailored to express the green fluorescent protein (GFP) within embryonic macrophages. Eggs were first candled - observing internal structures through transmittance of light through the shell. The presence or absence of an embryo and shell vessels were confirmed by rocking the egg and the observations were recorded. Eggs were labelled and placed in a chiller at 15℃

for storage where they could remain viable for up to two weeks from collection. Eggs were pre-labelled on collection with a hatch date. However, the maximum incubation time for experiments, in order to comply with legislation was 14 days. The collection day was defined to be day zero of incubation and eggs were also labelled with this date with a permanent marker.

6.2 Culturing

Eggs were acclimatised to room temperature on reception, then transferred to an incubation chamber where they were cultured at between 37-38.5℃. A humid environment was maintained, passively, with a water tray, which was replenished every 48 hours. The eggs come from a contaminated environment and as such there was no benefit to operating under the protection of a laminar flow hood. However, incubators were cleaned between batches along with benches, microscope stages and other equipment. Aseptic technique was employed when opening and handling internal structures. Instruments were sterilised before use and maintained aseptically in 70% ethanol between eggs.

6.3 Device sterilisation

Rows of test structures were transferred from dicing tape onto autoclave tape and placed in the bottom of a glass petri dish. The dish was then sealed in a sterilisation pouch. The test structures were sterilised by steam autoclave by the laboratory services department at the Roslin Institute. Figure 6.2 shows both *in vivo* test structures and *in vivo* devices. The black hatching on the sterilisation tape appears after autoclaving to indicate that sterilisation was successful.

6.4 Batches

A total of 103 eggs were used in the experiments collected in two batches, referred to as A and B throughout this chapter. In batch A all eggs were opened on day 8 (stage 34-35 Hamburger-Hamilton[374]) and divided randomly into implant and control groups. This experiment, due to the precipitous mortality rate, was terminated prematurely on day 11



Figure 6.2: Sterilised *in vivo* device and needle test structures ready for implantation.

to ensure some living specimens could be collected. In the subsequent batch (B), eggs were placed into 4 groups, to investigate the causes of mortality. The first group were left intact and incubated immediately, while a second were stored for 7 days, and incubated intact for 14 days. The last two groups were stored for 7 days then incubated for 7 days (stage 30-31 Hamburger-Hamilton[374]), opened and either implanted or incubated as open controls. Numbers of eggs in each group is tabulated later in Table 6.1. A timeline after collection of each batch is shown in Fig 6.3.

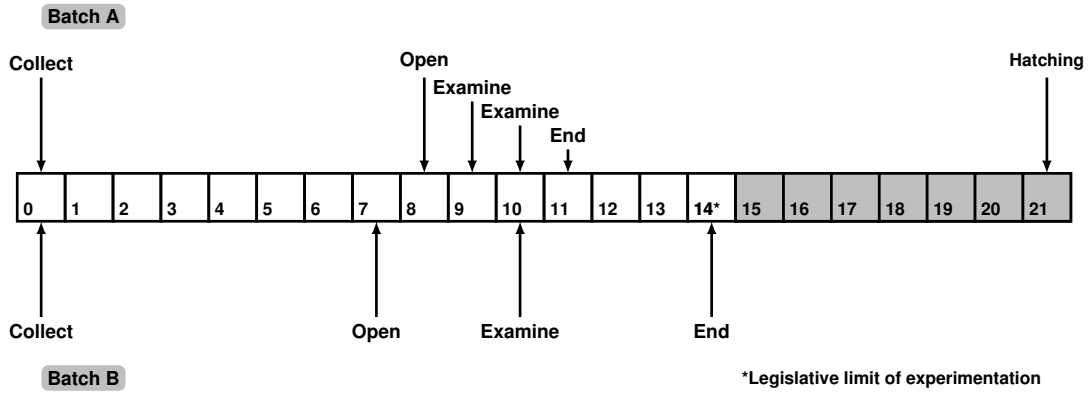


Figure 6.3: Timeline for batches A and B in days of incubation - days after collection.

6.5 Experimental procedure

6.5.1 Opening procedure

The outer surface of the eggs was examined for gross contamination, then the shell surface was cleaned with 70% ethanol. Eggs were candled using an LED light to identify the boundaries of the airspace and these were marked on the shell, Fig 6.4. The shell was stabilised by placing *Microporous tape* (3M) over the intended cut line. This reduced the production of shell fragments while opening. A selection of sterile instruments, including thumb forceps and small dissecting scissors were. First, the shell was pierced to create a small hole that allowed scissors to be introduced to remove a section of shell. Second, the opening was enlarged by cutting through the shell and overlying tape with scissors, separating the top part of the shell. This allowed access to the interior of the egg exposing the CAM. The fibrous inner shell membrane becomes more intimately associated with the CAM as development proceeds but is separate from the shell in the airspace. This membrane was separated hydraulically from the underlying chorio-allantoic tissue by injecting a 1 mL bleb of sterile PBS + penicillin streptomycin. In one group this membrane was removed prior to implantation and in another it was left intact. An opened egg with the CAM visible showing the shell membrane along with the normal appearance of the CAM can be seen in Fig 6.5.

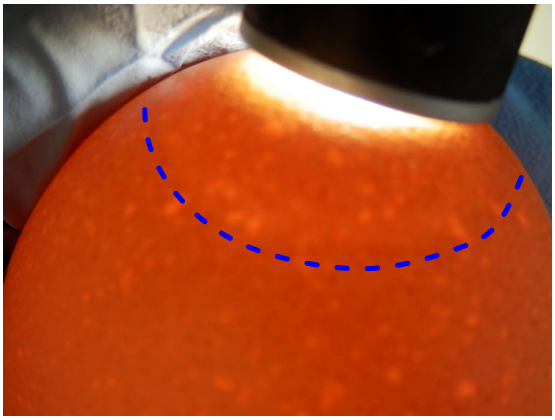


Figure 6.4: Boundary of the egg airspace visualised by candling (dashed line), annotation added for clarity.

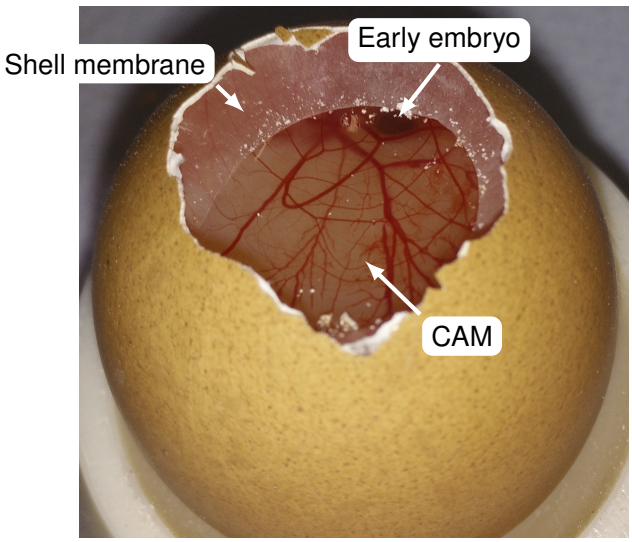


Figure 6.5: Open egg showing the the edge of removed shell membrane.

6.5.2 Implantation procedure

The CAM was examined and an implantation site was selected to avoid major (macroscopic) blood vessels as can be seen in Fig 6.6. The implantation device was lifted with forceps, and the lancet was used to create an injury in the CAM through to the albumen. The needle was inserted to the level of the stimulating electrode bringing the end of the device into contact with the full thickness of CAM. The opening in the shell was then closed with Microporous tape (3M) to partially restore the airspace micro-environment. The egg was then replaced in the incubator.

6.5.3 Monitoring

Eggs were periodically monitored for progress. To do this they were removed from the incubator, the tape was loosened from the shell window in order to inspect the CAM surface. Visual appearance was assessed and the embryo and vessels were observed for life signs. Any embryonic mortality was recorded. A living embryo could be identified by observing embryo movement, heart beat or pulse within the CAM vessels. An example setup for opening/implantation is shown in Fig 6.7.

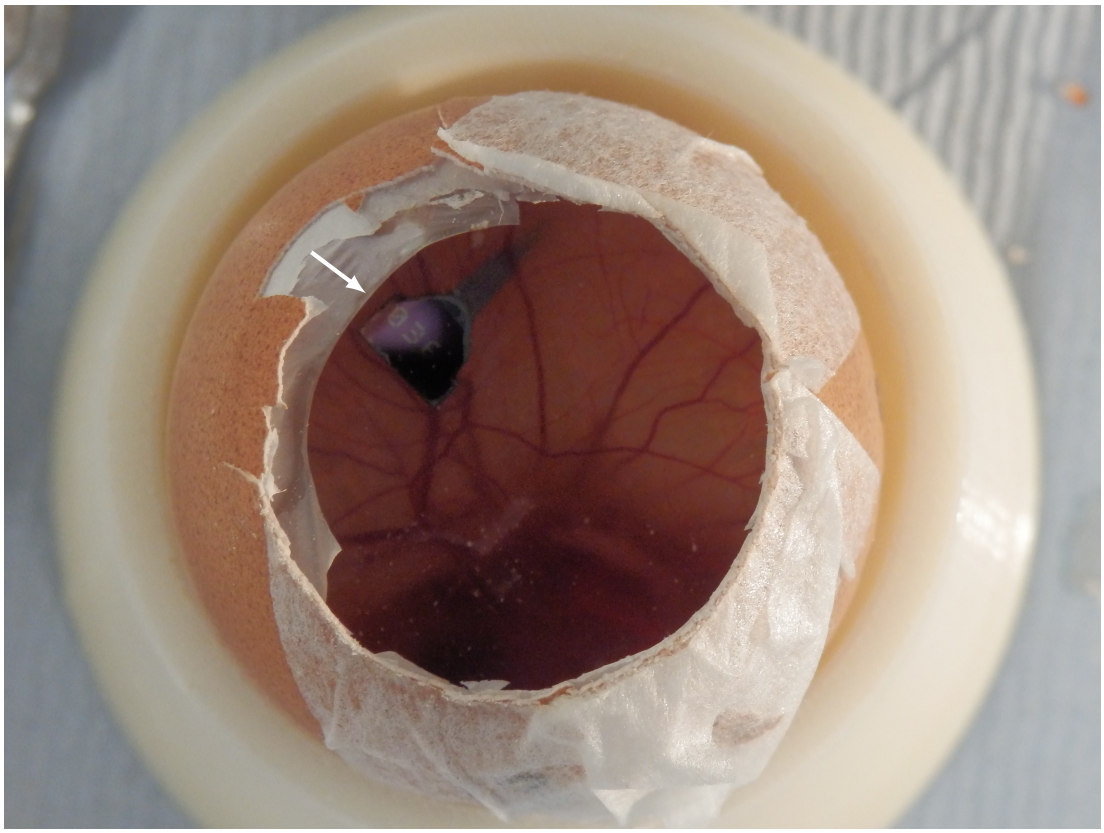


Figure 6.6: An opened egg with the shell membrane removed, implanted with a needle test structure (arrow).

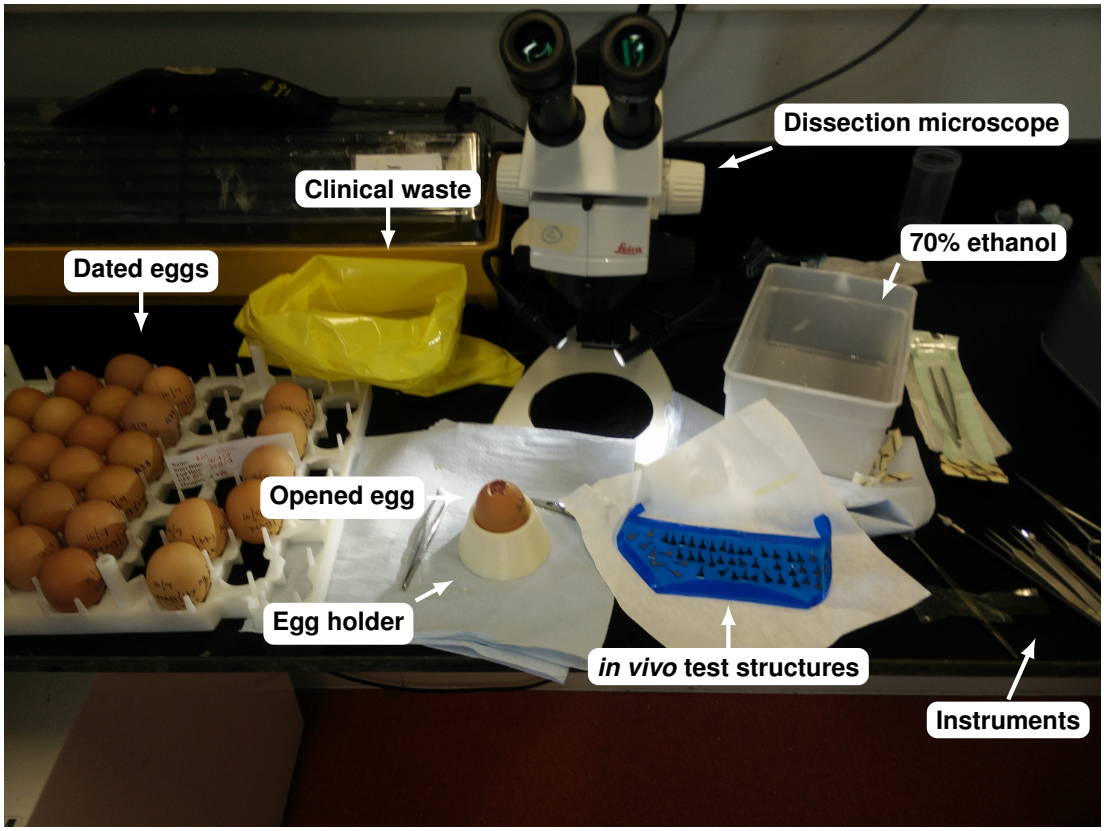


Figure 6.7: Setup for egg opening and implantation.

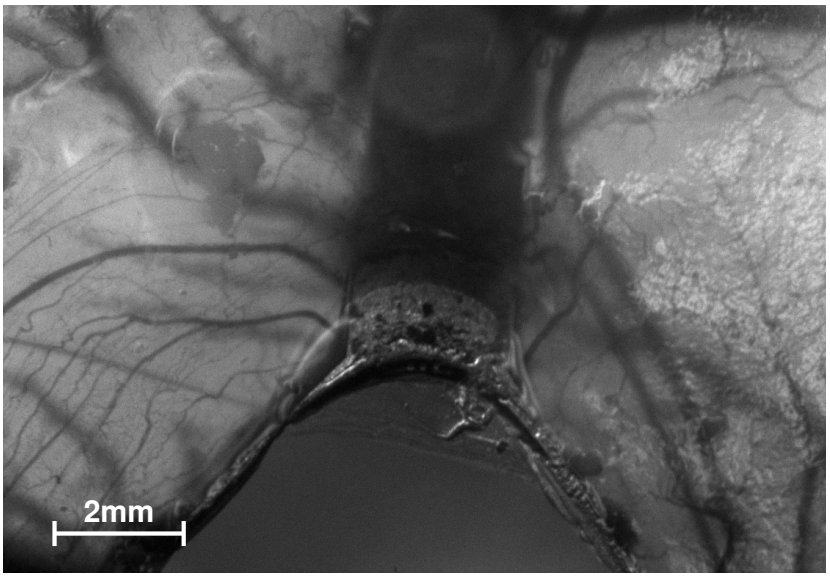


Figure 6.8: Live image implant site.

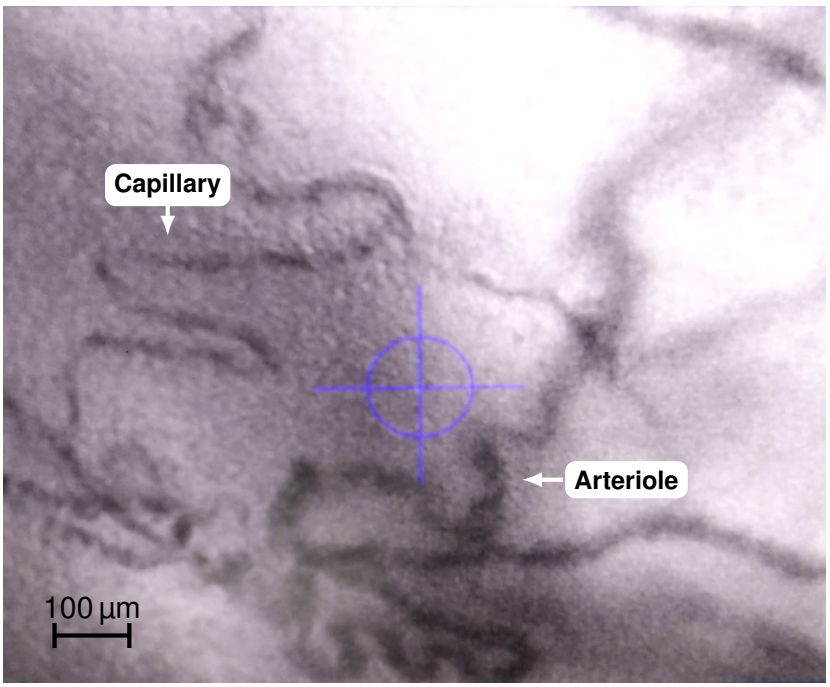


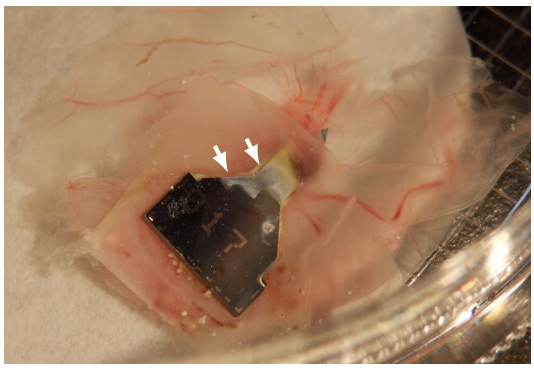
Figure 6.9: Live image of the surface of the CAM showing the micro-vasculature.

6.6 Live imaging

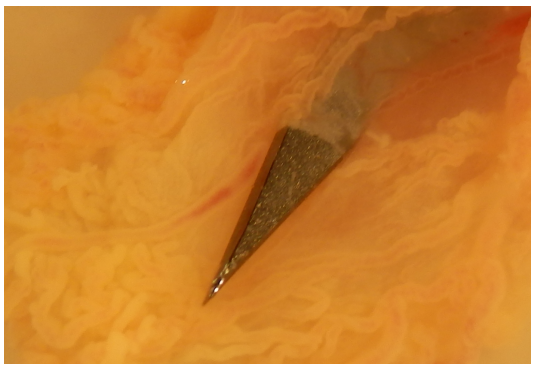
During implantation experiments, individual eggs were studied using a live imaging system, comprising a visible and fluorescent incident light microscope with a environmentally controlled stage permitting an egg to be incubated for time lapse experiments. A closer view of the interface between the implant and surrounding tissue, where it enters the CAM, can be seen in Fig 6.8, and a wider view in Fig 6.20. Figure 6.9 shows an example image from the surface of the CAM. Both capillaries and arterioles are visible, the image is a video frame where individual blood cells can be discriminated.

6.7 Collection and histology

All eggs were examined at the end of the experiment to ascertain the state of the embryos. Where eggs had not already been opened, this was done to facilitate these observations prior to euthanasia. At the end of the experiment, the region of the CAM containing the implantation site was carefully dissected out using scissors and forceps. A piece of filter paper was cut to fit into a plastic petri dish, which was then filled with neutral buffered formalin. The sampled tissue was placed into the saline on top of the filter paper. The paper



(a) Implant with *in-situ* proliferative tissue reaction and adhesion at the wound site (arrows).



(b) Implant viewed from the deep (allantoic) epithelial surface of the CAM.

Figure 6.10: Excised egg CAM tissue showing implants.

was then manipulated along with the margins of the tissue using the forceps to flatten the tissue and centre the implantation site, Fig 6.10. The implant was then carefully removed. After disruption of the membranes, embryos became non-viable and were humanely killed by decapitation. Egg waste was disposed following laboratory protocols for genetically modified clinical waste, implants were placed into a sharps container for disposal.

Samples were then transferred to the pathology department (Edinburgh Veterinary School) where they were processed. The plane of section was kept nominally the same as the tissue plane and serial sections were taken and stained with either Haematoxylin & Eosin (H&E) or Masson's Trichrome stain. In one case, that had been implanted with a centre point needle, a sequence of 100 sections was taken through the tissue. Of these 100, 34 sections, distributed over the interval, were stained with H&E and numbered sequentially allowing an image z-stack to be formed.

6.8 Microscopy

Slides were imaged at the Roslin bioimaging facility. Slides were first examined using an upright compound microscopes using Köhler illumination, and images were captured and processed with ImageJ[280]. This allowed examination over several different magnifications from gross structure, to individual cells along with some intra-cellular structures. Scanned images of whole slides, representing a section through the entirety of collected specimen, were also collected and, where sequential sections were available, formed into z-stack volumes. Slides were scanned using a Coolscan 5000 slide scanner (Nikon), which produced

images with dimensions: 5782x3946 pixels and a 6.35 µm pitch sufficient to resolve tissue layers but not detail of individual cells.

6.9 Measurement of responses

In eggs surviving to the end of the experiment, Histopathology was the main intended measurement. This would incorporate quantification of the tissue response surrounding the implant. The procedure was designed to allow a number of different visualisation mechanisms.

As the eggs expressed a fluorescent protein within their macrophages, this permitted these immune cells to be visualised in both live imaging, whole tissue mounts and, under certain conditions, histology.

The two histological stains employed offer different staining properties. H&E is commonly used as a general purpose stain, allowing cell type differentiation within and identification of some extracellular structures in histological sections. Masson's Trichrome stains fibrous connective tissue material, that contains collagen, a blue colour, an example of which can be viewed in Fig 6.17c.

6.10 Candling

The technique of candling (examining light transmitted through the egg) was used to predict the viability of eggs as well as to determining the position of the airspace (Fig 6.4) and was applied to all eggs. Eggs were candled on collection and a record made of evidence for fertilisation and presence of an embryo. The egg was rotated in the hand, illuminated and observed from both the top and bottom so that any structures in the vicinity of the shell, visible as shadows projected on the wall of the shell, could be detected. Observations were classified progressing in order of increasing precedence from: no evidence ($\varnothing$), visualisation of membranes, visualisation of yolk, visualisation of features of an embryo. The highest precedence observation was then recorded and could be compared with the state of the egg on opening.

6.11 Candling accuracy

The distribution of results of egg classification by candling, along with the ground truth discovered on opening is presented in Fig 6.11. Eggs where no evidence was seen, combined with those where membranes were visualised, accounted for 70% of observations. In the remainder, yolk or embryo structures were recorded. An observation of embryonic structures was the strongest signal of a living embryo (100%).

However, as the majority of the embryo population was viable it is clear the technique used failed to adequately identify this group. Retrospective analysis of the data available would suggest the best way to use these observations in practice is to group the lower and upper precedence observations into a binary classification test. Quantifying this test would be done through sensitivity and specificity, the formulae for which are shown in Equations 6.1 & 6.2.

$$\mathbf{Sensitivity} = \frac{\mathbf{P}(\mathbf{A}|\mathbf{Yolk} \cup \mathbf{Embryo})}{\mathbf{P}(\mathbf{A})} \tag{6.1}$$

$$\mathbf{Specificity} = \frac{\mathbf{P}(\mathbf{U} \cup \mathbf{EED}|\varnothing \cup \mathbf{Membranes})}{\mathbf{P}(\mathbf{U} \cup \mathbf{EED})} \tag{6.2}$$

Where A, U and EED refer to the embryo states: Alive, Unfertilised and Early embyronic death. $\varnothing$, Membranes, Yolk and Embryo refer to candling observations: no evidence observed, extra-embryonic membranes, yolk structures, and embryonic structures.

This approach lead to a 90% specificity, with the current data, but a poor sensitivity on the test at 33%. Observing only the low precedence signs (nothing observed and membranes) on candling successfully collects non-viable embryos, but likely misclassifies many viable embryos.

6.12 Egg mortality

Recordings were made of the state of each embryo when the shell was opened. Embryos were classified as living based on observation of embryonic heart beat, embryonic movement or pulsation of the CAM blood vessels. Dead embryos were subclassified on the basis of stage of embryonic development. Embryos at an equivalent stage to the live em-

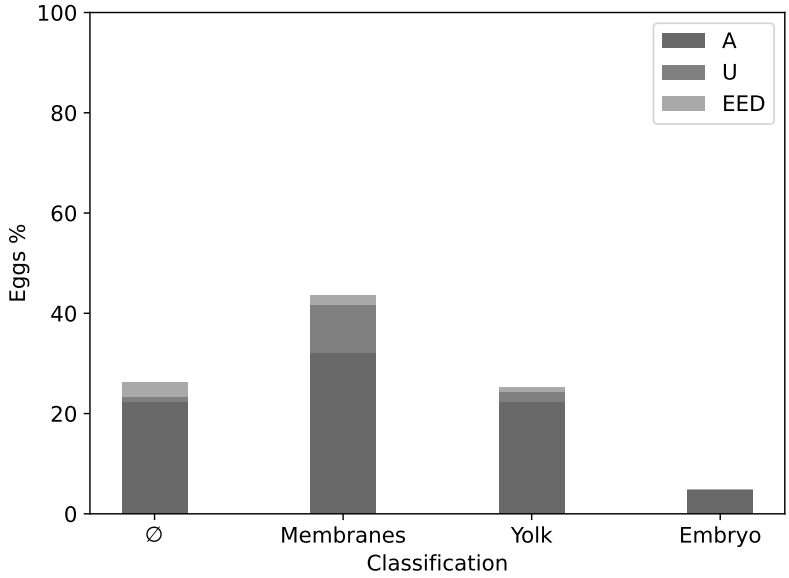


Figure 6.11: Candling classification and egg state on opening. Classes in order of precedence: embryonic structures, yolk structure, membranes and nothing observed (∅)

bryos were simply classed as dead, whereas those that had stalled at some earlier point were classed as early embryonic death (EED). All of the eggs showed evidence of structural organisation consistent with fertilisation. Figure 6.12 shows the state of all eggs used, approximately 80% (n=103) of eggs were alive, across both batches on the day of opening and were judged viable for use in experiments. All dead embryos discovered on opening were at a developmental stage: qualifying as EED. Consequently, no category for other mortality, annotated (D) elsewhere, appears in Figs 6.11 & 6.12.

6.13 Embryo survival

Embryos that were viable were subject to different experimental conditions and the proportion of mortality along with timing was recorded together with an assessment of cause, see Section 6.14. In addition to the two key interventions necessary for the function of the model (opening and implantation), data was collected on several other effects. These included: shell membrane removal, day of incubation (7 and 8) and the influence of (chilled) storage. Additionally, the timing of mortality was tracked with daily assessment of survival. In the implantation group, parameters of each implanted needle test structure were also recorded with the intention of correlating with tissue response. This was in order to opti-

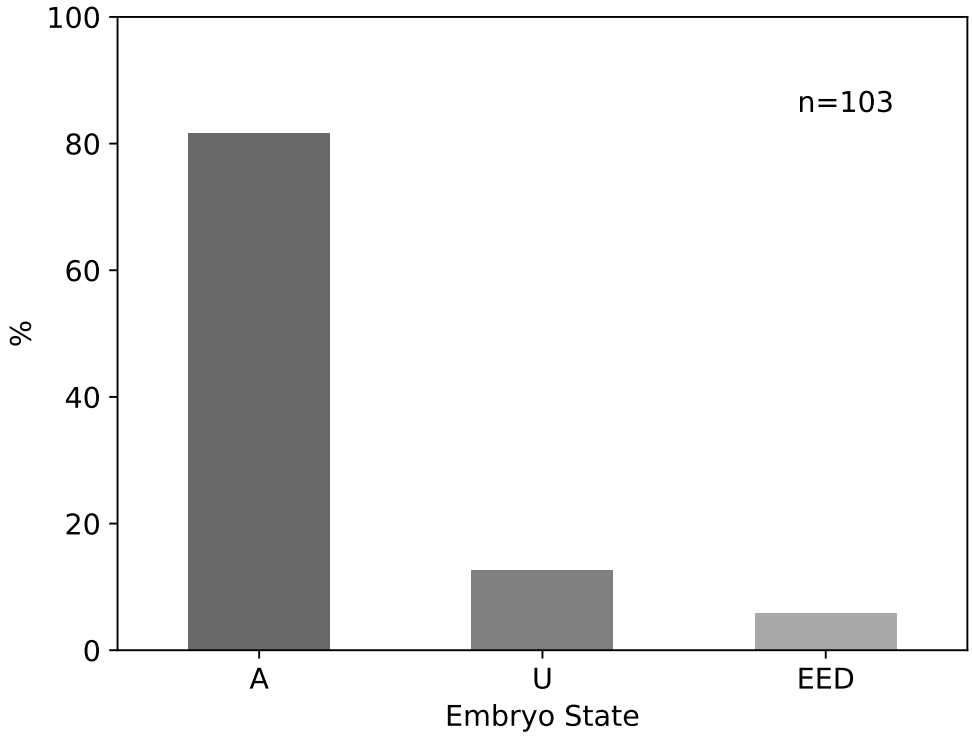


Figure 6.12: Egg state on opening: **A**-Alive,**U**-Unfertilised,**EED**-Early embryonic death.

mise parameters of the *in vivo* platform. As survival was the only measured outcome, data representing an incomplete central composite design (CCI) was collected.

6.13.1 Storage

Storage at temperatures over a wide range below physiological temperature (≈38 ℃) can be used as a technique to reversibly halt egg development, over timescales up to 35 days[375]. Embryonic development can be restarted by a two stage process of re-equilibration to room temperature followed by incubation as normal. This was judged to be potentially useful to even out supply of eggs for experiments, which were ordered and delivered in larger batches. Incubated eggs without opening resulted in only a single a single mortality (n=40) combining storage and immediate incubation, showing no effect on normal egg development of this process. Batch B eggs were also stored in advance of opening and implantation, see Section 6.13.2.

6.13.2 Batch comparison

Some tentative comparisons can be made between the two batches of eggs representing opening of day 8 (Batch A) and 7 (Batch B). Survival rates to the end of the experiment, shown in Table 6.1, were similar in both implanted and opened eggs suggesting that opening time (which corresponds to level of development) is less of a significant factor in egg survival. This comparison however, is confounded in that batch B eggs were subjected to storage prior to opening. Despite this, while it is possible there may be an influence on opening and implantation survival associated with egg storage the lack of effect in controls suggests that this is less likely to be a significant influence.

6.13.3 Effects of implantation and opening

A Kaplan-Meier plot shown in Fig 6.13 compared survival in implanted versus opened (control) eggs across the period of incubation. The two batches of eggs had differing opening times and endpoints, but were compared at identical points in gestation and embryonic development. Data from both batches are presented together over the interval covering day 8 to 11. Where only batch B data was available this has been indicated and batch A has been considered right-censored after this time point, which is represented by discontinuities in the curves. No mortality was seen in the first 24 hours in batch A controls, whereas there was 56% loss in the implant group over the same period. Subsequently, there is a precipitous drop in survival in the implanted group. Daily mortality continued in both groups with the implant group consistently showing lower survival than the control. On day 10 there was broad agreement between the two batches with only 35% of the implants remaining versus 77% of the controls in batch A and 33% versus 83% in batch B. Beyond day 11 when batch A was collected the data is right-censored with batch B data showing 17% survival to the end for implants versus 33% in the open controls.

Collected statistics for survival to experimental end and breakdown of mortality are shown for implants compared with controls in Table 6.2 and more generally in Table 6.1.

Batch	Alive	Dead					Total
		Purulent	Vascular	Dessication	Idiopathic	Subtotal	
Batch A - implants	5 (20.0%)	3 (12.0%)	2 (8.0%)	-	15 (60.0%)	20 (80.0%)	25
Batch B - implants	1 (16.7%)	-	-	3 (50.0%)	2 (33.3%)	5 (83.3%)	6
Batch A - opened	4 (57.1%)	1 (14.3%)	-	-	2 (28.6%)	3 (42.9%)	7
Batch B - opened	2 (33.3%)	-	-	1 (16.7%)	3 (50.0%)	4 (66.7%)	6
Batch B - incubate	25 (96.2%)	-	-	-	1 (3.8%)	1 (3.8%)	26
Batch B - incubate(after storage)	14 (100.0%)	-	-	-	-	-	14
Totals	51 (60.7%)	4 (4.8%)	2 (2.4%)	4 (4.8%)	23 (27.4%)	33 (39.3%)	84

Table 6.1: Statistics for survival and cause of death in eggs from two experimental batches depending on treatment. Causes of death discussed in Section 6.14.

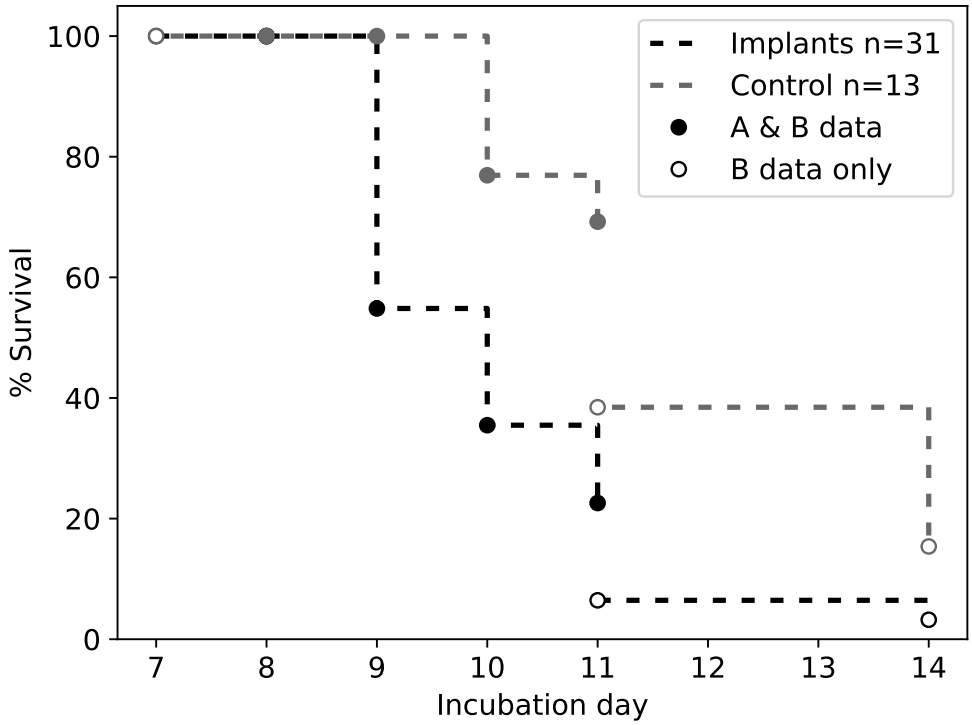


Figure 6.13: Kaplan-Meier curve showing embryo survival of eggs implanted with biosensor needle test structures on day 7/8 of incubation. Control eggs were opened and stored in the same condition without implantation of structures. Data from two batches of eggs are combined where the data overlapped.

Treatment	Alive	Dead					Total
		Purulent	Vascular	Dessication	Idiopathic	Subtotal	
Implants	6 (19.4%)	3 (9.7%)	2 (6.5%)	3 (9.7%)	17 (54.8%)	25 (80.6%)	31
Opened	6 (46.2%)	1 (7.7%)	-	1 (7.7%)	5 (38.5%)	7 (53.8%)	13
Totals	12 (27.3%)	4 (9.1%)	2 (4.5%)	4 (9.1%)	22 (50.0%)	32 (72.7%)	44

Table 6.2: Statistics for survival (to the end of experiment) and cause of death in implanted eggs against opened controls.

6.13.4 Membrane disruption

The effects of shell membrane removal are collected in Table 6.3. There was no apparent association with increased mortality in the implanted group at 19% (intact) and 20% (removed) survival. Totals across the two membrane treatments showed survival as 20% intact and 29% removed respectively.

Membrane		Outcome						Total
		Alive	Dead					
			Purulent	Vascular	Dessication	Idiopathic	Subtotal	
Intact	Implants	4	3	1	-	13	17	21
	Opened	1	1	-	-	1	2	3
	Total	5	4	1	-	14	19	24
Removed	Implants	3	1	1	3	7	12	15
	Opened	4	-	-	1	4	5	9
	Total	7	1	1	4	11	17	24

Table 6.3: Survival outcomes (to the end of experiment) and cause of death based on shell membrane disruption

6.13.5 Needle parameters

Survival and cause of mortality for implants based on the parameters of the implanted needle test structures are collected in Table 6.4. As can be seen the majority of implants were drawn from the centre point of the central composite (CCI) experimental design as discussed in Chapter 5. This bias is inherent in the experimental design as a mechanism to characterise variance of the response. However, centre points were also deliberately prioritised in the second batch of eggs. This was as a consequence of the high levels of mortality observed in the batch A; in order to focus the experimental power onto a single structure variant. Insufficient data exists to make any meaningful comparison between structures. The CCI column in Table 6.4 shows the number of surviving embryos required to complete the design and begin to optimise the needle parameters (N=54).

6.14 Pathologies

When an embryonic death was discovered, the egg was visually examined, in an attempt to ascertain a cause of death. This process in itself had inherent limitations, still allowed each case to be ascribed to one of several causes. These causes were kept distinct from EED and unfertilised loss of eggs in the experiments, as these resulted from external factors in the egg production process. If no cause could be immediately identified then the death was labelled as idiopathic. In these cases the tissue and embryo appeared fresh and identical to living specimens - with the exception of absent life signs. The three other causes were: purulent, desiccation and vascular.

Purulent eggs were those where the albumen had become opaque and malodorous,

Parameters		Outcome						Total	CCI
Shank Width(μm)	Aspect Ratio	Alive	Dead						
			Purulent	Vascular	Dessication	Idiopathic	Subtotal		
800.000000	3.000000	-	-	-	-	1	1	1	3
1078.248558	0.878680	1	-	-	-	1	1	2	4
	3.707107	1	-	1	-	-	1	2	4
1750.000000	0.000000	-	1	-	-	1	2	2	3
	0.878680	1	1	-	-	-	1	2	4
	3.000000	4	-	1	3	17	21	25	30
	3.707107	-	1	-	-	-	1	1	4
	4.000000	-	-	-	-	-	-	-	3

Table 6.4: Survival outcomes (to the end of experiment and cause of death by implanted structure parameters, parameters were drawn from a central composite design. The row containing the centre point of the design (and majority of implantations) is highlighted.

although, interestingly, hydrogen sulphide was not a noticeable component of this odour in any of the eggs. This change implied significant degradation of the internal structures concurrent with bacterial overgrowth. It was assumed the cause of mortality was that the embryo had succumbed to environmental infection. The risk of microbial access to the egg was markedly increased due to removal of the egg shell and membranes that normally act as barriers to such contamination.

Desiccated eggs appeared to have lost a large quantity of water to the environment. It was presumed that this preceded and was the cause of embryonic death.

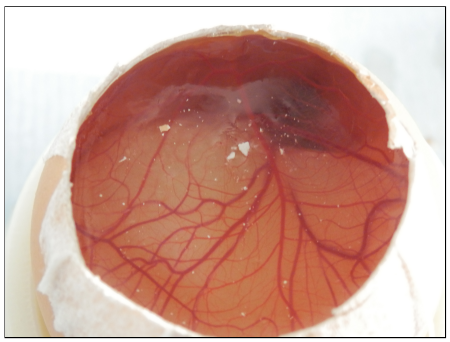
Vascular mortality was classified when significant haemorrhage was apparent, in particular in the region neighbouring the implant site (peri-implant). It was assumed here that disruption to the blood supply was responsible for embryonic death. Implantation sites were selected away from macroscopic CAM vessels as described in Section 6.5.2. However, as microscopy of the implant site in Fig 6.6 demonstrates, the density of micro-vasculature present in proximity to the implantation site made some vascular disruption inevitable.

Examples of the appearance of each pathology are illustrated in Fig 6.14. Cause of death are broken down in each of the data tables for the experiments. Table 6.1 provides an overview of causes of death across all experiments. Of the 33 recorded deaths, across all experiments, 70% (n=23) were classified as idiopathic, while the remaining 10 (30%) were classed as purulent, vascular or desiccation: 12%, 6% and 12% respectively.

6.15 Histopathology

Histopathological sections from select implanted eggs, that survived until the end of the experiment, were examined. Locating the implantation site within the images proved a non-trivial task. The low thickness of the tissue in the plane of section meant that tissue the undulated through the plane (orientation artefact), which combined with artefacts that are inherent to tissue processing (shrinking and tearing) produced many areas that appeared to be plausible injury sites. Despite these issues many structures could be identified within the histological sections. In one case using gross images to correlate the implant site and in another using images and Z-stack imaging.

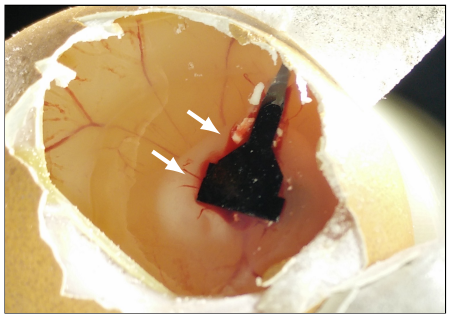
Some example sections are shown in Figs 6.15a and 6.15b demonstrating visualisation



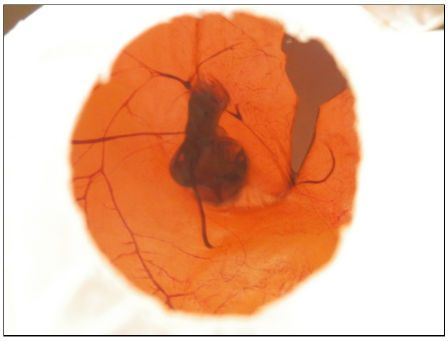
(a) Normal appearance of healthy CAM.



(b) Evidence of bacterial overgrowth.



(c) Peri-implant haemorrhage (white arrows).

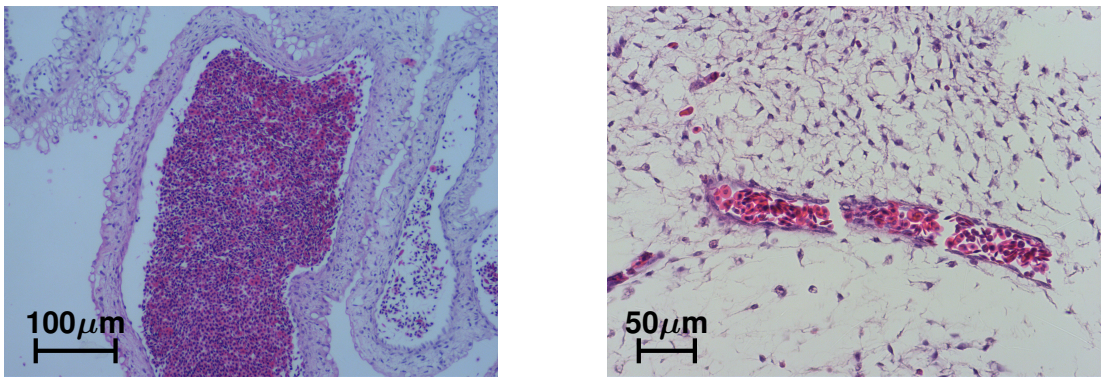


(d) Dessication.

Figure 6.14: Examples of the typical presentation of each egg pathology.

of the vascular structures in the CAM. A cross-section of normal CAM is shown in Fig 6.16 and annotated with each of the three layers: The mesoderm and the chorionic and allantoic epithelia. The chorionic layer appears thicker than in reality in this image due to obliquity of the plane of section.

An example is shown where a wound site was tracked from a macroscopic image of tissue in fixative just after collection, Fig 6.17a (red box). On histopathology images this wound site was found, by comparing the shape recognition of a nearby blood vessel, Fig 6.17b. A higher magnification image of a cross-section structure is shown in Fig 6.17c. This section was stained with Masson's trichrome and shows a transverse view of an arteriole. The blue staining shows collagen forming part of the ECM, round cells can be seen infiltrating the mesodermal layer of the tissue showing an immune response of the tissue. This reaction can be compared against the normal cross-section of the CAM that is shown in Fig 6.16. Excess keratin (pink staining) can also be seen on the chorionic epithelial surface, which appears hyperplastic. This keratosis is likely a consequence of the local reaction and irritation caused by the implant.



(a) Artery - H&E

(b) Arteriole - H&E.

Figure 6.15: Histopathological sections of CAM of vascular structures showing transverse section of an artery and longitudinal section of an arteriole.

6.15.1 Z-stack imaging

In order to aid in identification serial sections were produced through the tissue and scanned with a slide scanner. An example slide image is shown Fig 6.18, annotated with the major identifiable structures. Global registration of the images was performed using ImageJ[280]. This process ensured that most structures were at the same points within subsequent images, although artefacts such as shrinking, tearing, folding and curling and mounting distortion prevented perfect registration of all local features[376]. A 3D rendering of all the sections was visualised in paraview[377] and prominent vascular structures were identified. Segmentation of the vascular network was then carried out using the medical imaging analysis software 3D Slicer[378,379] using the "SlicerMorph" extension[380]. An annotated rendering of the 3D volume produced is shown in Fig 6.19 with vascular structures segmented in red. Two main bifurcation features in the vascular structures, labelled "A" and "B", can be identified within this data. These have been matched, both in terms of shape and by comparing scales to live images that showed both vascular structures of the CAM and the implant site itself. The positions of these structures are shown in Figs 6.20 and 6.21. Through this process, and using the *Chalaza* (an anatomical structure that connects the CAM to the embryo) as a reference point, it was possible to identify the implant site on several of the sections. The site is shown in Fig 6.22 demonstrating the viability of a second methodology for identification of the implant site enabling analysis tissue reaction and and a route to quantifying the vasculature surrounding the implant.

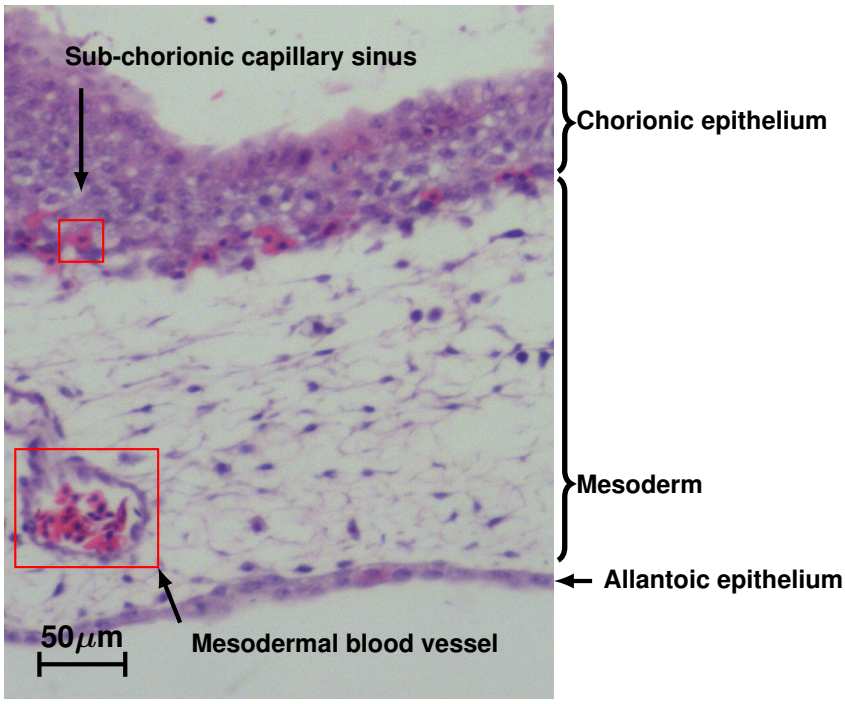
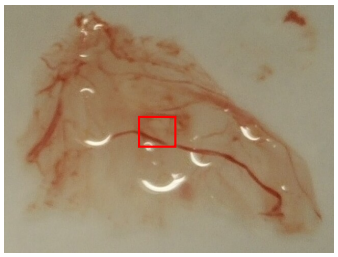
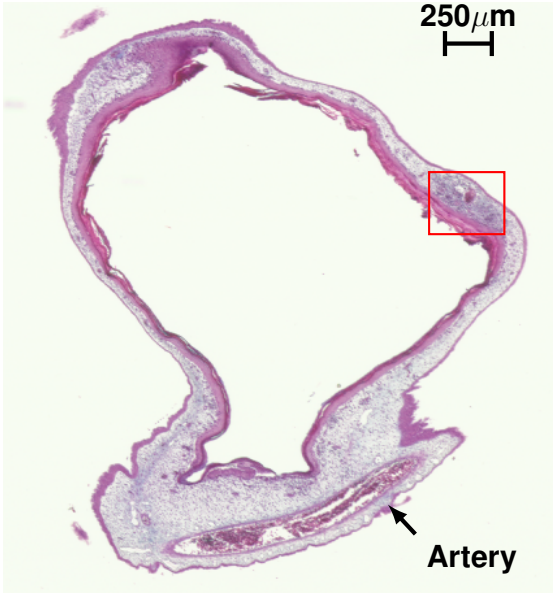


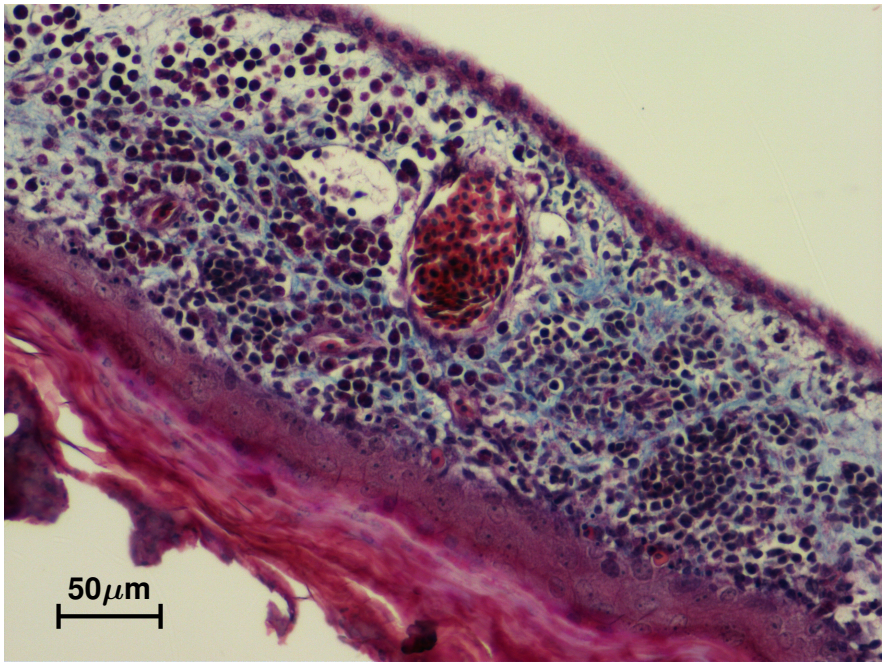
Figure 6.16: Cross-section of normal CAM - H&E.



(a) CAM in fixative just after dissection. Implant site and neighbouring blood vessel are visible (red box).



(b) Implant site from whole-slide scan stained with Masson's trichrome.



(c) Magnified image of red box in (b) showing a cross-section of implant site, stained with Masson's trichrome.

Figure 6.17: Exised CAM tissue and implant site at three magnifications.

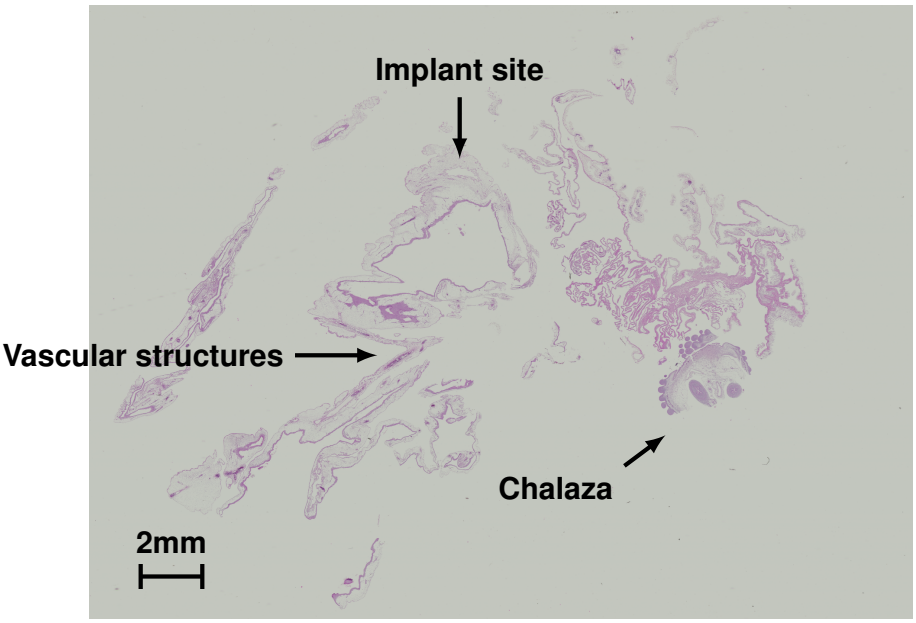


Figure 6.18: Example whole-slide image of CAM, H&E.

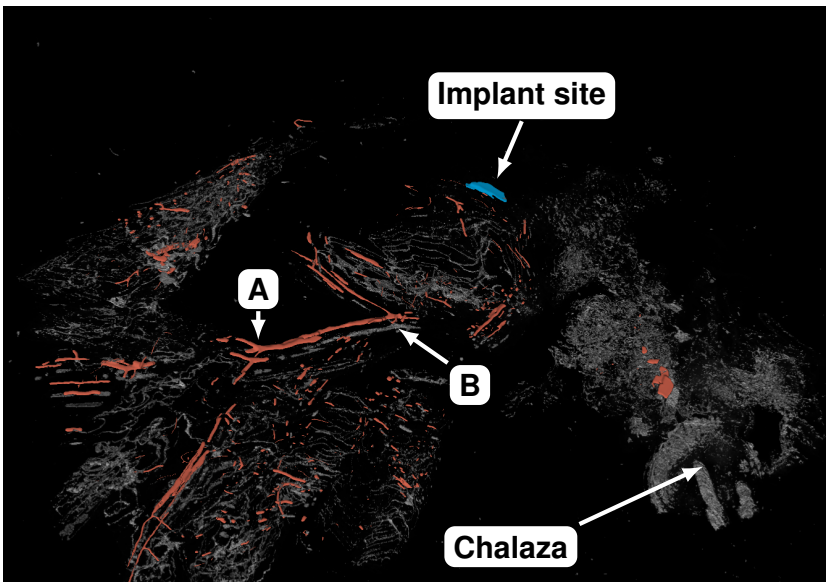


Figure 6.19: 3D reconstruction of z-stack whole-slide scan. Vascular structures have been segmented (red) along with the identified implant site (blue). A and B bifurcations are used were used for registration to live images.

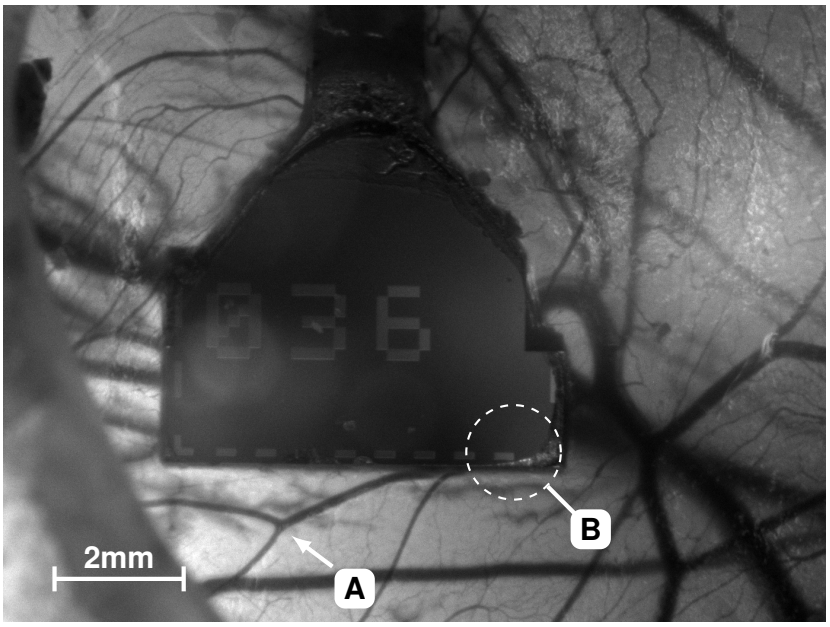


Figure 6.20: Live image of implanted test structure (central design), with surrounding vascular network visible.

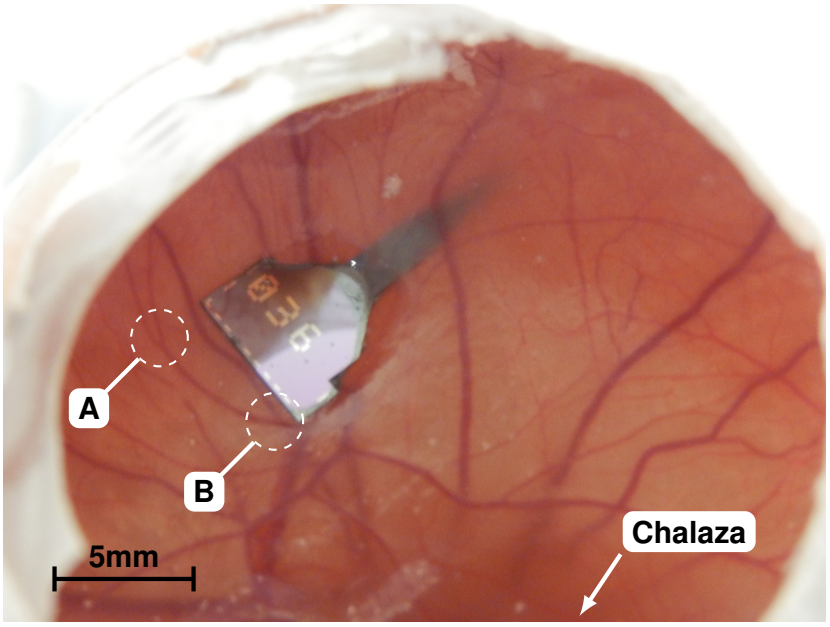


Figure 6.21: Test structure (central design) *in-situ* examined during experiment.

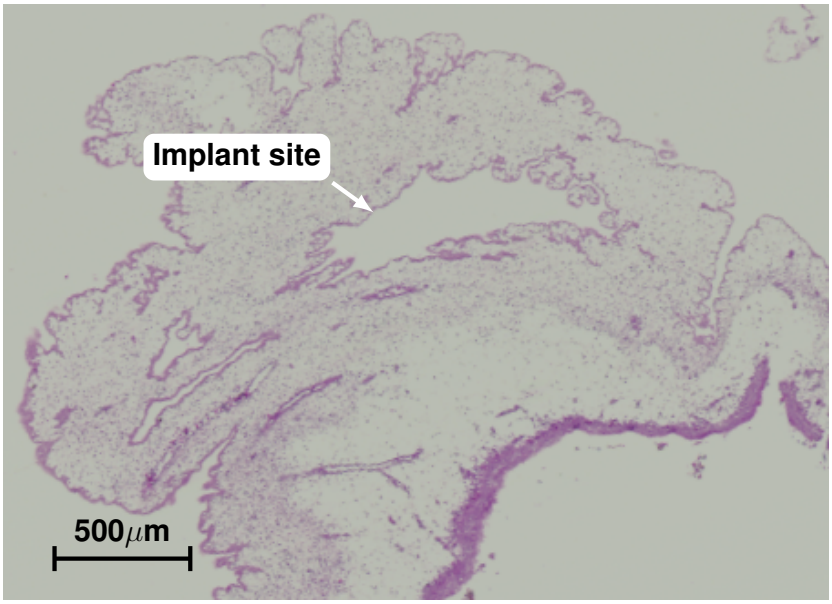


Figure 6.22: Identified implant site on whole-slide scan.

6.16 Discussion

Translation of novel biosensors and their constituent biomaterials, requires progression from biophysical, bench-based tests, and *in vitro* work, with cell culture to more representative *in vivo* models. Many cell culture approaches have the inherent limitation of using a single cell type, in many instances drawn from an immortalised cell line. Such lines often possess significant behavioural differences compared to their wild-type counterparts. Models must be able to recreate, to some degree, the interplay amongst multiple cells types and the environmental complexity found within tissues and organs. CAM assays are cheaper, as much as a factor of 100 more cost-effective, than using mice[381]. Due to its immobility it is also easier to work with than other animal models.

CAM as a model

The CAM is a complex temporary organ[382], suitable to early stage biomedical investigations and as an *in vivo* model for biofouling and FBR. CAM has been has found use in virology, wound healing assays[383], angiogenesis and vascular function[384,385], drug and toxicology testing[386], infection[387] and as host tissue for tumour xenografting in cancer biology[388,389]. Additionally, various forms of the CAM assay have been applied to biomaterial evaluation[390,391,392,393] and biosensor testing[394,155].

The CAM is one of the extra-embryonic tissues (along with the yolk sac and amnion). During a normal hatching the CAM is left attached to the shell[382]. It forms at day 6-7 by fusion of the chorion and allantois. The vascular supply comes from two arteries and veins and is subject to continual vascular growth and development. Due to the 2D nature and function of the CAM, primarily as an organ of exchange, its development is best measured by area of coverage. By day 14 the CAM covers 65 cm^2 of area[395], providing a large functional surface, some fraction of which can be co-opted for experimental manipulation without adversely influencing the developing embyro. The CAM forms a natural two-dimensional tissue analogue with highly vascularised tissue sandwiched between two epithelial layers, one interfaced with shell membrane (or air when separated) and the other bordering fluid. This allows visualisation of a functioning and developing vascular system, seemingly ideal for early assessment of biomaterials. Chick CAM is one of the models

suggested for intravital monitoring in biomaterials. The others include mice and zebrafish, which can be investigated with a number of microscopy techniques[396]. Each model has advantages and disadvantages, for example mice are mammals and are the main species used in early translational research, but are more expensive in use and require a higher degree of ethical oversight. Zebrafish and chickens on the other hand have physiologies and anatomical structures further evolutionarily separated from humans.

The CAM, if correctly harnessed, represents a ready made platform equivalent to organoids and organ on a chip approaches that seek to bridge the gulf between bench and *in vivo* testing on route to clinical testing and commercialisation.

Zebrafish embryos do show macrophage recruitment into wounded tissue, whereas this is not a feature of embryonic mice and chickens[373]. In addition to chickens (*Gallus domesticus*), CAM structures are also found in other egg laying species. Eggs vary in size making some less appropriate for *in ovo* techniques and some, such as ducks have a much longer gestation period[397], potentially lengthening the experimental window[398]. Behaviour of tumour cells in the CAM have performed equivocally against xenografted tumours in rats[399].

The low level of development of the embryo prior to 75% of gestation (15 days) precludes significant welfare concerns and consequently less regulatory oversight. The CAM is not innervated[399] and so manipulations do not cause pain and at early stages of embryogenesis the embryos are judged not to be capable of pain perception. As a result chick eggs and CAM make good 'alternative' models[400], often with no licensing requirements in many countries if the experiments do not run to, or near, hatching. It is the onset of probable pain perception that determines the experimental window. It is notable that CAM models from alternative avian species may have attractive properties depending on the application. As an example, longer gestation times, potentially extend the time period for experimental manipulation of the CAM[398]. When testing biomaterials, samples are often simply placed onto the CAM surface, whereas in this work devices are placed into a wound[391]. The CAM undergoes intense embryological development over the early period of gestation. This coincides with the interval of experimental manipulations (day 4–10)[395] and must be taken into account when interpreting results and inform any attempts at translation of results to mammalian models and clinical application.

Opening of the airspace that naturally forms at the blunt pole of the egg for *in ovo* manipulation was first used in a modern form for screening chemicals for toxicity[386] and was the approach taken in this work. An artificial airspace can, alternatively, be developed on the side of the egg by orienting the egg to move the airspace[390]. At early stages (day 3 or 4) the entire CAM can also be removed from the shell and placed in a watch glass, or a number of other containers, for culture. This *ex ovo* approach gives access to the entire developing CAM at the expense of greater equipment requirements and a much greater need for environmental control and aseptic handling[401].

Macgreen eggs are produced by transgenic chickens. Expression of fluorescent protein is linked to the promoter region of colony stimulating factor receptor, which is conserved across avian, aquatic (zebrafish) and mammalian species[373]. Alternative transgenics such as MacRed express a different fluorescent protein or can track alternative aspects for chick immune development. Avian immunity associated with innate responses to infection and wounding include a similar cadre of cell types to mammals. Macrophages, natural killer cells, thrombocytes are all found along with heterophils, which are capable of phagocytosis and are similar to mammalian neutrophils[402]. Birds lack factor XII - intrinsic factor contact activation, this may be significant in early stage implantation in the CAM[30]. Cell-mediated immunity appears in the second week of gestation and at least from day 12 and definitely by day 14[395]. However, innate response to injury does not require cell or humoral recognition. Non-specific inflammatory reactions occur after day 15 and grafted tissue survive is viable to day 18, after which immune rejection takes place. At this stage bacterial invasion and allografting of foreign immune cells can elicit a reaction containing lymphocytic immune cells on the CAM[403,373].

The responses of the CAM vary not only in magnitude, but by characteristics of the reaction and according to the specific biomaterial[392]. Commonly reported changes include: proliferation of the chorionic epithelium, reaction of the mesoderm with inflammatory infiltrate, multinucleated giant cell formation and development of connective tissue, haemorrhage and (re)growth of blood vessels[392]. Excisional wounds created in CAM tissue follows a path through: inflammatory infiltrate, chorionic hyperplasia, vascular density increase (around 3x normal) and scar tissue formation characterised by high fibroblast numbers and fibronectin deposition. A large amount of granulation tissue accumulates within sev-

eral days after the creation of a wound (at day 8)[404]. Capsule thicknesses around 100 µm have been reported to develop between day 8 and 14[156]. Such changes occur sequentially over several days following wounding of the CAM[383]. Similar observations were made with response to needle test structures and were visible in histopathological sections of wound edges. Especially hyperplasia of the chorionic epithelium and scar tissue formation, along with enhanced areas of connective tissue which were most prominent surrounding small vessels.

Ribatti *et al.*[383] describe a macrophage infiltrate, however their assay and morphological description were more consistent with granulocytic neutrophil-like heterophils. Macrophages[385] and fibroblasts are, however, strongly associated with the healing wounds in the CAM[404]. Artificial materials often appear to stimulate lower vascular development than allografts and biological materials[390,385]. Fibroblast growth factor, which has a stimulating effect on blood vessel growth is necessary for fast resolution of wounds[404].

The response of the vascular system to biomaterial contact can be measured by changes in vascular density[390]. Vessels can be induced to grow vertically out of the CAM surface into material placed onto it. Using an *ex ovo* technique containers with patterned grooves were able to exert control over the direction of developing blood vessels[405]. The CAM can respond to wounds in a similar manner to wound healing found in mammals (including humans) with re-establishment of epithelial continuity, blood vessel growth, and immune cell infiltration and matrix remodelling[401].

Electrical gradients are present within the chick embryo during development and disruption of these can cause developmental defects[406]. It is plausible but does not appear to have been significantly investigated that electrical gradients also involved in the development and re-establishment of tissue continuity in the CAM. Polyurethane biomaterials, surface modified to contain positive or negative charged surface groups varied in the level of inhibition of blood vessel growth[385].

Egg survival and optimisations

In this work, eggs were implanted with needle test structures, acted as analogues for the full *in vivo* platform. In some implanted eggs, embryos survived to the intended endpoint of the experiment on day 14. Variations in the protocol in the treatment of the CAM were recorded

to aid optimisation of the model. The CAM is often described as a useful alternative *in vivo* model in a number of biomedical fields. However, while methodology is often described in reasonable detail, the viability/mortality rate is rarely remarked upon when describing these procedures. Much optimisation has been carried in commercial settings. However, the aims of high hatch rates and healthy chicks, while aligned, are not identical to the use of extra-embryonic structures for research purposes. More recently, prompted by similar sentiment, attempts have been made to correct this gap in the literature. In particular with regard to egg viability rates to particular interventions[399]. In agreement with results in this thesis Kunz *et al.*[399] found that the majority of mortality occurred in the early period after opening and implantation. Eggs as delivered from the supplier had around 80% viability (fertilised and alive) on opening. Rates in the range 80-90% appear fairly typical[387].

Washing of eggs, prior to opening, is regularly carried out to decontaminate the shell. The most commonly used cleaning solutions are ethanol (this work) or water-based disinfectant[390]. Omission of ethanol cleaning of the shell and replacing it with water only cleaning did not increase the risk of contamination, but has been shown to markedly increase viability[399].The porosity of the shell would make it difficult to guarantee removal of contamination without exposing, and potentially adversely affecting, the embryo.

Rolling of eggs in the early period of incubation is often suggested to improve embryo viability as it mimics movements of the egg in a nest carried out by the hen. Some authors recommend agitation throughout gestation[399]. This would overlap with opening and implantation, necessitating a complex apparatus to prevent disruption resulting from relative motion of the tissue device interface.

In commercial systems, turning or rolling of eggs is recommended from day 3 of incubation. There tends to be agreement on the benefits of periodic motion, with eggs often being turned hourly hourly. However, the degree of turn varies in the range 30–180° per hour[382,407]. Turning at least 3 times daily appears to be a minimum, but little benefit is gained from more frequently than hourly[402]. In this work, eggs were not turned and showed less than 4% mortality, regardless of storage, if left unopened. This is in line with survival to hatching in similarly incubated unopened eggs[408]. Some motion does appear to be critical, particularly between 4 and 7 days, where it influences development of embryo and supporting fluids (by aiding mixing), and reduces a tendency for chicks to adhese to

the extra-embryonic membranes[407] and the gas exchange functions of the CAM.

The environmental conditions of the incubator show significant variation within the literature. The main parameters of interest are temperature and relative humidity. Temperatures within the range 37.8–39.6 ℃[399,409] are regularly reported. Beyond 40 ℃ alterations in metabolism are detectable[409] and a threshold of lethality is reached around 46–47 ℃[402]. Hypo and hyper-thermic conditions led to increased heart rates, increased incidence of malformations, alterations in voluntary embryonic motion and body weights. Higher temperatures 39.6 ℃ across the whole gestational length, but particularly later in gestation marginally reduced successful hatching[408]. Embryos are able to thermoregulate, to some degree, by altering the perfusion of blood through the body and CAM[402]

Humidity appears to be the least influential of the parameters (60-70%) is typical[399,391]. Normothermic at 55% relative humidity still resulted in >90 % survival, however at 40-45%[387] a higher mortality, concentrated in the early days of incubation[409]. Opening eggs with or without removal of the inner shell membrane reduced survival significantly. These data, when interpreted with reference to the unequal weightings of open controls under each treatment suggested that membrane removal is equivocal or a second order effect to egg opening. However, where the shell membrane was removed, dessication was a prominent pathology classification when mortality did occur (4/17) vs (0/19) in the intact group (Table 6.3). It may be the case that environmental control may be a particularly useful mechanism in reducing mortality.

When compared with negligible losses in incubated eggs, whether with or without storage it was clear that both opening and implantation were significant contributors to increased mortality rates with a sustained effect over the proposed experimental period. Comparing opened and implanted eggs, survival of implanted eggs was less than half that of eggs, where only the shell (+/- shell membranes) were removed (opened eggs).

Prevention of shell membrane binding to the CAM, and ease of separation can also be improved by interventions early in development. Placing a small initial hole in the shell at day 2[392] or 3[390,156], equalises ambient air pressure with the airspace and allows the CAM to separate from the shell membrane[381]. This is termed 'dropping the CAM' and is often further aided by removal of a small quantity (2–3 mL) of albumen to encourage separation of the membranes, again around day 3[392,395,404]. Visualisation of vessels and structures

when performing this procedure greatly reduces the risk of vascular injury and improves outcome[399].

Eggs were opened on day 7 and 8, the opening times along with the day for separating the shell membranes is subject to considerable variability in the literature. This may also be in part determined by the application and level of immunocompetence required by the model. Kunz *et al.*[399] reported >80% viability with their procedure and noted the best manipulation times (xenograft transplantation) were day 8[155] and 9[392], with poorer viability on day 7[155,391].

Using *ex ovo* technique has much higher requirements for sterility and a higher risk of dessication[398]. Despite this similarly high viability rates (to *in ovo*[399]) of >80 %[410] have been reported. Notably the viability rate was highly dependent upon experience with viability as low as 25% expected in initial batches handled by a novice worker. This approaches the 17% viability seen in implanted Batch B eggs.

Avoiding vascular damage theoretically only requires care selection of implantation site and accurate placement. Microscope image guidance may be beneficial, however another factor is the fact that vascular structures in the CAM are significantly less developed earlier in gestation.

Dessication was a key cause of mortality in opened eggs, in particular where the shell membrane, which appears to slow evaporative loss of moisture, was removed. Eggs being incubated to produce chicks appear to have increased requirements for environmental humidity, but not until much later in development. Some degree of water loss does appear to be normal and necessary for maximum embryonic survival when eggs experience 10-20% water loss[409]. Aside from humidity, the other factor affecting dessication is disruption of the eggshell and shell membranes, which form a natural barrier to evaporation. Water loss is driven by two factors: vapour conductance of the barriers and vapour pressure differential between the egg and the surrounding environment[402]. It is possible that the barrier tape used to close the shell window in this work was too porous compared to other tapes and window closing solutions. In one instance closed with a complete moisture barrier consisting of silicon grease and a glass coverslip[392]. The microporous tapes are not sterile and in some circumstances may contribute to bacterial contamination[411].

Dessication could be reduced by tighter control of environmental humidity along with

improving the moisture retention of the barrier tape that was used to cover each egg after opening. Vascular damage is impossible to completely eliminate with the size of implants used given the density of vascular structures present in the CAM. However, avoiding large vessels in selection of an implant site and ensuring the mechanical setup prevents pistoning[48]. While no obvious cause could be identified in the majority of eggs, a more systematic investigation of the microbiology and tissues of this group could provide greater insight into the mechanisms of mortality in the models.

Bacterial contamination was suspected in 12% of mortalities. The number is possibly higher, but would require culturing and detailed examination of the embryos to confirm. Bacterial counts on the surface and within the shell of the eggs varied from low thousands up to over a million[412]. Surprisingly, these numbers have been shown to fall over the course of standard incubation with only around 10% remaining at day 7, implying that the risk of bacterial invasion of the embryonic structures may be reduced the later the shell is opened. It is these contaminants that are targeted by washing the egg. Test structures were sterilised prior to implantation into the CAM, so the implants are almost certainly not responsible for introducing bacteria.

There are two routes of bacterial access to the internal structures in or around the embryo[413]: through the eggshell and across the CAM at the (open) airspace. Some observational evidence was seen of microbial causes of mortality in the opened eggs. Bacteria from enteric sources such as *E.coli*, *Klebsiella spp.* and *Salmonella Typhimurium* were infected into the CAM[387]. For some microbial agents, when deliberately inoculated, detection in the internal fluids corresponded to around 40% mortality beyond 24 hours after inoculation, rising to almost 80% at 42 hours. Cannulation and sampling of the allantoic fluid is clearly of utility to detect invasive species after 24 hours of incubation. In negative controls there was 100% survival and also no bacterial detected. This suggests environmental contamination may be less common.

Procedure changes involving splitting invasive processes over several days, interspersed with incubation as passage of dyes and latex beads through the CAM into the allantoic fluid was hypothesised to be related to micro-trauma introduced during manipulation have been suggested[387]. Allowing these to heal may restore some robustness to the physical barrier properties of the CAM. Infectious causes may be also be reduced by observing stricter

aseptic technique in handling the eggs, use of instruments and environmental disinfection. Altering the decontamination procedures applied to eggs themselves may also be considered. Culture and sensitivity sampling along with histopathology of infected tissue may allow identification the major bacterial species responsible, along with likely sources.

Implant toxicity of the components is another possible cause of mortality, however significant cytotoxicity was not seen on the *in vitro* devices despite using many of the same materials.

Storage of eggs that were unopened had no obvious influence on viability. It is less clear if stored eggs would respond differently to implantation but the use of egg storage is recoginised as standard practice for other biomedical uses of the chick egg[382]. The ability to store and thus stagger egg incubation greatly improves the value of the model if, due to availability of instrumentation, only a small number of eggs undergo experiments simultaneously. The effect of environmental conditions and storage time can influence the development of the embryo and even growth rates of the chick well after hatching[402].

Quantification and histology

The major measurements intended to quantify the immune reaction were based on histology in the region of the wound surrounding the implant. This provides a snapshot of the state of the tissue reaction at a single timepoint. Significant proliferation of tissue was observed around and in some cases onto the implanted structure. Analysis of images of serial sections allowed identification of implant sites and surrounding inflammatory reaction consistent with descriptions in the literature.

Macgreen eggs should also produce a signal showing the response of macrophages to the implant site. This property could be utilised in live and timelapse imaging of CAM. However, the expressed fluorophore (GFP) is destroyed by the molecular cross-linking induced by formaldehyde fixation[414], examination of this property could not be carried out in collected specimens. On histological sections, one aim was to quantify the tissue response with comparison to neighbouring healthy tissue, the needle backside (no electrical stimulation on an unpolished SiO_2 surface) and across different implants and stimulation conditions. To achieve this, there was a requirement to identify not only the injury site, but also to register the tissue reaction within a region of the *in vivo* device in contact at that

point (front/back). For sensor application, measurement of the local micro-vasculature, to the level of capillaries, would also be required. Historically this has been achieved by perfusion of the blood vessels and direct casting of the microvasculature of the CAM, allowing inferences about tissue oxygenation to be made[415]. More recently morphometric analysis of vascular structures visible within sections or total preparations (whole CAM) enables the same effect digitally[372]. Z-stack imaging allowed registration of histopathology images with those of the gross tissue images. This approach was useful to reconstruct major blood vessels around an implant and to produce a more complete picture of immune cell infiltrate that may surround an implant site and presents another alternative to casting and morphometric analysis.

Fixation of tissues was carried out after dissection of CAM, but before separation of tissue from implants - to which it was sometimes well adhesed. An alternative, possibly useful in preserving the structure of the delicate CAM, is to carry out all or part of the fixation step *in situ* . With these techniques formalin or an equivalent fixative is dispensed into the airspace over the CAM[385,392]. Application may also take the form of a mist[155].

Histologic quantification often includes counting fibroblasts, macrophages and blood vessels[404] When using the CAM for studies in angiogenesis (blood vessel growth) selective labelling of developing blood vessels in sampled histology has proven useful in aiding quantification and comparison[395]. Direct casting of the microvasculature of the CAM has historically been used to understand tissue oxygenation[415].

Several possible solutions to reliably acquiring images of implantation sites with reasonable planarity were suggested in discussions with a histopathologist. These included using tissue cassettes to capture tissue and marking the tissue with biopsy/tissue marking stain that would allow orientation and triangulation of the region of interest in the section. Tissue from the CAM can also be stabilised by mounting in agar[415].

Alternate sectioning directions are also possible in order to quantify thickness and extent of tissue reaction around a wound.

Tracking tissue orientation was difficult in explanted sections. Tissue marking ink could be used to distinguish the parts of the section in contact with the frontside and backside of the wafer and the expected location of structures of interest. Three points using multiple pigments would allow accurate registration that was insensitive against histologicial

sections being flipped during mounting.

Needle insertion and optimisation

In this work the generation of a tissue defect by needle insertion is itself responsible for triggering an immune response. To accurately assess the effect of altering surface charge, repeatability and control of the tissue device interface is required. Many needle based devices are designed to optimise biomechanical interactions on insertion as this is important *in vivo* . However, in this case an optimised design should be aimed at maximising viability and eliciting a consistent reaction, to allow comparisons between active biomaterial surfaces, the obverse unpolished surface (internal control) and unstimulated controls. Design of experiment approaches would enable optimisation, but require a much larger commitment of eggs or significant further optimisation of the CAM protocol to increase viability.

A total of 65% of the CCI design was completed over the two batches. Based on viability rate of 80% of delivered eggs and an observed implant survival rate (based on combined batch data) of 24%, a lower bound on the number of eggs required to complete an equivalent experimental design can be estimated at 282, using the formulae given in 6.3. This is more than double the quantity used.

$$\mathbf{Eggs} = \frac{\mathbf{Experiments}}{\mathbf{P(Viable)P(Survival)}} \tag{6.3}$$

Needle-like electrodes and microneedles, singly and in arrays have been used for vaccine and drug delivery, fluid sampling[416], oxygen measurement[417] and neural stimulation & recording[418]. Commercial 100 µm with needles composed of silicon iridium electrodes have been used successfully as sensors within CAM tissue[155]. Sensors fabricated on a device the dimensions and shape of a standard microscope, have also been employed[156]. However, these contained no needle features and were used only with an *ex ovo* CAM model. As a result, the sensor surface could not be brought into direct contact the CAM tissue, nor adequately stimulate an implantation injury.

Needle insertion forces are sensitive to geometry especially of the tip and cutting surfaces[419]. Insertion forces and thus biomechanical effects can also be altered by insertion velocity, vibration and drilling effects[416]. Forces have also been reduced using ultrasonic

vibration applied to the needle tip.[420]. Response surface designs have been implemented to optimise needle properties, insertional parameters in neural microelectrodes[363]. In addition to force measurement experiments, numerical modelling of Von mises strain at the needle tip and boundary of substrate and surface electrodes during simulated implantation has been used to optimise needle design[16]. In this work, needle test structures were placed manually, however as with other tissues instrumented measurement of insertional forces and application of repeatable implantation procedure may be beneficial in improving the reliability of the model and establishing the optimal needle geometry. The ability to section recovered tissue at small intervals means that the injury could potentially be much reduced. While this alteration in the platform design would make avoiding significant vascular structures easier on implantation it is not known to what extent it would improve egg viability. This issue is also resolvable through completion of optimisation of needle properties, which relies improvements to survival as outlined above.

CAM sensors

The immobile nature of the eggs and the complete exposure of the tissue of interest presents opportunities for additional instrumentation in tracking the health of the embryo with which the CAM is in symbiosis. Gathering data on immune reactions autonomously or continuously throughout an experiment could be enabled by a number of means. The periodic nature of egg assessment meant that very recent embryonic death could not be ruled out in these cases. Monitoring temperature and embryonic physiology (heart rate and oxygen saturation) *in vivo* could also provide additional information about causes of mortality and optimise embryo survival and the utility of the model.

Live imaging was demonstrated to be useful in visualising the injury site and studying the function of the vascular supply, down to the level of individual cells, in the neighbourhood of the implant. When combined with cell labelling, such as with the transgenic eggs, information about dynamic components of the immune reaction, cell migration and vascular proliferation become available through a number imaging modalities[396]. Alternative methods include serial ultrasonographic imaging to track the growth of xenografted tumours[389]. Photoacoustic tomography scanning has also been used to map the vascular system *in vivo*[421]. Commercial systems for tracking heart rate are also available to provide finer

granularity to mortality times than 24 hour assessments and do not require removal from the incubator[409].

Candling accuracy was very low at 33%, although the time of observations appears to be earlier than many such observations are commonly made. This approach could be used to provide good evidence that sufficient viable eggs had been obtained for a planned experiment. However, as with the reliance of manual observation of mortality (see Section 6.13), an instrumented approach could be beneficial.

More advanced methods for gathering information about the embyro are indicated to improve accuracy and decrease requirements for operator skill. Near infrared imaging to automate candling of eggs have been proposed[422]. Where images of transmitted light are taken, k-means clustering of image features and other machine vision approaches for automated candling are available[423,424]. Non-optical means can also be used to detect heart rate and pulse via motion[409]. Heart rates increase throughout incubation[402], but alterations are also linked to the presence of embryonic stressors.

As noted above, environmental control is important for embryonic survival and development[408]. Monitoring and recording of these properties form a component of model optimisation.

Sensors for oxygen, pH and impedance combined on a single device showed a response over 60 hours of implantation of increasing tissue impedance at low frequencies, corresponding to growing encapsulation and coinciding with reduced oxygen at the sensor surface, while pH initially represented extra-embryonic fluids (albumen and yolk) returned to physiological levels[156]. With the natural airspace technique there is also the possibility of adding conducting fluid placed in the airspace over a section of CAM, providing the opportunity to add external electrodes, like reference electrodes[394], reducing the requirement to produce complete microsystems to test prototype biosensors.

Implanted needle structures have been used to track the influence of the immune/healing response of the CAM through changes in electrical impedance were studied by Karp *et al.*[155]. After implantation to day 16, histology analysis of tissue showed hyperplasia of chorionic epithelium and macrophage activity, similar to observations by others and in this thesis. Electrically, there was very little alteration in magnitude of impedance through the experiment. A monotonic decline in phase was seen which was maximal at 1 kHz. Within

this frequency region signals are associated with cell membrane polarisation and so replacement of normal tissue with multinucleate giant cells, which was reported could be responsible for this[155].

6.16.1 Recommendations

From the results presented here and in the context of the recent literature the following points to optimise the CAM model for viability and recovery of tissue for quantification are made:

- Store and use multiple small batches to gain experience prior to first experimental work and plan around initial high mortality
- Dry decontamination followed by water washing, omit ethanol
- Implement early mechanical agitation, rolling or turning
- Maintain 60-70% relative humidity throughout, track environmental conditions
- Separate the invasive processes (opening/implantation) over several days
- Albumen draw or shell puncture for CAM separation, use aides to prevent vascular disruption
- Seal shell windows with non-porous barrier
- Minimise vascular damage on implantation
- Implant on day 8,9 or later, rather than day 7 or earlier
- Initial fix of tissue *in ovo* , before explantation and sampling for histology
- Histology markers for image registration
- Histology cassettes to enforce tissue planarity

6.17 Conclusion

This chapter detailed the development of needle like devices within the CAM of chick eggs as an *in vivo* model for testing electrically active biomaterials. An *in vivo* model using the chorioallantoic membrane of the chick embryo has been investigated for viability as a translational model for use in the development of implanted bioelectronic devices. Chick eggs are easily obtained and are a comparatively low cost when compared with other *in vivo* models. The availability of genetically-modified eggs provides a means of tracking immune response to implantation. Eggs can be cultured up to 14 days in the UK without a Home Office license making this model compatible with early stage bioelectronics research, especially where rapid prototyping is desirable. The tissue can be easily accessed *in ovo*, is vascularised and is capable of producing an immune response. The structure of the tissue approximates a two dimensional plane making it attractive in situations, for example in sensor development, where it could simplify biophysical considerations in analysing device performance.

Viable embryos were obtained at a rate of 80% of acquired eggs. These could be identified with high specificity but low sensitivity when traditional "candling" techniques were carried out with minimal experience. This technique was, however, very effective at identifying airspaces and allowing eggs to be opened providing access to the CAM for implantation. Opening and implantation could be carried out with relative ease and required minimal equipment or skill. The *in vivo* platform test structures could be sterilised in the laboratory in advance of implantation. They performed as designed, functioning as needles while penetrating the CAM, while not producing damage to deeper structures within the egg.

A surprisingly high mortality rate was observed amongst eggs where interventions had been carried out. Details about expected mortality, survival curves and the influence of various factors were investigated and quantified. An expected survival rate in implanted eggs after one week of incubation can be expected to be lower than 20%. In some cases greater than 50% loss could be expected 24 hours after implantation. Analysis of survival data allows the inference that multiple factors are driving this high mortality rate. In particular, the necessary step of opening eggs reduced survival by approximately two-thirds, a larger reduction than the relative loss produced by the added factor of implantation. Sepa-

rating these two processes provides a starting point for further investigation of the causes and mechanisms that underly the pathology. Shell membrane removal had no apparent influence on survival, and nor did opening time inside the 48 hour interval investigated here. Storage appears to be an appropriate way to provide a stable supply of eggs for experiments. Several mechanisms for cause of mortality have been identified along insights from the literature, concrete recommendations have been made to improve survival. These included environmental monitoring and control, along with improved aseptic processes and technique. Optimisation of survival would greatly increase the utility of the CAM as an *in vivo* model for implanted devices.

Mortality was fairly simple to identify but sampling was limited to 24 hour intervals. Due to this, automated monitoring may be beneficial and easier to implement due to the static nature of eggs in comparison to other *in vivo* models.

Similarly, the utility of a live imaging system has been demonstrated. This enabled views of implants, implantation sites and the surrounding vascular structures - down to the level of the individual blood cells and could be used to directly track cell movement in inflammatory processes. This was employed in this work to image surrounding vascular structures to provide registration data enabling identification of implant sites on histopathology sections. Using this approach, additional to the time-lapse imaging, would be useful for monitoring along with live tracking of immune response. The CAM tissue could be successfully dissected and separated from the implants despite observed tissue reaction and adhesion.

Histopathology was carried out on the recovered tissue. Two common stains have been employed here, however immunohistochemistry and fluorescent techniques that would complement the intrinsic properties of the transgenic eggs are available. Importantly, the implant site could be identified in more than one instance with the assistance of registration data and ante-mortem images. An immune response, characterised by infiltration of immune cells and consistent with the literature, could be identified on analysis of the surrounding tissue. Tracking of implant location using this registration data also meant vascular structures could be segmented and quantified in reference to the wound site.

Needle parameter optimisation for mortality would require at least double the number of eggs used across all experiments and more again for characterisation of tissue reaction.

However, the *in vivo* platform design has been validated in that some biological results could be obtained. Data is now available to provide estimates of the requirements for experiments allowing the feasibility of the future experiments to be accurately assessed.

A wide array of responses can potentially be quantified using a combination of the CAM model and the *in vivo* platform. These include manipulation of tissue reaction and the measurement of biosignals that can be validated using precise knowledge of the surrounding vascular structure that the model makes available. Overall the CAM is a promising model that has been shown to be compatible with the developed *in vivo* platform.

While challenges remain in producing adequate survival, successfully reaching and endpoint has been demonstrated to be feasible, as has measurement of tissue responses through a number of means.

Chapter 7

Conclusions

7.1 Summary

The clinical application of implanted sensors has been hampered by the effects of the immune response to biomaterials and the phenomena of biofouling. The causes and progression of these two issues, along with mechanisms by which they cause adverse effects have been extensively researched. Many approaches have been proposed to prevent or ameliorate these issues, primarily, but not limited to, selection and design of biomaterials. A recognition of the dynamic nature of the problem has led to an emerging consensus that biomaterials are required with material properites that may dynamically modulated. It is this class of 'active' biomaterials, which the current work has focused on. Specifically, the exploitation of electrical phenomena to mediate the interaction of biological processes. Capacitive and other non-faradaic means of electrical control appear attractive due to a number of advantages.

Immune cells and proteins are influenced by surface charge generated at the interface with biomaterials. This charge alters the structure of the double layer that forms on the solution side of the interface and can influence the intermolecular forces that form the biophysical basis of protein adsorption - a key component of biofouling. To explore this, capacitive interfaces were constructed by interposing a dielectric layer between an electrode and solution. When combined with another layer which tuned surface chemistry, the properties of this dielectric layer determine the physical and, consequently, the voltage dependent biological response of the surface. A platform was developed to enable

testing of the hypothesis by allowing fabricated electrodes to be brought into contact with cultured cells to perform *in vitro* experiments. Capacitively charged surfaces were tested with two cancer cell lines under several voltage conditions. Biological interactions were tracked using image analysis allowing multiple phenomena to be observed. A second platform was then designed to enable investigations in an *in vivo* model. This conserved many of the features of the *in vitro* platform to allow accelerated translation of devices to *in vivo* studies and the potential reuse of accessories and interfacing circuitry. An *in vivo* model, based on the chorioallantoic membrane of the chick egg was then investigated. Protocols were established and data was gathered about the response of the tissue to implanted test structures, rates and causes of mortality and means of quantifying the relative influence of a biomaterial.

7.2 Conclusions

This thesis presented the development of platforms to investigate the interaction of cells with biomaterial surfaces under electrical stimulation. This was in pursuit of a hypothesis that capacitively charged surfaces could be used to control biochemical and cellular surface interactions that are central to biofouling and the innate immune response to biomedical implants. A voltage dependent effect on cell attachment was definitively demonstrated in one of two immortalised cancer cell lines, using a non-specific metric sensitive to both cell density and cell spreading in two different ways.

Capacitive charging of surfaces can influence MBA-MD-231 cells via a reduction of cell attachment. The effect was found to be voltage dependent, persisting across two time points spanning several days of contact with the surfaces under near continuous stimulation. A second cell line, MCF-7, did not show sufficient evidence of difference compared to controls. It is unclear whether this is an effect of differences in cell biology or an artefact of the method of quantification. As a result of device construction the voltage required to produce a measurable influence on cells was lower than previously reported for passive capacitive surfaces, but extended over a wider range than the capacitive regime of bioelectrodes. It was also shown that the biochemical processes that govern detachment of cells from biosurfaces are sensitive to and, if measured, can convey information about the

prior quality of cell interaction with a biomaterial. The versatility of the *in vitro* platform was demonstrated through observation of a re-distribution of cells relative to an electrode undergoing electrochemical oxidation peaking 275 µm from the electrode edge. These phenomena have potential applications in managing the immune response to implanted materials and suggests that capacitively charged surfaces hold promise as active biomaterials.

An *in vivo* platform was developed to advance this approach in a biological environment of higher complexity. Devices could be successfully implanted *in ovo* into the CAM However, implantation increased embryo mortality and without further optimisation to the protocol just less than 20% implanted eggs survived one week of implantation. On the basis of the gathered statistics, estimates of the number of eggs required to complete a study could be made. This provides further useful information for researchers considering the use of the CAM model. A number of concrete recommendations were put forward, based on the observations. These inform best practice to maximise, and outline promising steps to optimise, egg viability and complement recent literature. The use of digital manufacturing techniques for *in vivo* platform development, highlighted a novel approach of tightly integrating implantable device design and fabrication with high throughput *in vivo* testing that is uniquely accessible using the CAM model. Poor viability of the eggs used in this work prevented the full realisation of needle geometry optimisation. However a proof of concept was achieved.

7.3 Future work

Future work could be divided between enhancements to the developed platforms and further investigation of the biological effects of capacitive charging, *in vitro* and *in vivo* .

For the platforms, additional features could be explored, for example reference and counter electrode integration in to the upper chamber of the *in vitro* platform to aide characterisation of the capacitive properties of the dielectric layers in solution. Additionally, having validated the platforms, biosensors and other devices could be quickly prototyped and tested by exploiting the electrical breakout offered by the platforms. To further probe the biological effect of capacitive charging, integration of the platforms with a live-imaging

culture system with higher resolution and access to fluorescence would be beneficial.

Further investigation of capacitive charging involving wider voltage ranges and the high voltages and pre-polarisation as applied in previous electret literature would shed light on the degree to which electrical control of biological effects is possible using this approach. Study of additional cell lines, in particular macrophages like RAW.264 that can show phenotypic polarisation, a key determinant of the FBR outcome, would also be useful. Coincident with biological methods to provide a deeper understanding of cell surface interactions, gene expression, and the dynamics of intracellular structures on charged surfaces could be the subject of further cell stimulation experiments. Investigation of the influence of protein adsorption could be carried out indirectly, through a clotting assay and, more directly, using surface quantification techniques and FRET based conformational studies. Lastly, electrical control of the Vroman effect may be possible, allowing precise control, via dynamically charged surfaces, over the evolution of an adsorbed protein film.

With the *in vivo* model the key priority with the CAM is the optimisation of the egg viability, along with associated needle design and histology protocol. In terms of capacitive biomaterials, using live imaging to track dynamic immune response to charged surfaces, and histological characterisation of other metrics associated with the immune response and FBR are then the next logical steps.

More generally, there are opportunities to create a convenient, inexpensive and efficacious *in vivo* testing environment. Of particular interest is the well established use of xenografted tumours in the CAM. Biosensors implanted into xenografts, that can express a wide range of tumour behaviours, can be used to measure properties of tumours in an highly controlled *in vivo* environment. Control of environmental conditions, including ambient gas concentrations and direct manipulations of vascular function can be used to relate sensor performance to physiological and pathophysiological changes in the tissue.

Glossary of terms

ABS acrylonitrile butadiene styrene.

AFM Atomic force microscopy.

anoikis Cell death triggered in many healthy cells after failure to find and attach to a surface or extracellular scaffold.

BioMEMS Biological Microelectromechanical system.

C_4F_8 Octafluorocyclobutane. Used in DRIE to produce a passivating fluoropolymer on sidewalls.

CAM Chorio-allantoic membrane - a component of the shell membranes of the developing chick egg.

CCI Central composite experimental design of the inscribed type. The design is scaled so that factor limits are respected.

confluency Cell cuture: Area occupied by cells mass expressed as a percentage of total area.

CVD Chemical vapour deposition.

DAPI Fluorescent stain for DNA.

die Circuit formed on a piece of semiconductor material, processed on, and cut from a wafer.

DLVO Model of the inter-surface potential between bodies in an aqueous solution; incorporating van der Waals, electrostatic and in some cases acid-base interactions.

DMEM Dulbecco's modified Eagle Solution - Culture medium.

DOE Design of experiments, an approach to generating efficient sets of experimental parameters to explore multiple factors simultaneously.

DRIE Deep reactive ion etching.

ECM Extracellular matrix.

EDA Electronic design automation.

EDL Electric double layer.

EED Early embryonic death, failure of development of the chick embryo, occurring prior to opening eggs after day 7 of development.

EWOD Electrowetting on dielectric, a combination of conducting electrode and dielectric layers can control.

FAK Focal adhesion complex. Collection of proteins forming a transmembrane struture mechanically connecting cell interior to environment.

FBGC Foreign-body giant cells, large immune cells created by merging of tissue macrophages in chronic inflammatory tissues.

FBR Foreign body response, a sustained immune reaction triggered by frustrated healing that results from the continued presence of an implanted device.

FBS Foetal bovine serum. A source of proteins and growth factors commonly used to supplement mammalian cell culture media.

FDM Fused deposition modelling - a type of 3D printing.

FEP Fluoroinated ethylene propylene, fluoropolymer with greater formability than PTFE(Teflon).

FRET Förster resonance energy transfer.

GFP Green fluorescent protein.

H&E Haematoxylin and Eosin, a common histological two component stain.

Hamburger-Hamilton A commonly referenced sequence of defined stages in the development of the chick embryo.

HDMS Hexamethyldisilazane.

HMWK High molecular weight kininogen. Coagulation and inflammatory initiating protein.

HSEC-8 Samtec edge card connector used for connections to wafer devices.

HSV Hue saturation value a three component colourspace alterative to RGB.

I-line One of the emission peaks of a mercury vapour lamp (365nm) used for photoresist exposure.

Idiopathic A pathological process with no identified cause.

IMS Industrial methylated spirits.

ITO Indium tin oxide. A transparent electrically conductive coating.

JSON Javascript object notation - a serisalisation file format.

OCP Open circuit potential. Electrodes immersed in solution will spontaneously form a surface potential which is present even if not external power source is connected.

PBS Phosphate buffered saline.

PBST PBS with additional detergent (Tween 20) used increase permeability of cells and tissues for immunohistology along with other applications.

PCB Printed circuit board.

PECVD Plasma enhanced chemical vapour deposition.

PEDOT Poly(3,4-ethylenedioxythiophene and variants. An electroactive conducting polymer.

PEG Polyethylene glycol, a hydrophilic molecule often functionalised onto surfaces as an anti-fouling layer.

phagocytosis The process of immune cells engulfing foreign material in order to destroy it and/or remove it from the body.

PMMA Poly(Methyl methacrylate) an early biocompatible polymer widely used.

PNG Portable Network Graphics - an image file format.

PPy Polypyrrole, a common electroactive polymer.

PTFE Polytetrafluoroethylene, a fluoropolymer encountered under the trade name teflon ®.

Purulent Accumulation of material containing some combination of: Microbes, dead cell fragments, degraded ECM and immune cells. Colloquially referred to as 'pus'.

PVDF polyvinylidene fluoride. A fluoropolymer with electroactive and piezoelectric properties.

PZC Potential of zero charge. The potential applied to a surface necessary to counteract native or acquired charge.

PZT Lead zirconia titanate. A commonly used piezoelectric material.

RGD A peptide composed of an amino acid triplet containing: arginine, glycine and asparagine. A binding site, found in the protein fibronectin, which acts as target for many integrins and facilitates cell attachment.

RIE Reactive ion etching.

SAM Self assembled monolayer: a chemical with an affinity for a surface but where build up of more than molecular layer is unfavourable.

SEM Scanning electron microscopy.

Sensitivity True positive rate of a binary classification test.

SF_6 Sulphur hexafluoride. A silicon etchant gas used in DRIE.

SMU Source measure unit.

Specificity True negative rate of a binary classification test.

TCPS Tissue culture polystyrene, Polystyrene treated with corona dischage to increase surface energy and improve biocompatibility.

TMAH Tetra Methyl Ammonium Hydroxide. Photoresist developer.

ToF-SIMS Time of flight secondary ion mass spectrometry.

References

[1] M. J. Madou, *Fundamentals of microfabrication / Marc Madou.* Boca Raton, Fla. ; London: CRC Press, 1997.

[2] Research and Markets. “Health sensors market size, share & trends analysis report by product (wearable, ingestible/implantable), by application (wellness monitoring, sensor therapeutics), by region, and segment forecasts, 2018 - 2025.” (Jun. 2018), [Online]. Available: `https://www.researchandmarkets.com/research/dg63bj` (visited on 11/14/2021).

[3] C. M. Magin, S. P. Cooper, and A. B. Brennan, “Non-toxic antifouling strategies,” *Materials Today*, vol. 13, no. 4, pp. 36–44, 2010.

[4] P. A. Vinagre, T. Simas, E. Cruz, E. Pinori, and J. Svenson, “Marine biofouling: A european database for the marine renewable energy sector,” *Journal of marine science and engineering*, vol. 8, no. 7, pp. 495–, 2020.

[5] “A short history on pacemakers,” *International journal of cardiology*, vol. 169, no. 4, pp. 244–248, 2013.

[6] A. Mudry and M. Mills, “The early history of the cochlear implant: A retrospective,” *JAMA otolaryngology - head and neck surgery*, vol. 139, no. 5, pp. 446–453, 2013.

[7] W. Greatbatch and C. Holmes, “History of implantable devices,” *IEEE Engineering in Medicine and Biology Magazine*, vol. 10, no. 3, pp. 38–41, 2002.

[8] M. C. Hacker, J. Krieghoff, and A. G. Mikos, “Chapter 33 - synthetic polymers,” in *Principles of Regenerative Medicine (Third Edition)*, A. Atala, R. Lanza, A. G. Mikos, and R. Nerem, Eds., Third Edition, Boston: Academic Press, 2019, pp. 559–590.

[9] R. A. Normann and E. Fernandez, “Clinical applications of penetrating neural interfaces and utah electrode array technologies,” *Journal of neural engineering*, vol. 13, no. 6, pp. 061 003–061 003, 2016.

[10] A. R. Harris and G. G. Wallace, “Electrochemical methods for analysing and controlling charge transfer at the electrode–tissue interface,” *Current Opinion in Electrochemistry*, vol. 16, pp. 143–148, 2019, Electrochemical Materials and Engineering • Sensors and Biosensors.

[11] J. M. Anderson, “Biological responses to materials,” *Annual Review of Materials Science*, vol. 31, pp. 81–110, 2001.

[12] *The Immune Response to Implanted Materials and Devices The Impact of the Immune System on the Success of an Implant / edited by Bruna Corradetti.* 1st ed. 2017. Cham: Springer International Publishing, 2017.

[13] D. P. Vasconcelos, A. P. Águas, M. A. Barbosa, P. Pelegrín, and J. N. Barbosa, “The inflammasome in host response to biomaterials: Bridging inflammation and tissue regeneration,” *Acta Biomaterialia*, vol. 83, pp. 1–12, 2019.

[14] M. R. Major, V. W. Wong, E. R. Nelson, M. T. Longaker, and G. C. Gurtner, “The Foreign Body Response: At the Interface of Surgery and Bioengineering,” *Plastic and Reconstructive Surgery*, vol. 135, no. 5, pp. 1489–1498, 2015.

[15] A. Kral, F. Aplin, and H. Maier, “Tissue reaction to neuroprostheses,” *Prostheses for the Brain*, pp. 135–148, 2021.

[16] T. D. Kozai, A. S. Jaquins-Gerstl, A. L. Vazquez, A. C. Michael, and X. T. Cui, “Brain tissue responses to neural implants impact signal sensitivity and intervention strategies,” *ACS Chemical Neuroscience*, vol. 6, no. 1, pp. 48–67, 2015.

[17] C. D. Mills and K. Ley, “M1 and m2 macrophages: The chicken and the egg of immunity,” *Journal of innate immunity*, vol. 6, no. 6, pp. 716–726, 2014.

[18] K. M. Hotchkiss, N. M. Clark, and R. Olivares-Navarrete, “Macrophage response to hydrophilic biomaterials regulates MSC recruitment and T-helper cell populations,” *Biomaterials*, vol. 182, no. August, pp. 202–215, 2018.

[19] A. Dievernich, P. Achenbach, L. Davies, and U. Klinge, “Characterization of innate and adaptive immune cells involved in the foreign body reaction to polypropylene meshes in the human abdomen,” *Hernia*, vol. 26, no. 1, pp. 309–323, 2022.

[20] A. M. Tanneberger *et al.*, “Multinucleated giant cells within the in vivo implantation bed of a collagen-based biomaterial determine its degradation pattern,” *Clinical Oral Investigations*, vol. 25, no. 3, pp. 859–873, 2021.

[21] O. Veiseh *et al.*, “Size- and shape-dependent foreign body immune response to materials implanted in rodents and non-human primates,” *Nature Materials*, vol. 14, no. 6, pp. 643–651, 2015.

[22] Y. Wang, S. Vaddiraju, B. Gu, F. Papadimitrakopoulos, and D. J. Burgess, “Foreign body reaction to implantable biosensors: Effects of tissue trauma and implant size,” *Journal of Diabetes Science and Technology*, vol. 9, no. 5, pp. 966–977, 2015.

[23] J. E. Sanders, C. E. Stiles, and C. L. Hayes, “Tissue response to single-polymer fibers of varying diameters: Evaluation of fibrous encapsulation and macrophage density,” *Journal of Biomedical Materials Research*, vol. 52, no. 1, pp. 231–237, 2000.

[24] G. Cannon and J. Swanson, “The macrophage capacity for phagocytosis,” *Journal of Cell Science*, vol. 101, no. 4, pp. 907–913, Apr. 1992.

[25] J. A. Champion, A. Walker, and S. Mitragotri, “Role of particle size in phagocytosis of polymeric microspheres,” *Pharmaceutical Research*, vol. 25, no. 8, pp. 1815–1821, 2008.

[26] S. Sharma, B. J. Berne, and S. K. Kumar, “Thermal and structural stability of adsorbed proteins,” *Biophysical Journal*, vol. 99, no. 4, pp. 1157–1165, 2010.

[27] D. Depan and R. D. Misra, “The development, characterization, and cellular response of a novel electroactive nanostructured composite for electrical stimulation of neural cells,” *Biomaterials Science*, vol. 2, no. 12, pp. 1727–1739, 2014.

[28] C. Sperling, M. Fischer, M. F. Maitz, and C. Werner, “Blood coagulation on biomaterials requires the combination of distinct activation processes,” *Biomaterials*, vol. 30, no. 27, pp. 4447–4456, 2009.

[29] E. A. Vogler and C. A. Siedlecki, “Contact activation of blood-plasma coagulation,” *Biomaterials*, vol. 30, no. 10, pp. 1857–1869, 2009.

[30] O. V. Sjaastad, *Physiology of domestic animals / Øystein V. Sjaastad, Knut Hove, Olav Sand.* Oslo: Scandinavian Veterinary Press, 2003.

[31] C. Sperling, M. F. Maitz, S. Grasso, C. Werner, and S. M. Kanse, “A Positively Charged Surface Triggers Coagulation Activation Through Factor VII Activating Protease (FSAP),” *ACS Applied Materials and Interfaces*, vol. 9, no. 46, pp. 40 107–40 116, 2017.

[32] S. Franz, S. Rammelt, D. Scharnweber, and J. C. Simon, “Immune responses to implants - A review of the implications for the design of immunomodulatory biomaterials,” *Biomaterials*, vol. 32, no. 28, pp. 6692–6709, 2011.

[33] R. Klopfleisch and F. Jung, “The pathology of the foreign body reaction against biomaterials,” *Journal of Biomedical Materials Research - Part A*, vol. 105, no. 3, pp. 927–940, 2017.

[34] Y. Mao and J. E. Schwarzbauer, “Fibronectin fibrillogenesis, a cell-mediated matrix assembly process,” *Matrix biology*, vol. 24, no. 6, pp. 389–399, 2005.

[35] S. Jhunjhunwala *et al.*, “Neutrophil responses to sterile implant materials,” *PloS one*, vol. 10, no. 9, e0137550–e0137550, 2015.

[36] Z. Xia and J. T. Triffitt, “A review on macrophage responses to biomaterials,” *Biomedical Materials*, vol. 1, no. 1, 2006.

[37] H. Zhou, Y. Xue, L. Dong, and C. Wang, “Biomaterial-based physical regulation of macrophage behaviour,” *Journal of Materials Chemistry B*, vol. 9, no. 17, pp. 3608–3621, 2021.

[38] A. B. Kummarapurugu, S. Zheng, J. Ma, S. Ghosh, A. Hawkridge, and J. A. Voynow, “Neutrophil Elastase Triggers the Release of Macrophage Extracellular Traps Relevance to Cystic Fibrosis,” *American Journal of Respiratory Cell and Molecular Biology*, vol. 66, no. 1, pp. 76–85, 2022.

[39] Y. S. Bae *et al.*, “Macrophages generate reactive oxygen species in response to minimally oxidized low-density lipoprotein: Toll-like receptor 4- and spleen tyrosine kinase-dependent activation of NADPH oxidase 2,” *Circulation Research*, vol. 104, no. 2, pp. 210–218, 2009.

[40] S. N. Christo, K. R. Diener, A. Bachhuka, K. Vasilev, and J. D. Hayball, “Innate Immunity and Biomaterials at the Nexus: Friends or Foes,” *BioMed Research International*, vol. 2015, 2015.

[41] W. G. Brodbeck, M. MacEwan, E. Colton, H. Meyerson, and J. M. Anderson, “Lymphocytes and the foreign body response: Lymphocyte enhancement of macrophage adhesion and fusion,” *Journal of Biomedical Materials Research - Part A*, vol. 74, no. 2, pp. 222–229, 2005.

[42] A. A. Abraham *et al.*, “Foreign Body Reaction to a Subcutaneously Implanted Self-Cleaning, Thermoresponsive Hydrogel Membrane for Glucose Biosensors,” *ACS Biomaterials Science and Engineering*, vol. 4, no. 12, pp. 4104–4111, 2018.

[43] K. E. Kubow *et al.*, “Mechanical forces regulate the interactions of fibronectin and collagen i in extracellular matrix,” *Nature Communications*, vol. 6, 2015.

[44] B. D. Ratner, “Reducing capsular thickness and enhancing angiogenesis around implant drug release systems,” *Journal of Controlled Release*, vol. 78, no. 1-3, pp. 211–218, 2002.

[45] W. G. Brodbeck, M. S. Shive, E. Colton, Y. Nakayama, T. Matsuda, and J. M. Anderson, “Influence of biomaterial surface chemistry on the apoptosis of adherent cells,” *Journal of Biomedical Materials Research*, vol. 55, no. 4, pp. 661–668, 2001.

[46] W. G. Brodbeck *et al.*, “Biomaterial adherent macrophage apoptosis is increased by hydrophilic and anionic substrates in vivo,” *Proceedings of the National Academy of Sciences of the United States of America*, vol. 99, no. 16, pp. 10 287–10 292, 2002.

[47] W. M. GRILL and J. T. MORTIMER, “Electrical properties of implant encapsulation tissue,” *Annals of biomedical engineering*, vol. 22, no. 1, pp. 23–33, 1994.

[48] K. L. Helton, B. D. Ratner, and N. A. Wisniewski, “Biomechanics of the sensor-tissue interface-effects of motion, pressure, and design on sensor performance and the

foreign body response-part i: Theoretical framework," *Journal of diabetes science and technology*, Interstitial Fluid Physiology as It Relates to Glucose Monitoring Technologies, vol. 5, no. 3, pp. 632–646, 2011.

[49] K. L. Helton, B. D. Ratner, and N. A. Wisniewski, "Biomechanics of the sensor-tissue interface-effects of motion, pressure, and design on sensor performance and foreign body response-part ii: Examples and application," *Journal of diabetes science and technology*, Interstitial Fluid Physiology as It Relates to Glucose Monitoring Technologies, vol. 5, no. 3, pp. 647–656, 2011.

[50] Z. Wang, S. Wang, Y. Marois, R. Guidoin, and Z. Zhang, "Evaluation of biodegradable synthetic scaffold coated on arterial prostheses implanted in rat subcutaneous tissue," *Biomaterials*, vol. 26, no. 35, pp. 7387–7401, 2005.

[51] T. O. Socarrás, A. C. Vasconcelos, P. P. Campos, N. B. Pereira, J. P. C. Souza, and S. P. Andrade, "Foreign body response to subcutaneous implants in diabetic rats," *PloS one*, vol. 9, no. 11, e110945–e110945, 2014.

[52] M. J. Mahoney and J. Leighton, "The Inflammatory Response to a Foreign Body within Transplantable Tumors," *Cancer Research*, vol. 22, no. 3, pp. 334–338, 1962.

[53] M. Gray *et al.*, "Biocompatibility of common implantable sensor materials in a tumor xenograft model," 2018-10-27.

[54] L. M. Szott and T. A. Horbett, "Protein interactions with surfaces: Cellular responses, complement activation, and newer methods," *Current Opinion in Chemical Biology*, vol. 15, no. 5, pp. 677–682, 2011.

[55] S. A. Tofail and J. Bauer, "Electrically Polarized Biomaterials," *Advanced Materials*, vol. 28, no. 27, pp. 5470–5484, 2016.

[56] R. M. Cornelius, J. MacRi, and J. L. Brash, "Interfacial interactions of apolipoprotein AI and high density lipoprotein: Overlooked phenomena in blood-material contact," *Journal of Biomedical Materials Research - Part A*, vol. 99 A, no. 1, pp. 109–115, 2011.

[57] R. Gifford, J. J. Kehoe, S. L. Barnes, B. A. Kornilayev, M. A. Alterman, and G. S. Wilson, "Protein interactions with subcutaneously implanted biosensors," *Biomaterials*, vol. 27, no. 12, pp. 2587–2598, 2006.

[58] E. Delivopoulos, M. M. Ouberai, P. D. Coffey, M. J. Swann, K. M. Shakesheff, and M. E. Welland, “Serum protein layers on parylene-c and silicon oxide: Effect on cell adhesion,” *Colloids and surfaces, B, Biointerfaces*, vol. 126, pp. 169–177, 2015.

[59] E. Lutanie, J. C. Voegel, P. Schaaf, M. Freund, J. P. Cazenave, and A. Schmitt, “Competitive adsorption of human immunoglobulin G and albumin: Consequences for structure and reactivity of the adsorbed layer,” *Proceedings of the National Academy of Sciences of the United States of America*, vol. 89, no. 20, pp. 9890–9894, 1992.

[60] P. Parhi, A. Golas, and E. A. Vogler, *Role of proteins and water in the initial attachment of mammalian cells to biomedical surfaces: A review*. 2010, vol. 24, pp. 853–888.

[61] E. A. Vogler, “Protein adsorption in three dimensions,” *Biomaterials*, vol. 33, no. 5, pp. 1201–1237, 2012.

[62] A. Cadilhe, N. A. Araújo, and V. Privman, “Random sequential adsorption: From continuum to lattice and pre-patterned substrates,” *Journal of Physics Condensed Matter*, vol. 19, no. 6, 2007.

[63] J. Kim, “Mathematical modeling approaches to describe the dynamics of protein adsorption at solid interfaces,” *Colloids and Surfaces B: Biointerfaces*, vol. 162, pp. 370–379, 2018.

[64] C. B. Anfinsen, “Principles that govern the folding of protein chains,” *Science (American Association for the Advancement of Science)*, vol. 181, no. 4096, pp. 223–230, 1973.

[65] T. Kajander *et al.*, “Buried charged surface in proteins,” *Structure (London)*, vol. 8, no. 11, pp. 1203–1214, 2000.

[66] M. L. Godek, R. Michel, L. M. Chamberlain, D. G. Castner, and D. W. Grainger, “Adsorbed serum albumin is permissive to macrophage attachment to perfluorocarbon polymer surfaces in culture,” *Journal of Biomedical Materials Research - Part A*, vol. 88, no. 2, pp. 503–519, 2009.

[67] P. Lin, L. Ding, C. W. Lin, and F. Gu, “Nonfouling property of zwitterionic cysteine surface,” *Langmuir*, vol. 30, no. 22, pp. 6497–6507, 2014.

[68] M. Liu, Y. Zhang, M. Wang, C. Deng, Q. Xie, and S. Yao, “Adsorption of bovine serum albumin and fibrinogen on hydrophilicity-controllable surfaces of polypyrrole doped with dodecyl benzene sulfonate-A combined piezoelectric quartz crystal impedance and electrochemical impedance study,” *Polymer*, vol. 47, no. 10, pp. 3372–3381, 2006.

[69] S. Mitra, “Protein adsorption on biomaterial surfaces: Subsequent conformational and biological consequences -a review,” *Journal of Surface Science and Technology*, vol. 36, pp. 7–38, Jun. 2020.

[70] D. Faulón Marruecos, D. K. Schwartz, and J. L. Kaar, “Impact of surface interactions on protein conformation,” *Current Opinion in Colloid and Interface Science*, vol. 38, pp. 45–55, 2018.

[71] S. L. Hirsh, D. R. McKenzie, N. J. Nosworthy, J. A. Denman, O. U. Sezerman, and M. M. Bilek, “The Vroman effect: Competitive protein exchange with dynamic multilayer protein aggregates,” *Colloids and Surfaces B: Biointerfaces*, vol. 103, pp. 395–404, 2013.

[72] R. E. Baier, “Surface behaviour of biomaterials: The theta surface for biocompatibility,” *Journal of Materials Science: Materials in Medicine*, vol. 17, no. 11, pp. 1057–1062, 2006.

[73] M. D. Lad, F. Birembaut, J. M. Matthew, R. A. Frazier, and R. J. Green, “The adsorbed conformation of globular proteins at the air/water interface,” *Physical Chemistry Chemical Physics*, vol. 8, no. 18, pp. 2179–2186, 2006.

[74] X. Chen, J. Chen, and N. Huang, “The structure, formation, and effect of plasma protein layer on the blood contact materials: A review,” *Biosurface and Biotribology*, no. August, pp. 1–14, 2021.

[75] M. Pegueroles, C. Tonda-Turo, J. A. Planell, F. J. Gil, and C. Aparicio, “Adsorption of fibronectin, fibrinogen, and albumin on TiO2: Time-Resolved Kinetics, structural changes, and competition study,” *Biointerphases*, vol. 7, no. 1-4, pp. 1–13, 2012.

[76] E. Ostuni *et al.*, “Self-assembled monolayers that resist the adsorption of proteins and the adhesion of bacterial and mammalian cells,” *Langmuir*, vol. 17, no. 20, pp. 6336–6343, 2001.

[77] D. G. Castner, “Biomedical surface analysis: Evolution and future directions (Review),” *Biointerphases*, vol. 12, no. 2, p. 02C301, 2017.

[78] G. Baneyx, L. Baugh, and V. Vogel, “Coexisting conformations of fibronectin in cell culture imaged using fluorescence resonance energy transfer,” *Proceedings of the National Academy of Sciences of the United States of America*, vol. 98, no. 25, pp. 14 464–14 468, 2001.

[79] M. Antia, L. D. Islas, D. A. Boness, G. Baneyx, and V. Vogel, “Single molecule fluorescence studies of surface-adsorbed fibronectin,” *Biomaterials*, vol. 27, no. 5, pp. 679–690, 2006.

[80] S. Basu, B. Gorai, B. Basu, and P. K. Maiti, “Electric Field-Mediated Fibronectin-Hydroxyapatite Interaction: A Molecular Insight,” *Journal of Physical Chemistry B*, vol. 125, no. 1, pp. 3–16, 2021.

[81] L. Vroman and A. Adams, “Findings with the recording ellipsometer suggesting rapid exchange of specific plasma proteins at liquid/solid interfaces,” *Surface science*, vol. 16, 1969-8.

[82] L. Vroman, “Finding seconds count after contact with blood (and that is all i did),” *Colloids and surfaces, B, Biointerfaces*, vol. 62, no. 1, pp. 1–4, 2008.

[83] H. Noh and E. A. Vogler, “Volumetric interpretation of protein adsorption: Competition from mixtures and the Vroman effect,” *Biomaterials*, vol. 28, no. 3, pp. 405–422, 2007.

[84] D. L. Elbert and J. A. Hubbell, “Surface treatments of polymers for biocompatibility,” *Annual Review of Materials Science*, vol. 26, no. 1, pp. 365–394, 1996.

[85] L. P. Kozlowski, “Proteome-pI: proteome isoelectric point database,” *Nucleic Acids Research*, vol. 45, no. D1, pp. D1112–D1116, Oct. 2016.

[86] M. Uhlén *et al.*, “Tissue-based map of the human proteome,” *Science*, vol. 347, no. 6220, p. 1 260 419, 2015.

[87] C. Prin, M. C. Bene, B. Gobert, P. Montagne, and G. C. Faure, “Isoelectric restriction of human immunoglobulin isotypes,” *Biochimica et Biophysica Acta*, vol. 1243, pp. 287–290, 1995.

[88] V. Trajkovski, L. Ajdinski, and M. Spiroski, “Plasma concentration of immunoglobulin classes and subclasses in children with autism in the republic of macedonia: Retrospective study,” *Croatian medical journal*, vol. 45, no. 6, pp. 746–749, 2004.

[89] M. Rocco, O. Aresu, and L. Zardi, “Conformational state of circulating human plasma fibronectin,” *FEBS Letters*, vol. 178, no. 2, pp. 327–330, 1984.

[90] D. E. LaCroix and M. Anand, “A model for the formation, growth, and dissolution of clots in vitro. Effect of the intrinsic pathway on antithrombin III deficiency and protein C deficiency,” *International Journal of Advances in Engineering Sciences and Applied Mathematics*, vol. 3, no. 1-4, pp. 93–105, 2011.

[91] S. P. Baba, S. Zehra, and B. Bano, “Purification and characterization of kininogens from sheep plasma,” *The Protein Journal*, vol. 24, no. 2, pp. 95–102, 2005.

[92] M. Rabe, D. Verdes, and S. Seeger, “Understanding protein adsorption phenomena at solid surfaces,” *Advances in Colloid and Interface Science*, vol. 162, no. 1-2, pp. 87–106, 2011.

[93] E. Syková and C. Nicholson, “Diffusion in brain extracellular space,” *Physiological Reviews*, vol. 88, no. 4, pp. 1277–1340, 2008.

[94] C. Nicholson and L. Tao, “Hindered diffusion of high molecular weight compounds in brain extracellular microenvironment measured with integrative optical imaging,” *Biophysical Journal*, vol. 65, no. 6, pp. 2277–2290, 1993.

[95] S. Arvidsson, A. Askendal, and P. Tengvall, “Blood plasma contact activation on silicon, titanium and aluminium,” *Biomaterials*, vol. 28, no. 7, pp. 1346–1354, 2007.

[96] B. Sivaraman and R. A. Latour, “Time-dependent conformational changes in adsorbed albumin and its effect on platelet adhesion,” *Langmuir*, vol. 28, no. 5, pp. 2745–2752, 2012.

[97] M. Dargahi, V. Nelea, A. Mousa, S. Omanovic, and M. T. Kaartinen, “Electrochemical modulation of plasma fibronectin surface conformation enables filament formation and control of endothelial cell-surface interactions,” *RSC Advances*, vol. 4, no. 88, pp. 47 769–47 780, 2014.

[98] K. D. Newman, P. Elamanchili, G. S. Kwon, and J. Samuel, "Protein and surface effects on monocyte and macrophage adhesion, maturation, and survival," *Journal of Biomedical Materials Research*, vol. 60, no. 3, pp. 487–496, 2002.

[99] I. Han, B. Vagaska, B. Joo Park, M. H. Lee, S. Jin Lee, and J. C. Park, "Selective fibronectin adsorption against albumin and enhanced stem cell attachment on helium atmospheric pressure glow discharge treated titanium," *Journal of Applied Physics*, vol. 109, no. 12, 2011.

[100] T. Miller and D. Boettiger, "Control of intracellular signaling by modulation of fibronectin conformation at the cell-materials interface," *Langmuir*, vol. 19, no. 5, pp. 1723–1729, 2003.

[101] D. W. Grainger, G. Pavon-Djavid, V. Migonney, and M. Josefowicz, "Assessment of fibronectin conformation adsorbed to polytetrafluoroethylene surfaces from serum protein of cell attachment in culture," *Journal of Biomaterials Science, Polymer Edition*, vol. 14, no. 9, pp. 973–988, 2003.

[102] C. Maas *et al.*, "Misfolded proteins activate Factor XII in humans, leading to kallikrein formation without initiating coagulation," *Journal of Clinical Investigation*, vol. 118, no. 9, pp. 3208–3218, 2008.

[103] R. Zhuo, C. A. Siedlecki, and E. A. Vogler, "Autoactivation of blood factor xii at hydrophilic and hydrophobic surfaces," *Biomaterials*, vol. 27, no. 24, pp. 4325–4332, 2006.

[104] C. Saltó *et al.*, "Control of neural stem cell adhesion and density by an electronic polymer surface switch," *Langmuir*, vol. 24, no. 24, pp. 14 133–14 138, 2008.

[105] H. Elwing, "Protein absorption and ellipsometry in biomaterial research," *Biomaterials*, vol. 19, no. 4, pp. 397–406, 1998.

[106] T. Goda and Y. Miyahara, "Interpretation of protein adsorption through its intrinsic electric charges: A comparative study using a field-effect transistor, surface plasmon resonance, and quartz crystal microbalance," *Langmuir*, vol. 28, no. 41, pp. 14 730–14 738, 2012.

[107] W. Wang *et al.*, “Super-Temporal-Resolved Microscopy Reveals Multistep Desorption Kinetics of α-Lactalbumin from Nylon,” *Langmuir*, vol. 34, no. 23, pp. 6697–6702, 2018.

[108] A. Vermeer, C. Giacomelli, and W. Norde, “Adsorption of igg onto hydrophobic teflon. differences between fab and fc domains,” *Biochimica et biophysica acta. General subjects*, vol. 1526, no. 1, pp. 61–69, 2001.

[109] A. W. Vermeer, C. E. Giacomelli, and W. Norde, “Adsorption of IgG onto hydrophobic teflon. Differences between the Fab and Fc domains,” *Biochimica et Biophysica Acta - General Subjects*, vol. 1526, no. 1, pp. 61–69, 2001.

[110] Y. Inoue, T. Nakanishi, and K. Ishihara, “Elastic repulsion from polymer brush layers exhibiting high protein repellency,” *Langmuir*, vol. 29, no. 34, pp. 10 752–10 758, 2013.

[111] A. Sethuraman, M. Han, R. S. Kane, and G. Belfort, “Effect of surface wettability on the adhesion of proteins,” *Langmuir*, vol. 20, no. 18, pp. 7779–7788, 2004.

[112] M. Kamińska *et al.*, “Interaction of parylene C with biological objects,” *Acta of Bioengineering and Biomechanics*, vol. 11, no. 3, pp. 19–25, 2009.

[113] R. G. Chapman, E. Ostuni, S. Takayama, R. E. Holmlin, L. Yan, and G. M. Whitesides, “Surveying for surfaces that resist the adsorption of proteins [3],” *Journal of the American Chemical Society*, vol. 122, no. 34, pp. 8303–8304, 2000.

[114] J. N. Longchamp *et al.*, “Imaging proteins at the single-molecule level,” *Proceedings of the National Academy of Sciences of the United States of America*, vol. 114, no. 7, pp. 1474–1479, 2017.

[115] F. Macritchie, “The adsorption of proteins at the solid/liquid interface,” *Journal of Colloid And Interface Science*, vol. 38, no. 2, pp. 484–488, 1972.

[116] J. J. Ramsden, “Experimental methods for investigating protein adsorption kinetics at surfaces,” *Quarterly Reviews of Biophysics*, vol. 27, no. 1, pp. 41–105, 1994.

[117] J. N. Israelachvili, *Intermolecular and surface forces / Jacob N. Israelachvili.* 3rd. ed. Waltham, MA: Academic Press, 2011.

[118] P. Tengvall, “Protein interactions with biomaterials,” *Comprehensive Biomaterials II*, vol. 4, no. March 2016, pp. 70–84, 2017.

[119] K. J. Aoki, “Frequency-dependence of electric double layer capacitance without Faradaic reactions,” *Journal of Electroanalytical Chemistry*, vol. 779, pp. 117–125, 2016.

[120] A. Velikonja, T. Slivnik, V. Kralj-Iglic, and A. Iglič, “The quadrupole moment of water molecules and the permittivity ofwater near a charged surface Ekaterina Gongadze1,” *Electrochimica Acta*, vol. 109, pp. 656–662, 2013.

[121] S. I. Jeon, J. H. Lee, J. D. Andrade, and P. G. De Gennes, “Protein-surface interactions in the presence of polyethylene oxide. I. Simplified theory,” *Journal of Colloid And Interface Science*, vol. 142, no. 1, pp. 149–158, 1991.

[122] A. W. Sonesson *et al.*, “Protein-surfactant interactions at hydrophobic interfaces studied with total internal reflection fluorescence correlation spectroscopy (TIR-FCS),” *Journal of Colloid and Interface Science*, vol. 317, no. 2, pp. 449–457, 2008.

[123] R. A. Hartvig, M. Van De Weert, J. Østergaard, L. Jorgensen, and H. Jensen, “Protein adsorption at charged surfaces: The role of electrostatic interactions and interfacial charge regulation,” *Langmuir*, vol. 27, no. 6, pp. 2634–2643, 2011.

[124] P. Y. J. Yeh, J. N. Kizhakkedathu, J. D. Madden, and M. Chiao, “Electric field and vibration-assisted nanomolecule desorption and anti-biofouling for biosensor applications,” *Colloids and Surfaces B: Biointerfaces*, vol. 59, no. 1, pp. 67–73, 2007.

[125] J. O. Bockris, M. A. V. Devanathan, and K. Müller, “On the structure of charged interfaces,” *Proceedings of the Royal Society of London. Series A, Mathematical and physical sciences*, vol. 274, no. 1356, pp. 55–79, 1963.

[126] C. J. Van Oss, *Interfacial forces in aqueous media / Carel J. van Oss.* Second edition. Boca Raton, Fla: Taylor & Francis, 2006.

[127] A. T. Poortinga, R. Bos, W. Norde, and H. J. Busscher, *Electric double layer interactions in bacterial adhesion to surfaces*. 2002, vol. 47, pp. 1–32.

[128] R. L. Fournier, *Basic transport phenomena in biomedical engineering / Ronald L. Fournier.* Second edition. New York ; Taylor & Francis, 2007.

[129] M. A. Butkus and D. Grasso, “Impact of aqueous electrolytes on interfacial energy,” *Journal of Colloid and Interface Science*, vol. 200, no. 1, pp. 172–181, 1998.

[130] X. Su and T. A. Hatton, “Electrosorption at functional interfaces: From molecular-level interactions to electrochemical cell design,” *Physical Chemistry Chemical Physics*, vol. 19, no. 35, pp. 23 570–23 584, 2017.

[131] P. M. Claesson, “Interactions between surfaces coated with carbohydrates, glycolipids, and glycoproteins,” in *Biopolymers at Interfaces*, M. Malmsten, Ed., 2nd. ed., Boca Raton: CRC Press, 2003, ch. 7.

[132] C. J. van Oss, “Chapter three - the extended dlvo theory,” in *The Properties of Water and their Role in Colloidal and Biological Systems*, ser. Interface Science and Technology, C. J. van Oss, Ed., vol. 16, Elsevier, 2008, pp. 31–48.

[133] E. A. Vogler, “Structure and reactivity of water at biomaterial surfaces,” *Advances in Colloid and Interface Science*, vol. 74, no. 1-3, pp. 69–117, 1998.

[134] M. Rahmoune and M. Latour, “Application of mechanical waves induced by piezofilms to marine fouling prevention,” *Journal of Intelligent Material Systems and Structures*, vol. 7, no. 1, pp. 33–43, 1996.

[135] C. K. Choi, A. E. English, K. D. Kihm, and C. H. Margraves, “Simultaneous dynamic optical and electrical properties of endothelial cell attachment on indium tin oxide bioelectrodes,” *Journal of Biomedical Optics*, vol. 12, no. 6, p. 64 028, 2007.

[136] S. F. Cogan, “Neural stimulation and recording electrodes,” *Annual Review of Biomedical Engineering*, vol. 10, pp. 275–309, 2008.

[137] P. M. McClatchey, E. S. McClain, I. M. Williams, J. M. GREGORY, D. CLIFFEL, and D. WASSERMAN, “962-p: Continuous glucose monitor readings lag interstitial glucose by several minutes,” *Diabetes (New York, N.Y.)*, vol. 68, no. Supplement 1, pp. 962–, 2019.

[138] J. M. Akers, P. H. Peckham, M. W. Keith, and K. Merritt, “Tissue response to chronically stimulated implanted epimysial and intramuscular electrodes,” *IEEE Transactions on Rehabilitation Engineering*, vol. 5, no. 2, pp. 207–220, 1997.

[139] W. M. Grill and J. Thomas Mortimer, “Electrical properties of implant encapsulation tissue,” *Annals of Biomedical Engineering*, vol. 22, no. 1, pp. 23–33, 1994.

[140] C. R. Bartoli, M. M. Nadar, and J. J. Godleski, “Capsule thickness correlates with vascular density and blood flow within foreign-body capsules surrounding surgically implanted subcutaneous devices,” *Artificial Organs*, vol. 34, no. 10, pp. 857–861, 2010.

[141] D. W. Grainger, “All charged up about implanted biomaterials,” *Nature biotechnology*, vol. 31, no. 6, pp. 507–509, 2013.

[142] P. C. S. Bota *et al.*, “Biomaterial topography alters healing in vivo and monocyte/-macrophage activation in vitro,” *Journal of Biomedical Materials Research - Part A*, vol. 95 A, no. 2, pp. 649–657, 2010.

[143] J. M. Morais, F. Papadimitrakopoulos, and D. J. Burgess, “Biomaterials/tissue interactions: Possible solutions to overcome foreign body response,” *AAPS Journal*, vol. 12, no. 2, pp. 188–196, 2010.

[144] M. J. Van Amerongen, G. Molema, J. Plantinga, H. Moorlag, and M. J. Van Luyn, “Neovascularization and vascular markers in a foreign body reaction to subcutaneously implanted degradable biomaterial in mice,” *Angiogenesis*, vol. 5, no. 3, pp. 173–180, 2002.

[145] C. R. Bartoli and J. J. Godleski, “Blood flow in the foreign-body capsules surrounding surgically implanted subcutaneous devices,” *The Journal of surgical research*, vol. 158, no. 1, pp. 147–154, Jan. 2010.

[146] N. Wisniewski, B. Klitzman, B. Miller, and W. M. Reichert, “Decreased analyte transport through implanted membranes: Differentiation of biofouling from tissue effects,” *Journal of Biomedical Materials Research*, vol. 57, no. 4, pp. 513–521, 2001.

[147] H. L. Prichard, T. Schroeder, W. M. Reichert, and B. Klitzman, “Bioluminescence imaging of glucose in tissue surrounding polyurethane and glucose sensor implants,” *Journal of Diabetes Science and Technology*, vol. 4, no. 5, pp. 1055–1062, 2010.

[148] E. Peltola *et al.*, “Biofouling affects the redox kinetics of outer and inner sphere probes on carbon surfaces drastically differently - implications to biosensing,” *Physical chemistry chemical physics : PCCP*, vol. 22, no. 29, pp. 16 630–16 640, 2020.

[149] H. E. Koschwanez and W. M. Reichert, “In vitro, in vivo and post explantation testing of glucose-detecting biosensors: Current methods and recommendations,” *Biomaterials*, vol. 28, no. 25, pp. 3687–3703, 2007.

[150] P. Dungel, N. Long, B. Yu, Y. Moussy, and F. Moussy, “Study of the effects of tissue reactions on the function of implanted glucose sensors,” *Journal of Biomedical Materials Research - Part A*, vol. 85, no. 3, pp. 699–706, 2008.

[151] C. Gabriel, S. Gabriel, and E. Corthout, “The dielectric properties of biological tissues: I. Literature survey,” *Physics in Medicine and Biology*, vol. 41, no. 11, pp. 2231–2249, 1996.

[152] J. Horn *et al.*, “Comparison of shape memory polymer foam versus bare metal coil treatments in an in vivo porcine sidewall aneurysm model: Comparison of shape memory polymer foam versus bare metal coil treatments,” *Journal of biomedical materials research. Part B, Applied biomaterials*, vol. 105, no. 7, pp. 1892–1905, 2017.

[153] A. K. Means *et al.*, “A self-cleaning, mechanically robust membrane for minimizing the foreign body reaction: towards extending the lifetime of sub-Q glucose biosensors,” *Journal of Materials Science: Materials in Medicine*, vol. 30, no. 7, 2019.

[154] A. Assmann *et al.*, “Acceleration of autologous invivo recellularization of decellularized aortic conduits by fibronectin surface coating,” *Biomaterials*, vol. 34, no. 25, pp. 6015–6026, 2013.

[155] F. B. Karp, N. A. Bernotski, E. A. Lopez, T. I. Valdes, K. F. Böhringer, and B. D. Ratner, “Foreign body response investigated with an implanted biosensor by in situ electrical impedance spectroscopy,” *8th World Biomaterials Congress 2008*, vol. 3, no. 1, p. 1682, 2008.

[156] M. Kubon *et al.*, “A microsensor system to probe physiological environments and tissue response,” *Proceedings of IEEE Sensors*, pp. 2607–2611, 2010.

[157] I. Holland, C. McCormick, and P. Connolly, “Towards non-invasive characterisation of coronary stent re-endothelialisation - an in-vitro, electrical impedance study,” *PloS one*, vol. 13, no. 11, e0206758–e0206758, 2018.

[158] S. Maity and A. Sarkar, *Monitoring fibrous capsule formation*. Elsevier Ltd, 2017, pp. 69–80.

[159] J. W. BENDER, H. I. FRIEDMAN, V. GIURGIUTIU, C. WATSON, M. FITZMAURICE, and M. L. YOST, “The use of biomedical sensors to monitor capsule formation around soft tissue implants,” *Annals of plastic surgery*, vol. 56, no. 1, pp. 72–77, 2006.

[160] D. K. Ahirwar *et al.*, “Non-contact method for directing electrotaxis,” *Scientific Reports*, vol. 5, pp. 1–12, 2015.

[161] A. A. Aly *et al.*, “Effects of 900-MHz radio frequencies on the chemotaxis of human neutrophils in vitro,” *IEEE Transactions on Biomedical Engineering*, vol. 55, no. 2, pp. 795–797, 2008.

[162] C. A. Chen, C. H. Chen, A. M. Ghaemmaghami, and S. K. Fan, “Separation of dendritic and T cells using electrowetting and dielectrophoresis,” *2012 7th IEEE International Conference on Nano/Micro Engineered and Molecular Systems, NEMS 2012*, pp. 183–186, 2012.

[163] F. Cunha, A. M. Rajnicek, and C. D. McCaig, “Electrical stimulation directs migration, enhances and orients cell division and upregulates the chemokine receptors cxcr4 and cxcr2 in endothelial cells,” *Journal of vascular research*, vol. 56, no. 1, pp. 39–53, 2019.

[164] R. K. Shepherd, G. M. Clark, R. C. Black, and J. F. Patrick, “The histopathological effects of chronic electrical stimulation of the cat cochlea,” *The Journal of Laryngology & Otology*, vol. 97, no. 4, pp. 333–342, 1983.

[165] D. B. McCreery, T. G. Yuen, and L. A. Bullara, “Chronic microstimulation in the feline ventral cochlear nucleus: Physiologic and histologic effects,” *Hearing Research*, vol. 149, no. 1-2, pp. 223–238, 2000.

[166] R. N. Andrews, C. C. Co, and C. C. Ho, “Engineering dynamic biointerfaces,” *Current Opinion in Chemical Engineering*, vol. 11, no. Figure 1, pp. 28–33, 2016.

[167] E. Wischerhoff *et al.*, “Controlled cell adhesion on peg-based switchable surfaces,” *Angewandte Chemie International Edition*, vol. 47, no. 30, pp. 5666–5668, 2008.

[168] N. Nath and A. Chilkoti, “Creating "smart" surfaces using stimuli responsive polymers,” *Advanced Materials*, vol. 14, no. 17, pp. 1243–1247, 2002.

[169] Y. Hao, H. Liu, G. Li, H. Cui, L. Jiang, and S. Wang, “Photo and Thermo Dual-Responsive Copolymer Surfaces for Efficient Cell Capture and Release,” *ChemPhysChem*, vol. 19, no. 16, pp. 2107–2112, 2018.

[170] J. Auernheimer, C. Dahmen, U. Hersel, A. Bausch, and H. Kessler, “Photoswitched cell adhesion on surfaces with RGD peptides,” *Journal of the American Chemical Society*, vol. 127, no. 46, pp. 16 107–16 110, 2005.

[171] Y. Ito *et al.*, “Nano-vibration effect on cell adhesion and its shape,” *Bio-medical materials and engineering*, vol. 21, no. 3, pp. 149–158, 2011.

[172] Y. Ito, T. Kimura, K. Nam, A. Katoh, T. Masuzawa, and A. Kishida, “Effects of vibration on differentiation of cultured PC12 cells,” *Biotechnology and Bioengineering*, vol. 108, no. 3, pp. 592–599, 2011.

[173] T. F. Corbiere and T. J. Koh, “Local low-intensity vibration improves healing of muscle injury in mice,” *Physiological Reports*, vol. 8, no. 2, pp. 1–13, 2020.

[174] I. Puhar, L. Ma, D. Suleimenova, V. Chronopoulos, and N. Mattheos, “The effect of local application of low-magnitude high-frequency vibration on the bone healing of rabbit calvarial defects-a pilot study,” *Journal of Orthopaedic Surgery and Research*, vol. 11, no. 1, pp. 1–7, 2016.

[175] S. Kopyl, R. Surmenev, M. Surmeneva, Y. Fetisov, and A. Kholkin, “Magnetoelectric effect: principles and applications in biology and medicine– a review,” *Materials Today Bio*, vol. 12, no. August, p. 100 149, 2021.

[176] D. S. Wong *et al.*, “Magnetically Tuning Tether Mobility of Integrin Ligand Regulates Adhesion, Spreading, and Differentiation of Stem Cells,” *Nano Letters*, vol. 17, no. 3, pp. 1685–1695, 2017.

[177] H. Kang *et al.*, “Remote Control of Multimodal Nanoscale Ligand Oscillations Regulates Stem Cell Adhesion and Differentiation,” *ACS Nano*, vol. 11, no. 10, pp. 9636–9649, 2017.

[178] H. Kang *et al.*, “Remote Manipulation of Ligand Nano-Oscillations Regulates Adhesion and Polarization of Macrophages in Vivo,” *Nano Letters*, vol. 17, no. 10, pp. 6415–6427, 2017.

[179] A. Vinhas, A. F. Almeida, A. I. Gonçalves, M. T. Rodrigues, and M. E. Gomes, “Magnetic stimulation drives macrophage polarization in cell to–cell communication with Il-1β primed tendon cells,” *International Journal of Molecular Sciences*, vol. 21, no. 15, pp. 1–15, 2020.

[180] S. K. Boda, G. Thrivikraman, and B. Basu, “Magnetic field assisted stem cell differentiation - Role of substrate magnetization in osteogenesis,” *Journal of Materials Chemistry B*, vol. 3, no. 16, pp. 3150–3168, 2015.

[181] B. Özkale, M. S. Sakar, and D. J. Mooney, “Active biomaterials for mechanobiology,” *Biomaterials*, vol. 267, no. July 2020, 2021.

[182] F. A. Pennacchio, L. D. Garma, L. Matino, and F. Santoro, “Bioelectronics goes 3D: New trends in cell-chip interface engineering,” *Journal of Materials Chemistry B*, vol. 6, no. 44, pp. 7096–7101, 2018.

[183] D. Wirtz, P. C. Searson, and B. Wildt, “Triggering cell detachment from patterned electrode arrays by programmed subcellular release,” *Nature protocols*, vol. 5, no. 7, pp. 1273–1280, 2010.

[184] Q. Wei *et al.*, “Protein interactions with polymer coatings and biomaterials,” *Angewandte Chemie - International Edition*, vol. 53, no. 31, pp. 8004–8031, 2014.

[185] S. Jeon, J. Lee, J. Andrade, and P. De Gennes, “Protein—surface interactions in the presence of polyethylene oxide: I. simplified theory,” *Journal of colloid and interface science*, vol. 142, no. 1, pp. 149–158, 1991.

[186] R. G. Chapman *et al.*, “Polymeric thin films that resist the adsorption of proteins and the adhesion of bacteria,” *Langmuir*, vol. 17, no. 4, pp. 1225–1233, 2001.

[187] L. Yang *et al.*, “High-throughput methods in the discovery and study of biomaterials and materiobiology,” *Chemical reviews*, vol. 121, no. 8, pp. 4561–4677, 2021.

[188] Q. Zhou, L. Ge, C. F. Guimarães, P. T. Kühn, L. Yang, and P. van Rijn, “Development of a Novel Orthogonal Double Gradient for High-Throughput Screening of Mesenchymal Stem Cells–Materials Interaction,” *Advanced Materials Interfaces*, vol. 5, no. 18, pp. 4–11, 2018.

[189] H. Kaji, M. Kanada, D. Oyamatsu, T. Matsue, and M. Nishizawa, “Microelectrochemical approach to induce local cell adhesion and growth on substrates,” *LANGMUIR*, vol. 20, no. 1, pp. 16–19, Jan. 2004.

[190] C. Zhao *et al.*, “Microelectrochemical modulation of micropatterned cellular environments,” *LANGMUIR*, vol. 24, no. 14, pp. 7605–7613, Jul. 2008.

[191] X. Jiang, R. Ferrigno, M. Mrksich, and G. M. Whitesides, “Electrochemical desorption of self-assembled monolayers noninvasively releases patterned cells from geometrical confinements,” *Journal of the American Chemical Society*, vol. 125, no. 9, pp. 2366–2367, 2003, PMID: 12603104.

[192] M. Gabi, A. Larmagnac, P. Schulte, and J. Vörös, “Electrically controlling cell adhesion, growth and migration,” *Colloids and Surfaces B: Biointerfaces*, vol. 79, no. 2, pp. 365–371, 2010.

[193] S. S. Shah *et al.*, “Micropatterning of Proteins and Mammalian Cells on Indium Tin Oxide,” *ACS APPLIED MATERIALS & INTERFACES*, vol. 1, no. 11, pp. 2592–2601, Nov. 2009.

[194] O. Guillaume-Gentil, M. Gabi, M. Zenobi-Wong, and J. Voeroes, “Electrochemically switchable platform for the micro-patterning and release of heterotypic cell sheets,” *BIOMEDICAL MICRODEVICES*, vol. 13, no. 1, pp. 221–230, Feb. 2011.

[195] S. S. Shah *et al.*, “Exercising spatiotemporal control of cell attachment with optically transparent microelectrodes,” *LANGMUIR*, vol. 24, no. 13, pp. 6837–6844, Jul. 2008.

[196] M. N. Yousaf, B. T. Houseman, and M. Mrksich, “Using electroactive substrates to pattern the attachment of two different cell populations,” *Proceedings of the National Academy of Sciences*, vol. 98, no. 11, pp. 5992–5996, 2001.

[197] W. S. Yeo and M. Mrksich, “Electroactive substrates that reveal aldehyde groups for bio-immobilization,” *Advanced Materials*, vol. 16, no. 15, pp. 1352–1356, 2004.

[198] S. H. Yoon and M. R. K. Mofrad, “Cell adhesion and detachment on gold surfaces modified with a thiol-functionalized RGD peptide,” *Biomaterials*, vol. 32, no. 30, pp. 7286–7296, 2011.

[199] S. S. Shah *et al.*, “Electrochemical release of hepatocyte-on-hydrogel microstructures from ITO substrates,” *ANALYTICAL AND BIOANALYTICAL CHEMISTRY*, vol. 402, no. 5, pp. 1847–1856, Feb. 2012.

[200] W. S. Yeo and M. Mrksich, “Electroactive self-assembled monolayers that permit orthogonal control over the adhesion of cells to patterned substrates,” *Langmuir*, vol. 22, no. 25, pp. 10 816–10 820, 2006.

[201] A. Mahapatro, D. M. Johnson, D. N. Patel, M. D. Feldman, A. A. Ayon, and C. M. Agrawal, “The use of alkanethiol self-assembled monolayers on 316l stainless steel for coronary artery stent nanomedicine applications: An oxidative and in vitro stability study,” *Nanomedicine*, vol. 2, no. 3, pp. 182–190, 2006.

[202] A. Shaver, S. D. Curtis, and N. Arroyo-Currás, “Alkanethiol monolayer end groups affect the long-term operational stability and signaling of electrochemical, aptamer-based sensors in biological fluids,” *ACS applied materials & interfaces*, vol. 12, no. 9, pp. 11 214–11 223, 2020.

[203] K. M. Persson *et al.*, “Electronic Control of Cell Detachment Using a Self-Doped Conducting Polymer,” *ADVANCED MATERIALS*, vol. 23, no. 38, pp. 4403+, Oct. 2011.

[204] Y. Zhu, L. Yao, Z. Liu, W. Weng, and K. Cheng, “Electrical Potential Specified Release of BSA/Hep/Polypyrrole Composite Film and Its Cellular Responses,” *ACS Applied Materials and Interfaces*, vol. 11, no. 28, pp. 25 457–25 464, 2019.

[205] J. Y. Wong, R. Langer, and D. E. Ingber, “Electrically conducting polymers can noninvasively control the shape and growth of mammalian cells,” *Proceedings of the National Academy of Sciences of the United States of America*, vol. 91, no. 8, pp. 3201–3204, 1994.

[206] J. Liao *et al.*, "Reversibly controlling preferential protein adsorption on bone implants by using an applied weak potential as a switch," *Angewandte Chemie (International ed.)*, vol. 53, no. 48, pp. 13 068–13 072, 2014.

[207] Y. Guan, D. Yu, H. Sun, J. Ren, and X. Qu, "Aβ aggregation behavior at interfaces with switchable wettability: a bioinspired perspective to understand amyloid formation," *Chemical Communications*, vol. 57, no. 21, pp. 2641–2644, 2021.

[208] C. L. Yeunz, P. Iqbal, M. Allan, M. Lashkor, J. A. Preece, and P. M. Mendes, "Tuning specific biomolecular interactions using electro-switchable oligopeptide surfaces," *Advanced Functional Materials*, vol. 20, no. 16, pp. 2657–2663, 2010.

[209] A. Pranzetti, M. Davis, C. L. Yeung, J. A. Preece, P. Koelsch, and P. M. Mendes, "Direct Observation of Reversible Biomolecule Switching Controlled by Electrical Stimulus," *Advanced Materials Interfaces*, vol. 1, no. 5, pp. 1–4, 2014.

[210] C. L. Yeung *et al.*, "Modulation of Biointeractions by Electrically Switchable Oligopeptide Surfaces: Structural Requirements and Mechanism," *Advanced Materials Interfaces*, vol. 1, no. 2, pp. 1–7, 2014.

[211] M. Lashkor, F. J. Rawson, A. Stephenson-Brown, J. A. Preece, and P. M. Mendes, "Electrically-driven modulation of surface-grafted RGD peptides for manipulation of cell adhesion," *CHEMICAL COMMUNICATIONS*, vol. 50, no. 98, pp. 15 589–15 592, 2014.

[212] C. C. A. Ng *et al.*, "Using an electrical potential to reversibly switch surfaces between two states for dynamically controlling cell adhesion," *Angewandte Chemie International Edition*, vol. 51, no. 31, pp. 7706–7710, 2012.

[213] L. A. Prezyna, G. E. Wnek, Y. J. Qiu, and J. R. Reynolds, "Interaction of cationic polypeptides with electroactive polypyrrole/poly(styrene sulfonate) and poly(N-methylpyrrole)/poly(styrenesulfonate) films," *Synthetic Metals*, vol. 41, no. 3, pp. 979–981, 1991.

[214] C. E. Schmidt, V. R. Shastri, J. P. Vacanti, and R. Langer, "Stimulation of neurite outgrowth using an electrically conducting polymer (conductive polymer oxidized polypyrrole nerve regeneratio pc-12 cell electrical stimulatio neuronal stimulation)," *Applied Biological Sciences*, vol. 94, no. August, pp. 8948–8953, 1997.

[215] S. Sirivisoot, R. Pareta, and T. J. Webster, “Electrically controlled drug release from nanostructured polypyrrole coated on titanium,” *Nanotechnology*, vol. 22, no. 8, 2011.

[216] Y. Li, K. G. Neoh, and E. T. Kang, “Plasma protein adsorption and thrombus formation on surface functionalized polypyrrole with and without electrical stimulation,” *Journal of Colloid and Interface Science*, vol. 275, no. 2, pp. 488–495, 2004.

[217] Z. Zhou, W. Li, T. He, P. Yu, G. Tan, and C. Ning, “Controllable Protein Adsorption and Bacterial Adhesion on Polypyrrole Nanocone Arrays,” *Journal of Materials Science and Technology*, vol. 32, no. 9, pp. 950–955, 2016.

[218] X. Liu, K. J. Gilmore, S. E. Moulton, and G. G. Wallace, “Electrical stimulation promotes nerve cell differentiation on polypyrrole/poly (2-methoxy-5 aniline sulfonic acid) composites,” *Journal of Neural Engineering*, vol. 6, no. 6, 2009.

[219] J. Baumgartner, J. I. Jönsson, and E. W. Jager, “Switchable presentation of cytokines on electroactive polypyrrole surfaces for hematopoietic stem and progenitor cells,” *Journal of Materials Chemistry B*, vol. 6, no. 28, pp. 4665–4675, 2018.

[220] A. M. Wan, D. J. Brooks, A. Gumus, C. Fischbach, and G. G. Malliaras, “Electrical control of cell density gradients on a conducting polymer surface,” *Chemical Communications*, no. 35, pp. 5278–5280, 2009.

[221] A. M. Wan, R. M. Schur, C. K. Ober, C. Fischbach, D. Gourdon, and G. G. Malliaras, “Electrical control of protein conformation,” *Advanced Materials*, vol. 24, no. 18, pp. 2501–2505, 2012.

[222] M. ElMahmoudy *et al.*, “Electrically controlled cellular migration on a periodically micropatterned PEDOT:PSS conducting polymer platform,” *Journal of Applied Polymer Science*, vol. 136, no. 5, pp. 1–10, 2019.

[223] Y. Hao *et al.*, “Electrochemical Responsive Superhydrophilic Surfaces of Polythiophene Derivatives towards Cell Capture and Release,” *ChemPhysChem*, vol. 19, no. 16, pp. 2046–2051, 2018.

[224] D. R. Merrill, M. Bikson, and J. G. R. Jefferys, “Electrical stimulation of excitable tissue: Design of efficacious and safe protocols,” *Journal of Neuroscience Methods*, vol. 141, no. 2, pp. 171–198, 2005.

[225] B. Cortese, I. E. Palamà, S. D'Amone, and G. Gigli, "Influence of electrotaxis on cell behaviour," *Integrative Biology (United Kingdom)*, vol. 6, no. 9, pp. 817–830, 2014.

[226] M. Zhao *et al.*, "Electrical signals control wound healing through phosphatidylinositol-3-OH kinase-γ and PTEN," *Nature*, vol. 442, no. 7101, pp. 457–460, 2006.

[227] S. Koyama and M. Aizawa, "Physical modulation of cellular information networks," in *Bioengineering in Cell and Tissue Research*, Berlin, Heidelberg: Springer Berlin Heidelberg, pp. 37–61.

[228] S. Koyama, "Electrically modulated attachment and detachment of animal cells cultured on an optically transparent patterning electrode," *Journal of Bioscience and Bioengineering*, vol. 111, no. 5, pp. 574–583, 2011.

[229] N. Holmström, A. Askendal, and P. Tengvall, "In vitro studies on blood protein adsorption to gold and pyrolytic carbon at pre-set electrical potentials," *Colloids and Surfaces B: Biointerfaces*, vol. 11, no. 5, pp. 265–271, 1998.

[230] A. Kotwal and C. E. Schmidt, "Electrical stimulation alters protein adsorption and nerve cell interactions with electrically conducting biomaterials," *Biomaterials*, vol. 22, no. 10, pp. 1055–1064, 2001.

[231] B. Beykal, M. Herzberg, Y. Oren, and M. S. Mauter, "Influence of surface charge on the rate, extent, and structure of adsorbed Bovine Serum Albumin to gold electrodes," *Journal of Colloid and Interface Science*, vol. 460, pp. 321–328, 2015.

[232] A. Pranzetti *et al.*, "An electrically reversible switchable surface to control and study early bacterial adhesion dynamics in real-time," *Advanced Materials*, vol. 25, no. 15, pp. 2181–2185, 2013.

[233] I. Gall, M. Herzberg, and Y. Oren, "The effect of electric fields on bacterial attachment to conductive surfaces," *Soft Matter*, vol. 9, no. 8, pp. 2443–2452, 2013.

[234] S. Koyama *et al.*, "Attachment and Detachment of Living Microorganisms Using a Potential-Controlled Electrode," *Marine Biotechnology*, vol. 15, no. 4, pp. 461–475, 2013.

[235] A. Y. Tsivadze *et al.*, “Electrochemical activity and morphology of human erythrocytes at optically transparent ITO electrode,” *Doklady Physical Chemistry*, vol. 477, no. 1, pp. 201–204, 2017.

[236] C. Thamaraiselvan, A. Ronen, S. Lerman, M. Balaish, Y. Ein-Eli, and C. G. Dosoretz, “Low voltage electric potential as a driving force to hinder biofouling in self-supporting carbon nanotube membranes,” *Water Research*, vol. 129, pp. 143–153, 2018.

[237] L. Koefoed, S. U. Pedersen, and K. Daasbjerg, “Bipolar electrochemistry—A wireless approach for electrode reactions,” *Current Opinion in Electrochemistry*, vol. 2, no. 1, pp. 13–17, 2017.

[238] L. Abad, A. M. Rajnicek, and N. Casañ-Pastor, “Electric field gradients and bipolar electrochemistry effects on neural growth: A finite element study on immersed electroactive conducting electrode materials,” *Electrochimica Acta*, vol. 317, pp. 102–111, 2019.

[239] S. Guette-Marquet, R. Basseguy, C. Roques, and A. Bergel, “The electrochemical potential is a key parameter for cell adhesion and proliferation on carbon surface,” *Bioelectrochemistry*, vol. 144, p. 108 045, 2022.

[240] T. L. Rose, E. M. Kelliher, and L. S. Robblee, “Assessment of capacitor electrodes for intracortical neural stimulation,” *Journal of Neuroscience Methods*, vol. 12, no. 3, pp. 181–193, 1985.

[241] I. De, P. Sharma, and M. Singh, “Emerging approaches of neural regeneration using physical stimulations solely or coupled with smart piezoelectric nano-biomaterials,” *European Journal of Pharmaceutics and Biopharmaceutics*, vol. 173, no. May 2021, pp. 73–91, 2022.

[242] C. Ribeiro, V. Sencadas, D. M. Correia, and S. Lanceros-Méndez, “Piezoelectric polymers as biomaterials for tissue engineering applications,” *Colloids and Surfaces B: Biointerfaces*, vol. 136, pp. 46–55, 2015.

[243] C. Ribeiro *et al.*, “Dynamic piezoelectric stimulation enhances osteogenic differentiation of human adipose stem cells,” *Journal of Biomedical Materials Research - Part A*, vol. 103, no. 6, pp. 2172–2175, 2015.

[244] G. Xia, B. Song, and J. Fang, “Electrical Stimulation Enabled via Electrospun Piezoelectric Polymeric Nanofibers for Tissue Regeneration,” *Research*, vol. 2022, pp. 1–23, 2022.

[245] B. N. Johnson and R. Mutharasan, “Reduction of nonspecific protein adsorption on cantilever biosensors caused by transverse resonant mode vibration,” *Analyst*, vol. 139, no. 5, pp. 1112–1120, 2014.

[246] M. Acosta *et al.*, “Cytotoxicity, chemical stability, and surface properties of ferroelectric ceramics for biomaterials,” *Journal of the American Ceramic Society*, vol. 101, no. 1, pp. 440–449, 2018.

[247] P. Saxena and P. Shukla, “A comprehensive review on fundamental properties and applications of poly(vinylidene fluoride) (PVDF),” *Advanced Composites and Hybrid Materials*, vol. 4, no. 1, pp. 8–26, 2021.

[248] P. K. Szewczyk *et al.*, “Surface-Potential-Controlled Cell Proliferation and Collagen Mineralization on Electrospun Polyvinylidene Fluoride (PVDF) Fiber Scaffolds for Bone Regeneration,” *ACS Biomaterials Science and Engineering*, vol. 5, no. 2, pp. 582–593, 2019.

[249] R. F. Valentini, T. G. Vargo, J. A. Gardella, and P. Aebischer, “Patterned neuronal attachment and outgrowth on surface modified, electrically charged fluoropolymer substrates,” *Journal of biomaterials science. Polymer ed.*, vol. 5, no. 1-2, pp. 13–36, 1994.

[250] P. Aebischer, R. F. Valentini, P. Dario, C. Domenici, and P. M. Galletti, “Piezoelectric guidance channels enhance regeneration in the mouse sciatic nerve after axotomy,” *Brain Research*, vol. 436, no. 1, pp. 165–168, 1987.

[251] E. G. Fine, R. F. Valentini, R. Bellamkonda, and P. Aebischer, “Improved nerve regeneration through piezoelectric vinylidenefluoride-trifluoroethylene copolymer guidance channels,” *Biomaterials*, vol. 12, no. 8, pp. 775–780, 1991.

[252] K. Zhang *et al.*, “A spatially varying charge model for regulating site-selective protein adsorption and cell behaviors,” *Biomaterials Science*, vol. 7, no. 3, pp. 876–888, 2019.

[253] J. Li *et al.*, “Surface Charge Regulation of Osteogenic Differentiation of Mesenchymal Stem Cell on Polarized Ferroelectric Crystal Substrate,” *Advanced Healthcare Materials*, vol. 4, no. 7, pp. 998–1003, 2015.

[254] A. Singh and A. K. Dubey, “Improved antibacterial and cellular response of electrets and piezobioceramics,” *Journal of biomaterials applications*, vol. 36, no. 3, pp. 441–459, 2021.

[255] C. Zhang *et al.*, “A Novel Approach to Enhance Bone Regeneration by Controlling the Polarity of GaN/AlGaN Heterostructures,” *Advanced Functional Materials*, vol. 31, no. 5, pp. 1–12, 2021.

[256] C. Ning *et al.*, “Built-in microscale electrostatic fields induced by anatase-rutile-phase transition in selective areas promote osteogenesis,” *NPG Asia Materials*, vol. 8, no. September 2015, 2016.

[257] R. Kapur, J. Lilien, and J. Black, “Field-dependent fibroblast orientation on charged surfaces is independent of polarity and adsorbed serum proteins,” *Biomaterials*, vol. 14, no. 11, pp. 854–860, 1993.

[258] R. Kapur, J. Lilien, G. L. Picciolo, and J. Black, “Human monocyte morphology is affected by local substrate charge heterogeneity,” *Journal of Biomedical Materials Research*, vol. 32, no. 1, pp. 133–142, 1996.

[259] Q. Qiu, M. Sayer, M. Kawaja, X. Shen, and J. E. Davies, “Attachment, morphology, and protein expression of rat marrow stromal cells cultured on charged substrate surfaces,” *Journal of Biomedical Materials Research*, vol. 42, no. 1, pp. 117–127, 1998.

[260] M. Xian *et al.*, “Electrical Field Induce mBMSCs Differentiation to Osteoblast via Protein Adsorption Enhancement,” *Colloids and Surfaces B: Biointerfaces*, vol. 209, no. P2, p. 112 158, 2021.

[261] R. F. Valentini, P. Aebischer, T. G. Vargo, and J. A. Gardella, “Patterned neuronal attachment and outgrowth on surface modified, electrically charged fluoropolymer substrates,” *Journal of Biomaterials Science, Polymer Edition*, vol. 5, no. 1-2, pp. 13–36, 1994.

[262] X. Zhang *et al.*, “Piezoelectric Nanotopography Induced Neuron-Like Differentiation of Stem Cells,” *Advanced Functional Materials*, vol. 29, no. 22, pp. 1–10, 2019.

[263] A. K. Dubey, P. Agrawal, R. D. K. Misra, and B. Basu, “Pulsed electric field mediated in vitro cellular response of fibroblast and osteoblast-like cells on conducting austenitic stainless steel substrate,” *Journal of Materials Science: Materials in Medicine*, vol. 24, no. 7, pp. 1789–1798, 2013.

[264] S. Gribi, S. du Bois de Dunilac, D. Ghezzi, and S. P. Lacour, “A microfabricated nerve-on-a-chip platform for rapid assessment of neural conduction in explanted peripheral nerve fibers,” *Nature Communications*, vol. 9, no. 1, pp. 1–10, 2018.

[265] G. M. Xiong, A. T. Do, J. K. Wang, C. L. Yeoh, K. S. Yeo, and C. Choong, “Development of a miniaturized stimulation device for electrical stimulation of cells,” *Journal of biological engineering*, vol. 9, no. 1, pp. 14–14, 2015.

[266] J. Y. Wong, R. Langer, and D. E. Ingber, “Electrically conducting polymers can noninvasively control the shape and growth of mammalian cells.,” *Proceedings of the National Academy of Sciences*, vol. 91, no. 8, pp. 3201–3204, 1994.

[267] T. J. Zajdel, G. Shim, and D. J. Cohen, “Come together: On-chip bioelectric wound closure,” *Biosensors and Bioelectronics*, vol. 192, no. July, p. 113 479, 2021.

[268] S. Jain, A. Sharma, and B. Basu, “Vertical electric field stimulated neural cell functionality on porous amorphous carbon electrodes,” *Biomaterials*, vol. 34, no. 37, pp. 9252–9263, 2013.

[269] A. N. Kuzovlev, A. K. Evseev, I. V. Goroncharovskaya, A. K. Shabanov, and S. S. Petrikov, “Optically transparent electrodes to study living cells: A mini review,” *Biotechnology and Bioengineering*, vol. 118, no. 7, pp. 2393–2400, 2021.

[270] D. Mergel, “Thin films of ITO as transparent electrodes,” *Vakuum in Forschung und Praxis*, vol. 18, no. SUPPL. 1, pp. 15–18, 2006.

[271] Y. Temiz, R. D. Lovchik, G. V. Kaigala, and E. Delamarche, “Lab-on-a-chip devices: How to close and plug the lab?” *Microelectronic Engineering*, vol. 132, pp. 156–175, 2015.

[272] M. Köfferlein, *Klayout*, version 0.25, Nov. 12, 2017.

[273] SAMTEC, *Samtec hsec8-ra brochure*, https://suddendocs.samtec.com/catalog_english/hsec8_ra.pdf, Accessed: 2021-07-16, 2021.

[274] Y. Li, *Developing cmos compatible electro wetting-on-dielectric (ewod) microfluidic technology / yifan li.* 2007.

[275] B. Columbia, "The determination of the thickness, dielectric constant, and other properties of anodic oxide films on tantalum from the interference colours," *Proceedings of the Royal Society of London. Series A. Mathematical and Physical Sciences*, vol. 244, no. 1236, pp. 41–53, 1958.

[276] S. Dueñas, E. Castán, J. Barbolla, R. R. Kola, and P. A. Sullivan, "Tantalum pentoxide obtained from TaNx and TaSi2 anodisation: An inexpensive and thermally stable high k dielectric," *Solid-State Electronics*, vol. 45, no. 8, pp. 1441–1450, 2001.

[277] P. Virtanen *et al.*, "SciPy 1.0: Fundamental Algorithms for Scientific Computing in Python," *Nature Methods*, vol. 17, pp. 261–272, 2020.

[278] R. Pethig, *Introductory bioelectronics : for engineers and physical scientists / Ronald Pethig, Stewart Smith.* Chichester: J. Wiley, 2012.

[279] A. Stalder, T. Melchior, M. Müller, D. Sage, T. Blu, and M. Unser, "Low-bond axisymmetric drop shape analysis for surface tension and contact angle measurements of sessile drops," *Colloids and Surfaces A: Physicochemical and Engineering Aspects*, vol. 364, no. 1-3, pp. 72–81, Jul. 2010, http://bigwww.epfl.ch/publications/stalder1001.html.

[280] J. Schindelin *et al.*, "Fiji: An open-source platform for biological-image analysis," *Nature methods*, vol. 9, no. 7, pp. 676–682, 2012.

[281] Chemours, *Teflon af technical brochure*, https://www.teflon.com/en/-/media/files/teflon/teflon-af-solutions-product-info.pdf?rev=d9599cbc84714bdfb582ccf47
Accessed: 2021-07-16, 2021.

[282] AGC Chemicals Inc., *Cytop fluoropolymer technical brochure*, https://www.agc-chemicals.com/file.jsp?id=file/Cytop_tech15_EN.pdf, Accessed: 2021-07-11, 2021.

[283] D. Han and S. Y. Moon, “Rapid formation of transparent superhydrophobic film on glasses by he/ch4/c4f8 plasma deposition at atmospheric pressure,” *Plasma processes and polymers*, vol. 12, no. 2, pp. 172–179, 2015.

[284] S. ZIMMERMANN *et al.*, “Influence of the additives argon, o2, c4f8, h2, n2 and co on plasma conditions and process results during the etch of sicoh in cf4 plasma,” *Microelectronic engineering*, vol. 88, no. 5, pp. 671–676, 2011.

[285] D. Nečas and P. Klapetek, “Gwyddion: An open-source software for spm data analysis,” *Open Physics*, vol. 10, no. 1, pp. 181–188, 2012.

[286] S. Zhao *et al.*, “Electrotaxis-on-a-chip (etc): An integrated quantitative high-throughput screening platform for electrical field-directed cell migration,” *Lab on a chip*, vol. 14, no. 22, pp. 4398–4405, 2014.

[287] T. J. Zajdel, G. Shim, and D. J. Cohen, “Come together: On-chip bioelectric wound closure,” *Biosensors and Bioelectronics*, vol. 192, p. 113 479, 2021.

[288] V. Balasubramanian, P.-F. Ruedi, Y. Temiz, A. Ferretti, C. Guiducci, and C. C. Enz, “A 0.18 <formula formulatype="inline"><tex notation="tex">μm</tex></formula> biosensor front-end based on <formula formulatype="inline"><tex notation="tex">$1/f$</tex></formula> noise, distortion cancelation and chopper stabilization techniques,” *IEEE Transactions on Biomedical Circuits and Systems*, vol. 7, no. 5, pp. 660–673, 2013.

[289] Y. Li *et al.*, “Wireless Driven EWOD Technology for MEMS Pond Skater Application MEMS actuators can . . .,” pp. 306–309, 2008.

[290] T. G. Vladkova, “Surface engineered polymeric biomaterials with improved biocontact properties,” *International Journal of Polymer Science*, vol. 2010, 2010.

[291] F. Mugele and J. C. Baret, “Electrowetting: From basics to applications,” *Journal of Physics Condensed Matter*, vol. 17, no. 28, 2005.

[292] L. Young, “Anodization Constants for Tantalum,” *Journal of The Electrochemical Society*, vol. 124, no. 4, pp. 528–529, 1977.

[293] C. Chaneliere, J. L. Autran, R. A. Devine, and B. Balland, “Tantalum pentoxide (Ta2O5) thin films for advanced dielectric applications,” *Materials Science and Engineering R: Reports*, vol. 22, no. 6, pp. 269–322, 1998.

[294] J. D. Sloppy, Z. Lu, E. C. Dickey, and D. D. MacDonald, “Growth mechanism of anodic tantalum pentoxide formed in phosphoric acid,” *Electrochimica Acta*, vol. 87, pp. 82–91, 2013.

[295] B. Ilic, D. Czaplewski, P. Neuzil, T. Stanczyk, J. Blough, and G. J. Maclay, “Preparation and characterization of platinum black electrodes,” *Journal of Materials Science*, vol. 35, no. 14, pp. 3447–3457, 2000.

[296] S. E. Stanca *et al.*, “Chemical and Electrochemical Synthesis of Platinum Black /639/638/161 /639/638/224 /639/301/357/537 /145 article,” *Scientific Reports*, vol. 7, no. 1, pp. 1–8, 2017.

[297] J. C. Everts and M. Ravnik, “Complex electric double layers in charged topological colloids,” *Scientific Reports*, vol. 8, no. 1, pp. 1–10, 2018.

[298] E. Oishi, N. Araki, T. Goto, H. Awano, and T. Takahashi, “The Effect of the Terminal Functional Groups on Fluoropolymer on Electrowetting Device Performance,” *Technologies*, vol. 7, no. 3, p. 52, 2019.

[299] S. Zanini, R. Barni, R. D. Pergola, and C. Riccardi, “Modification of the PTFE wettability by oxygen plasma treatments: Influence of the operating parameters and investigation of the ageing behaviour,” *Journal of Physics D: Applied Physics*, vol. 47, no. 32, 2014.

[300] T. Chandy, G. S. Das, R. F. Wilson, and G. H. Rao, “Use of plasma glow for surface-engineering biomolecules to enhance bloodcompatibility of Dacron and PTFE vascular prosthesis,” *Biomaterials*, vol. 21, no. 7, pp. 699–712, 2000.

[301] H. Yasuda and M. Gazicki, “Biomedical applications of plasma polymerization and plasma treatment of polymer surfaces,” *Biomaterials*, vol. 3, no. 2, pp. 68–77, 1982.

[302] F. Liu and D. W. Grainger, “Fluorinated biomaterials,” *Comprehensive Biomaterials II*, vol. 1, no. August 2016, pp. 648–663, 2017.

[303] V. F. Cardoso, D. M. Correia, C. Ribeiro, M. M. Fernandes, and S. Lanceros-Méndez, “Fluorinated polymers as smart materials for advanced biomedical applications,” *Polymers*, vol. 10, no. 2, pp. 1–26, 2018.

[304] V. H. Dalvi and P. J. Rossky, “Molecular origins of fluorocarbon hydrophobicity,” *Proceedings of the National Academy of Sciences of the United States of America*, vol. 107, no. 31, pp. 13 603–13 607, 2010.

[305] M. A. Butkus and D. Grasso, “Impact of aqueous electrolytes on interfacial energy,” *Journal of colloid and interface science*, vol. 200, no. 1, pp. 172–181, 1998.

[306] T. Chandy, G. S. Das, R. F. Wilson, and G. H. Rao, “Use of plasma glow for surface-engineering biomolecules to enhance bloodcompatibility of dacron and ptfe vascular prosthesis,” *Biomaterials*, vol. 21, no. 7, pp. 699–712, 2000.

[307] J. M. Legeais, L. P. Werner, G. Legeay, B. Briat, and G. Renard, “In vivo study of a fluorocarbon polymer-coated intraocular lens in a rabbit model,” *Journal of Cataract and Refractive Surgery*, vol. 24, no. 3, pp. 371–379, 1998.

[308] J. B. Chae, J. O. Kwon, J. S. Yang, D. Kim, K. Rhee, and S. K. Chung, “Optimum thickness of hydrophobic layer for operating voltage reduction in EWOD systems,” *Sensors and Actuators, A: Physical*, vol. 215, pp. 8–16, 2014.

[309] H. Wu *et al.*, “Electrically controlled localized charge trapping at amorphous fluoropolymer–electrolyte interfaces,” *Small (Weinheim an der Bergstrasse, Germany)*, vol. 16, no. 2, e1905726–n/a, 2020.

[310] Y. Sakane, Y. Suzuki, and N. Kasagi, “The development of a high-performance perfluorinated polymer electret and its application to micro power generation,” *Journal of Micromechanics and Microengineering*, vol. 18, no. 10, 2008.

[311] K. Y. Law and H. Zhao, *Surface wetting: Characterization, contact angle, and fundamentals*. 2015, pp. 1–162.

[312] G. S. Tzeng, H. J. Chen, Y. Y. Wang, and C. C. Wan, “The effects of roughening on teflon surfaces,” *Surface and Coatings Technology*, vol. 89, no. 1-2, pp. 108–113, 1997.

[313] I. Muzammil *et al.*, “Tunable surface chemistry and wettability of octafluorocyclobutane and acrylic acid copolymer combined LDPE substrate by pulsed plasma polymerization,” *Journal of Coatings Technology and Research*, vol. 17, no. 3, pp. 621–632, 2020.

[314] R. E. Hirschberg, M. Scharnberg, S. Schröder, S. Rehders, T. Strunskus, and F. Faupel, "Electret films with extremely high charge stability prepared by thermal evaporation of Teflon AF," *Organic Electronics*, vol. 57, no. November 2017, pp. 146–150, 2018.

[315] CiteAb Ltd., *Top 100 cited cell lines in 2021*, https://blog.citeab.com/top-100-cited-cell-lines-of-2021/, Accessed: 2023-01-15, 2022.

[316] J. R. Marland *et al.*, "Real-time measurement of tumour hypoxia using an implantable microfabricated oxygen sensor," *Sensing and Bio-Sensing Research*, vol. 30, p. 100 375, 2020.

[317] A. Bairoch, "The cellosaurus, a cell-line knowledge resource," *Journal of biomolecular techniques*, vol. 29, no. 2, pp. 25–38, 2018.

[318] J. Canny, "A computational approach to edge detection," *IEEE transactions on pattern analysis and machine intelligence*, vol. PAMI-8, no. 6, pp. 679–698, 1986.

[319] K. Wada, *labelme: Image Polygonal Annotation with Python*, https://github.com/wkentaro/labelme, 2016.

[320] BioTek®, *Using Phenol Red to Assess pH in Tissue Culture Media*, https://www.biotek.com/assets/tech_resources/Phenol%20Red%20Basics%20App_Note.pdf, Accessed: 2021-11-10, 2018.

[321] B. L. WELCH, "The generalisation of student's problems when several different population variances are involved," *Biometrika*, vol. 34, no. 1-2, pp. 28–35, 1947.

[322] *Dowsil ™ 3140 rtv coating: Technical data sheet*, 11-3214-01 D, 2018.

[323] X. Liu *et al.*, "A comparison of in vitro cytotoxicity assays in medical device regulatory studies," *Regulatory Toxicology and Pharmacology*, vol. 97, no. June, pp. 24–32, 2018.

[324] H. Cui, Y. Qin, G. L. Liu, and G. W. Padua, "MDA-MB-231 and HeLa cells attachment to nanostructured zein surfaces," *Journal of Bioactive and Compatible Polymers*, vol. 33, no. 4, pp. 361–370, 2018.

[325] K. K. Treloar and M. J. Simpson, "Sensitivity of Edge Detection Methods for Quantifying Cell Migration Assays," *PLoS ONE*, vol. 8, no. 6, 2013.

[326] F. D'Anselmi *et al.*, "Metabolism and cell shape in cancer: A fractal analysis," *International Journal of Biochemistry and Cell Biology*, vol. 43, no. 7, pp. 1052–1058, 2011.

[327] W. Chen *et al.*, "Nanoroughened surfaces for efficient capture of circulating tumor cells without using capture antibodies," *ACS Nano*, vol. 7, no. 1, pp. 566–575, 2013.

[328] C. Sanchez *et al.*, "Oblique illumination in microscopy: A quantitative evaluation," *Micron (Oxford, England : 1993)*, vol. 105, pp. 47–54, 2018.

[329] M. Imaninezhad, J. Schober, D. Griggs, P. Ruminski, I. Kuljanishvili, and S. P. Zustiak, "Cell attachment and spreading on carbon nanotubes is facilitated by integrin binding," *Frontiers in bioengineering and biotechnology*, vol. 6, pp. 129–129, 2018.

[330] X. Liu, J. Y. Lim, H. J. Donahue, R. Dhurjati, A. M. Mastro, and E. A. Vogler, "Influence of substratum surface chemistry/energy and topography on the human fetal osteoblastic cell line hFOB 1.19: Phenotypic and genotypic responses observed in vitro," *Biomaterials*, vol. 28, no. 31, pp. 4535–4550, 2007.

[331] J. Flusser, T. Suk, and B. Zitová, *2D and 3D Image Analysis by Moments*. 2016, pp. 1–529.

[332] G. Weitz-Schmidt and S. Chreng, *Cell adhesion assays*. 2011, vol. 757, pp. 15–30.

[333] M. Bizjak, P. Malavašič, K. Dolinar, J. Pohar, S. Pirkmajer, and M. Pavlin, "Combined treatment with Metformin and 2-deoxy glucose induces detachment of viable MDA-MB-231 breast cancer cells in vitro," *Scientific Reports*, vol. 7, no. 1, pp. 1–14, 2017.

[334] N. I. DeNardis, J. P. Ilić, I. Ružić, and G. Pletikapić, "Cell adhesion and spreading at a charged interface: Insight into the mechanism using surface techniques and mathematical modelling," *Electrochimica Acta*, vol. 176, pp. 743–754, 2015.

[335] V. Svetličić, N. Ivošević, S. Kovač, and V. Žutić, "Charge displacement by adhesion and spreading of a cell," *Bioelectrochemistry*, vol. 53, no. 1, pp. 79–86, 2001.

[336] N. Ke, X. Wang, X. Xu, and Y. A. Abassi, "The xcelligence system for real-time and label-free monitoring of cell viability," *Mammalian Cell Viability*, Methods in Molecular Biology, vol. 740, pp. 33–43, 2011.

[337] Y. Abassi, “Dynamic Monitoring of Cell Adhesion and Spreading,” *Biochemica*, vol. 1, no. Lm, pp. 17–19, 2009.

[338] A. Kulpa and N. Jaeger, “Comparison of the optical properties of tantalum pentoxide, ta 2o 5, anodically grown from e-beam deposited tantalum, ta, with ta 2o 5 e-beam deposited from a ta 2o 5 source,” in *ECS Transactions*, vol. 41, 2011, pp. 311–314.

[339] X. Zheng, H. Baker, W. S. Hancock, F. Fawaz, M. McCaman, and E. Pungor, “Proteomic analysis for the assessment of different lots of fetal bovine serum as a raw material for cell culture. Part IV. Application of proteomics to the manufacture of biological drugs,” *Biotechnology Progress*, vol. 22, no. 5, pp. 1294–1300, 2006.

[340] G. McHale, C. V. Brown, M. I. Newton, G. G. Wells, and N. Sampara, “Dielectrowetting driven spreading of droplets,” *Physical Review Letters*, vol. 107, no. 18, pp. 1–4, 2011.

[341] S. De Vitis *et al.*, “Surface enhanced Raman spectroscopy measurements of MCF7 cells adhesion in confined micro-environments,” *Optics and Lasers in Engineering*, vol. 76, pp. 9–16, 2016.

[342] M. Hervy, “Modulation of cell structure and function in response to substrate stiffness and external forces,” *Journal of Adhesion Science and Technology*, vol. 24, no. 5, pp. 963–973, 2010.

[343] J. Kobayashi, Y. Arisaka, N. Yui, Y. Akiyama, M. Yamato, and T. Okano, “Effect of temperature changes on serum protein adsorption on thermoresponsive cell-culture surfaces monitored by a quartz crystal microbalance with dissipation,” *International journal of molecular sciences*, vol. 19, no. 5, May 2018.

[344] Y. Kurashina, M. Hirano, C. Imashiro, K. Totani, J. Komotori, and K. Takemura, “Enzyme-free cell detachment mediated by resonance vibration with temperature modulation,” *Biotechnology and Bioengineering*, vol. 114, no. 10, pp. 2279–2288, 2017.

[345] O. I. Aleksandrova, S. A. Aleksandrova, V. P. Khomutov, M. S. Morgunov, and M. I. Blinova, “Viability of Different Types of Cells Cultivated on the Surface of Medical Electret,” *Technical Physics*, vol. 63, no. 9, pp. 1304–1310, 2018.

[346] J. Pu, C. D. McCaig, L. Cao, Z. Zhao, J. E. Segall, and M. Zhao, “EGF receptor signalling is essential for electric-field-directed migration of breast cancer cells,” *Journal of Cell Science*, vol. 120, no. 19, pp. 3395–3403, 2007.

[347] D. Wu, X. Ma, and F. Lin, “DC Electric Fields Direct Breast Cancer Cell Migration, Induce EGFR Polarization, and Increase the Intracellular Level of Calcium Ions,” *Cell Biochemistry and Biophysics*, vol. 67, no. 3, pp. 1115–1125, 2013.

[348] B. Zhang, Y. Li, and F. Wang, “Electrochemical corrosion behaviour of microcrystalline aluminium in acidic solutions,” *Corrosion science*, vol. 49, no. 5, pp. 2071–2082, 2007.

[349] B. Zhang, Y. Li, and F. Wang, “Electrochemical corrosion behaviour of microcrystalline aluminium in acidic solutions,” *Corrosion Science*, vol. 49, no. 5, pp. 2071–2082, 2007.

[350] L. Yu *et al.*, “Metabolomic analysis reveals the mechanism of aluminum cytotoxicity in HT-29 cells,” *PeerJ*, vol. 2019, no. 8, pp. 1–20, 2019.

[351] B. Song, Y. Gu, J. Pu, B. Reid, Z. Zhao, and M. Zhao, “Application of direct current electric fields to cells and tissues in vitro and modulation of wound electric field in vivo,” *Nature Protocols*, vol. 2, no. 6, pp. 1479–1489, 2007.

[352] A. C. Ribeiro, A. J. Valente, A. J. Sobral, V. M. Lobo, H. D. Burrows, and M. A. Esteso, “Diffusion coefficients of aluminium chloride in aqueous solutions at 298.15, 303.15 and 315.15k,” *Electrochimica Acta*, vol. 52, no. 23, pp. 6450–6455, 2007.

[353] S. L. Payne, M. Levin, and M. J. Oudin, “Bioelectric Control of Metastasis in Solid Tumors,” *Bioelectricity*, vol. 1, no. 3, pp. 114–130, 2019.

[354] E. Vargas-Accarino, C. Herrera-Montávez, S. R. Y. Cajal, and T. Aasen, “Spontaneous cell detachment and reattachment in cancer cell lines: An in vitro model of metastasis and malignancy,” *International Journal of Molecular Sciences*, vol. 22, no. 9, pp. 1–19, 2021.

[355] K. Zhu, N. R. Hum, B. Reid, Q. Sun, G. G. Loots, and M. Zhao, “Electric Fields at Breast Cancer and Cancer Cell Collective Galvanotaxis,” *Scientific Reports*, vol. 10, no. 1, pp. 1–11, 2020.

[356] I. Dobrzyńska, E. Skrzydlewska, and Z. A. Figaszewski, “Changes in electric properties of human breast cancer cells,” *Journal of Membrane Biology*, vol. 246, no. 2, pp. 161–166, 2013.

[357] J. Parssinen *et al.*, “Enhancement of adhesion and promotion of osteogenic differentiation of human adipose stem cells by poled electroactive poly(vinylidene fluoride),” *Journal of Biomedical Materials Research - Part A*, vol. 103, no. 3, pp. 919–928, 2015.

[358] “Spontaneous electrification of fluoropolymer-water interfaces probed by electrowetting,” *Faraday discussions*, vol. 199, pp. 29–47, 2017.

[359] L. H. Gabrielli, *Gdspy*, GitHub repository: `https://github.com/heitzmann/gdspy`, 2020.

[360] J. Okudaira Sadayuki (Ome, J. Kawakami Hiroshi (Hachioji, J. Kure Tokuo (Tokyo, J. Tsujimoto Kazunori (Higashiyamato, and J. Tachi Shinichi (Sayama, “Dry etching by alternately etching and depositing,” 4 985 114, Jan. 1991.

[361] M. Kintel, *Openscad: The programmers Solid 3D CAD modeller*, version 2019.05.

[362] N. Otsu, “A threshold selection method from gray-level histograms,” *IEEE transactions on systems, man, and cybernetics*, vol. 9, no. 1, pp. 62–66, 1979.

[363] A. Andrei, M. Welkenhuysen, B. Nuttin, and W. Eberle, “A response surface model predicting the in vivo insertion behavior of micromachined neural implants,” *Journal of Neural Engineering*, vol. 9, no. 1, 2012.

[364] M. R. Marks, K. Y. Cheong, and Z. Hassan, “A review of laser ablation and dicing of Si wafers,” *Precision Engineering*, vol. 73, no. March 2021, pp. 377–408, 2022.

[365] J.-H. Chang, P.-L. Chen, C.-C. Huang, G.-H. Cao, and J.-Y. Wang, “Alternative dicing solution of multi-project wafer (mpw) by stealth dicing,” in *2016 IEEE 18th Electronics Packaging Technology Conference (EPTC)*, 2016, pp. 277–280.

[366] D. Hartl, D. Lagoudas, R. Malak, M. Frecker, and Z. Ounaies, “Active materials and structures for origami engineering,” *Smart Materials and Structures*, vol. 23, no. 9, p. 090 201, Aug. 2014.

[367] S. Franssila, *Introduction to microfabrication*. John Wiley & Sons, 2010.

[368] R. Wang, W. Zhao, W. Wang, and Z. Li, “A flexible microneedle electrode array with solid silicon needles,” *Journal of microelectromechanical systems*, vol. 21, no. 5, pp. 1084–1089, 2012.

[369] A. Mills, “Porous platinum morphologies: Platinised, sponge and black,” *Platinum Metals Review*, vol. 51, no. 1, p. 52, 2007.

[370] P. Sullivan, A. Tsiamis, M. Rondé, A. Walton, S. Smith, and J. Terry, “Automated generation, fabrication and measurement of parametric test structures for rapid prototyping using optical maskless lithography,” in *2020 IEEE 33rd International Conference on Microelectronic Test Structures (ICMTS)*, 2020, pp. 1–6.

[371] A. Kuzminienė, S. Šalomskaitė-Davalgienė, I. Balnyte, J. Palubinskienė, A. Valančiūtė, and V. Ulozas, “Evaluation of the chicken embryo chorioallantoic membrane model for laryngeal tumor transplantation,” *Papers on Anthropology*, vol. 20, p. 229, 2012.

[372] V. F. Maksimov, I. M. Korostyshevskaya, and S. A. Kurganov, “Functional morphology of chorioallantoic vascular network in chicken,” *Bulletin of Experimental Biology and Medicine*, vol. 142, no. 3, pp. 367–371, 2006.

[373] A. Balic *et al.*, “Visualisation of chicken macrophages using transgenic reporter genes: Insights into the development of the avian macrophage lineage,” *Development (Cambridge)*, vol. 141, no. 16, pp. 3255–3265, 2014.

[374] V. Hamburger and H. L. Hamilton, “A series of normal stages in the development of the chick embryo,” *Developmental dynamics*, vol. 195, no. 4, pp. 231–272, 1992.

[375] M. P. Tesarova, M. Skoupa, M. Foltyn, Z. Tvrdon, and M. Lichovnikova, “Research note: Effects of preincubation and higher initiating incubation temperature of long-term stored hatching eggs on hatchability and day-old chick and yolk sac weight,” *Poultry science*, vol. 100, no. 8, pp. 101 293–101 293, 2021.

[376] S. Taqi, S. Sami, L. Sami, and S. Zaki, “A review of artifacts in histopathology,” *Journal of oral and maxillofacial pathology : JOMFP*, vol. 22, no. 2, pp. 279–279, 2018.

[377] J. Ahrens, B. Geveci, and C. Law, *ParaView: An End-User Tool for Large Data Visualization, Visualization Handbook*. Elsevier, 2005.

[378] A. Fedorov *et al.*, “3d slicer as an image computing platform for the quantitative imaging network,” *Magnetic resonance imaging*, vol. 30, no. 9, pp. 1323–1341, 2012.

[379] B. Inc. “3d slicer - image computing platform.” (Aug. 9, 2021), [Online]. Available: `https://www.slicer.org` (visited on 11/01/2021).

[380] S. Rolfe *et al.*, “Slicermorph: An open and extensible platform to retrieve, visualize and analyse 3d morphology,” *Methods in ecology and evolution*, vol. 12, no. 10, pp. 1816–1825, 2021.

[381] P. Nowak-Sliwinska, T. Segura, and M. L. Iruela-Arispe, “The chicken chorioallantoic membrane model in biology, medicine and bioengineering,” *Angiogenesis*, vol. 17, no. 4, pp. 779–804, 2014.

[382] R. Bellairs and M. Osmond, “Extra-embryonic membranes,” in *Atlas of Chick Development*, Third edition., Academic Press, 2014, pp. 127–129.

[383] D. Ribatti, A. Vacca, G. Ranieri, S. Sorino, and L. Roncali, “The chick embryo chorioallantoic membrane as an in vivo wound healing model,” *Pathology Research and Practice*, vol. 192, no. 10, pp. 1068–1076, 1996.

[384] S. Majumder, M. Ilayaraja, H. R. Seerapu, S. Sinha, J. H. Siamwala, and S. Chatterjee, “Chick embryo partial ischemia model: A new approach to study ischemia Ex Vivo,” *PLoS ONE*, vol. 5, no. 5, 2010.

[385] G. Zwadlo-Klarwasser, K. Görlitz, B. Hafemann, D. Klee, and B. Klosterhalfen, “The chorioallantoic membrane of the chick embryo as a simple model for the study of the angiogenic and inflammatory response to biomaterials,” *Journal of Materials Science: Materials in Medicine*, vol. 12, no. 3, pp. 195–199, 2001.

[386] N. P. LÜPKE, “The hen’s egg test (HET)—an alternative toxicity test,” *British Journal of Dermatology*, vol. 115, pp. 133–135, 1986.

[387] R. Adam *et al.*, “The avian chorioallantoic membrane in ovo - A useful model for bacterial invasion assays,” *International Journal of Medical Microbiology*, vol. 292, no. 3-4, pp. 267–275, 2002.

[388] N. A. Lokman, A. S. F. Elder, C. Ricciardelli, and M. K. Oehler, “Chick chorioallantoic membrane (cam) assay as an in vivo model to study the effect of newly identified molecules on ovarian cancer invasion and metastasis,” *International Journal of Molecular Sciences*, vol. 13, no. 8, pp. 9959–9970, 2012.

[389] J. Eckrich *et al.*, “Monitoring of tumor growth and vascularization with repetitive ultrasonography in the chicken chorioallantoic-membrane-assay,” *Scientific Reports*, vol. 10, no. 1, pp. 1–14, 2020.

[390] J. Azzarello, M. A. Ihnat, B. P. Kropp, L. A. Warnke, and H. K. Lin, “Assessment of angiogenic properties of biomaterials using the chicken embryo chorioallantoic membrane assay,” *Biomedical Materials*, vol. 2, no. 2, pp. 55–61, 2007.

[391] L. F. N. Dourado, C. N. da Silva, R. G. Arribada, and A. d. S. C. Júnior, “Assessment of Biocompatibility and Vascular Effects of Polymeric Materials Using Chick Chorioallantoic Membrane, an Alternative Method,” *Macromolecular Symposia*, vol. 394, no. 1, pp. 1–5, 2020.

[392] K. Spanel-Borowski, “The chick chorioallantoic membrane as test system for biocompatible materials,” *Research in Experimental Medicine*, vol. 189, no. 1, pp. 69–75, 1989.

[393] U. Klueh, D. I. Dorsky, F. Moussy, and D. L. Kreutzer, “Ex ova chick chorioallantoic membrane as a novel model for evaluation of tissue responses to biomaterials and implants,” *Journal of Biomedical Materials Research - Part A*, vol. 67, no. 3, pp. 838–843, 2003.

[394] T. I. Valdes, U. Klueh, D. Kreutzer, and F. Moussy, “Ex ova chick chorioallantoic membrane as a novel in vivo model for testing biosensors,” *Journal of Biomedical Materials Research - Part A*, vol. 67, no. 1, pp. 215–223, 2003.

[395] D. Ribatti, “The chick embryo chorioallantoic membrane (CAM) assay,” *Reproductive Toxicology*, vol. 70, pp. 97–101, 2017.

[396] E. Dondossola and P. Friedl, “Host responses to implants revealed by intravital microscopy,” *Nature Reviews Materials*, vol. 7, no. 1, pp. 6–22, 2022.

[397] W. S. Lusimbo, F. A. Leighton, and G. A. Wobeser, “Histology and ultrastructure of the chorioallantoic membrane of the mallard duck (Anas platyrhynchos),” *Anatomical Record*, vol. 259, no. 1, pp. 25–34, 2000.

[398] B. Kundeková, M. Máčajová, M. Meta, I. Čavarga, and B. Bilčík, “Chorioallantoic membrane models of various avian species: Differences and applications,” *Biology*, vol. 10, no. 4, pp. 1–24, 2021.

[399] P. Kunz, A. Schenker, H. Sähr, B. Lehner, and J. Fellenberg, “Optimization of the chicken chorioallantoic membrane assay as reliable in vivo model for the analysis of osteosarcoma,” *PLoS ONE*, vol. 14, no. 4, pp. 1–16, 2019.

[400] J. Tannenbaum and B. T. Bennett, “Russell and Burch’s 3Rs then and now: The need for clarity in definition and purpose,” *Journal of the American Association for Laboratory Animal Science*, vol. 54, no. 2, pp. 120–132, 2015.

[401] D. Ribatti, *The chick embryo chorioallantoic membrane in the study of angiogenesis and metastasis Domenico Ribatti.* Dordrecht: Springer, 2010.

[402] *Sturkie’s avian physiology / edited by G. Causey Whittow.* 5th edition. San Diego: Academic Press, 2000.

[403] B. D. Jankovic, K. Isakovic, M. L. Lukic, N. L. Vujanović, S. Petrović, and B. M. Marković, “Immunological capacity of the chicken embryo. I. Relationship between the maturation of lymphoid tissues and the occurrence of cell mediated immunity in the developing chicken embryo,” *Immunological Communications*, vol. 29, no. 3, pp. 497–508, 1975.

[404] D. Ribatti, B. Nico, A. Vacca, L. Roncali, and M. Presta, “Endogenous and exogenous fibroblast growth factor-2 modulate wound healing in the chick embryo chorioallantoic membrane,” *Angiogenesis*, vol. 3, no. 1, pp. 89–95, 1999.

[405] W. Huang, M. Itayama, F. Arai, K. S. Furukawa, T. Ushida, and T. Kawahara, “An angiogenesis platform using a cubic artificial eggshell with patterned blood vessels on chicken chorioallantoic membrane,” *PLoS ONE*, vol. 12, no. 4, pp. 1–20, 2017.

[406] C. D. McCaig, A. M. Rajnicek, B. Song, and M. Zhao, “Controlling cell behavior electrically: Current views and future potential,” *Physiological Reviews*, vol. 85, no. 3, pp. 943–978, 2005.

[407] D. C. Deeming, “The role of egg turning during incubation,” *Avian Biology Research*, vol. 2, no. 1-2, pp. 67–71, 2009.

[408] D. Narinç, S. Erdoğan, E. Tahtabiçen, and T. Aksoy, “Effects of thermal manipulations during embryogenesis of broiler chickens on developmental stability, hatchability and chick quality,” *Animal*, vol. 10, no. 8, pp. 1328–1335, 2016.

[409] R. M. Noiva, A. C. Menezes, and M. C. Peleteiro, “Influence of temperature and humidity manipulation on chicken embryonic development,” *BMC Veterinary Research*, vol. 10, no. 1, pp. 1–10, 2014.

[410] N. Mangir, S. Dikici, F. Claeyssens, and S. Macneil, “Using ex Ovo Chick Chorioallantoic Membrane (CAM) Assay to Evaluate the Biocompatibility and Angiogenic Response to Biomaterials,” *ACS Biomaterials Science and Engineering*, vol. 5, no. 7, pp. 3190–3200, 2019.

[411] K. Ausen, M. L. Kroknes, G. Gunnarson, and A. Radtke, “Applying Unsterile Microporous Tape onto Surgical Wounds: Tape Contamination and Clinical Rationale,” *Plastic and Reconstructive Surgery - Global Open*, pp. 1–7, 2021.

[412] R. Gentry and C. Quarles, “The Measurement of Bacterial Contamination on Egg Shells,” *Poultry Science*, vol. 51, no. 3, pp. 930–933, 1972.

[413] K. De Reu *et al.*, “Eggshell factors influencing eggshell penetration and whole egg contamination by different bacteria, including Salmonella enteritidis,” *International Journal of Food Microbiology*, vol. 112, no. 3, pp. 253–260, 2006.

[414] A. Nakagawa, K. V. Alt, K. D. Lillemoe, C. Fernández-del Castillo, A. L. Warshaw, and A. S. Liss, “A method for fixing and paraffin embedding tissue to retain the natural fluorescence of reporter proteins,” *BioTechniques*, vol. 59, no. 3, pp. 153–155, 2015.

[415] G. J. Burton and M. E. Palmer, “The chorioallantoic capillary plexus of the chicken egg: A microvascular corrosion casting study,” *Scanning Microscopy*, vol. 3, no. 2, pp. 549–558, 1989.

[416] Y. C. Kim, J. H. Park, and M. R. Prausnitz, “Microneedles for drug and vaccine delivery,” *Advanced Drug Delivery Reviews*, vol. 64, no. 14, pp. 1547–1568, 2012.

[417] J. H. Lee, T. S. Lim, Y. Seo, P. L. Bishop, and I. Papautsky, “Needle-type dissolved oxygen microelectrode array sensors for in situ measurements,” *Sensors and Actuators, B: Chemical*, vol. 128, no. 1, pp. 179–185, 2007.

[418] P. J. Rousche and R. A. Normann, “Chronic intracortical microstimulation (ICMS) of cat sensory cortex using the utah intracortical electrode array,” *IEEE Transactions on Rehabilitation Engineering*, vol. 7, no. 1, pp. 56–68, 1999.

[419] Y. Wang, B. L. Tai, R. K. Chen, and A. J. Shih, “The needle with lancet point: Geometry for needle tip grinding and tissue insertion force,” *Journal of Manufacturing Science and Engineering, Transactions of the ASME*, vol. 135, no. 4, pp. 1–7, 2013.

[420] A. C. Barnett, J. A. Jones, Y. S. Lee, and J. Z. Moore, “Compliant needle vibration cutting of soft tissue,” *Journal of Manufacturing Science and Engineering, Transactions of the ASME*, vol. 138, no. 11, pp. 1–9, 2016.

[421] J. Eom, S. J. Park, and B. H. Lee, “ Noncontact photoacoustic tomography of in vivo chicken chorioallantoic membrane based on all-fiber heterodyne interferometry,” *Journal of Biomedical Optics*, vol. 20, no. 10, p. 106 007, 2015.

[422] E. Adjanohoun, *Egg candling method*, European patent: EP20120184782 20090806, 2018.

[423] S. Saifullah, “K-Means Clustering for Egg Embryo’S Detection Based-on Statistical Feature Extraction Approach of Candling Eggs Image,” *Sinergi*, vol. 25, no. 1, p. 43, 2020.

[424] M. Hashemzadeh and N. Farajzadeh, “A Machine Vision System for Detecting Fertile Eggs in the Incubation Industry,” *International Journal of Computational Intelligence Systems*, vol. 9, no. 5, pp. 850–862, 2016.